Large Eddy Simulation of Turbulent Supersonic Combustion and Characteristics of Supersonic Flames

Wenlei Luo

Submitted in accordance with the requirements for the degree of
Doctor of Philosophy

Under the supervision of

Professor Mohamed Pourkashanian

Professor Derek Ingham

Dr Lin Ma

The University of Leeds

School of Chemical and Process Engineering

Energy Technology and Innovation Initiative (ETII)

September, 2014

The candidate confirms that the work submitted is his own, except where work which has formed part of jointly authored publications has been included. The contribution of the candidate and the other authors to this work has been explicitly indicated below. The candidate confirms that appropriate credit has been given within the thesis where reference has been made to the work of others.

The work contained within this thesis is my own primary research. The other authors were my supervisors who acted in an advisory role and gave suggestions regarding the research direction and analysis methods.

Achievements and publications

International conferences:

- W. Luo, L. Ma, D.B. Ingham, M. Pourkashanian, Z. Fan and W. Huang, Numerical investigation of reacting flow in a scramjet engine using flamelet and flamelet/progress variable models, 8th Mediterranean Combustion Symposium, Cesme, September 8-13, 2013. (Chapter 5)

Journal papers:

- Zhouqin Fan, Weidong Liu, Mingbo Sun, Zhenguo Wang, Fengchen Zhuang, Wenlei Luo, Theoretical analysis of flamelet model for supersonic turbulent combustion. Science China Technological Sciences, 2012. 55(1): p. 193-205. (Cited as a reference)
- W. Luo, M. Pourkashanian, D.B. Ingham, L. Ma, Hybrid Reynolds-Averaged Navier-Stokes/Large Eddy Simulation of supersonic combustion with a strut flame holder using flamelet and unsteady flamelet/progress variable models, in preparation. (Chapter 5)
- W. Luo, M. Pourkashanian, D.B. Ingham, L. Ma, Z. Fan, Characteristics of a supersonic flame and flameholding mechanisms in a cavity-based supersonic combustor, in preparation. (Chapter 6)

Acknowledgements

I would like to express my sincere gratitude to my primary supervisor, Professor Mohamed Pourkashanian, for offering me an opportunity to pursue a PhD under his guidance and for his steadfast support. Also I thank him for considering my research interests carefully and providing the excellent world-class computing facilities to perform my research work.

I wish to express my deep sense of gratitude to my co-supervisors, Professor Derek Ingham and Dr Lin Ma, for the immense patience, support and encouragement that they have given to me. I also would like to express my very great appreciation to them for considering my ideas and interests carefully and keeping me on track. Also, I am particularly grateful for the support and assistance given by Professor Zhenguo Wang, in the National University of Defense Technology in China.

Further, I would like to acknowledge the help provided by Dr Kevin Hughes, Miss Lisa Flaherty and Miss Charlotte Kelsall. Also, I am grateful to the following people who have helped me, Mr. Yang Fei, Mr. Guangyuan Xu, Miss Yanling Yang, Mr. Guangping Dong, Miss Fangting Hu, Mr. Jun Yang, Mr. Xin Yang, Mr. Chunlei Ren, Mr. Ning Wang, Dr Mingbo Sun and Dr Zhouqin Fan.

I give my gratitude to the financial support from the University of Leeds and China Scholarship Council (CSC) for funding my studies and living costs in Leeds.

Finally, I extremely appreciate the support that I received from my family and Miss Yuanyuan Zhou for being very supportive especially at hard times.

Abstract

In this thesis we investigate the supersonic combustion in scramjet combustors with strut and cavity flame holders through the Reynolds-Averaged Navier–Stokes (RANS) and Large Eddy Simulation (LES) strategies.

Firstly, the Unsteady Flamelet/Progress Variable (UFPV) model for turbulent combustion in low-speed flows is introduced and extended to supersonic flows and a new strategy is developed to create probability density function look-up tables for the UFPV model.

Secondly, the RANS modelling is employed to a strut-based scramjet combustor using the flamelet and UFPV models and the latter shows a better performance. Subsequently, the LES modelling is performed with the UFPV model and the UFPV model gives good predictions on comparing the numerical results to the experimental data.

Thirdly, the LES modelling is employed to a cavity-based scramjet combustor. The results obtained indicate that the local extinction and autoignition events are very common phenomena in the supersonic flame and the UFPV model is able of predicting these events with reasonable accuracy. Further, an activation-energy-asymptotic-based Damköhler number concept is a valuable metric to identify flame weakening and extinction in supersonic flames. Together with the OH radicals, the distribution of the HO_2 radicals can assist in identifying the autoignition events in the supersonic flame.

Finally, analysing the flameholding mechanisms of the cavity, it is found that the cavity provides a stable ignition source to the fluid. Further, the combustion in the cavity is dominated by flame propagation. However, on the outer interface of the air and hydrogen streams, the combustion is mainly dominated by autoignition. Both autoignition and flame propagation contribute to the combustion in the mixing layer. Also the combustion in the cavity mixing layer has effects on the induction reactions in the wake of the hydrogen jet and reduces the induction time of the autoignition.

Contents

Figures

Tables

Nomenclature

Roman Letters

A	Area of the combustor, [m^2]
C	Reaction progress variable
c_p, C_p	Specific heat at constant pressure, [J/kg/K]
C_s	Smagorinsky constant
D	Diffusion coefficient, [m^2/s]
D^{sgs}	Dissipation of the subgrid-scale kinetic energy, [$kg/m/s^3$]
Da	Damköhler number
e, E	Internal energy per unit mass, [J/kg]
f	Mixture fraction
$\widetilde{f''^2}$	Variance of the mixture fraction
$f(\ )$	Generic function
F	Blending function
$G(\ )$	Convolution kernel
h, H	Enthalpy per unit mass, [J/kg]
k	Turbulent kinetic energy, [J/kg]
Ma	Mach number
Ns	Number of the chemical species
P	Pressure, [Pa]

$P(\ )$	Probability density function
P_k	Production of the turbulent kinetic energy, [kg/m/s^3]
Pr	Prandtl number
q	Heat flux, [W/m^2]
R	Ideal gas constant, [J/mol/K]
Re	Reynolds number
S_{ij}	Large scale velocity tensor, [1/s]
Sc	Schmidt number
t, T	Time, [s]
T	Temperature, [K]
u	Velocity, [m/s]
U	Mean velocity [m/s], conservative flux
x_i	Cartesian direction components
X	Location in the streamwise direction, [m]
Y	Mass fraction
Y	Location in the transverse direction, [m]
Z	Location in the spanwise direction, [m]

Greek Letters

$\beta(\ )$	Beta function

Γ	Diffusive transport coefficient, [1/s]
$\delta( )$	Delta function
Δ	Grid filter width [m] or difference operator
$\overline{\Delta}$	Grid filter width, [m]
ε	Turbulent dissipation rate, [J/kg/s]
λ	Reaction progress parameter
μ	Dynamic viscosity (laminar), [kg/m/s]
μ_t	Dynamic eddy viscosity (turbulent), [kg/m/s]
ξ, η, ζ	Coordinates in the computational domain
ρ	Density, [kg/m^3]
τ	Stress tensor, [Pa]
τ_{ij}^{sgs}	Sub-grid scale stress, [Pa]
ϕ	Generic scalar variable
χ	Scalar dissipation rate, [1/s]
ω	Specific dissipation rate, [1/s]
$\dot{\omega}$	Reaction rate, [kg/m^3/s]
Ω	Spatial discretization operator

Diacritical Marks

$\tilde{\phi}$	Favre averaged or Favre filtered value of ϕ

$\overline{\phi}$	Reynolds averaged or mean of ϕ
$\phi^{"}$	Fluctuations of ϕ

Subscripts and Superscripts

AEA	Large activation energy asymptotic analysis
C	Reaction progress variable
eff	Effective
fuel	Fuel
H	Hydrogen element
hyb	Hybrid
i	Cartesian directions or element *i*
j	Cartesian directions
k	Cartesian directions or turbulent kinetic energy
m	Chemical species
max	Maximum
min	Minimum
O	Oxygen element
ox	Oxidiser
ref	Reference state or value
rms	Root mean square

st	Stoichiometric
sgs	Sub-grid scale
t	Turbulent

Abbreviations

2D	2-Dimensional
3D	3-Dimensional
AEA	Activation Energy Asymptotic Analysis
CFD	Computational Fluid Dynamics
CFL	Courant-Friedrichs-Lewy
CMC	Conditional Moment Closure
DNS	Direct Numerical Simulation
FPV	Flamelet/Progress Variable
LES	Large Eddy Simulation
PDF	Probability Density Function
RANS	Reynolds Averaged Navier Stokes
RMS	Root Mean Square
SGS	Subgrid Scale
SLFM	Steady Laminar Flamelet Model
UFPV	Unsteady Flamelet/Progress Variable

Chapter 1
Introduction

1.1. Introduction

The ramjet, with a subsonic air speed at its combustion chamber entrance, is a remarkable air-breathing engine, which is an invention attributed to Rene Lorin in 1913. A typical ramjet engine is schematically shown in Figure 1.1 [1]. Above a flight Mach number of about 3, cycles using rotating machinery, compressors, etc., become inefficient, and actually are no longer required to increase the pressure, which can be achieved through an internal geometry change. The change in the structure extends the operation beyond the flight speed when the gas turbine engine is not efficient.

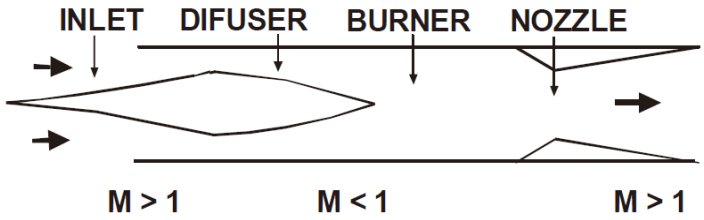

Figure 1.1 Schematic of a typical ramjet engine [1].

As the Mach number increases further, the pressure losses and the elevated temperature, led by shock waves, preclude completion of the combustion, which results in energy loss. If the flow in the combustor is maintained to be supersonic, heat will be added through combustion in the supersonic flow. For hypersonic vehicles, this way of combustion is efficient, and this kind of ramjet is called the supersonic combustion ramjet, i.e. scramjet. However, the supersonic combustion phenomena do not only take place in scramjets. Therefore, for a better understanding

of the supersonic combustion phenomena, and the optimization of the combustion performance of scramjets, it is essential to clarify the concept of supersonic combustion [2].

What does supersonic combustion mean? There are two kinds of definitions for its literal meaning [3]. Firstly, supersonic combustion can be understood as the combustion in supersonic flows; secondly, it can be defined as the combustion for which the velocity to the unburned gases is higher than the sound speed of the unburned gases. According to the first definition, all combustion in supersonic flows is supersonic combustion, no matter whether the reacting flow is supersonic or not. In contrast, subsonic combustion should be understood to be the combustion in subsonic flow. Evidently, on the one hand, the first definition does not reflect the physical mechanisms of combustion, which should not depend on a changeable reference system [4], and on the other hand, the first definition does not take the changeable reference system into account. However, the second definition reflects both of them. Therefore, more strictly in the viewpoint of combustion mechanisms, one should choose the second definition for supersonic combustion. Thus, supersonic combustion is the combustion where the velocity between the combustion zone and the unburned gas is higher than that of the sonic of the unburned gas [3]. Then the concepts of subsonic and supersonic combustion can correspond to the concepts of deflagration and detonation [5]. However, the first definition emphasizes the flow in general, and is related to the scope of the combustion investigation. To distinguish the above two definitions, the first definition is referred to as “combustion in supersonic flow”.

1.1.1. Supersonic combustion ramjet engine cycle

A typical scramjet engine is mainly composed of an inlet, isolator section, combustion chamber and nozzle [6,7]. The traditional scramjet engine is

schematically shown in Figure 1.2 [1]. The inflow air at supersonic speeds is compressed and then expands to a lower, albeit still supersonic speed at the entrance of the combustor. Gas or liquid fuel is injected (transverse, streamwise or at an angle) from the walls and/or in the stream (such as struts, tubes, pylons, etc.). The fuel begins to mix with the air. Then the igniter ignites the mixture. If the temperature is high enough, an igniter is not necessary. The mixture burns in a generally diverging combustor. A flame holder is always required to maintain the combustion in supersonic flows.

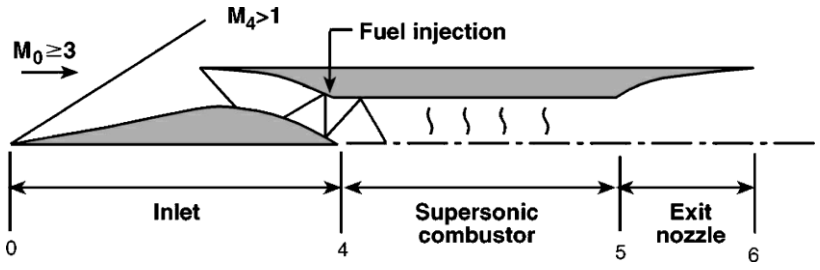

Figure 1.2 Schematic of a traditional scramjet engine [1].

A shock train, which may vary in strength between the equivalent of a normal and no shock, located upstream of the combustor entrance. It is generated by the combined effects of heat addition, diverging area in the scramjet combustor, and the absence of a geometric exit nozzle throat. The strength of this shock train depends mainly on the flight conditions, inlet compression or inlet exit Mach number M_4, overall engine fuel/air ratio, and supersonic combustor area ratio (A_5/A_4). This shock train is different to the subsonic combustion ramjet's terminal normal shock system.

From Figures 1.1 and 1.2, we can see the differences between the ramjet and scramjet. The ramjet requires a physical throat in the nozzle to maintain the desired inlet conditions and thus form a subsonic flow in the combustor. In contrast, the scramjet combustor has an increasing area as heat is released through combustion in

the supersonic flow. The gas expands in the nozzle, and then the heat energy of the gas is converted into kinetic energy.

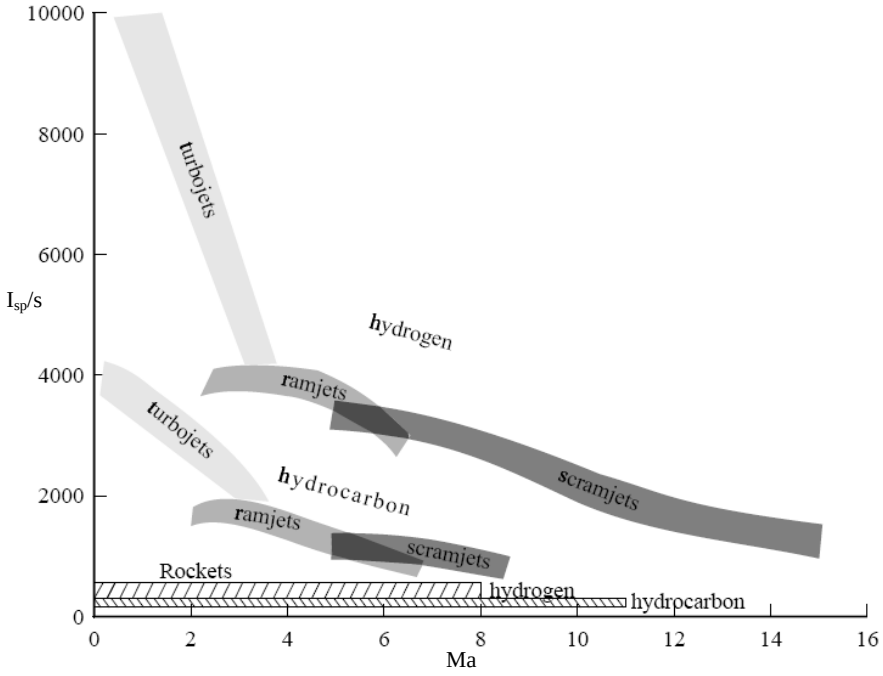

Figure 1.3 Specific impulses of rocket propulsion and several air-breathing cycles, i.e. ramjets, scramjets and turbojets [8].

Figure 1.3 shows the specific impulses of rocket propulsion and several air-breathing cycles, i.e. ramjets, scramjets and turbojets [8]. This figure indicates the advantage of the scramjet engine when the flight Mach number is larger than about 6. Also it shows that the scramjet is currently the most promising engine for hypersonic flight. Table 1.1 indicates a comparison of several important parameters for the ramjet and scramjet, which have the same speed and inlet contraction ratios, at a flight Mach number of 12 and at an altitude of 40 km [9]. Hydrogen is used as the fuel and it is added downstream of the inlet in both cases. For the ramjet, it is assumed that a normal shock is produced at the end of the inlet by the correct selection of the nozzle area.

Table 1.1 Comparison of several important parameters between the ramjet and scramjet [9].

Combustor Chamber Entrance	**Supersonic**	**Subsonic**	**Combustion Chamber Exit**	**Supersonic**	**Subsonic**
Ratio of burner entrance to capture area	0.023	0.023	Ratio of exit area to capture area	0.061	0.024
Stagnation pressure recovery	0.5	0.013	Ratio of nozzle throat to capture area	0.061	0.015
Pressure (atm)	2.7	75	Pressure (atm)	2.7	75
Temperature (K)	1250	4500	Temperature (K)	2650	4200
Mach number	4.9	0.33	Mach number	3.3	0.38

From Table 1.1, we can see that there are significant differences in the stagnation pressure recovery between the two cases. Because of the absence of a normal shock, the stagnation pressure recovery is about 30 times less in the subsonic combustion ramjet in comparison with the scramjet. This means that the ramjet will lose more engine thrust than does the scramjet [10]. Another important difference between the subsonic and supersonic combustion ramjet is the temperature in the combustion chamber entrance. The temperature at the subsonic case is 4500K, which is quite large and will lead to severe dissociation problems. Thus, the subsonic combustion chamber becomes overheated. Under this high temperature, recombination reactions cannot take place in the combustor. Heat release occurs only in the nozzle, where the temperature decreases due to the expansion effect.

Thus, the nozzle has to be sufficiently long to ensure that the reaction is fulfilled. The nozzle is very long and heavy. In contrast, the scramjet has a considerably lower pressure loss and temperature. Finally, the scramjet is of lighter construction and has an overall increase in system efficiency [1].

Although the scramjet offers these unique capabilities, from the point of view of technology, the cycle of the scramjet engine has a large number of complex technical problems and challenges because of the low static temperatures and short combustor residence times (of the order of 1 ms). How to achieve highly efficient and stable supersonic combustion in the combustor is the most basic and difficult critical technology. Over more than 50 years of effort and exploration by scientists and engineers, some of the key technologies have been overcome, but the supersonic flow and combustion mechanisms is still a conundrum which needs much more depth and meticulous investigation [11].

1.1.2. History and evolution of scramjet development

The scramjet, due to its relative simple structure and good performance, has become the first choice for vehicles whose cruising Mach number is in the range 5 to 15 [7]. During the last fifty years, the scramjet has drawn the researchers' attention and become quite a hot topic in aerospace and aeronautic research. The interest in the scramjet has grown to global proportions [12], and in some countries, such as the US, Russia, Germany, China, Australia, India, etc., much effort has been invested into this undoubted challenging research field [13]. Significant progress has been made in the development of hypersonic technology, particularly in the field of scramjet engines.

Many excellent review papers have chronicled international scramjet development [14,13,15-21]. Ferri [14] reviewed the scramjet technology in 1968. Waltrup et al. [15] reviewed US scramjet development in 1976, international

supersonic combustion development [16] in 1987, ramjet and scramjet propulsion development for the US Navy missiles in 1997 [17], the US Navy scramjet and mixed-cycle engine development in 2002 [18]. Andrews provided a review of NASA's hypersonic research engine project in 1993 [19] and a historical review of scramjet development and testing in the US in 2001 [20]. Curran [13] provided a general review of the first 40 years of international scramjet engine development in 2001. Fry [21] presented a very thorough development history and principal contributing development programs of the ramjet and scramjet. In 2005, Hallion [12] reviewed the history of hypersonics and divided it into several eras. The eras are "Round One and Two: From X-1 Through X-15 and Related Efforts, 1946-1968", "Round Three: Concepts and Programs for Global Hypersonic Flight, 1952-1964", "The Transatmospheric Imperative, 1964-1995", and "Hypersonics in the Post-NASP Era". In 2001, McClinton et al. [22] discussed the scramjet development in the US in terms of generations. They divided the scramjet development history into four generations: the first generation 1960–1973, the second generation 1969–1984, the third generation 1984–1994, and the fourth generation from 1995-today. The four generations, each of which is distinguished by its unique contributions of the understanding level of supersonic combustion, are subsequently listed. Fry [21] summarizes the scramjet evolution in the era from 1955 to today and provides originating country, engine/vehicle names, development dates, performance, physical characteristics, and state of development. There are several categories about the generation of scramjet development. In this report, we adopt the classification used by Fry [21].

1.1.2.1. The first generation scramjet development (Beginning: 1946–1973)

Along with the development of ramjet engines, the concept of adding heat to a supersonic airstream was advanced in the latter past of the 1940s [1]. Then,

supersonic combustion ramjets became a hot topic for hypersonic vehicles. The first generation of scramjet development witnessed the start of worldwide major scramjet development projects, which demonstrated the merits of the scramjet in hypersonic propulsion. During this era, the scramjet was well developed by worldwide scientists and engineers.

More closely related to the evolution of hypersonic vehicles was the progressive march of the X-series of supersonic and hypersonic explorers, the rocket-propelled transonic and supersonic research aircraft of 1946-1959, and the hypersonic X-15 from 1959 to 1968 [12]. The US Air Force, NASA, and the US Navy sponsored a number of programs. These programs were contracted by Marquardt, General Electric, United Technology Research Center (UTRC), Garrett, and General Applied Sciences Laboratory (GASL). These contractors tested the scramjet engine flowpaths at no large than about Mach 7. Most tests utilized hydrogen as the fuel and the US Air Force utilized hydrocarbons as well.

The first known scramjet was a fixed-geometry engine model designed by Ferri in 1960 [21]. This scramjet model was fabricated, and was tested in the GASL combustion-heated high-enthalpy blowdown tunnel in 1963. These tests demonstrated that scramjets can be a viable propulsion system for hypersonic vehicles. The first generation scramjet development, which was the early, large and notable projects in the US, was the NASA Hypersonic Research Engine (HRE) project. A pretest model of the HRE is given by Figure 1.4. The HRE project was started in 1964. Its goals were to build and test hypersonic geometry variable, hydrogen fueled and cooled ramjet–scramjet engines, which were to be flight tested on the rocket-powered X-15A-2. The program progressed through numerous tests on the components, including inlet, combustor, and nozzle, flowpath tests. During the HRE program, 107 tests were performed on the dual-model scramjet engines. From these tests, scientists obtained an important and comprehensive database on the inlet

and combustor performance at Mach 5-7. During the 1960s, combined cycle propulsion attracted the researchers' attention as well, such as the Rocket-Based Combined Cycle (RBCC). The early Marquardt Ejector Ramjet (ERJ) engine is a precursor of today's RBCC engines.

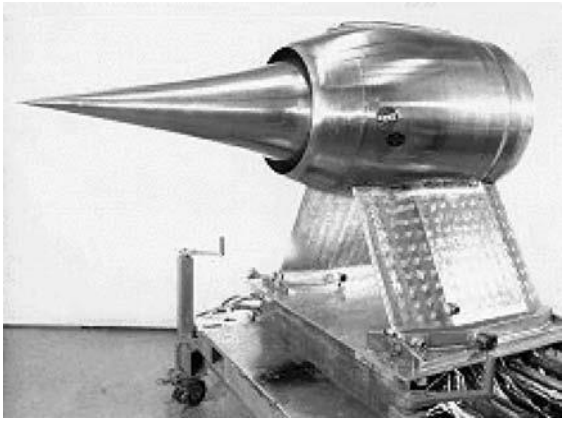

Figure 1.4 A prototype model of the HRE [1].

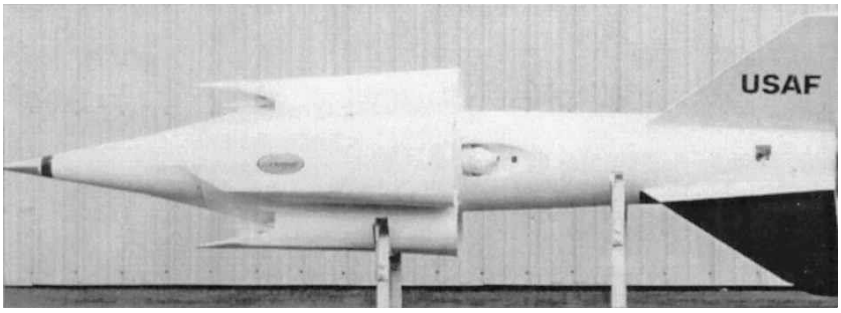

Figure 1.5 The US Air Force IFTV concept [23].

The US Air Force utilized hydrocarbons, and the US Navy (APL) performed several different hydrocarbon studies in the Supersonic Combustion Ramjet (SCRAM) project. The US Air Force funded the Scramjet Incremental Flight Test Vehicle (IFTV) program, which was initiated in April 1965. Figure 1.5 gives a photograph of the vehicle of the IFTV concept [23]. Another interesting engine concept, which was called the low-speed fixed geometry supersonic combustion ramjet, was developed at GASL under the US Air Force sponsorship program in

1964–1968. A model of the low-speed fixed geometry supersonic combustion ramjet is given in Figure 1.6 [23].

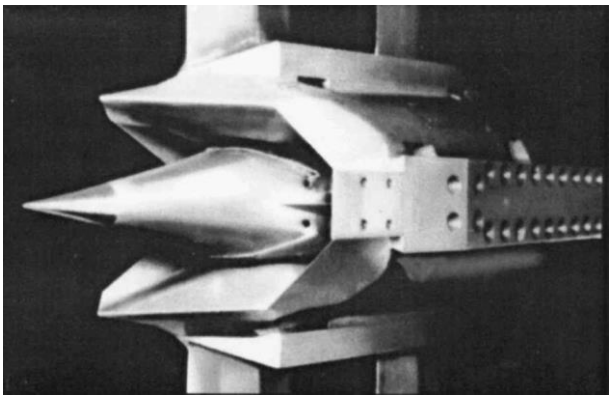

Figure 1.6 Low-speed fixed geometry supersonic combustion ramjet [23].

In the mid of 1950s, the US Navy initiated the support of hypersonic propulsion research activities, known as the ERJ program performed by JHU/APL. The goal of this program was to demonstrate the feasibility of burning fuels on the underside of wings when flying at supersonic or hypersonic speeds. This program led to the following Supersonic Combustion Ramjet Missile (SCRAM) program, which was initiated by the US Navy in 1961 and terminated in 1977. The SCRAM program was to develop and demonstrate the necessary technology for scramjet-powered missiles. A number of inlets, isolators, fuel injectors, liquid and gaseous fuels, ignition aids, and combustors were tested between Mach 3 and 8. Generally speaking, the SCRAM program was successful. However, there were still some shortcomings [21]: (i) logistically unsuitable pyrophoric and toxic liquid fuels and blends, (ii) absence of sufficient room to house an active seeker, and (iii) passive cooling requirements for the entire vehicle.

In Europe, interest in supersonic combustion paralleled that in the United States throughout the 1960s and 1970s. Virtually at the same time as the HRE, the USSR began their scramjet research in the late 1950s and had an extensive program

in supersonic combustion and scramjet propulsion since the 1960s. In 1966, France initiated the ESOPE program. Similar to HRE, the ESOPE was to demonstrate a dual-mode scramjet in a flight-test program at Mach 7. During the period 1970 to 1972, a number of ground tests were performed in Europe.

In the 1960s, Canada began her research on supersonic combustion at MacGill University. The research was mainly on hypersonic inlet aerodynamics and gun launched scramjet flight testing. In Germany, most of the reported work was on fundamental supersonic combustion. In France, both fundamental and applied research was being pursued. In the early 1970s, connected pipe tests were conducted by the French National Aerospace Research Center (ONERA) at Mach 6 conditions.

After a decade of effort, the performance and operability of the scramjet was successfully demonstrated [14]. Then, the US Air Force withdrew from research on the scramjet, but returned with the National Aerospace Plane (NASP) program in 1984 which belongs to the second generation development. NASA turned to the development and validation of airframe-integrated engine flowpaths [21].

1.1.2.2. The second generation scramjet development (Airframe Integration: 1974–1985)

After the first generation development, the focus of hypersonic propulsion changed into the airframe integration of hypersonic vehicles [24]. NASA Langley Research Center (LaRC) led a research program which focused on the sidewall compression scramjet engine. The research efforts developed a number of test facilities, test methodologies, cycle analysis, data analysis, and Computational Fluid Dynamics (CFD). The facilities, which were developed at NASA LaRC, for efficient scramjet testing, was the most advanced at that time. They developed a number of component test facilities as well, including a combustion-heated direct-connect combustor facility and a Mach 4, high-pressure inlet test facility. Modest-sized

facilities also remained available at GASL and were used to handle higher pressure validation tests [13]. Component tests were developed to form a database which is used to verify the analytical and computational methods. The computational methods became popular and were used to calculate internal flows, such as shear and heat transfer to the combustor walls, fuel mixing, and estimated the finite-rate chemistry effects on combustion.

The US JHU/APL initiated the hypersonic dual-combustor ramjet (DCR) engine as a successor to the SCRAM concept. Accordingly, the US Navy began to develop a Mach 4-6 hypersonic wide-area defense missile (HyWADM) in 1977. The missile used a DCR propulsion system. The HyWADM program finished in 1986.

At NASA LaRC and GASL, aerodynamic and Propulsion-Airframe Integration (PAI) tests were performed to quantify the performance of scramjet-powered vehicles. By the middle of the 1970s, about 1000 tests had been performed on three engines. During these tests, hydrogen and several hydrocarbons, such as methane, ethane, and ethylene, had been used as the fuel. The test results demonstrated the required thrust, operability, and fuel cooling requirements to allow a credible vehicle design. The scramjet module and direct-connect research and testing using gaseous hydrocarbon fuels was started at NASA LaRC in the late 1970s and was subsequently interrupted by the NASP program. However, these studies validated the predicted scramjet performance and provided some justification for starting the NASP program. After NASP, the US Air Force took the lead in this field [20]. The research showed that the second generation scramjet was a good design, but considerable refinement and development were still required.

1.1.2.3. The third generation scramjet development (NASP: 1986–1994)

In 1986, the US NASP program was formulated. The emergence of the NASP produced a new promotion to hypersonic research activities. The objective of the

NASP program was to develop a single-stage-to-orbit (SSTO) vehicle. The vehicle was powered by a combined cycle engine that uses air-breathing propulsion for the transatmospheric part of the trajectory, and rocket propulsion for the final orbit. A typical conceptive vehicle was the X-30 [25], which was a “hypersonic combined-cycle airbreathing capable” engine [26]. The NASP represented a significant step forward from the Space Shuttle. Figure 1.7 [1] shows a concept of a proposed NASP configuration as anticipated towards the end of the 1980s.

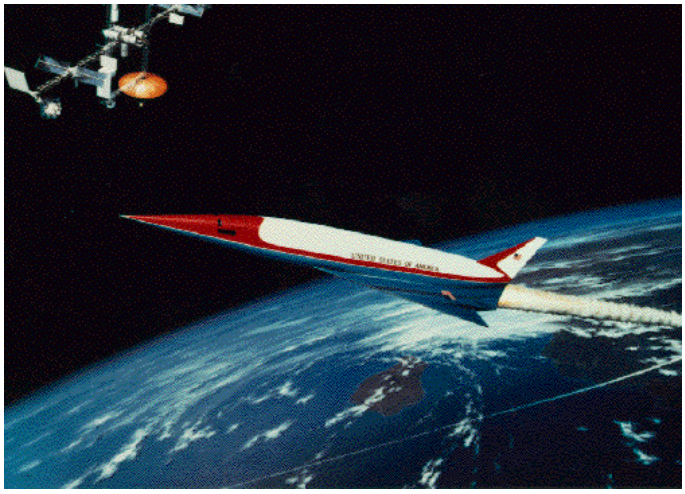

Figure 1.7 A concept of a proposed NASP configuration [1].

The NASP program aggressively promised an ultimate flight velocity at Mach 25 in 1984. It posed technological challenges in materials, propulsion, aerodynamics, sustainability and flight control. Such an aggressive approach was backed off by subsequent development activities. Actually, scramjet technology for space access remained at least one generation behind the scramjet technology for missiles. The facilities at that time could not meet the requirement for testing at such high Mach numbers. Therefore the test Mach number never reached 7. “The NASP program's 7-year history has been characterized by turmoil, changes in focus, and unmet expectations” [27]. Finally, NASP collapsed in 1995, because of numerous difficulties, including declining support, rising costs, questionable performance, and

serious and persistent technical challenges. However, it was still a catalyst for noticeable advances made in related topics, including materials, aerodynamics and flight control.

International activity in this period increased. When the NASP was approaching its end, France performed her Program of Research and Technology for Airbreathing Hypersonic Aircraft (PREPHA). Also, the program focused on the SSTO vehicle. It aimed at developing a knowledge base on hydrogen-fueled dual-mode ramjet technology for single-stage-to-orbit applications, and it assisted French researchers in making great advances in material testing, modeling, and development of ground-testing capabilities [28]. Germany began the development of the SANGER II program in 1987 as a proposed fully reusable Two-Stage-To-Orbit (TSTO) concept vehicle [29].

Japan performed research on the development of combined cycle engine technology for TSTO applications. The Air Turbo Ramjet Engine with EXpander cycle (ATREX), which was one element of this program, was an experimental precooled jet engine that worked as a turbojet at low speeds and a ramjet up to Mach 6.0. A number of sea level static tests have been conducted since 1990 on the ATREX-500, and wind-tunnel tests began from 1992 on the engine models. Future flight tests of the ATREX are planned.

During this era, Russia accelerated their research activities on the scramjet. Russia developed Kholod as a first generation hypersonic flying laboratory [30]. The Kholod is showed in Figure 1.8. Then, with the purpose of developing combined propulsion systems for advanced reusable space transportation, Russia performed the ORYOL program. Finally, Russia employed another first generation flight-test vehicle GELA Phase I for the development of Mach 3 ramjet missile propulsion systems [21].

Figure 1.8 The Russian Kholod first generation HFL (1991–1998) [30].

Looking back over the third generation of scramjet development, a number of programs for hypersonic vehicles were performed by several countries. The NASP program gave a fresh impetus to the US scramjet development. The facilities for supersonic combustion tests were greatly developed and enhanced. However, there was another significant achievement, namly the Computational Fluid Dynamics (CFD) technology. Supported by the development of computer technology, predictive models for both fluid and solid mechanics were advanced, including numerical schemes and the modeling of the physical processes. CFD became a significant tool for external aerodynamics and internal flows predictions, as well as for chemical-reaction modeling for propulsion applications.

1.1.2.4. The fourth generation scramjet development (Resurgence: 1995–present)

After the NASP finished in 1995, research on hypersonic vehicles came to the Post-NASP era. A number of organizations in the academic and industry world, including NASA, the Department of Defense, DARPA, and Sandia, continued to perform many new programs and activities on hypersonic vehicles, such as the Hypersonic Flight Test Experiments (HYFLITE) program, Hypersonic Scramjet Technology Project (HySTP), Advanced Reusable Transport (ART), Spaceliner,

Affordable Rapid Response Missile Demonstrator (AARMD), X-33, X-34, X-38, and X-43[31,32]. However, most of these activities failed, or faced an uncertain future, because of technological complexity, too much cost, or shifting priorities.

In the US, there were three new programs: Hypersonic Technology/Hydrocarbon Scramjet Engineering Technology (HyTech/HySET) program, performed by the US Air Force; the joint LaRC and Dryden Flight Research Center hypersonic X-plane (Hyper-X) program in 1996, performed by NASA; and Spaceliner/Advanced Space Transportation Program (ASTP)/the Hypersonic Investment Area of Next Generation Launch Technology (NGLT), performed by NASA [21]. Wakened by the cancellation of NASP Program, the new programs mostly focused on the lower hypersonic operational range.

The goal of the HyTech/HySET program is to develop a liquid hydrocarbon-fueled scramjet engine. Figure 1.9 shows the GRE-1 engine, which is a hydrocarbon fueled and cooled scramjet model, in the wind tunnel at GASL. Over the past 8 years, the HyTech/HySET program has made significant achievements in the following areas, including ignition and flame holding methodologies, endothermic fuels technology, high-temperature materials, low-cost manufacturing technology for scramjet engines, and detection and cleaning procedures for coked heat exchangers [21].

Figure 1.9 The GRE-1 engine in the wind tunnel at GASL [1].

Hyper-X is a major new initiative by NASA that advances the performance of hydrogen-fueled scramjet airframe-integrated vehicles. This program was initiated by LaRC and Dryden Flight Research Center in 1996, and it is still underway [26]. The first test vehicle, the X-43A, which is a small hypersonic aircraft, is about 12 ft in length and has about a 5-ft wingspan [33], seen Figure 1.10. It was designed to operate at speeds greater than about Mach 7, i.e. about 8,050 km/h at altitudes of 30,000 m or more. The vehicle was air launched with a booster stage from a B-52 aircraft, flew at Mach 7 and 10, and then crashed into the ocean without recovery [34]. Figure 1.11 shows the strategy of Hyper-X flight test [35]. Figure 1.12 shows the photographs of B-52 with hyper-X release and the ignition of Pegasus rocket booster [21] during the flight test.

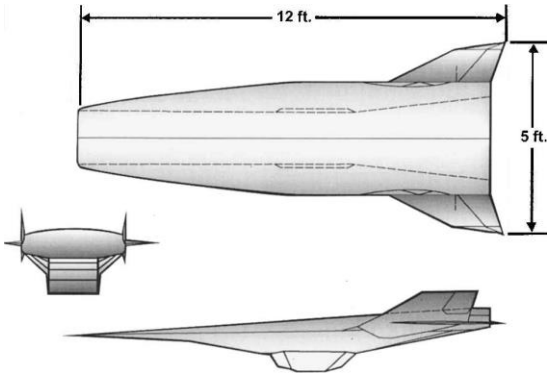

Figure 1.10 Schematic of the NASA Hyper-X research vehicle [33].

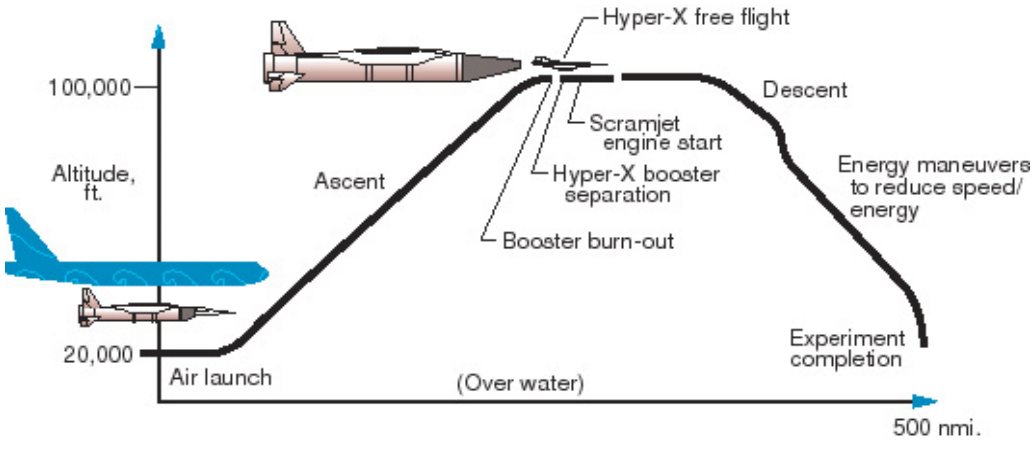

Figure 1.11 Strategy of the Hyper-X flight test [35].

Figure 1.12 The B-52 with hyper-X release and the ignition of Pegasus rocket booster [21].

On 16 November 2004, the third flight of the X-43A successfully set a new speed record of 12,144 km/h (Mach 9.8). The vehicle was boosted by a Pegasus rocket which was launched from a Boeing B-52 at an altitude of 13,157 meters. During free flight, the scramjet engine operated for about ten seconds. This test was a successful attempt to fly an integrated hypersonic airframe–scramjet engine. In addition the demonstration of the feasibility of scramjet propulsion, it provides an invaluable flight database, which is impossible to acquire in ground-testing facilities. This is very important for the further development of scramjets.

The X-51A hydrocarbon-fueled engine has undergone several ground-testing programs. Researchers and engineers expected the X-51A to sustain as much as 4 min of scramjet-powered operation. On 25 May 2010, the X-51A Waverider hypersonic demonstrator successfully completed its first powered flight. The vehicle flew for over 200 seconds and reached a speed of Mach 5. Although it did not meet the planned 300 second flight duration, the flight had the longest scramjet burn time of 140 seconds. An AFRL spokesman said “the first flight was ‘a solid B’ and we will get an A next time.”

On June 13th 2011, the X-51 Waverider’s second hypersonic test flight was carried out. The X-51A under the wing of a B-52 is shown in Figure 1.13 [36] The

hypersonic aircraft, which was expected to reach a speed of Mach 6, was successfully boosted to just over Mach 5 during its flight over the Point Mugu Naval Air Test Range, and the scramjet engine lit. However, the aircraft did not go according to plan as the aircraft failed to achieve full power. This was because the vehicle experienced an inlet un-start when the fuel was transferred from ethylene to JP7. The vehicle attempted to restart but failed. Then, the vehicle continued in a controlled flight orientation until it flew into the ocean within the test range. According to Charlie Brink, the Air Force Research Laboratory's X-51A program manager reviewed that they were very pleased with the data collected on this flight and the data will be used to identify the cause of the anomaly. “We will continue to examine the data to learn even more about this new technology,” he also said, “Every time we test this new and exciting technology, we get that much closer to success.” Boeing and Pratt-Whitney Rocketdyne built four X-51A flight test vehicles with the program goal of reaching Mach 6 in hypersonic flight [36].

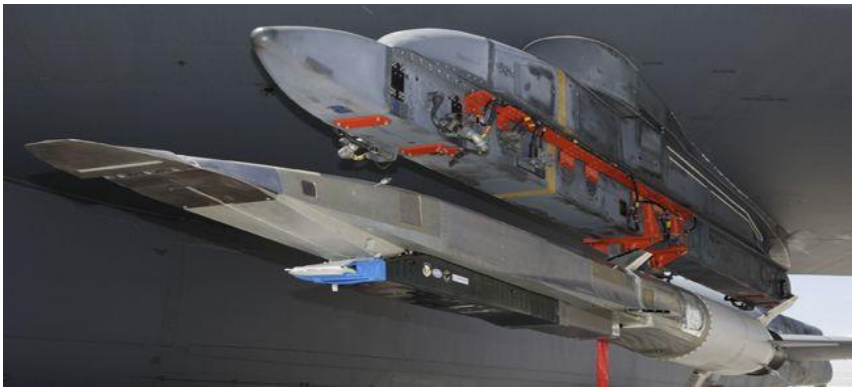

Figure 1.13 The X-51A under the wing of a B-52, June 2011 [36].

On 1 May 2013, the X-51A performed its first fully successful flight test on its fourth and final test flight. After been launched from a B-52 and carried up to Mach 4.8 by a booster engine, the X-51A separated cleanly from the booster and ignited the scramjet engine, and then the X-51A accelerated to Mach 5.1. After exhausting its fuel, the vehicle sustained controlled flight for 240 seconds, and then the vehicle

continued to send back telemetry data until it plunging into the Pacific Ocean. The success of the final test of the X-51A puts a satisfactory end to the technology demonstration program, and proves the viability of air-breathing and high-speed scramjet propulsion using hydrocarbon fuels.

There is another long-term program in NASA, which is to reduce the cost and improve the safety of the scramjet launch systems by 2025. This program was established during the late 1990s and it was led by NASA's Marshall Space Flight Center. Development of a third generation launch vehicle technology was referred to by several names, such as Spaceliner, Advanced Space Transportation Program (ASTP), and the Hypersonic Investment Area of Next Generation Launch Technology (NGLT). These programs focus on the development of technologies in two main areas: propulsion and airframes [21].

In this period, in the scramjet field, international researches in Russia, France, Germany, Japan, Australia, and China, have become more active. The Japanese National Aerospace Laboratory–KPL began to design and test a side-wall compression-type scramjet engine in 1991. The first generation of the hydrogen-fueled engine model (E-1) was tested from 1994 to 1999 at Mach 4–6. The majority of the testing was conducted on a heat-sink hardware, with a limited water-cooled and liquid hydrogen-cooled testing [37]. Two new facilities were built to support these activities, a freejet-type hypersonic propulsion wind tunnel (RJTF1) and a free-piston high-enthalpy shock tunnel (HIEST2) [38]. After some improvements to the E-1, which mainly focused on the attainment of a positive net thrust and the combustion performance at Mach 8 conditions, KPL began in 2000 to test the second generation E-2 engine until today. In cooperation with Germany, France initiated the program of Joint Airbreathing Research for Hypersonic Application Research (JAPHAR). Then, France performed the PREPHA and Germany performed the Sänger programs, both of which to pursue hypersonic airbreathing

propulsion research for reusable space launcher applications. Together with France, Russia initiated the Wide Range Ramjet (WRR) program to develop the reusable space launcher technology. Also Russia has performed the second generation hypersonic flying laboratory work with Gela Phase II and the Mig-31 HFL [21]. A photograph of the GELA/Raduga operational flight test vehicle is shown in Figure 1.14. With international support, Australia conducted the world's first verified demonstration of supersonic combustion in a flight environment under HyShot.

Figure 1.14 Russian GELA/Raduga operational flight test vehicle [21].

In contrast to the paper studies and analysis, the post-NASP "real world" witnessed some significant accomplishments, in particular in the field of scramjet propulsion. Fry [21] gave a very detailed review on the development and evolution of scramjet programs during this era.

1.1.3. General state of scramjet technology

Hypersonic technology has been under theoretical, numerical and experimental development since the 1950s. As a result of research over the last 60 years, significant progress has been made, especially in the field of scramjet engines. A large number of programs on hypersonic vehicles have been performed. By 2014, the US, Russia, France, Germany, Australia, Japan, China, etc. have achieve great

breakthroughs on scramjet technology [7], and Russia, the US and Australia successively performed flight demonstration tests. These tests are very significant, particularly the state of flight testing at Mach > 6, such as the X-43 test. They can not only demonstrate the feasibility of scramjet technology, but also be used to validate ground testing and numerical simulation results. Nowadays, hypersonic airbreathing engines are being investigated and developed for application into reusable hypersonic cruise vehicles and cruise missiles. From the history and evolution of scramjet development, we can foresee the era of hypersonic flight will be a reality in the near future.

1.2. Motivation and objectives

It is well-known that hypersonic air-breathing propulsion systems encounter some novel and troublesome constraints in combustion problems [9,39]. In the scramjet, the internal flow is supersonic and the fuel remains for only a very short period of time (of the order of 1 ms) in the combustion chamber. During this period, the fuel has to be mixed on a molecular level with the air and the reactions and heat release have to be completed before the fuel leaves the combustor. Over the last half of the last century or so, experimental facilities for scramjet combustion measurements have developed. However, for the reasons of extreme complexity and cost, there are only a few run-time facilities that are available worldwide [40]. For instance, the seven-year X-43 program and the ten-year X-51 program, which were performed by NASA [41], approximately took $230 million and $300 million, respectively.

In contrast to the experimental investigation, the CFD approach is a cost-efficient way of investigating combustion in scramjet combustors. With the development of advanced computer technology and numerical methods, CFD can

provide high-quality results and the required accuracy, and reduce the length and cost of the design cycle of scramjet engines. In the design of a hypersonic propulsion system, CFD has several roles: (i) serves as an engineering tool for the detailed design and analysis, (ii) provides input data for cycle decks and performance codes, (iii) is used to guide the develop of an engine concept, (iv) determines the effects of the facility on testing, for example, the effects of contaminants in a combustion heated facility on an engine combustor test, and (v) is used to predict flowfield measurements as a complement to measured data during and following a test [6].

Over the last 30 years or so, CFD has been extensively investigated, and it has gradually become a major research tool and it has played an extensive role in the field of aeronautics and astronautics. In the CFD field, there are three common approaches for turbulence modeling, Reynolds-Averaged Navier–Stokes equations (RANS), Large-Eddy Simulation (LES), and Direct Numerical Simulation (DNS). All these three approaches have been used in the numerical simulations of compressible turbulent flows. However, the simulation of supersonic mixing and combustion in a scramjet combustor brings many challenges. Even for the non-reacting flows, when the Mach number is sufficiently high, the way to properly treat compressibility effects on the turbulence is far from being well resolved [42]. In addition, the scramjet combustor needs a flame holder in order to stabilize the combustion processes. The complex geometries bring complexity to the flow field and additional difficulties for accurate simulations.

Ladeinde [40] reviewed the scramjet combustion simulation at the 47th American Institute of Aeronautics and Astronautics (AIAA) Aerospace Sciences Meeting (ASM), which took place in Orlando at 5-8 January, 2009. In his review, which covered the fundamental problem of supersonic mixing layers, high-speed combustion modeling efforts, and actual calculations of realistic scramjet

combustors, he pointed out that the RANS approach dominates the turbulence modeling of the system, and there is only a handful of LES work. Also, nearly all the numerical investigations are virtually based on low-order schemes. However, the demands for performing LES modelling of the non-reacting and reacting flows in a scramjet using high order numerical schemes are increasing. Further, he revealed that various combustion models have been used for supersonic combustion simulations and there appears to be a growing use of the flamelet methods.

Reviewing the development of scramjet combustion simulations, future research areas should include the investigation of high-order methods for scramjet combustor calculations, more advanced turbulence-chemistry interaction models, including the conditional PDF procedure, and the application of such flamelet-based methods to realistic scramjet systems. Further, although several important phenomena and characteristics of the supersonic combustion are experimental and numerical investigated, there are still many open questions regarding the physical mechanisms of local extinction, reignition, autoignition and flameholding under various configurations. The present research focus on the development of advanced combustion models like the Unsteady Flamelet/Progress Variable (UFPV) model for turbulent combustion in high-speed flows. Also, the characteristics of the supersonic combustion in scramjet combustors with strut and cavity flame holders are investigated.

The specific objectives of the current research are as follows:

(i) Extend the UFPV model, which was originally developed for simulating turbulent combustion in low-speed flows, to the revised UFPV model which takes into account the effects of compressibility and could be employed to simulate the supersonic reacting flows.

(ii) Validate the predicative capability of the revised UFPV model for simulating the supersonic flames in strut-based and cavity-based scramjet combustors.

(iii) Understand the mixing process, local extinction and autoignition phenomena, flame characteristics and flameholding mechanisms in a supersonic combustor with a cavity flameholder.

In order to obtain the above objectives, the following work is performed:

(i) The Unsteady Flamelet/Progress Variable (UFPV) model for turbulent combustion in low-speed flows is introduced and extended to supersonic flows and a new strategy is developed to generate probability density function look-up tables for the UFPV model.

(ii) The UFPV model and look-up table generation strategy are built into an in-house FORTRAN based hybrid RANS/LES codes.

(iii) The RANS and LES modelling are employed to a strut-based scramjet combustor using the flamelet and UFPV models.

(iv) The LES modelling is employed to a cavity-based scramjet combustor.

(v) The indicators for local extinction and autoignition events are developed in order to identify these phenomena in the supersonic flame.

(vi) The flame characteristics and flameholding mechanisms in a cavity flameholder with fuel injected upstream are analysed.

1.3. Thesis outline

The present research investigates the supersonic combustion in scramjet combustors with strut and cavity flameholders through the RANS and LES

strategies, and the flamelet and the UFPV combustion models are employed. The organization of the thesis is given as follows:

Chapter 1: The history, evolution and general state of scramjet development are reviewed. Further, the motivation behind the present research and the specific objectives are discussed.

Chapter 2: Numerical simulations of the compressible turbulent flow using the RANS, LES and DNS approaches are reviewed and discussed. Also, the modelling of non-premixed, premixed and partially premixed turbulent combustion, including supersonic turbulent combustion, is reviewed. Finally, the main characteristics and problems associated with combustion in high speed flows are concluded and discussed.

Chapter 3: The concepts of LES and the basic theory behind are discussed. Further, the numerical approaches, including the spatial discretization schemes, the procedures used to solve the equations in time and the treatments of the boundaries are discussed. Finally, the multiblock and parallel computing strategies used in the present study are briefly presented.

Chapter 4: The theory behind the steady flamelet and the UFPV combustion models are discussed. Further, the UFPV model is developed and built into the hybrid RANS/LES in-house code for the simulations of supersonic flames. The steady and unsteady flamelet libraries are generated and converted into the look-up tables. Finally, the solution procedures of the UFPV model and the flow chart for the hybrid RANS/LES modelling of the supersonic flames are present.

Chapter 5: RANS and LES investigations of non-reacting and reacting flows are performed to model the DLR case in order to validate the flamelet and the UFPV combustion models, as well as to enhance our understanding of the mixing and

combustion characteristics of the gaseous fuel injected from the base of a strut, which is installed in the center of the supersonic combustor.

Chapter 6: Large eddy simulations are performed to model the non-reacting and reacting flows in the supersonic combustor with a cavity flameholder, so as to validate the flamelet and the UFPV combustion models, as well as to understand the mixing, local extinction and autoignition, flameholding and combustion characteristics of the gaseous fuel injected upstream of the cavity.

Chapter 7: The conclusions and major contributions from the present studies are presented. Also, the scope and recommendations for the future work are discussed.

Chapter 2
Review of the scramjet combustion numerical simulations

In contrast to the experimental study, the CFD approach is a cost-efficient way of investigating non-reacting and reacting flows in a scramjet. With the development of advanced computer technology and numerical methods, CFD can provide high-quality results and the required accuracy, and reduce the length and cost of the design cycle of scramjet engines. Over the last 30 years or so, the RANS, LES and DNS approaches has been employed to simulate the compressible turbulent flows and numerous CFD codes have been developed for the simulations.

Baurle [43] provided an overview of the modeled equations typically employed by commercial quality CFD software codes for high-speed combustion applications. In this paper, he emphasized the salient features and shortcomings of the averaged governing equation set. Based on these models, the US Air Force and NASA have built the VULCAN, a widely-used, multi-grid, flux-difference-split and finite-volume code. This code is for high-speed reacting flow simulations [44]. Other relevant reviews, although they are not exactly from the conclusions of supersonic combustion simulations, they are still helpful for the understanding of the turbulence models and the combustion modeling. Givi [45] provided a review of the sub-grid scale (SGS) modeling as required for LES for the turbulent combustion. Givi [46] presented another review devoted primarily to SGS closure based on the filtered density function (FDF), which is a method that is analogous to the probability density function (PDF) modeling. A more recent review of the FDF method was provided by Givi et al. [47]. Heinz [48] highlighted the fundamental differences between RANS and LES combustion models for non-premixed and premixed turbulent combustion. Finally, Grinstein [49] addressed modeling issues

relevant to the CFD of turbulent non-premixed jet flames, including sub-grid and super-grid modeling. Transitional jet diffusion flames of the hydrogen/air and propane/air types were reviewed, and the models for the turbulence, chemical reactions, volume expansion, and heat release were discussed.

In the following work, a review of the scramjet combustion numerical simulation is presented, covering the compressible turbulent flow and combustion aspects in the scramjet combustor. Also the main characteristics and problems associated with of combustion in high speed flows are concluded and discussed.

2.1. Numerical simulation of compressible turbulent flow

To enhance the mixing and maintain the flame, a flame holder is required in the scramjet combustor, and this increases the complexity of the flow. The flow field in the combustor of a scramjet engine is complicated by: (i) a wide range of flow velocities (high-Reynolds-number flow regimes dominate this flow field with embedded regions of low speed in the recirculation regions), (ii) small and large scale vertical flows (for mixing), (iii) separated flows (for the flame holder), (iv) complex mixing phenomena, (v) finite rate chemical reactions, (vi) high temperatures and heat fluxes, (vii) high degrees of anisotropy and non-equilibrium transfer of turbulence energy, and (viii) interactions between turbulence and kinetics [6]. Thus, researchers require the development of more appropriate turbulence models and high order schemes in order to obtain more details and to be able to accurately predict the flow field in the scramjet combustor. Compressibility should be of much concerned when modeling the turbulence. Also the capture of the shock waves should be carefully investigated. In this thesis, the following reviews the application of the RANS, LES and DNS approaches when simulating the flow field in scramjet combustors.

2.1.1. RANS approach

The RANS model is the most common turbulence modelling approach, and it is based on a statistical treatment of the fluctuations about a stationary, or a slowly varying flow, whereby an instantaneous quantity is decomposed into its time-averaged and fluctuating quantities [50]. The RANS equations are time-averaged equations of the fluid flow motion and is primarily used to describe turbulent flows [51]. It is well known that the RANS approach has the most computational efficiency and the RANS simulations are now widely used in the design process of scramjet engines. Computation results have shown that the RANS approach is helpful for determining optimal fuel injector arrangements, investigating trends noted during testing, and extracting various aspects of engine efficiency [43]. Jones and Whitelaw [52] published a review in 1982 which described and appraised components of the calculation methods based on the solution of the conservation equations in differential form for the velocity, temperature and concentration fields in turbulent combusting flows. Bardina et al. [53] have implemented four turbulence models, which are the two-equation k-ε model of Launder and Sharma, the two-equation k-ω model of Wilcox, the two equation k-ω Shear-Stress Transport (SST) model of Menter, and the one-equation eddy-viscosity model of Spalart and Allmaras, and the simulation results were evaluated against eight selected experimental flow fields.

Jeung et al. [54] simulated the supersonic combustion for hypersonic propulsion. The turbulence closure is achieved by means of the Mentor's SST model which is based on the k-ω two-equation formulation [55]. This model is the blending of the standard k-ε model and the Wilcox k-ω model. When calculating the ram accelerator, the simple Baldwin-Lomax model was employed. The governing equations, including the compressible Navier-Stokes energy equations and species

transport equations, were discretized numerically by a finite volume approach. The numerical methods of the simulation were as follows: Roe's flux-difference splitting, differentiable limiter function, Monotone Upstream-centered Schemes for the Conservation Laws (MUSCL), spatial total variation diminishing (TVD), and second-order implicit time integration with 4 Newton sub-iteations pertime step. The compact fluorescent lamp was set to be 2. The results showed a wide range of phenomena that results from the interactions among the injector flows, shock waves, shear layers, and oscillating cavity flows. However, he was not concerned with the interaction between the turbulence and chemical reactions. Xiao et al. [56] simulated the scramjet flows with variable turbulent Prandtl and Schmidt numbers, and the k-ζ model was employed. The numerical methods for his simulations were as follows: North Carolina State University REACTMB code [57], spatial TVD upwind with flux splitting method of Edwards [58], second-order Essentially Non-Oscillatory (ENO), central differences for the viscous and diffusion terms and plannar relaxation.

Brown [59] validated the turbulence models for hypersonic flows, including the SST and the Wilcox models, along with compressibility corrections and a means to be able to specify transition. The validation provided an assessment of the heat transfer predictive capability of the turbulence models. Based on the Menter's Baseline model and the Menter's SST model, Baurle and Eklund [60] preformed the RANS calculations for a US Air Force Research Laboratory/Aerospace Propulsion Office scramjet combustor designed for a Mach 4.0–6.5 flight. Calculations were performed at the minimum (Mach 4.0) and maximum (Mach 6.5) flight design conditions. The numerical methods of his simulation were as follows: structured grid topology, cell-centered finite volume, low-diffusion flux-split mode of Edwards [57], MUSCL, van Leer flux limiter, steady state, and diagonalized approximate factorization scheme. The compact fluorescent lamp is between 1.5 and 2.0. Overall, his solution sensitivity to grid resolution was small relative to the solution sensitivity to the modeling uncertainties.

2.1.2. LES approach

A promising alternative to RANS for the simulation of fluid flows is the LES approach. This offers significant advantages that overcome many of the shortcomings associated with the statistical representation of single-point RANS closures. LES is an emerging technique for obtaining an approximation to turbulent flow fields. It was initially proposed in 1963 by Joseph Smagorinsky to simulate atmospheric air currents [61]. Then, in 1970, Deardorff [62] used LES to simulate the three-dimensional turbulent channel flow at large Reynolds numbers. From then on, the study of LES has grown rapidly and it is currently applied in a wide variety of engineering applications, including combustion [63] and acoustics [64]. Pope [65] and Garnier et al. [66] provided expositions on the fundamentals and applications of the LES method.

LES is an improvement over the widely prevalent practice of obtaining the mean of turbulent flows when the flow has large scale, low frequency and unsteadiness. Most of the transport of mass, momentum, and energy (of the order of 90%) is achieved by the large eddies. In contrast, the primary role of the small eddies is to dissipate the fluctuations. Hence, the large eddies tend to interact directly with the mean flow [43]. The principal operation in LES is low-pass filtering. Mathematically, LES can be considered as separating the velocity field into a resolved and a sub-grid part. The resolved part of the field represent the “large” eddies, while the subgrid part of the velocity represent the “small scales” whose effect on the resolved field is included through the subgrid-scale model [67]. This requires either high-order numerical schemes, or fine grid resolution if low-order numerical schemes are employed. Pope [65] addresses the question of how a fine grid resolution is required to resolve a filtered velocity field. The filtering operation in LES can be implicit or explicit.

Mathew [68] produced an introduction to this method, in which the general formulations of LES and the more common modelling for flows without reactions were discussed. Grinstein [69] showed that implicit filtering recognizes the sub-filter scale model will dissipate in the same manner as many numerical schemes, and in this way, the numerical discretization scheme or the grid can be assumed to be the LES low-pass filter. This method takes full advantage of the grid resolution, and eliminates the computational cost of calculating a sub-filter scale model term. However, it is difficult to determine the shape of the LES filter that is associated with some numerical issues [70].

With the development of LES theory, a number of codes incorporate the LES for the turbulence modeling. These codes are comprised of one or more sub-grid models. For the calculation cost of the LES, all these codes support parallel computing. The Viscous Upwind ALgorithm for Complex Flow Analysis (VULCAN) [44] was created from LARCK as part of a RAM/SCRAMJET CFD code development project conducted under a contract to the Air Force Research Lab, Propulsion Directorate, at the Wright Patterson Air Force Base (1996-1997). The code is a structured grid, cell centred, finite volume and density based method, and Smagorinsky sub-grid model is performed in the LES simulation.

Wind-US is a computational platform which may be used to numerically solve various sets of equations that govern the physical phenomena under investigation. Currently, the code supports the solution of the Euler and Navier-Stokes equations of fluid mechanics, along with the supporting equation sets that govern the turbulent and chemically reacting flows [71]. Wind-US is produced by the National Program for Applications-Oriented Research in CFD (NPARC) Alliance. The NPARC is a partnership between the NASA Glenn Research Center (GRC) and the Arnold Engineering Development Center (AEDC). Wind-US has a wide variety of numerical algorithms and physical models to choose from [72]. Both structured

grids and unstructured grids can be chosen. Ideal gas, equilibrium air, frozen multi-species flows, and reacting flows can be modeled. For turbulent flows, a selection of algebraic, one-, and two-equation RANS models are available, along with a Rumsy-Gatski algebraic Reynolds stress model. If a time-accurate simulation is required, one of the several available hybrid RANS/LES turbulence models can be employed. Nelson [72] pointed out that the recent enhancements are being performed, including an improved unstructured grid solver, improved chemistry modeling, and improved stability of the structured grid solver.

Ott [73] used the CRUNCH code to examine modeling upgrades for scramjet flowpath predictions. CRUNCH [74] has been developed by Combustion Research and Flow Technology Inc. (CRAFT Tech®). The overview of CRUNCH is that it: (i) is a multi-element unstructured grid, all-speed Navier-Stokes code (it is from incompressible to supersonic flows), (ii) emphasizes the geometrically complex and or moving multi-body problems (advanced dynamic grid capabilities), (iii) has multi-phase capabilities for cavitating flows as well gas/liquid systems, such as cryogenic tanks, (iv) uses generalized equations of state for real fluids, including supercritical flows at high pressures, gas/liquid mixtures at subscritical pressures, and (v) emphasizes the cryogenic and non-cryogenic liquid flow systems, including turbopumps and feed systems, as well real fluid combustion at high pressures.

The CFD Research Branch of the Aeromechanics Division of Air Force Research Laboratory (AFRL) developed a fundamental CFD computer code, known as FDL3DI. It uses an implicit approximately factored, finite-difference spatial operator in a Newton-like iteration to solve the three-dimensional N-S equations and it achieves sixth-order accurate compact-difference results [75]. This CFD software enhancement improves the researchers ability to carry out direct numerical and large-eddy simulation computations for geometrically complex configurations [76]. In addition, some codes in other fields contain LES closure, such as Falcon, CEDRE,

OpenFOAM, PMB3D, etc. [77]. Some commercial CFD softwares, such as ANSYS FLUENT, STAR-CD and FASTRAN, have LES closure as well. Several sub-grid models are involved in these softwares. For instance, ANSYS FLUENT 13.0 has four sub-grid models, which are the Smagorinsky-Lilly Model, Dynamic Smagorinsky-Lilly Model, Wall-Adapting Local Eddy-Viscosity (WALE) Model and Dynamic Kinetic Energy Subgrid-Scale Model.

In the LES, the smaller turbulent scales tend to be isotropic and less dependent on the boundary conditions and flow type than the larger scales [43] and the grid size of a scramjet combustor for LES is tremendous. Spalart [78] has estimated that the application of traditional LES to an aircraft wing would require of the order of 10^{20} floating point operations. This value is approximately one million times that of the largest RANS calculations attempted today. The computational cost of LES prohibits its use as an engineering design tool for most practical applications, especially for high Reynolds number flows and near-wall turbulent flows. When using LES, the full capture of the coherent structure in the boundary layer requires a very dense grid, the size of which is of the order of $Re^{1.8}$. However, the simulation of the flow field far from boundary just needs a grid size of the order of $Re^{0.4}$ [79]. The hybrid RANS/LES is a well-developed approach which can use RANS for the near-wall calculations and LES for the main flow simulations. Sun [11] reviewed the application and the development of the hybrid RANS/LES approach. Sun [80] developed a hybrid RANS/LES approach as well, which is based on the Menter k-ω SST model [81,55]. The hybrid methodology was conducted to investigate the supersonic flow over two-dimensional open cavities for scramjet applications. His numerical results agree well with the experimental data for the dominant frequencies and time-averaged surface pressure profiles inside the cavity.

Although LES is a more computationally expensive technique than RANS, it is still a good choice for the simulation of special flow issues, such as shear flows,

development of mixing layers, gas injections, etc. LES offers two significant advantages: firstly, the large-scale motion of the turbulence that contains most of the turbulent kinetic energy and the dynamics of the turbulence is resolved; secondly, knowledge of the large-scale dynamics and the assumption that an applied model should be valid independently of the filter size leads to the formulation of the so-called dynamic models [82], where the model coefficients are determined as part of the solution procedure [63].

2.1.3. DNS approach

DNS is a simulation in computational fluid dynamics in which the full Navier-Stokes equations are numerically solved without any turbulence model [83]. This means that the whole range of spatial and temporal scales of the turbulence must be resolved. All the spatial scales of the turbulence must be resolved in the computational mesh, from the smallest dissipative scales (Kolmogorov microscales), up to the integral scale, associated with the motions containing most of the kinetic energy [83].

One can estimate that the number of floating-point operations required to complete the simulation is proportional to the number of mesh points and the number of time steps, and in conclusion, the number of operations grows as Re^3 for 3-D simulation. Therefore, the computational cost of DNS is very high, even for low Reynolds numbers. For the Reynolds numbers encountered in most industrial applications, the computational resources required by a DNS would exceed the capacity of the most powerful computers currently available. However, direct numerical simulation is a useful tool in fundamental research in turbulence. It is possible to perform “numerical experiments” using the DNS approach. The information from DNS allows a better understanding of the physics of turbulence, while it may be very difficult or impossible to obtain such information by

experiments. Furthermore, DNS approach is useful in the development of turbulence models for practical applications, such as sub-grid scale models for LES and models for methods that solve the RANS.

DNS of turbulent flows has been reviewed by Modi [84] in 1999, including the background of DNS, the importance of DNS in turbulence, the related numerical issues (e.g. the available methods, boundary conditions, spatial and temporal discretizations), and the impact of DNS on turbulence modelling. Finally, the future possibilities of this tool are contemplated. Martin [85] studied reacting turbulence in hypersonic flows using both the DNS and LES approaches in 1999. He concluded the numerical challenges for DNS and LES for highly compressible turbulence in [86]. Li et al. [87] reviewed his recent studies on compressible turbulence by using direct numerical simulation (DNS), including DNS for isotropic turbulence, turbulent mixing-layer, turbulent boundary-layer and shock/boundary-layer interaction. During his research, turbulence statistics, compressibility effects, turbulent kinetic energy budget, coherent structures and the mechanism of sound source in turbulent flows are studied based on the DNS data. His work shows that DNS is a powerful tool for the mechanistic study of compressible turbulence. Several studies of compressible shear/mixing layer have been performed with the DNS approach, see the references [88-92] and the references cited therein.

In all, the flow in the scramjet combustor is not only high-speed and compressible, but also it includes a mixing/shear layer, and compression and expansion waves. For combustor modeling, several improvements in the efficiency of steady-state and temporal Navier-Stokes codes are required to be performed with the necessary accuracy and design turn-around time. Multigrid methods offer promise for significantly enhancing the convergence rates, but the application of multigrid methods to reacting flows also results in additional challenges for the success of the method [93]. Current research on multigrid methods in high speed

reacting flows has resulted in a significant improvement in the convergence rates over the single grid methods. In the future dynamic grid adaptation will become even more important for capturing the complex flow structures in combustors, in particular the shock-expansion and vertical structure in the flow. Accurate resolution of the vertical flows requires very high resolution in order to conserve angular momentum. Again, there is a serious need for improved turbulence modeling in high speed reacting flows, both to model the turbulence field and to properly couple the effects of the interaction between chemical reactions and the turbulence. Promising work is again taking place in this field using several approaches. Techniques using velocity composition probability density functions have been successfully applied to incompressible reacting flows, and this work is now being extended [94] to model compressible reacting flows. Work is also underway [95] to apply LES techniques to compressible reacting flows. Sub-grid scale models for the LES of these flows are currently being developed using methods previously applied for modeling the full range of flow scales. Finally, further work is required on the DNS approach. One possible direction is to optimize the DNS code so that it can produce more accurate predictions and have a higher computational efficiency. The other direction is to use higher order schemes to study the mechanics of the flow in a scramjet combustor.

2.2. Modeling of turbulent combustion

Combustion in turbulent flows, or more generally, turbulent combustion or turbulent reacting flows, is a phenomenon of importance in both nature and technology [96]. In nature, the combustion in turbulent flows is common in many systems, and it is important in numerous processes, such as energy generation, materials processing, and pollution control. Combustion in turbulent flows is the main approach to get energy for domestic heating, power generation and transportation [97]. In technology, in order to be able to perform three-dimensional

time-dependent simulations of turbulent flows with combustion, it is usually not realistic to solve transport equations for all species occurring in the chemical reaction process. Therefore, it is common to apply a reduction technique to limit the number of transport equations. Due to the interaction between the flow and the heat release, combustion normally takes place within a turbulent rather than a laminar flow field. However, the modelling and prediction of the behaviour of turbulent, reacting and compressible flow are generally much more difficult than that of non-reacting flows. Firstly, in addition to the conservation of mass and momentum, the conservation of energy as well as gas laws must be considered due to the compressibility of the flow. Secondly, the conservation equations which are for the chemical species and reactions must be included. Thirdly, the gradients of the temperature, density, and species concentration are considerable in the flow field due to the chemical reactions and heat release. Further, the effects of thermal radiation are non-negligible, especially when the particles present. Finally, in high speed flows, compressibility has a significant effect on the modelling of the flow and combustion.

To conceptually simplify the problem of turbulent combustion modelling, the technical processes in gaseous turbulent combustion are often subdivided in terms of mixing, i.e. premixed, non-premixed, and partially premixed turbulent combustion. This classification is helpful for the development and utilization of the combustion models. In a premixed turbulent combustion, e.g. the combustion in lean-burn gas turbines or in homogeneous charge spark-ignition internal combustion engines, the premixed fuel and oxidant are ignited locally and then the flame propagates through the mixture. In contrast, in a non-premixed turbulent combustion, for example the combustion in diesel engines, the fuel and air are introduced in two separate streams, and therefore the flame can exist where the fuel and air are mixed locally at the molecular level. In this condition, the mixing process has a significant effect on the combustion. It is widely held that premixed turbulent combustion is inherently more

complex than non-premixed turbulent combustion [98], and this is due to the much stronger coupling between the chemistry and the turbulence. In fact, the absolutely premixed and non-premixed turbulent combustions are ideal conditions. In addition to premixed and non-premixed combustion, partially premixed combustion plays, at least to some extent, an important role in practical applications [97]. In many practical combustion systems, including scramjet and gas turbine engines, the basic assumption of either classical premixed or non-premixed combustion theories cannot be thoroughly satisfied [99]. For example, in a combustion chamber, it is possible for the fuel and air to mix somewhat before the ignition occurs. Combustion is then sometimes described as partially premixed. Concerning the combustion in a scramjet combustor, the internal flow is supersonic and the fuel remains for only a very short period of time (of the order of 1 ms), during which the fuels have to be mixed on a molecular level with the air and the reactions and heat release have to be completed before the fuel leaves the combustor. The modelling of supersonic combustion is discussed in a separate sub-section.

2.2.1. Modelling of non-premixed turbulent combustion

For non-premixed turbulent combustion, including the compressible reacting flow, the original paradigm has the viewpoint that the combustion is basically mixing controlled. Burke and Schumann [100] studied the laminar diffusion flames. In their work, the mixing is dominated by molecular diffusion in laminar flows and the flame is situated at the surface where the fuel and oxidant are in stoichiometric conditions. Under these conditions, the reaction zone is very thin compared with the diameter of the flame. The main idea of mixing controlled combustion is that the chemical rates are much faster than the mixing by molecular diffusion. Hawthorne et al. [101] published a classical paper in which the flame length and mean structure of turbulent jet diffusion flames are studied and are found to correlate well with the

mixing laws of turbulent jets. Homsy [102] experimentally investigated a jet diffusion flame and found that the flame lengths were controlled by mixing. However, the buoyancy was very important in determining rates of mixing in such flames and a modified Froude number was needed to incorporate the effects of buoyancy on mixing. Ferri and Fox [103] discussed the fluid dynamics of supersonic combustion. In their work, the interference between the combustion process and the supersonic flow secondary to the combustion region is described. In the early 1970s, as a result of pressures for reduction in air pollution emissions, researchers got interested in the effects of chemical kinetics, particularly for pollutants such as nitric oxide which is formed by relatively slow reactions. Bilger et al. [99] reviewed the development of the mixing controlled paradigm from the 1960s to 1990s, and numerous important simulation and experimental results were discussed.

In the early 1980s, the laminar flamelet paradigm appeared [104]. The laminar flamelet concept views a turbulent diffusion flame as an ensemble of laminar diffusion flamelets. As functions of the mixture fraction and scalar dissipation, the libraries of quantities such as composition, temperature, and reaction rates are pre-calculated, and then the results are used to obtain closure for the chemistry–turbulence interactions. Furthermore, detailed chemical reaction mechanisms and molecular diffusion processes can be included in these laminar flame calculations [99]. Peters [105] reviewed the work relevant to the flamelet concept, including laminar flame studies, asymptotic analysis, theory of turbulence and percolation theory. His review tried to gather and integrate the material in order to derive a self-consistent formulation, and a coordinate-free formulation of the flamelet structure was given under the assumption of equal diffusivities. Liew et al. [106] described a model which permits the incorporation of complex hydrocarbon chemistry into a detailed flow field prediction for turbulent non-premixed combustion, and this improvement was successful in matching experimental CO concentrations, in comparison with calculations assuming chemical equilibrium. Research has revealed

that the laminar flamelet paradigm can provide an accurate description for sufficiently large turbulence scales and low turbulence intensities for combustion chemistry that is close to irreversible [99]. In high speed reacting flows, local extinction and re-ignition normally present due to the interaction between the flame and the shock wave. Under this unsteady condition, however, the stationary laminar flamelet equations will be invalid [107]. So, there are still strong arguments against the flamelet models, including the effects of variations in scalar dissipation through flamelets and the influence of neglected advection terms in the transport equations [108]. In fact, the range of validity of flamelet models is not yet agreed. During recent years, to develop the flamelet paradigm, the stationary laminar flamelet equations has been modified to include effects of transients [108]. Modifications to accommodate the effects of the advection terms and to incorporate a Lagrangian viewpoints [99] are also employed. However, the LES incorporating such modifications has been successfully employed [63]. Researchers continue to work on new interpretations of the flamelet paradigm[109]. Detail literature and concept review of the flamelet modelling will be given in the next chapter.

The probability density function (PDF) methods were developed for turbulent reactive flows in the mid-1970s. Dopazo and O'Brien[110] were the first to consider a modelled equation for the PDF of a set of scalars that describes the thermochemical state of a reacting medium to model mixing and chemical reaction in turbulent reacting flows. The relationship between particle models and PDF methods was established by Pope [111]. By then, the particle methods have become the dominant approach for modelling and solving PDF transport equations. Haworth [112] present a comprehensive up-to-date (2010) review which emphasizes the progress in PDF methods that has been made over approximately the past 20–25 years. The primary advantages of the PDF approach are that: independent turbulent fluctuations of all species can be represented, the direct effects of reaction appear in closed form in the PDF equations, and no modelling is required to close the reaction

term in the PDF equations [99]. However, a mixing model is required to account for mixing by molecular diffusion. The primary mixing models used are: Interaction by Exchange with the Mean (IEM) or, equivalently, Linear Mean Square Estimation Model (LMSE); the Modified Curl model (MC); and the Euclidean Minimum Spanning Tree (EMST) model [99]. For PDF method, Most modern numerical solution algorithms employ a Lagrangian particle Monte Carlo algorithm. Xu and Pope [113] accurately represent the level of local extinction in a series of piloted-jet flames of methane using a joint velocity–composition–turbulence frequency probability density function (PDF) model. The comparison between the calculation results and the experimental data demonstrate the ability of the PDF model to represent, quantitatively, the processes of local extinction and reignition [113]. Hsu et al. [114] extend the PDF method to compressible reacting flows. Two supersonic diffusion flames are studied using the proposed PDF model and the results are compared with experimental data; marked improvements over solutions without PDF are observed. PDF methods have also been applied to the more challenging bluff-body stabilised jet flames and to the swirling bluff-body flames, and results illustrate that the application of PDF method is adequate for these complex recirculating flow [99]. The PDF methods have reached the level of maturity that they are available in commercial CFD codes, such as ANSYS Fluent V13.0, for use both in research and in industrial applications. More information about PDF method can be found in Haworth [112] and a recently published book by Echekki and Mastorakos [115].

The Conditional Moment Closure (CMC) method was independently proposed to simulate non-premixed turbulent combustion by Kilmenko [116] and Bilger [117]. Kilmenko [116] emphasized that it was more rigorous to calculate the turbulent diffusion in the mixing fraction space than in the physical space. Bilger [117] developed the CMC method based on the derivation of the experimental results that the fluctuations in the reacting scalars can be associated with fluctuations

in the mixing fraction. The basic concept of CMC is that the fluctuations in temperature and composition can be linked to the fluctuations in one or two key variables. In non-premixed combustion, mixture fraction is the key variable of interest. In many turbulent reacting flows, the values of the temperature and species mass fractions are found to vary little from others that have the same value of the mixture fraction [99]. In 1999, Kilmenko and Bilger [118] published the first comprehensive review of the CMC method. Sabelnikov et al. [119] presented an extension to the classical stretched flamelet model based on the CMC method, and accounted for the fluctuations of the velocity in the supersonic combustion field.

Great efforts have been made in advancing this method. During the last decade, the first major focus of CMC has been on the theoretical development of modelling of the flame regimes where local correlations between reacting scalars and mixture fraction are weakened. The second major focus has been on the application of the method to more complex flow geometries and flame conditions. Peters [97] pointed out that in the homogeneous flow case the first-order moment CMC equations are identical to the flamelet equations. In flames with significant local extinction and re-ignition, it has been found [120] that such first-order closure is not sufficiently accurate. This means that higher-order closure is needed if we require more information and more accuracy, and the calculation cost increases tremendously. More information about the CMC method can be found in Bilger et al. [99] and a recently published book by Echekki and Mastorakos [115].

2.2.2. Modelling of premixed turbulent combustion

Premixed turbulent combustion in technical devices often occurs in thin flame fronts which propagate into the unburnt reactants. The propagation of these fronts and the heat release is governed by the interaction of transport and chemistry within the fronts. Premixed combustion is much more difficult to model than non-premixed

combustion for the reason that it usually occurs as a thin, propagating flame that is stretched and contorted by turbulence. Different forms of paradigms have been proposed by Borghi [121], Peters [122], and Pitsch [63]. Modelling of premixed combustion has been widely and deeply developed for many decades. Most of the premixed turbulent combustion models are variants of the flamelet concept [63]. Other models that have been proposed include the thickened flame model and the linear eddy model. A literature review of premixed turbulent combustion models and applications is presented in [97]. Bilger [99] concluded that the models were used in the premixed turbulent combustion, including Damköhler paradigm, Bray–Moss–Libby (BML) models, coherent flamelet and flame surface density models, the level set approach, thickened flame-front paradigms. Pitsch [63] reviewed the regimes in premixed combustion large eddy simulations and presented a discussion of the two most widely used formulations in the flamelet regime, the flame surface density models and the level set (G equation) approach. Cant [115] presented a brief review of current modelling practice covering some simple models together with the flame surface density approach, the G equation and the more recent scalar dissipation rate model. Zimont [123-126] performed much research work on the premixed combustion modelling. In ANSYS FLUENT, the turbulent premixed combustion model is based on the work by Zimont et al. [124]. This model involves the solution of a transport equation for the reaction progress variable, the closure of which is based on the definition of the turbulent flame speed [127].

Knudsen et al. [128] analysed the premixed flamelet models for large eddy simulation of turbulent combustion. In their study, it was confirmed that the use of only a level set in a typical presumed PDF flamelet model was shown to produce significant errors, and it was recognized that a new method of coupling a level set and a progress variable in presumed PDF approaches was needed. In principle, the CMC approach, which has been proved successful in non-premixed combustion, could be extended to treat premixed flames, possibly by using the reaction progress

variable as a conditioning variable [115]. The use of a marker field variable has been suggested, but it is questionable whether this would bring any advantage over the existing level set approach [115]. One promising method is the Conditional Source Term Estimation (CSTE) approach [129]. The CSTE approach is closely related to CMC and may provide a realistic way to model chemical effects in the premixed flames. There have been applications of PDF transport modelling to premixed flames. Lindstedt and Vaos [130] applied a transported PDF approach to model premixed turbulent flames over a wide range of Reynolds numbers and convincing results have been obtained. The advantage of the PDF approach is its potential for generality. However, the computational cost is high and there are technical issues concerned with the modelling of mixing processes in the presence of the high scalar gradients that are typical of premixed flames [115]. The thin flame front paradigms may be the closest to what is of practical importance. However, the thickened flame model allows species mass fractions to be directly transported, and their chemistry to be described using Arrhenius rates. Also, it overcomes the issue of resolution by artificially broadening reactive scalar profiles and results robustness. But its drawbacks are obvious: on the one hand, it changes the nature of the turbulence and chemistry interaction in the flow; on the other hand, it typically does not permit the use of detailed chemical mechanisms [128].

2.2.3. Modelling of partially premixed turbulent combustion

As discussed at the beginning of §2.2, in many combustion systems, before the fuel and the oxidizer enter the flame, they are partially premixed. Partially premixed combustion plays, at least locally, an important role in practical applications. The most important distinction of partial premixing is between non-uniform combustible mixtures in which the compositions excludes stoichiometric mixtures and those in which stoichiometric mixtures do occur [99]. The distinction is helpful to distinguish

different categories of partial premixing. Peters [97] presented the regimes of the partially premixed combustion in the fourth chapter of his book “Turbulent Combustion”. Bilger [99] outlined the partially premixed combustion regimes and discussed the challenge of its modelling.

The partially premixed combustion mode may have a significant impact on the overall burning rate and flame stability. Therefore, the modelling of partially premixed combustion is very important and has got the attention and effort of researchers and engineers. The main challenge in the modelling of partially premixed combustion is to achieve a dual description of varying premixed fronts and trailing diffusion flames. Although the premixed and non-premixed are not antagonistic, they lead to flames with fundamentally different properties. In the point of view of premixed combustion regimes, the combustion is recognised to be propagated by the thin flame front. However, in the non-premixed combustion regimes, the diffusion flame is more mixing controlled. The difference between the two regimes makes it very difficult and complicated, and to some extent unlikely, to develop a numerical model for a diffusion flame which can properly describe both regimes [131]. Vervisch [132] pointed out that the development of theoretical LES models for the partially premixed turbulent combustion is made more difficult by uncertainties concerning the small-scale structure of the flame.

Currently, models which are developed for premixed and non-premixed combustion have been combined to simulate partially premixed combustion. For instance, joint level set and flamelet approach has been used to simulation the partially premixed combustion in a cavity-based scramjet combustor [11]. Domingo et al. [131] developed a new approach for the LES of partially premixed combustion. They derived an expression for a flame index based on the scalar product of fuel and oxidizer normal vectors suitable for LES. This flame index allows for quantifying the occurrence of the two combustion regimes: premixed and

non-premixed. The flame index approach is based on the C equation, where C is defined as the progress variable. Different reaction rates (source term in the C equation) modelling for premixed turbulent flames can be used and any sub-grid closure for non-premixed turbulent combustion, such as PDF, CMC and flamelets, may be used within this approach. It is a quite interesting and promising method to deal with premixed combustion. In ANSYS FLUENT, a simple combination of the nonpremixed and the premixed model is used to simulate partially premixed combustion. It solves a transport equation for the mean reaction progress variable to determine the position of the flame front, as well as the mean mixture fraction and the mixture fraction variance [127]. Zimmermann and Pfitzner [133] developed a model for partially premixed combustion by combining purely non premixed and perfectly premixed combustion models. Bilger [99] pointed out that it is not yet clear to what extent it is necessary to take account in the local reaction zone when modelling the various scalar dissipations and equivalent terms that appear in most models. The PDF methods have yielded excellent predictions of the Sandia non-premixed jet flames which may be recognized as partially premixed to some extent at some section in the flow field. It can even predict significant local extinction of these flames [99]. The success of the current generation of PDF models implies that their mixing closures are adequate for the local reaction zone structure, at least for these particular experiments. Also, CMC contains no representation of triple flames or edge flames but makes adequate predictions of the lifted flame. Bilger [99] concluded that we do not yet know how much detail of the local flame structure is required, and we cannot yet determine the range of applicability of the various modelling approaches for partially premixed turbulent combustion.

2.2.4. Modelling of turbulent supersonic combustion

To model the turbulent supersonic combustion, the understanding of its physics is quite crucial. From the 1950s, much effort has been on the understanding

of the supersonic combustion regimes, including experimental and numerical studies, but there are still numerous uncertainties and misunderstandings on this topic. The flame regimes may differ from those in subsonic combustion. Raman measurements of mixing and finite-rate chemistry in supersonic hydrogen/air non-premixed flame showed that this type of combustion is significantly different from combustion in low-speed flows [134]. Cheng et al. [134] suggested that finite-rate effects become particularly important in supersonic flows. Balakrishan and Williams [135] indicated that laminar flamelets are likely to exist in supersonic combustion under the conditions of their studies.

Ingenito and Bruno [136] reviewed the physics and regimes of supersonic combustion and analyzed the effects of Mach number and compressibility on turbulence and combustion. From their conclusions, we can get the ideas that the dissipative eddies are larger in supersonic flow than that in subsonic flow. Ingenito and Bruno [136] also pointed out that in supersonic combustion flames, the smallest eddies may be larger than the flame thickness, which means they can only wrinkle the flame without entering the flame. This conclusion impacts the choice of models for the interaction between chemistry and turbulence in supersonic combustion, depending not only on Reynolds but also on the Mach number. The LES reported in [136] indicated that supersonic combustion occurs in the flamelets-in-eddies regime, and the results showed reasonable prediction of the flame anchoring, the temperature, and the pressure distribution.

The categories of turbulent supersonic combustion vary with different fuel and oxider injection methods. Normally, in the scramjet chamber, the fuel (hydrogen or hydrocarbons) is injected to the supersonic air flow, and then the fuel is ignited. The turbulent supersonic combustion is normally regarded as non-premixed combustion. However, the flame holders such as strut and cavity are always installed in the combustor in order to maintain the flame, and they will change the flow and mixing

characteristics of the fuel and the air. So, in some section of the flow field, especially the recirculation zone, partially premixed combustion may occur.

The RANS approach has the most computational efficiency and has been widely used in the modeling of turbulent supersonic combustion. However, the modelling of all turbulence scales precludes the detailed prediction of the supersonic combustion flow flied. Although the DNS approach solves the whole range of spatial and temporal scales of the turbulence, the computational cost is too high for the modelling of supersonic combustion. A promising method for simulating scramjet combustion is LES in which the large turbulence scales are explicitly computed and only the small-scale and low-energy eddies are modelled. The direct computation of the large energy containing eddies gives LES more generality than RANS and the modelling of small eddies reduce the requirement to the mesh size and computational resources. In LES, the following combustion models are usually chosen: (i) reduced or global reaction mechanisms with Arrhenius rate expressions, (ii) flamelet models, (iii) linear eddy models, (iv) thickened flame models, and (v) PDF methods. Amongst these models, the flamelet model and PDF methods are promising and mostly used for the simulation of scramjet combustion [11].

Ladeinde [40] reviewed the application of both the assumed and transported PDF approach in the supersonic combustion modelling efforts. An assumed PDF model has been widely used for scramjet simulation. Baurle et al. [137] used the assumed and evolution PDFs to compare their relative performance in the modeling of turbulent reacting flow and the later one showed better computational efficiency. Also, the assumed PDF method has been added into the VULCAN code. Unfortunately, the assumed PDFs were found to be unable to accurately predict high-order correlations, such as terms involving the chemical production source [40]. Although the transported PDF approach is the most comprehensive treatment of supersonic combustion, there are issues related to computational efficiency,

chemical non-equilibrium, and the modelling of compressible turbulence. Thus, simplified, albeit finite-rate, models, such as the flamelet models are very interesting and promising. The fundamental concepts and mathematical formulations are given in Chapter 4.

2.3. Characteristics and problems of combustion in high speed flows

2.3.1. Characteristics of combustion in high speed flows

As shown in previous work [138,50,139-141], high speed flows are compressible, coupling the changes of velocity, density, pressure, and temperature. In the regime of turbulent combustion in high-speed flows, density variations arise not only from the heat release in combustion, but also from viscous heating, compression, and expansions associated with the high-speed. In supersonic flows, it is possible that the increase in the kinetic energy has a much larger effect than the heat release energy. Under this condition, the combustion has less effect on the density changes than does the compressibility [11]. In fact, at high Mach number, mixing and combustion are driven not only by vortex stretching as in subsonic reacting flows, but also by compressibility and baroclinic effects. In addition, dilatation favours combustion by increasing the reaction rates as supersonic combustion occurs locally at approximately constant volume condition [142].

2.3.2. Effects of compressibility

When using the LES approach, the sub-grid model, which was first developed from low speed and incompressible flows, has to be concerned more carefully. Research has shown that the Morkovin hypothesis is not tenable any more when the Mach number of the incoming flow is larger than about 3. (The Morkovin's

hypothesis is that turbulence structure is unaffected by pressure or density fluctuations if they are small compared to the mean pressure or density, which is normally understood as turbulence pulsing Mach number no large than 0.3 [143].) When the turbulence pulsing Mach number is smaller than about 0.3, the flow Mach number is small as well, and the compressibility can be unconcerned. However, it is not tenable for some practical situations, such as in gas turbines, ramjets and scramjets. Especially for scramjets, the flow velocity in the combustor can be very high, and the acoustic characteristics have a significant effect on the flow and the combustion; and therefore, the compressibility cannot be neglected. However, the difficulty of considering compressibility when simulating turbulence is just as big as it is important [144]. However, compressibility has different effects on different kinds of flows. For instance, the effects on the free shear/mixing layer and near-wall shear layer are quite different. At present, it is impossible to build a current compressibility-modified turbulence model which can be used in any kind of flows [145]. According to the discussion of Bradshaw [146] and the difficulty that compressibility brings, simulations on high speed complex turbulent flows always neglects the compressibility and directly uses the incompressible turbulent model. Ingenito et al. [147,148] took into account the effect of compressibility on the reaction rates and on the mixing. However, their simulation results and subgrid models need more validation.

2.3.3. Self-ignition, extinction and reignition

Supersonic flows have a high enthalpy and the stagnation temperature can be very high. The ignition delay can be shortened under this condition, so the fuel/air mixture may ignite by itself. The temperature and fuel distribution in the supersonic flow field is uneven, and this will cause the local extinction phenomena during the progress of the flame transmission and diffusion. The mixture may be reignited due

to the nonuniformity in the flow field. To simulate self-ignition, extinction, and reignition, detailed chemical kinetics is required. Once the chemical reaction deviates from the equilibrium state, some turbulent combustion models will lose their effectiveness.

2.3.4. Effect of shock waves

On the one hand, if there is an obstruction in the supersonic flow, a shock wave will be present. The shock wave is a kind of discontinuity, and its capture in 3D numerical simulation needs a much denser mesh in the flow field. On the other hand, the shock wave changes the flame structure. When the shock wave passes by the flame fronts, the local temperature changes, which are caused by the shock wave and combustion, may have the same order. The chemical reaction rate increases and the local pressure changes. When the shock wave passes by the unburned fuel/air mixture, the mixture may self-ignite, due to the increase in the temperature when the mixture passes the shock wave. Under these conditions, the hypotheses of some combustion models, e.g. LEM and Flamelet model, should be recalculated. Also results obtained from these models should be treated with discretion [11].

2.4. Closure

In this chapter, a review of the scramjet combustion numerical simulation is presented. Firstly, numerical simulations of the compressible turbulent flow using the RANS, LES and DNS approaches are discussed. Secondly, the modelling of non-premixed, premixed and partially premixed turbulent combustion is reviewed. Further, the development of the modelling of the turbulent supersonic combustion is reviewed and discussed. Finally, the main characteristics and problems associated with combustion in high speed flows are concluded and discussed, and it is found

that advance turbulence models and turbulent combustion models are in high demand in the accurate prediction of the supersonic flames and with acceptable computational costs.

Chapter 3
Turbulence LES modelling and numerical approach

During the last three decades, the LES technique has been developed considerably, including the underline theories, new models and more efficient numerical schemes. Nowadays, LES has become a powerful technology for the modelling of turbulent flows and combustion. In LES, the scales of turbulence are separated into large scales and small scales or namely Sub-Grid Scales (SGS). In order to define these two categories, a filter length has been determined. The scales whose characteristic size is larger than the filter length are recognized as the large scales, or the so called large eddies. The others are small or sub-grid scales. The large scale structures, which are the nature of the flow and depend strongly on the boundary conditions, dominate the turbulent flow, and they are responsible for most of the transport of the mass and momentum.

In contrast to the large scales, the sub-grid scales mainly dissipate the fluctuations of the transported quantities and only slightly affect the mean characteristics of the flow. The small scales are more universal in nature and therefore more amenable to be modelled than are the large scales. The above analysis is the physical basis of LES. The large scales are directly computed whilst the influence of the small scales on the large scales is modelled with appropriate SGS mathematical models [65]. Therefore, LES employs filtered Navier–Stokes equations and these provide a description of the space and time dependence of the resolved large scales. Since the chemical reactions occur at the smallest scales, there is no resolved portion of the chemical source term in LES. Therefore, combustion needs to be modelled in a similar manner to RANS. As regards the LES, this predicts the turbulent mixing which is mainly controlled by the large scales and it is

the key to the chemical conversion, being more accurate than RANS, and LES brings improvements to the predictions of the turbulent reacting flows [149]. In the following section, the basic theory behind the LES method is discussed in detail.

3.1. Turbulence LES modelling

3.1.1. Navier–Stokes equations of gaseous combustion

The equations governing gaseous combustion are summarized by Equation (3.1). They are valid for a mixture of ideal gases in local thermodynamic equilibrium and chemical non-equilibrium.

$$\begin{aligned}
&\text{Mass:} && \frac{\partial \rho}{\partial t} + \frac{\partial \rho u_i}{\partial x_i} = 0, \\
&\text{Momentum:} && \frac{\partial \rho u_i}{\partial t} + \frac{\partial \left(\rho u_i u_j + p\delta_{ij} - \tau_{ij}\right)}{\partial x_j} = 0, \\
&\text{Energy:} && \frac{\partial \rho E}{\partial t} + \frac{\partial \left[(\rho E + p)u_i + q_i - u_j \tau_{ji}\right]}{\partial x_i} = 0, \\
&\text{Species:} && \frac{\partial \rho Y_m}{\partial t} + \frac{\partial}{\partial x_i}\left[\rho Y_m \left(u_i + V_{i,m}\right)\right] = \dot{\omega}_m,
\end{aligned} \tag{3.1}$$

where, $m = 1, 2, \ldots, Ns$ and Ns is the number of the chemical species, Y_m, $V_{i,m}$ and $\dot{\omega}_m$ are the mass fraction, diffusion velocity and source term of the chemical species m, respectively, and $V_{i,m}$ can be given by

$$V_{i,m} = -\frac{D_m}{Y_m}\frac{\partial Y_m}{\partial x_i}, \tag{3.2}$$

where D_m is the mass diffusion coefficient. To be consistent with the mass conservation law, it is clear that

$$\sum_{m=1}^{Ns} Y_m V_{i,m} = 0\,, \sum_{m=1}^{Ns} \dot{\omega}_m = 0. \tag{3.3}$$

In Equations (3.1), τ_{ij} is the viscous stress and can be given by

$$\tau_{ij} = 2\mu\left(S_{ij} - \frac{1}{3}S_{kk}\delta_{ij}\right),$$
$$S_{ij} = \frac{1}{2}\left(\frac{\partial u_i}{\partial x_j} + \frac{\partial u_j}{\partial x_i}\right) \tag{3.4}$$

where μ is the molecular viscosity and can be obtained from Sutherland equations:

$$\mu = \mu_0\left(\frac{T}{T_0}\right)^{1.5}\left(\frac{T_0 + T_s}{T + T_s}\right), \tag{3.5}$$

where $\mu_0 = 1.7161\text{e} - 7\ (\text{Pa}\cdot\text{s})$, $T_0 = 273.16$ K and $T_s = 124$ K for air. It should be noted that the summation of the species conservation equations in Equation (3.1) yields the total mass conservation, thus one of these $Ns + 1$ equations is redundant.

If the radiation and Dufour effects are neglected [150], the heat fluxes q_i can be given by

$$q_i = -\kappa\frac{\partial T}{\partial x_i} + \rho\sum_{m=1}^{N} h_m\, Y_m V_{i,m}, \tag{3.6}$$

where κ is the thermal conductivity and $\kappa = c_p\mu/\text{Pr}$. Pr is the Prandtl number and $c_p = \sum_{m=1}^{Ns} c_{p,m}\, Y_m$, where $c_{p,m}$ is the specific heat at constant pressure of the species m and can be obtained from

$$c_{p,m} = a_{1,m} + a_{2,m}T + a_{3,m}T^2 + a_{4,m}T^3 + a_{5,m}T^4, \tag{3.7}$$

and the parameters $a_{1,m}, \ldots, a_{5,m}$ can be found in [151]. Further, the gaseous mixture should satisfy the thermodynamic state equation:

$$P = \rho T\sum_{m=1}^{N}\frac{Y_m R_u}{M_m}, \tag{3.8}$$

where $R_u = 8.314\ \text{J}/(\text{mol}\cdot\text{K})$ and M_m is the molecular weight of the species m. The temperature is implicitly related to the internal energy or enthalpy through

$$\rho E = \rho\left(e + \frac{1}{2}u_k u_k\right), e = \sum_{m=1}^{N_m} Y_m\, h_m - \frac{p}{\rho}, \tag{3.9}$$

where e and h are the internal energy and enthalpy per unit mass which are functions of the temperature only for an ideal gas, and h_m can be given by

$$h_m = \int_{T_0}^{T} c_{p,m} dT + h_m^0, \tag{3.10}$$

where T_0 is the reference temperature and usually $T_0 = 298.16\,\mathrm{K}$, and h_m^0 is the enthalpy of formation of the species m.

When numerically solving the above equations in DNS, the velocity field has to be resolved on length scales down to the Kolmogorov scale. In LES, a low-pass filter is used to distinguish the solution space into resolved and unresolved scales. Then the filtered velocity field can be adequately resolved on a relatively coarse grid. Specifically, the required grid spacing is proportional to the specified filter width [65]. The filtering is represented mathematically in the physical space as a convolution product. The general filtering operation introduced by Leonard [152] is defined by:

$$\bar{f}(x,y,z,t) = \iiint_{-\infty}^{+\infty} G(x-x', y-y', z-z') f(x,y,z,t) dx dy dz, \tag{3.11}$$

where $\bar{f}(x,y,z,t)$ is the resolved part of the space time variable $f(x,y,z,t)$, G is the convolution kernel and this is associated with the cut-off scales $\bar{\Delta}$ in space. $f'(x,y,z,t)$ is denoted as the difference between f and $\bar{f}$:

$$f' = f - \bar{f}. \tag{3.12}$$

Three particular convolution filters are commonly used for performing the spatial scale separation, namely, the Box or top hat filter, the Gaussian filter, and the spectral or sharp cut-off filter [66]. Each filter has a length scale $\bar{\Delta}$ associated with it and is taken to be intermediate between the Kolmogorov length scale and the integral length scale. The box filter is adopted in the present LES, as it fits naturally into a finite difference discretization of the continuous governing equations, namely

$$\bar{\Delta} = 2(\Delta x \Delta y \Delta z)^{1/3}, \tag{3.13}$$

where $\bar{\Delta}$ is the characteristic width of the filter, Δx, Δy and Δz refer to the width of the finite volume in the coordinate directions. A typical rectangular top-hat filter of the three widths Δ_i can be defined as follows:

$$G(x_i - x_i') = \begin{cases} \prod_{i=1}^{3} \frac{1}{\Delta_i} & if \ |x_i'| \leq \Delta_i/2 \\ 0 & otherwise \end{cases}. \tag{3.14}$$

Researchers dealing with LES in compressible flows have used a change of variable in which the filtered variables are weighted by the density [66]. Mathematically, this change of variables is written as follows:

$$\overline{\rho\phi} = \bar{\rho}\tilde{\phi}. \tag{3.15}$$

Any scalar or vector variable can be decomposed into a low frequency part $\tilde{\phi}$ and a high frequency part $\phi^{"}$:

$$\phi = \tilde{\phi} + \phi^{"}. \tag{3.16}$$

More information about the differential interpretation of the filters, discrete representation of filters, filtering of discontinuities, filtering associated to the numerical method and Favre filtering can be found in [66].

3.1.2. Formulation of the filtered governing equations

In the regime of flamelet combustion models, the mixture fraction theory is employed. Further, the set of species transport equations are not solve. Instead, the species concentrations are derived from the predicted scalars (could be mixture fraction and progress variable), and this is the reason why the flamelet model is very efficient for combustion modelling. More information about mixture fraction theory and the flamelet model can be found in Chapter 4, [97] and [127].

In the present study, the hybrid RANS/LES method, which was developed by Fan et al. [153] is employed. A blending function F is defined in order to switch the RANS turbulence models in the near-wall region to the LES subgrid-scale turbulence models in the far-wall region. Thus, the hybrid turbulent viscosity can be given by

$$\mu_t^{hyb} = F\mu_t^{RANS} + (1-F)\mu_t^{LES}, \tag{3.17}$$

where μ_t^{RANS} and μ_t^{LES} is the turbulent viscosity obtained from the RANS model and the LES subgrid-scale model. F is the blending function which facilitates merging the RANS and LES descriptions of the flow and the cases $F = 0$ and 1 correspond to a fully LES model and a fully RANS model, respectively.

In the regime of hybrid RANS/LES, the filtered governing equations are given by

$$\begin{aligned}
&\text{Mass:} && \frac{\partial \bar{\rho}}{\partial t} + \frac{\partial(\bar{\rho}\tilde{u}_i)}{\partial x_i} = 0, \\
&\text{Momentum:} && \frac{\partial(\bar{\rho}\tilde{u}_i)}{\partial t} + \frac{\partial\left[\bar{\rho}\tilde{u}_i\tilde{u}_j + \bar{\rho}\delta_{ij} - \bar{\tau}_{ij} + \tau_{ij}^{hyb}\right]}{\partial x_j} = 0, \\
&\text{Energy:} && \frac{\partial\left(\bar{\rho}\tilde{E}\right)}{\partial t} + \frac{\partial\left[\left(\bar{\rho}\tilde{E} + \bar{p}\right)\tilde{u}_i + \bar{q}_i - \tilde{u}_j\bar{\tau}_{ji} + H_i^{hyb} + \sigma_{ij}^{hyb}\right]}{\partial x_i} = 0, \\
&\text{Species:} && \frac{\partial \bar{\rho}\tilde{\phi}_n}{\partial t} + \nabla\cdot\left(\bar{\rho}\tilde{u}\tilde{\phi}_n - \bar{\rho}\bar{D}\nabla\tilde{\phi}_n + \tilde{\phi}_n^{hyb}\right) = \tilde{\dot{\omega}}_n, (n = 1, 2, \ldots),
\end{aligned} \tag{3.18}$$

where $\bar{\rho}$, $\tilde{u}$, $\tilde{E}$ and $\bar{p}$ are the filtered density, velocity, total energy and static pressure of the gas, respectively. $\tilde{E}$ can be given by

$$\tilde{E} = \sum_{m=1}^{Ns} \tilde{h}_m\tilde{Y}_m - \frac{\bar{p}}{\bar{\rho}} + \frac{1}{2}\tilde{u}_k\tilde{u}_k + \tilde{k}, \tag{3.19}$$

where $\tilde{h}_m$ is the total enthalpy of the species m and can be obtained through the polynomial fitting method [154]. $\tilde{k}$ (also can denoted as k^{SGS}) is the filtered turbulent kinetic energy and $\tilde{k} = (1/2)[\widetilde{u_k u_k} - \tilde{u}_k\tilde{u}_k]$. In general, the scalars ϕ_n in

Equation (3.18) could include the mixture fraction, a particular species, or some more complicated composite quantity. In the present research, the scalar equations considered are for the mixture fraction f and the progress variable C. The mixture fraction is a conserved scalar, thus the source term in its transport equation is not present. More information about f and C can be found in Chapter 4.

The terms $\bar{\tau}_{ij}$ and $\bar{q}_i$ in Equation (3.18) can be given by

$$\begin{aligned} \bar{\tau}_{ij} &= 2\bar{\mu}\left(\tilde{S}_{ij} - \frac{1}{3}\tilde{S}_{kk}\delta_{ij}\right), \\ \bar{q}_i &= -\bar{\kappa}\frac{\partial \tilde{T}}{\partial x_i} - \bar{\rho}\sum_{m=1}^{Ns}\tilde{h}_m\overline{D}_m\frac{\partial \tilde{Y}_m}{\partial x_i}, \end{aligned} \tag{3.20}$$

where $\bar{\kappa}$ is the thermal conductivity and $\bar{\kappa} = C_p(\tilde{T})\bar{\mu}/\mathrm{Pr}$. $C_p(\tilde{T})$ is the specific heat at constant pressure, $\overline{D}_m$ is the diffusion coefficient and $\overline{D}_m = \bar{\mu}/(\bar{\rho}\mathrm{Sc})$, where Sc is the Schmidt number.

In order to close Equation (3.18), the terms τ_{ij}^{hyb}, H_i^{hyb}, σ_{ij}^{hyb} and $\tilde{\phi}_k^{hyb}$, i.e. the filtered stress tensor, enthalpy flux, shear stress tensor and scalar flux, are required to be modelled. As recommended by Sun [11] and Fan [154], these terms can be given by

$$\begin{cases} \tau_{ij}^{hyb} = \mu_t^{hyb}\left(\dfrac{\partial \tilde{u}_i}{\partial x_j} + \dfrac{\partial \tilde{u}_j}{\partial x_i} - \dfrac{2}{3}\dfrac{\partial \tilde{u}_k}{\partial x_k}\delta_{ij}\right) - \dfrac{2}{3}\bar{\rho}\tilde{k}\delta_{ij} \\ H_i^{hyb} = -\dfrac{\mu_t^{hyb}}{\mathrm{Sc}_t}\displaystyle\sum_{m=1}^{Ns}\tilde{h}_m\frac{\partial \tilde{Y}_m}{\partial x_i} - \dfrac{C_p(\tilde{T})\mu_t^{hyb}}{\mathrm{Pr}_t}\dfrac{\partial \tilde{T}}{\partial x_i} \\ \sigma_{ij}^{hyb} = -\tilde{u}_j\tau_{ij}^{hyb} \\ \tilde{\phi}_k^{hyb} = \dfrac{\mu_t^{hyb}}{\mathrm{Pr}_t}\dfrac{\partial \tilde{\phi}_k}{\partial x_i} \end{cases}, \tag{3.21}$$

where Pr_t and Sc_t are the turbulent Prandtl and Schmidt numbers, respectively. In the present study, both Pr_t and Sc_t take a constant value 0.9, which is recommended by [11]. The hybrid turbulent viscosity μ_t^{hyb} is calculated using a hybrid turbulent model given by Equation (3.17).

In the present research, μ_t^{RANS} is obtained from the $k-\omega$ SST turbulent model and the governing equations are given by

$$\frac{\partial \bar{\rho} k^{RANS}}{\partial t} + \frac{\partial (\bar{\rho} k^{RANS} \tilde{u}_i)}{\partial x_i} = \frac{\partial}{\partial x_i}\left[\left(\mu + \frac{\mu_t^{RANS}}{\sigma_k^{RANS}}\right)\frac{\partial k^{RANS}}{\partial x_i}\right] + P_k^{RANS} - \bar{\rho}\beta^* k^{RANS}\tilde{\omega}, \tag{3.22}$$

$$\frac{\partial \bar{\rho}\tilde{\omega}}{\partial t} + \tilde{u}_i \frac{\partial (\bar{\rho}\tilde{\omega})}{\partial x_i} = \frac{\partial}{\partial x_i}\left[(\mu + \sigma_\omega \mu_t^{RANS})\frac{\partial \tilde{\omega}}{\partial x_i}\right] + P_\omega - \beta \bar{\rho}\tilde{\omega}^2 + \frac{2(1-F_1)\bar{\rho}\sigma_{\omega 2}}{\tilde{\omega}}\frac{\partial k^{RANS}}{\partial x_i}\frac{\partial \tilde{\omega}}{\partial x_i}. \tag{3.23}$$

In the above equations, β, β^*, σ_ω and $\sigma_{\omega 2}$ are the parameters in the $k-\omega$ SST turbulent model. P_k^{RANS} is the production of the turbulent kinetic energy k^{RANS} and is given by

$$P_k^{RANS} = \tau_{ij}^{RANS}\frac{\partial \tilde{u}_i}{\partial x_j},$$
$$\tau_{ij}^{RANS} = \mu_t^{RANS}\left(2\tilde{S}_{ij} - \frac{2}{3}\frac{\partial \tilde{u}_k}{\partial x_k}\delta_{ij}\right) - \frac{2}{3}\bar{\rho}k^{RANS}\delta_{ij}. \tag{3.24}$$

In the $k-\omega$ SST turbulent model, the turbulent viscosity is given by

$$\mu_t^{RANS} = \frac{a_1 \rho k^{RANS}}{\max(a_1\omega, SF_2)}, \tag{3.25}$$

where S and F_2 are the strain rate magnitude and the blending function, respectively. For the reason that the Reynolds number of the supersonic flows in the present study is high, the parameter a_1 takes a constant value 1.0 [127]. More information about the parameters and blending functions in the $k-\omega$ SST model can be found in Menter [55] and Sun [11].

Concerning the quantity μ_t^{LES}, the Smagorinsky-Lilly model [149] provides an approximation for the subgrid-scale turbulent eddy viscosity. The Smagorinsky model relates the turbulent viscosity μ_t^{LES} to the filter width Δ with the filtered large scale velocity tensor $\tilde{S}_{ij}$. The relationship is given as follows:

$$\mu_t^{LES} = \bar{\rho}(C_s\Delta)^2\left|\tilde{S}_{ij}\right|, \tag{3.26}$$

where C_s is the Smagorinsky-Lilly constant. The proportionality constant C_s in this model is suggested to be taken to be between 0.17 and 0.21 by Lilly [127]. However, near the solid boundary the value of the constant 0.17 was found to cause excessive damping of large-scale fluctuations in the presence of the mean shear and in transitional flows, and that means the value of C_s has to be reduced in such regions [127]. In fact, C_s is not a physical quantity, and it is not a universal constant even for a specific flow and flow solver. This is the most serious shortcoming of this simple model. Further, the Smagorinsky-Lilly model assumes locally isotropic turbulence and therefore does not take into consideration the effects of inhomogeneities. In order to overcome these shortcomings, Yoshizawa et al. [155] presented a subgrid-scale model in which the subgrid-scale kinetic energy is calculated using a separate transport equation, as follows:

$$\frac{\partial\bar{\rho}k^{sgs}}{\partial t} + \frac{\partial(\bar{\rho}k^{sgs}\tilde{u}_i)}{\partial x_i} = \frac{\partial}{\partial x_i}\left[\left(\frac{\mu_t^{LES}}{\mathrm{Pr}_t}\right)\frac{\partial k^{sgs}}{\partial x_i}\right] + P_k^{SGS} - D^{sgs}, \tag{3.27}$$

where P_k^{SGS} and D^{sgs} are the production and dissipation of the subgrid-scale kinetic energy k^{sgs}.

In order to close Equation (3.27), Yoshizawa et al. [155] recommended to employ the following equations:

$$\begin{aligned} \mu_t^{LES} &= C_\mu\bar{\rho}\sqrt{k^{sgs}}\Delta, \\ D^{sgs} &= C_d\bar{\rho}(k^{sgs})^{\frac{3}{2}}/\Delta. \end{aligned} \tag{3.28}$$

In the present study, the Yoshizawa subgrid-scale model is employed to model the subgrid-scale turbulent viscosity. The parameters C_μ and C_d take the values 0.02075 and 1.0, respectively, which are used and recommended by Sun [11].

Once μ_t^{RANS} and μ_t^{LES} are solved, the hybrid turbulent viscosity μ_t^{hyb} can be calculated through Equation (3.17). In the present research, the blending function which is developed by Sun [11], is employed to blend the solutions obtained from the LES and the RANS, and the blending function is given by

$$F = \tanh(\eta^4),$$
$$\eta = \max\left(\frac{\alpha\sqrt{k}}{0.09\omega d}, \frac{500\mu}{\rho\omega d^2}\right). \tag{3.29}$$

where d is the distance between the grid node and the nearest wall surface. The parameter α takes a constant value 1.505, and this is recommended by Sun [11]. This blending function has been validated to be efficient to provide a smooth transition between the RANS and LES, and also produce good predictions for compressible flows, including the flows with an adverse pressure gradient.

It should be noted that the equations given in this section are nonlinear equations and also highly coupled to each other. Therefore, it is impossible to obtain an analytical solution. However, numerical solutions can be obtained based on the numerical techniques which are discussed in the following section.

3.2. Numerical approach

The numerical techniques for the RANS/LES method contain the spatial discretization schemes, the procedures used to solve the equations in time and the treatment of the boundaries. Advanced discretization schemes, proper boundary conditions and multi-block computing technique are utilized in the present hybrid RANS/LES code in order to increase the simulation accuracy and reduce the computational time and cost.

3.2.1. Spatial discretization

An important feature of compressible flows is the existence of shocks and often complicated structures in the smooth part of the solution. This gives the challenge of choosing the spatial discretization schemes so that the solver is non-oscillatory and also has high order accuracy. Further, the high order finite difference schemes could assist in improving the efficiency of numerical computations. For instance, these schemes can be used either to reduce the computational cost for a given accuracy by reducing the mesh size or to increase the accuracy for a fixed mesh size. Shu [156] reviewed the popular class of high order numerical methods for solving convection dominated partial differential equations, including the Weighted Essentially Non-Oscillatory (WENO) finite difference schemes, the WENO finite volume schemes, and the discontinuous Galerkin (DG) finite element schemes, as well as their applications in CFD.

The WENO scheme is an improvement based upon the ENO scheme and it has a better performance in robustness, smoothness of fluxes, steady state convergence and efficiency. More details of the ENO and the WENO schemes can be found in Shu [157]. In the present RANS/LES code, which was originally developed by Sun [11], the spatial discretization is based on the fifth-order WENO scheme for the convective fluxes and the second-order accurate-centred scheme for the diffusive fluxes. In order to employ the finite differences, the physical domain needs to be transformed to a computational domain, i.e. $(x, y, z) \rightarrow (\xi, \eta, \zeta)$. Thus the spatial partial differential operator is converted in the following format:

$$\begin{aligned} \frac{\partial}{\partial x} &\rightarrow \left(\frac{\partial \xi}{\partial x}\right)\frac{\partial}{\partial \xi} + \left(\frac{\partial \eta}{\partial x}\right)\frac{\partial}{\partial \eta} + \left(\frac{\partial \zeta}{\partial x}\right)\frac{\partial}{\partial \zeta}, \\ \frac{\partial}{\partial y} &\rightarrow \left(\frac{\partial \xi}{\partial y}\right)\frac{\partial}{\partial \xi} + \left(\frac{\partial \eta}{\partial y}\right)\frac{\partial}{\partial \eta} + \left(\frac{\partial \zeta}{\partial y}\right)\frac{\partial}{\partial \zeta}, \\ \frac{\partial}{\partial z} &\rightarrow \left(\frac{\partial \xi}{\partial z}\right)\frac{\partial}{\partial \xi} + \left(\frac{\partial \eta}{\partial z}\right)\frac{\partial}{\partial \eta} + \left(\frac{\partial \zeta}{\partial z}\right)\frac{\partial}{\partial \zeta}. \end{aligned} \tag{3.30}$$

More information about this transformation and the solutions for obtaining $\partial\xi/\partial x$, etc. are introduced in detail by Anderson [158].

Finite difference methods have the same format for one and more space dimensions; therefore, we introduce the numerical schemes for the simplest case, i.e. a one-dimensional conservation equation in the computational domains:

$$\frac{\partial u}{\partial t}+\frac{\partial f(u)}{\partial \xi}=0. \tag{3.31}$$

In the following work, the $f(u)|_{\xi=\xi_i}$ is denoted by f_i. The equation (3.31) approximates the derivative $\partial f/\partial\xi$ by a conservative difference, and then the following equation is obtained:

$$\frac{\partial u_i}{\partial t}=-\frac{1}{\Delta\xi_i}\left(\hat{f}_{i+1/2}-\hat{f}_{i-1/2}\right), \tag{3.32}$$

where $\hat{f}_{i+1/2}$ and $\hat{f}_{i-1/2}$ are the numerical flux, which typically is a Lipschitz continuous function of several neighboring values, e.g. f_{i-2}, f_{i-1}, f_i, f_{i+1} and f_{i+2}.

If $\hat{f}_{i+1/2}\geq 0$, the fifth-order finite difference WENO scheme has the flux given by the linear convex combination of the three third-order approximations $\hat{f}^{(1)}_{i+1/2}$, $\hat{f}^{(2)}_{i+1/2}$ and $\hat{f}^{(3)}_{i+1/2}$:

$$\hat{f}_{i+1/2}=\omega_1\hat{f}^{(1)}_{i+1/2}+\omega_2\hat{f}^{(2)}_{i+1/2}+\omega_3\hat{f}^{(3)}_{i+1/2}. \tag{3.33}$$

In the above equation, $\hat{f}^{(i)}_{i+1/2}$ are the three third order fluxes in the three stencils $S_1=\{\xi_{i-2},\ \xi_{i-1},\ \xi_i\}$, $S_2=\{\xi_{i-1},\ \xi_i,\ \xi_{i+1}\}$ and $S_3=\{\xi_i,\ \xi_{i+1},\ \xi_{i+2}\}$, respectively, and can be written as follows:

$$\begin{aligned}
\hat{f}^{(1)}_{i+1/2}&=\frac{1}{3}f_{i-2}-\frac{7}{6}f_{i-1}+\frac{11}{6}f_i,\\
\hat{f}^{(2)}_{i+1/2}&=-\frac{1}{6}f_{i-1}+\frac{5}{6}f_i+\frac{1}{3}f_{i+1},\\
\hat{f}^{(3)}_{i+1/2}&=\frac{1}{3}f_i+\frac{5}{6}f_{i+1}-\frac{1}{6}f_{i+2}.
\end{aligned} \tag{3.34}$$

The nonlinear weights ω_i are given by

$$\omega_i = \frac{\alpha_n}{\sum_{n=1}^{3}\alpha_n}, \quad \alpha_n = \frac{\gamma_n}{(\varepsilon+\beta_n)}. \tag{3.35}$$

and the linear weights γ_n are given by $\gamma_1 = 1/10$, $\gamma_2 = 3/5$ and $\gamma_3 = 3/10$. The parameter ε is a small value which is used to avoid the denominator becoming 0, and as recommended by Sun [11], it is taken as $\varepsilon = 1.0\mathrm{e}-15$ in the present study. Further, the smoothness indicators β_n are given by

$$\begin{aligned}
\beta_1 &= \frac{13}{12}(f_{i-2} - 2f_{i-1} + f_i)^2 + \frac{1}{4}(f_{i-2} - 4f_{i-1} + 3f_i)^2, \\
\beta_2 &= \frac{13}{12}(f_{i-1} - 2f_i + f_{i+1})^2 + \frac{1}{4}(f_{i-1} - f_{i+1})^2, \\
\beta_3 &= \frac{13}{12}(f_i - 2f_{i+1} + f_{i+2})^2 + \frac{1}{4}(3f_i - 4f_{i+1} + f_{i+2})^2.
\end{aligned} \tag{3.36}$$

For scalar equations without the property $\hat{f}_{i+1/2} \geq 0$, we could split the flux into two part as follows:

$$\hat{f}_{i+1/2} = \hat{f}^{+}_{i+1/2} + \hat{f}^{-}_{i+1/2}, \qquad \left(\hat{f}^{+}_{i+1/2} \geq 0,\ \hat{f}^{-}_{i+1/2} < 0\right) \tag{3.37}$$

and apply the above procedure to $\hat{f}^{+}_{i+1/2}$, and a mirror image (with respect to i+1/2) procedure to $\hat{f}^{-}_{i+1/2}$. Similarly, the above reconstruction procedure could be performed to $\hat{f}_{i-1/2}$. It should be noted that, in the computational domains, $\xi_i = i$ and i is the number indicator of the mesh points.

When employing the fifth-order WENO scheme to the three-dimensional conservation equations, i.e.

$$\frac{\partial U}{\partial t} + \frac{\partial F(U)}{\partial \xi} + \frac{\partial G(U)}{\partial \eta} + \frac{\partial H(U)}{\partial \zeta} = \frac{\partial F_v(U)}{\partial \xi} + \frac{\partial G_v(U)}{\partial \eta} + \frac{\partial H_v(U)}{\partial \zeta} + S(U), \tag{3.38}$$

a decoupling procedure is required, and the above equations could be given by

$$\frac{\partial U}{\partial t} + A\frac{\partial U}{\partial \xi} + B\frac{\partial U}{\partial \eta} + C\frac{\partial U}{\partial \zeta} = \frac{\partial F_v(U)}{\partial \xi} + \frac{\partial G_v(U)}{\partial \eta} + \frac{\partial H_v(U)}{\partial \zeta} + S(U), \tag{3.39}$$

where U is the conservative flux and $U = (\bar{\rho}, \bar{\rho}\tilde{u}, \bar{\rho}\tilde{v}, \bar{\rho}\tilde{w}, \bar{\rho}\tilde{e})$, F, G and H are the convective fluxes, F_v, G_v and H_v are the diffusive fluxes, and S is the source term. A, B and C are the Jacobian matrix base on the Roe average and could be calculated

using the parameters at $\xi_{i+1/2}$. Here, we introduce the procedure of performing the fifth-order WENO scheme to the one-dimensional equation:

$$\frac{\partial U}{\partial t}+\frac{\partial F(U)}{\partial \xi}=\frac{\partial U}{\partial t}+A\frac{\partial U}{\partial \xi}=0. \tag{3.40}$$

If A is invertible and its eigenvalues and eigenvectors are real numbers, there is a diagonal matrix $\Lambda = LAR$, where L and R are the matrixes composed of the left and right eigenvectors of A. Hence, A can be decomposed into the very special form $A = R\Lambda L$. The one-dimensional equations may be given by:

$$\frac{\partial U}{\partial t}+A\frac{\partial U}{\partial \xi}=\frac{\partial U}{\partial t}+R\Lambda L\frac{\partial U}{\partial \xi}=0. \tag{3.41}$$

Here, we define $W = LU$ and $\Lambda = \Lambda^{+} + \Lambda^{-}$, and the above equation can be transformed into:

$$\frac{\partial W}{\partial t}+\Lambda^{+}\frac{\partial W}{\partial \xi}+\Lambda^{-}\frac{\partial W}{\partial \xi}=0. \tag{3.42}$$

In the present study, Λ^{+} and Λ^{-} are calculated using the following equations:

$$\Lambda^{+}=\frac{(\Lambda+|\Lambda|_{max})}{2},\ \Lambda^{+}=\frac{(\Lambda-|\Lambda|_{max})}{2},|\Lambda|_{max}=\lambda_{max}I, \tag{3.43}$$

where λ_{max} and I are the maximum eigenvalue of A and the identity matrix, respectively. Further, the fifth-order WENO scheme can be employed to Equation (3.42) following the procedure performed for the one-dimensional conservation equation. Finally, the original conservative flux U can be obtained from $U = RW$.

According to the discretization of the diffusive fluxes, the second-order accurate-centred scheme is employed, and it is validated to be an effective scheme when modelling high Reynolds number compressible turbulent flows [159]. The discretization equation is given by

$$\left(\frac{\partial F_v(U)}{\partial \xi}\right)_i=\frac{F_v(U)_{i+1/2}+F_v(U)_{i-1/2}}{\Delta\xi_i}+O(\Delta\xi_i^2). \tag{3.44}$$

3.2.2. Time advancement scheme

For compressible flow simulations, a very popular time advancement scheme, i.e. a temporal discretization method, for solving the semi-discretization conservation equations:

$$\frac{dU}{dt} = -\Omega(U), \tag{3.45}$$

is the high order Runge-Kutta method, which has a Total Variation Diminishing (TVD) property [11]. In Equation (3.45), Ω denotes the spatial discretization operator and it is possibly nonlinear. In the present study, the second-order Runge-Kutta method is employed and the time marching procedure can be given by

$$\begin{aligned} U^{(0)} &= U^n, \\ U^{(1)} &= U^{(0)} - \Delta t \cdot \Omega\left(U^{(0)}\right), \\ U^{(2)} &= \frac{1}{2}U^{(0)} + \frac{1}{2}U^{(1)} - \frac{1}{2}\Delta t \cdot \Omega\left(U^{(1)}\right), \\ U^{n+1} &= U^{(2)}, \end{aligned} \tag{3.46}$$

where Δt is the time step and is restricted to the stability limit of the underlying solver. At each cell of the domain, the local time step Δt_{local} is determined by the Courant-Friedrichs-Lewy (CFL) condition [127] and can be calculated as follows [160]:

$$\frac{1}{\Delta t_{local}} \geq \frac{1}{\Delta t_\xi} + \frac{1}{\Delta t_\eta} + \frac{1}{\Delta t_\zeta} + \frac{1}{\Delta t_{vis,\xi}} + \frac{1}{\Delta t_{vis,\eta}} + \frac{1}{\Delta t_{vis,\zeta}}, \tag{3.47}$$

where Δt_l and $\Delta t_{vis,l}$ are the convective time step and the viscous time step in the l direction ($l = \xi, \eta$ and ζ to indicate the three coordinate directions), respectively. The convective time steps satisfy the following relations:

$$\frac{\mathrm{CFL}}{\Delta t_l} \geq \lambda_l = \left| U_l + a\sqrt{\beta_l^2} \right|, \tag{3.48}$$

where U_l is the contravariant velocity for the l direction, a is the local speed of sound and λ_l is the eigenvalue. U_l, a and β_l can be calculated using the following equations:

$$\beta_l = \sqrt{l_x^2 + l_y^2 + l_z^2}, \tag{3.49}$$

$$U_l = ul_x + vl_y + wl_z, \tag{3.50}$$

$$a = \sqrt{\gamma P/\rho}, \tag{3.51}$$

where u, v and w are the velocity components in the X, Y and Z directions, respectively. The ratio of specific heats γ takes a constant value 1.40, which is recommended by Sun [11]. The terms l_x are defined as $l_x = \partial l/\partial x$, i.e. the terms $\partial\xi/\partial x$, $\partial\eta/\partial x$ and $\partial\zeta/\partial x$ in Equation (3.30). On the other hand, the viscous contributions to the time step are given by:

$$\frac{\mathrm{CFL}}{\Delta t_{vis,l}} \geq \lambda_{vis,l} = \frac{\mu}{\rho}\left\{\beta_l\left[max\left(\frac{4}{3}, \frac{\gamma}{\mathrm{Pr}}\right)\right] + \frac{1}{3}\left(\left|l_x l_y + l_x l_z + l_y l_z\right|\right)\right\}. \tag{3.52}$$

As has been revealed by Gottlieb and Shu [161], the second Runge-Kutta method has a CFL coefficient equal to 1. In order to keep the solution stable, a lower CFL value 0.5 is employed in the present study. After solving Equation (3.47), the local time step at each cell is obtained. In order to maintain time accuracy of the solution, it is recommended to employ the same time step, which is the minimum of all the local time steps, in each cell when marching the explicit time procedure [127]. Therefore, this minimum local time step, also known as the global-time step Δt_{global}, is employed to march the calculation procedure, which is given by Equation (3.46).

3.2.3. Boundary conditions

Initial and boundary conditions are required for solving all the partial differential equations. Dirichlet and Neumann conditions are applied for the variables at the boundaries in the present study. In Dirichlet boundary condition, the

scalar variables on the boundaries are specified, while in the Neumann boundary condition, the gradients of the scalar variables in the surface normal direction are specified.

The inflow boundaries employ the Dirichlet boundary conditions and all the variables, e.g. density, pressure, temperature, velocity, etc. at the air stream inlet and hydrogen jet inlet are prescribed with fixed values. As the flow fields under consideration here are supersonic, all variable values at the outlet are extrapolated from the interior predictions. For the wall boundaries, both the slip wall and no-slip wall assumptions have been considered. The adiabatic no-slip wall boundary conditions are given as follows:

$$\begin{gathered} u|_{wall} = 0, v|_{wall} = 0, w|_{wall} = 0, \\ \frac{\partial T}{\partial n} = 0, \\ k = 0, \omega = \frac{60\mu}{\rho\beta_1 d^2} \cdot \frac{1}{\mathrm{Re}}, \end{gathered} \tag{3.53}$$

where k, ω, μ, ρ, d, β_1 and Re are the turbulent kinetic energy, the specific dissipation, the laminar viscosity, the density, the distance between the first grid point and the wall, a constant of 0.075 and the Reynolds number of the inflow, respectively. While, the slip wall condition is defined by treating the boundaries as frictionless surfaces and therefore the fluid adjacent to the wall is allowed to flow in the direction parallel to the boundary but cannot penetrate the wall, i.e. $\mathbf{V} \cdot n = 0$.

In the present study, symmetry boundary conditions may be employed when the physical geometry has mirror symmetry. On the symmetry plane, the normal velocity component is zero, and the normal gradient of all flow variables are zero. Therefore the symmetry boundary condition can be interpreted as the slip wall boundary conditions. When the physical geometry and the flow have a periodical nature, periodic boundary conditions may be employed. The no-pressure-gradient

translational periodic boundary condition is built into the in-house code. More information about the periodic boundary conditions may be found in [127].

3.2.4. Multiblock and parallel computing

In order to reduce the computing time and take advantage of the computational resources, multiblock and parallel computing strategies are employed in the present study. The original multiblock structured mesh split into a new set of several sub-domains, and then the sub-blocks are generated based on the sub-domains. The connectivity between the adjacent blocks is shown in Figure 3.1. For the fifth-order WENO scheme, three ghost points are required for the boundary condition treatments and the information exchanges between blocks, see the red points in Figure 3.1. Finally, the sub-blocks are employed by the in-house code to simulate the non-reacting and reacting flows in the configuration. Figure 3.2 illustrates the procedure of simulating a configuration using the multiblock and parallel computing strategies.

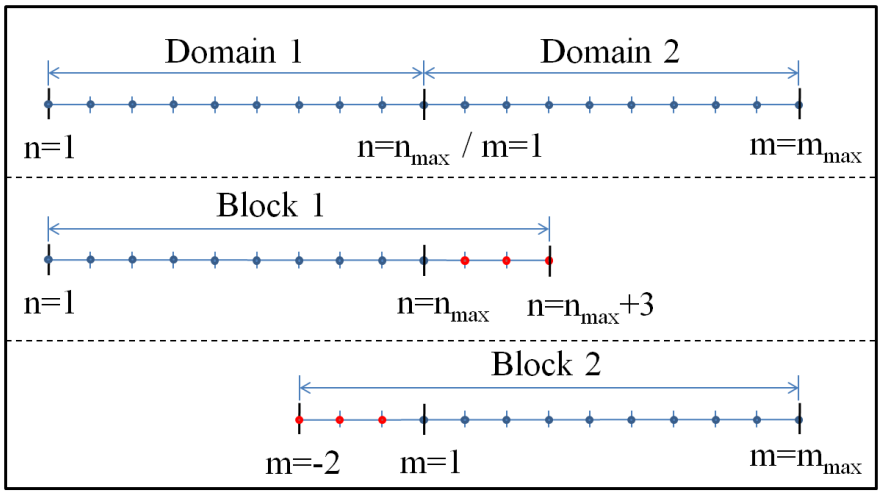

Figure 3.1 A schematic of the sub-domains and sub-blocks. The red dot shows the ghost points that are needed for boundary condition treatments and information exchanges between blocks.

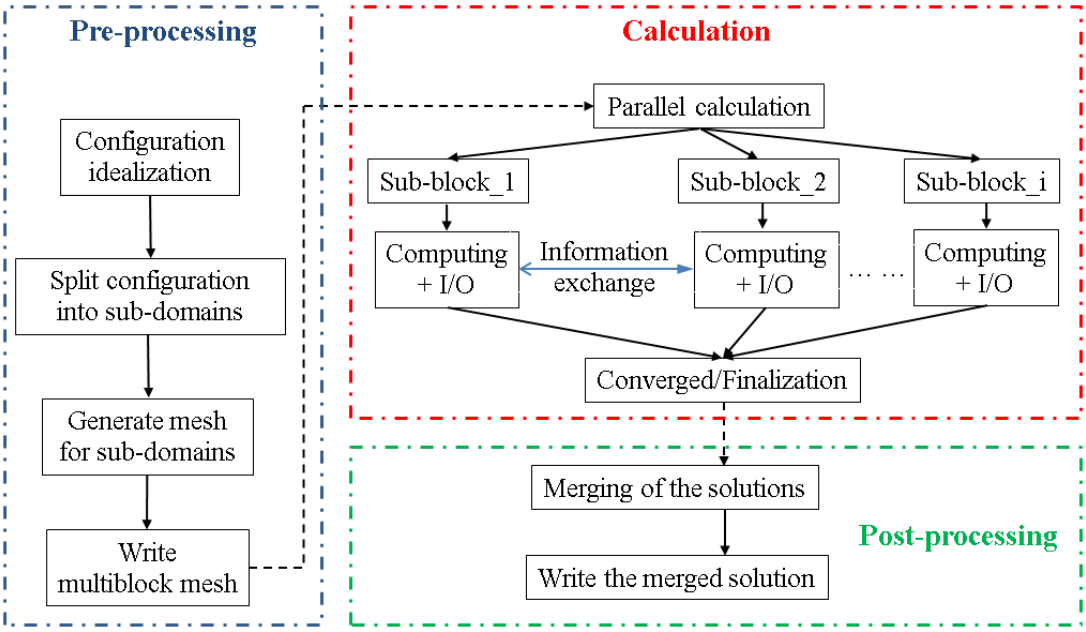

Figure 3.2 Overview of the multiblock and parallel computing strategies.

3.3. Closure

In this chapter, the concepts of LES and the basic theory behind are first discussed. Secondly, the formulation of the filtered governing equations for the hybrid RANS/LES method, i.e. the mass, momentum, scalar and enthalpy conservation equations, is discussed. Thirdly, the numerical approaches, including the spatial discretization schemes and the procedures used to solve the equations in time, are presented. Further, the boundary conditions used for the inflow, outflow, solid wall, etc., are discussed. Finally, the multiblock and parallel computing strategies used in the present study are briefly presented.

Chapter 4
Supersonic combustion modelling

Combustion is defined as a chemical process by which a fuel and an oxidiser react to produce energy, usually in the form of heat. The direct approach of handling combustion is to solve the transport equations for all the species involved in any fuel and oxidiser with the set of chemical reaction mechanisms. However, the chemical mechanisms normally involve tens of species and hundreds of elementary reactions. Solving for this large number of transport equations is too costly, and unrealistic to some extent, with the LES method [162]. Thus, a combustion model is required to consider both the accuracy and the computational efficiency of the combustion simulation. Conserved scalar mixture fraction based models appear to offer the most effective description of the chemistry for the non-premixed combustion. The flamelet models are mixture fraction based methods. The progress variable approach for the non-premixed and the partially premixed flames with the flamelet model, which belongs to the conserved scalar mixture fraction approach, has proved to be a good method for the LES for supersonic combustion [163].

4.1. Combustion modelling

4.1.1. Conserved scalar mixture fraction approach

The basis of the conserved scalar approach is as follows: under the assumption of the Lewis number being unity, equal diffusivity and adiabatic conditions, the conserved scalars can be related to the mixture fraction which is a single normalized conserved scalar. Therefore, the solution of these conserved scalars, such as the

element mass fraction of the species, can be reduced to the solution of the transport equation for the mixture fraction. Then, all the species mass fractions and temperature are calculated from the mixture fraction.

The mixture fraction can be written in terms of the atomic mass fraction as follows [127]:

$$f = \frac{Y_m - Y_{m,ox}}{Y_{m,fuel} - Y_{m,ox}}, \tag{4.1}$$

where Y_m is the elemental mass fraction for the species m. The subscript "*ox*" and "*fuel*" denote the values at the oxidizer stream inlet and at the fuel stream inlet, respectively. It is clear that this definition is based on a particular element. To overcome this problem, Bilger [164] suggested a definition which is based on a linear combination of elemental mass fractions of *C*, *H* and *O*:

$$f = \frac{2\left(Y_c - Y_{c,2}\right)/M_c + \left(Y_H - Y_{H,2}\right)/2Y_H - \left(Y_O - Y_{O,2}\right)/M_o}{2\left(Y_{c,1} - Y_{c,2}\right)/M_c + \left(Y_{H,1} - Y_{H,2}\right)/2Y_H - \left(Y_{O,1} - Y_{O,2}\right)/M_o}, \tag{4.2}$$

where the subscripts 1, 2, *C*, *H* and *O* denote the fuel stream, air stream, carbon, hydrogen and oxygen elements, respectively, and *M* represents the molecular weight. This definition of mixture fraction has been widely adopted [149].

4.1.2. Steady Laminar Flamelet Model (SLFM)

The basic models that are used to establish the relationship between the chemical state and mixture fraction are based on the general assumption of 'fast' chemistry. Under this condition, the chemical kinetics is infinitely fast in comparison to other processes in the flow. Also, the flamelet concept assumes that the chemical time scales are shorter than the turbulent time scales so that the flame can be approximated as one-dimensional. SLFM solves the one-dimensional, steady and diffusion-reaction equations which are termed as the flamelet equations. These solutions represent laminar diffusion flamelets. The laminar flamelet model deals

with non-equilibrium effects with detailed chemistry and is considered as an extension of the conserved scalar approach. A turbulent flame is recognized as an ensemble of laminar diffusion flamelets which are thin reacting diffusive layers. In order to account for the effect of turbulence on flamelets, the scalar dissipation rate χ is introduced as an additional parameter. Hence, the flamelet becomes a function of the mixture fraction and the scalar dissipation rate. The turbulent mean reactive scalar variables can be obtained through integrating the laminar flamelets with the combined PDFs of the mixture fraction and the scalar dissipation rates. The flamelet approach decouples the chemical kinetics from the turbulent reacting flow. The computation of the chemistry can be stored in a tabulated form as a function of several scalars, such as mixing fraction and scalar dissipation rate. Therefore, flamelet modeling is quite economic and allows for the detailed chemical kinetics.

4.1.2.1. Flamelet equations

The flamelet equations was firstly derived by Peters [105]. The equation describes the reactive diffusive structure in the vicinity of the flame surface as a function of the mixture fraction. Under the assumption of equal diffusivity and a Lewis number of unity, the field equation for the mixture fraction that determines the flame surface location is given by:

$$\frac{\partial(\rho f)}{\partial t} + \frac{\partial\left(\rho u_j f\right)}{\partial x_j} = \frac{\partial}{\partial x_j}\left(\rho \Gamma \frac{\partial f}{\partial x_j}\right). \tag{4.3}$$

On solving the above equation, we can obtain the distribution of the mixture fraction as a function of space *x* and time *t*.

In this study, we employ the FlameMaster code to generate the flamelet libraries. The FlameMaster code is a C++ computer program for 0D combustion and 1D laminar flame calculations [165]. In this code, the counterflow diffusion flame which is a commonly used laminar flame type is employed to represent the flamelets

in the turbulent flow [127]. The laminar counterflow diffusion flame equations, i.e. the governing transport equations for the species mass fractions Y_i and temperature T, are given by Pitsch and Peters [166]. Peters [105] pointed out that the combustion essentially takes place in the vicinity of the stoichiometric surface if the gradient of the local mixture fraction is sufficiently high. Henceforth, through setting the mixture fraction to be stoichiometric, i.e. $f(x,t) = f_{st}$, we can obtain the flame. The laminar counterflow diffusion flame equations can be transformed from physical space to mixture fraction space, i.e. from space with x as the independent variable to the space with f as the independent variable [127].

The reactive scalar in the normal to the f direction is assumed to be much larger than those in the other directions. Then, with the assumption of Lewis number being unity and neglecting the radiation effects, the flamelet equations can be expressed as follows [127]:

$$\rho \frac{\partial Y_m}{\partial t} = \rho \frac{\chi}{2}\left(\frac{\partial^2 Y_m}{\partial f^2}\right) + \dot{\omega}_m, \tag{4.4}$$

$$\rho \frac{\partial T}{\partial t} - \rho \frac{\chi}{2}\left(\frac{\partial^2 Y_m}{\partial f^2}\right) - \rho \frac{\chi}{2C_p}\left(\frac{\partial T}{\partial f}\frac{\partial C_p}{\partial f}\right) - \sum_{m=1}^{Ns} \rho \frac{\chi}{2}\frac{C_{pm}}{C_p}\left(\frac{\partial Y_m}{\partial f}\frac{\partial T}{\partial f}\right) + \frac{1}{C_p}\sum_{m=1}^{Ns} h_m \dot{\omega}_m = 0. \tag{4.5}$$

In the above equations, ρ is the density, χ is the instantaneous scalar dissipation rate, T is the temperature, $\dot{\omega}$ is the reaction rate, C_p is the specific heat at constant pressure, h is the enthalpy, and the subscript m refers to the chemical species m [149]. The instantaneous scalar dissipation rate χ represents the influence of the flow field on the local flame structure and it is defined as follows [127]:

$$\chi = 2\Gamma\left(\frac{\partial f}{\partial x_j}\right)^2, \tag{4.6}$$

where Γ is a representative diffusion coefficient. It has the dimensions 1/s and may be regard as the inverse of a characteristic diffusion time. Research has shown that

the scalar dissipation rate plays an important role in flamelet models for non-premixed combustion [162]. It should be noted that the scalar dissipation rate χ, varies along the axis of the flamelet. Physically, as the flame is strained, the gradient of f at the stoichiometric position increases and the corresponding scalar dissipation rate χ_{st} can be used as a non-equilibrium parameter. As χ_{st} decreasing towards 0, the chemistry tends to equilibrium while non-equilibrium increases as χ_{st} increases due to aerodynamic straining [127].

4.1.2.2. Probability density function

In principle, both the mixture fraction and the scalar dissipation rate are fluctuating quantities. In order to consider the statistical characteristics of these two parameters, a presumed probability density function $P(f)$ is introduced. In adiabatic systems, the density-weighted mean scalar variables in a turbulent field, such as the mean species mass fractions and the temperature, can be computed as follows [162]:

$$\tilde{\phi}_i = \int_0^1 \phi_i(f)\tilde{P}(f)df, \tag{4.7}$$

where $\tilde{P}(f)$ in the above equation is the Favre filtered probability density function for the mixture fraction. Considering the PDF, the mean scalar variables which are functions of the mixing fraction and the scalar dissipation rate, can be given by:

$$\tilde{\phi}_i = \int_0^\infty \int_0^1 \phi_i(f;\chi_{st})\tilde{P}(f;\chi_{st})df d\chi_{st}. \tag{4.8}$$

The mixture fraction represents the characteristics of the large scales, while the scalar dissipation rate represents the mixing of the small scales. Thus, the joint PDF is normally assumed to be statistically independent between f and χ_{st} [105], namely

$$\tilde{P}(f;\chi_{st}) = \tilde{P}(f)\tilde{P}(\chi_{st}). \tag{4.9}$$

The most widely used shape of the assumed PDFs are the β-PDF function for the mixing fraction and the log-normal distribution for the scalar dissipation rate [162]. More information about the β-PDF function and the log-normal function can be found in §4.3 and in [154,162].

The shape produced by these functions depends solely on the mean mixture fraction $\tilde{f}$, and its variance $\widetilde{f''^2}$. These two parameters can be obtained from solving their respective transport equations, namely

$$\frac{\partial(\rho\tilde{f})}{\partial t}+\frac{\partial(\rho\tilde{f}u_j)}{\partial x_j}=\frac{\partial}{\partial x_j}\left(\frac{\mu_t}{\sigma_{\tilde{f}t}}\frac{\partial\tilde{f}}{\partial x_j}\right), \tag{4.10}$$

$$\frac{\partial\left(\rho\widetilde{f''^2}\right)}{\partial t}+\frac{\partial\left(\rho\widetilde{f''^2}u_j\right)}{\partial x_j}=\frac{\partial}{\partial x_j}\left(\frac{\mu_t}{\sigma_{\widetilde{f''^2}t}}\frac{\partial\widetilde{f''^2}}{\partial x_j}\right)+2\frac{\mu_t}{\sigma_{\widetilde{f''^2}t}}\left(\frac{\partial\widetilde{f''^2}}{\partial x_j}\right)^2-\bar{\rho}\tilde{\chi}. \tag{4.11}$$

However, in LES, the most used methods for obtaining $\tilde{f}$ and $\widetilde{f''^2}$ are to solve the transport equation for the mean mixture fraction and to model the subgrid variance [149].

4.1.2.3. Limitations of the SLFM

In the flamelet concept, the stretch on the flamelet increases as the scalar dissipation rate increases. Once the increase achieves a particular limit, the heat loss in the special zone (e.g. in the vicinity of the fuel injector), may balance the heat generation from the chemical reactions. Beyond this limit, the flamelet will be extinguished. After the quenching, the flamelet is assumed to be in the pure mixing state. In fact, the local extinction and re-ignition process is very rapid. So it is reasonable to assume that the turbulent flame is an ensemble of fully burning flamelets and purely mixing flamelet. Ferreira [167] pointed out that if there is sufficient residence time for the flame to approach steady state then the above-mentioned method for accounting for the local extinction and re-ignition is reasonable. However, the scalar dissipation rate changes rapidly with the turbulent

fluctuations, especially in supersonic reacting flows. Thus, the steady flame structure assumption is not strictly tenable. This means that the SLFM is incapable of handling the local extinction and re-ignition problem. Moreover, since the SLFM is based upon the assumption of infinity fast chemistry, the SLFM is incapable of handling the slow reaction processes, such as the production of NOx. To overcome these problems, a transient model has been recommended to consider the unsteady effects. However the computational cost is increased when employing such an unsteady flamelet model. Several advanced flamelet models have been reviewed by Sadasivuni [149]. One promising flamelet-based model is the Unsteady Flamelet/Progress Variable (UFPV) approach [168,162,149], which is developed and extended to model supersonic flames in the present work.

4.1.3. Unsteady flamelet/progress variable approach

The Flamelet/Progress Variable approach (FPV) was firstly proposed by Pierce for LES calculations based on a steady-state laminar flamelet library [150]. His supervisor Moin [168] extended this work and published another paper in 2004. In this FPV approach, a flamelet parameter, based on a reactive scalar is used rather than the scalar dissipation rate. This allows, in principle, the prediction of the unsteady phenomena, such as the local extinction and re-ignition of the flame. With the FPV approach, the full range of steady states, including the partially extinguished state solutions, can be considered in the flamelet libraries. Studies by Pierce and Moin [168] have shown better predictions of the flame stabilization region with the FPV approach in comparison to the SLFM.

The FPV approach has been further investigated and developed by Ihme and Pitsch [169,170]. As the transient solution of the flamelets is expected to predict the flame extinction and re-ignition phenomena, the steady flamelet/progress variable (SFPV) approach has been extended to the UFPV model. The UFPV approach

employs an unsteady flamelet formulation to describe the transient evolution of all the thermochemical quantities, and has been developed for the prediction of autoignition in turbulent lifted flames [171]. It has been revealed that the UFPV approach has the potential to predict the local extinction and reignition phenomena in partially premixed flames [149]. Therefore, the UFPV model, which combines the unsteady flamelet formulation with the progress variable approach, is a good choice for the simulation of supersonic combustion.

The FPV model is similar to the SLFM, while the two parameters of the flamelet solutions become the mixture fraction *f* and a reaction progress parameter λ. The progress parameter λ is normally related to the reaction progress variable *C*, which replaces the scalar dissipation rate. The reaction progress variable can be defined in different ways. The transport equation for the filtered reaction progress variable is given as follows [149]:

$$\frac{\partial(\rho C)}{\partial t}+\frac{\partial\left(\rho C u_j\right)}{\partial x_j}=\frac{\partial}{\partial x_j}\left(\rho \Gamma_c \frac{\partial C}{\partial x_j}\right)+\rho \dot{\omega}_c, \tag{4.12}$$

where Γ_C and $\dot{\omega}_C$ are the diffusivity and the source term of the progress variable, respectively. In the present study, the progress variable is defined as the mass fraction of water vapour, i.e. $C = YH2O$, which is a widely used definition of the progress variable for Hydrogen/Air flames [172,154]. With the assumption of the Lewis number being unity, the filtered transport equation for the reaction progress variable can be given as follows:

$$\frac{\partial\left(\bar{\rho}\tilde{C}\right)}{\partial t}+\frac{\partial\left(\bar{\rho}\tilde{C}\tilde{u}_j\right)}{\partial x_j}=\frac{\partial}{\partial x_j}\left(\left(\frac{\mu}{\mathrm{Pr}}+\frac{\mu_t}{\mathrm{Pr}_t}\right)\frac{\partial \tilde{C}}{\partial x_j}\right)+\bar{\rho}\widetilde{\dot{\omega}}_C. \tag{4.13}$$

The steady flamelet solutions can be expressed in terms of the flamelet parameter as $\phi_i=\phi_i(f,\lambda)$. The definition of λ can be found in §4.2.2. Then, the filtered values of the reactive scalars in the LES can be determined as follows:

$$\tilde{\phi}_i=\int_0^1\int_{\lambda_{min}}^{\lambda_{max}}\phi_i\,(f;\lambda)\tilde{P}(f,\lambda;x,t)\,df\,d\lambda. \tag{4.14}$$

The parameters f and λ are assumed to be independent of each other, so the Favre filtered can be expressed as follows:

$$\tilde{P}(f,\lambda;x,t) = \tilde{P}(f)\tilde{P}(\lambda). \tag{4.15}$$

Similar to the SLFM, the introduction of PDF makes the scalar $\tilde{\phi}_i$ in the FPV model become a function of the mean mixture fraction, mixture fraction variance and flamelet parameter, i.e. $\tilde{\phi}_i = \tilde{\phi}_i(\tilde{f}, \widetilde{f''^2}, \lambda)$. The function $\tilde{\phi}_i$ can be the filtered temperature, filtered species mass fraction or the filtered source term of the progress variable. The flamelet parameter λ can be replace by the filtered progress variable $\tilde{C}$, which is discussed in detail in §4.3.2, and then we obtain $\tilde{\phi}_i = \tilde{\phi}_i(\tilde{f}, \widetilde{f''^2}, \tilde{C})$.

Sadasivuni [149] analysed the formulation of the UFPV model and indicated that the flamelet solution in the UFPV model can be parameterized with the mixture fraction *f*, flamelet parameter λ and stoichiometric scalar dissipation rate χ_{st}. Therefore, the scalars can be expressed as $\phi_i = \phi_i(f, \lambda, \chi_{st})$. Similar to the FPV method, through replacing the values of λ by $\widetilde{C}$, the scalars $\tilde{\phi}_i$ become a function of the mean mixture fraction, mixture fraction variance, mean progress variable and the mean scalar dissipation rate, i.e. $\tilde{\phi}_i = \tilde{\phi}_i(\tilde{f}, \widetilde{f''^2}, \tilde{C}, \widetilde{\chi_{st}})$. Then, the filtered species mass fraction and the filtered source term of the progress variable, molecular weight and enthalpy flux can be given as follows:

$$\begin{cases} \tilde{Y}_m = \tilde{Y}_m(\tilde{f}, \widetilde{f''^2}, \tilde{C}, \widetilde{\chi_{st}}) \\ \widetilde{\omega}_C = \widetilde{\omega}_C(\tilde{f}, \widetilde{f''^2}, \tilde{C}, \widetilde{\chi_{st}}) \\ M_m = M_m(\tilde{f}, \widetilde{f''^2}, \tilde{C}, \widetilde{\chi_{st}}) \\ H = H(\tilde{f}, \widetilde{f''^2}, \tilde{C}, \widetilde{\chi_{st}}) \end{cases}. \tag{4.16}$$

The values of the four parameters $\widetilde{f}$, $\widetilde{f''^2}$, $\widetilde{C}$ and $\widetilde{\chi_{st}}$, are obtained from the hybrid RANS/LES solution of their governing equations and models, and then they are used to obtain the mean scalars from the look-up tables using an interpolation technique. The generation of the look-up tables and the interpolation technique are presented in the following two sections.

4.2. Flamelet generation

As has been discussed in §4.1.2 and §4.1.3, in the regime of the flamelet combustion model, the complex chemistry of the combustion process may be reduced to two variables, i.e. the mixture fraction f and the scalar dissipation rate χ, and this reduction allows the flamelet calculations to be pre-processed and stored in look-up tables. In this study, we employ the FlameMaster code [165] to generate the flamelets, i.e. the flamelet libraries. These flamelets contain the dependence of the mixture fraction on the temperature and all the mass and mole fractions of the species involved in the chemical mechanism at different scalar dissipation rates. Further, in this thesis, both steady and unsteady flamelets are generated, and then the flamelets are processed into look-up tables using a pre-PDF module in the in-house code and these PDF look-up tables are employed in the flamelet model and the UFPV model, respectively.

4.2.1. Steady flamelets

The steady flamelet model is developed by assuming that the flame structure is in steady state, and then the time derivative terms in Equations (4.4) and (4.5) can be neglected and we obtain the following:

$$\rho\frac{\chi}{2}\left(\frac{\partial^2 Y_m}{\partial f^2}\right)+\dot{\omega}_m=0, \tag{4.17}$$

$$\rho\frac{\chi}{2}\left(\frac{\partial^2 Y_m}{\partial f^2}\right)+\rho\frac{\chi}{2C_p}\left(\frac{\partial T}{\partial f}\frac{\partial C_p}{\partial f}\right)+\sum_{m=1}^{Ns}\rho\frac{\chi}{2}\frac{C_{pm}}{C_p}\left(\frac{\partial Y_m}{\partial f}\frac{\partial T}{\partial f}\right)=\frac{1}{C_p}\sum_{m=1}^{Ns}h_m\dot{\omega}_m. \tag{4.18}$$

The flamelets can be generated by solving the above flamelet equations with the given scalar dissipation rate and boundary conditions. A series of flamelets are generated using the FlameMaster code [165] under the boundary conditions shown in Table 4.1, in which Y, T and P are the mass fraction of the species, the static temperature of the reactants and the pressure in the burner. These boundary

conditions correspond to the supersonic flame at the Institute for Chemical Propulsion of the German Aerospace Centre (DLR) [173-175], i.e. the DLR supersonic flame, which we investigate in Chapter 5. From Table 4.1, it is clear that the fuel stream is pure hydrogen while the oxidizer stream consists of hot air, thus the DLR supersonic flame is under strictly non-premixed conditions. Further, when generating the flamelets, the San Diego Mechanism, which was develop by Williams and his co-works at the University of California, San Diego [176], is employed. This mechanism has been widely used in CFD predictions of the hydrogen and hydrocarbon combustion [177] and also it has been successfully employed to generate flamelets for supersonic flames [154].

Table 4.1 The fuel and oxidiser boundary conditions for the flamelet generation of the DLR supersonic flame.

	YO_2	YN_2	YH_2O	YH_2	T (K)	P (bar)
Fuel	0	0	0	1.0	250	1.0
Oxidiser	0.232	0.736	0.032	0	340	1.0

Figure 4.1 shows a series of flamelet profiles which are obtained from the solutions of the steady flamelet Equations (4.17) and (4.18) using the FlameMaster code for the DLR supersonic flame. It is clear that, at a fixed χ_{st}, the *T*, *YH2O* and *YOH* attain the maximum value near the stoichiometric mixture fraction f_{st} (f_{st} = 0.0284 for the DLR supersonic flame), and this is because the combustion and heat release of the non-premixed flame under or near the stoichiometric condition is the most intense. In the meantime, the reactants are consumed rapidly in the $f = f_{st}$ region and therefore a steep decrease in the O2 profiles is found there, see in Figure 4.1(c).

From Figure 4.1, we observe that the scalar dissipation rate has a significant effect on the flamelets. At a very low strain rate, i.e. χ_{st} = 0.001 s^{-1}, the flame is almost under equilibrium conditions and has a peak temperature and *YH2O* of about 2400 K and 0.27, respectively. As the scalar dissipation rate increases, the value of the peak temperature and *YH2O* decreases due to stronger straining and greater heat lost to the outer regions of the reaction zone.

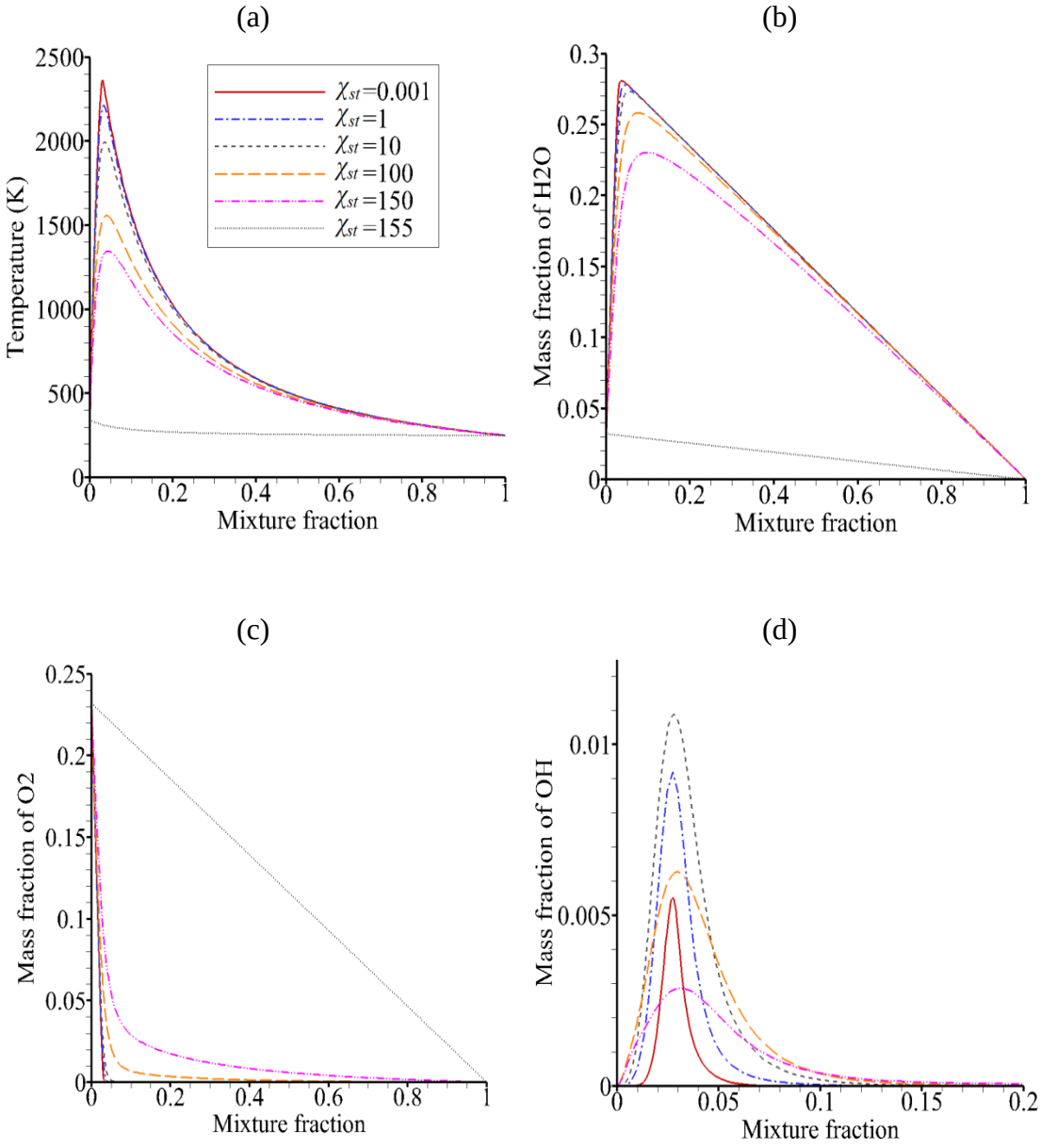

Figure 4.1 The profiles of (a) temperature, (b) *YH2O*, (c) *YO2* and (d) *YOH* obtained from the steady flamelet solutions, under χ_{st} = 0.001, 1, 10, 100, 150 and 155 1/s, for the DLR supersonic flame.

At χ_{st} = 155 s^{-1}, the flamelets are extinguished and the profiles present pure mixing of the reactants. However, the profiles of the mass fraction of OH, which is one of the intermediate species during the reaction, shows different behaviours to the profiles of *YH2O*, see Figures 4.1(b) and 4.1(d). It is clear that the intermediate species OH is mainly distributed in the region near $f = f_{st}$ and reach a maximum concentration near the stoichiometric conditions. However, the peak value of *YOH* is not a monotonic function of the scalar dissipation rate. The peak value of the *YOH*, at χ_{st} = 0.001 s^{-1} (near the equilibrium conditions), is about 0.005, reaches the maximum value at χ_{st} = 10 s^{-1}, decreases as χ_{st} keeps increasing and becomes zero at χ_{st} = 155 s^{-1} (quenching conditions). Also, it is observed that the *YOH* profiles become broader as χ_{st} increases. This means that the straining effect departs the flame from chemical equilibrium and thickens the flame front in the mixture fraction space.

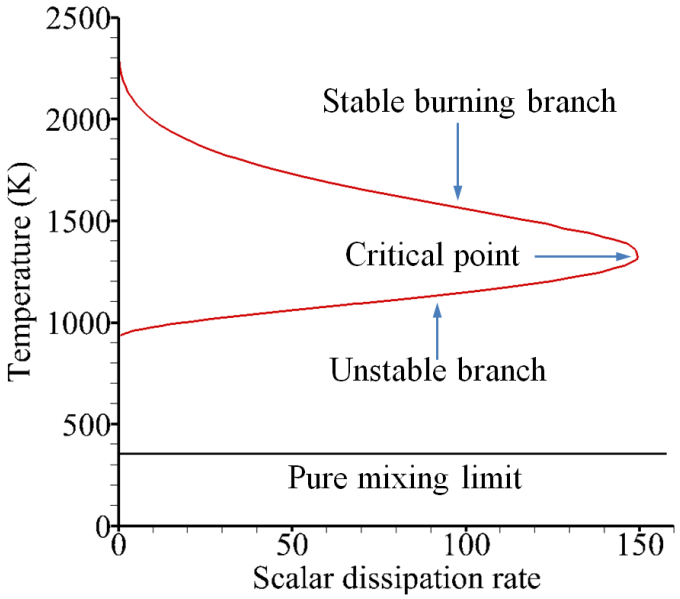

Figure 4.2 The S-shaped curve for the DLR supersonic flame.

Figure 4.2 illustrates the S-shaped curve, i.e. the locus of the stoichiometric temperature for all the solutions of the steady flamelet equations for the DLR

supersonic flame. In Figure 4.2, the curves can be divided into three branches, namely the top burning branch, the middle unstable branch and the bottom extinguished branch (or pure mixing limit), which correspond to the fully burning, partially extinguished and completely extinguished states, respectively. On the stable burning branch, the stoichiometric temperature decreases with an increase in the scalar dissipation rate. This is because the mixing of the reactant is enhanced due to the stronger straining (larger scalar dissipation rate), and therefore the hot reaction products are better mixed with the cold reactants, and thus a lower stoichiometric temperature is produced. When the scalar dissipation rate reaches the critical point, e.g. $\chi_{st} \approx 152$ s^{-1} in this case, the flamelet solutions change to the unstable branch or jump to the extinguished branch, and this is related to the decrease or increase in the scalar dissipation rates when calculating the flamelets.

Along the unstable branch in Figure 4.2, it is clear that the scalar dissipation rate decreases with decreasing temperate in order to maintain the combustion and keep the mixing in balance with the lower reaction rates. On the extinguished branch, the chemical kinetics are negligible, the reactants are in pure mixing states and the temperature of the mixture is independent of the dissipation rate. Further, see Figure 4.1, a discontinuity between the burning states, e.g. χ_{st} = 0.001, 1, 10, 100, and 150 s^{-1}, and the quenching state, e.g. χ_{st} = 155 s^{-1} can be clearly observed and this is because that the partially extinguished state, shown in Figure 4.2, is not accounted for in the steady flamelet model, and this is one of the shortcomings of the SLFM.

In the present steady flamelet study, a total of 28 flamelet libraries, including 27 libraries on the stable burning branch and 1 library on the extinguished branch, are provided as the input to the pre-integration code which generates the look-up tables for the flamelet modelling of the DLR supersonic flame. While for the LES flamelet modelling of a supersonic flame in a cavity based combustor, a total of 30 flamelet libraries, including 29 libraries on the stable burning branch and 1 library

on the extinguished branch, are generated under the fuel and oxidiser boundary conditions and those are provided in Chapter 6.

4.2.2. Unsteady flamelets

The steady flamelet model gives access to simulate turbulent flames with detailed chemical mechanisms and advanced turbulence models without an enormous computational cost when applied to various configurations. It allows the correct description of the flames under high Damköhler number (the ratio of a characteristic fuel–air mixing time divided by a characteristic chemical time) and it has been widely employed for the simulation of turbulent non-premixed combustion [115]. However, as has been discussed in §4.2.1, the steady flamelet model only takes the stable burning and fully extinguished branches of the S-shaped curve into account but the unstable partially extinguished branch is neglected, and this makes the steady flamelet model incomplete. Therefore it is not sufficient to capture the local extinction and autoignition events and the transient effects in a turbulent flame. The UFPV approach derives motivation from some of these fundamental problems with the steady flamelet model for non-premixed combustion. In the UFPV model, unsteady flamelets are primarily utilized which are the solutions of the flamelet Equations (4.4) and (4.5).

The flamelet calculation is performed using both the steady and the unsteady module in the FlameMaster code. Similar to the generation of the steady flamelets, the radiation effects are neglected and the Lewis number is assumed to be unity for all species. The procedure of the generation of the unsteady flamelet is give as follows:

(i) Three lists of scalar dissipation rates, denoted as χ_{ref}, χ_{ref}^{-} and χ_{ref}^{+} are generated. The minimum and maximum of χ_{ref} correspond to the (nearly)

equilibrium and the fully extinguished states. The χ_{ref}^{-} and χ_{ref}^{+} are slight smaller and larger than χ_{ref}.

(ii) The steady flamelets on the unstable branch are generated under $\chi_{st} = \chi_{ref}^{-}$ and χ_{ref}^{+} conditions.

(iii) The unsteady flamelets are calculated using the unsteady module in the FlameMaster code. Because of the unstable nature of the flamelets on the middle branch, as the time increases, if the steady flamelets for $\chi_{st} = \chi_{ref}^{+}$ are employed as the initial conditions, the stoichiometric temperature from the flamelet solutions for $\chi_{st} = \chi_{ref}$ tends to increase and reach the stable burning branch. Therefore the unsteady flamelets above the middle unstable branch are obtained. Similarly the unsteady flamelets below the unstable branch can be obtained if the steady flamelets for $\chi_{st} = \chi_{ref}^{-}$ are employed as the initial conditions.

(iv) Combining the flames obtained from the two runs in (iii), the unsteady flamelets for $\chi_{st} = \chi_{ref}$ are obtained.

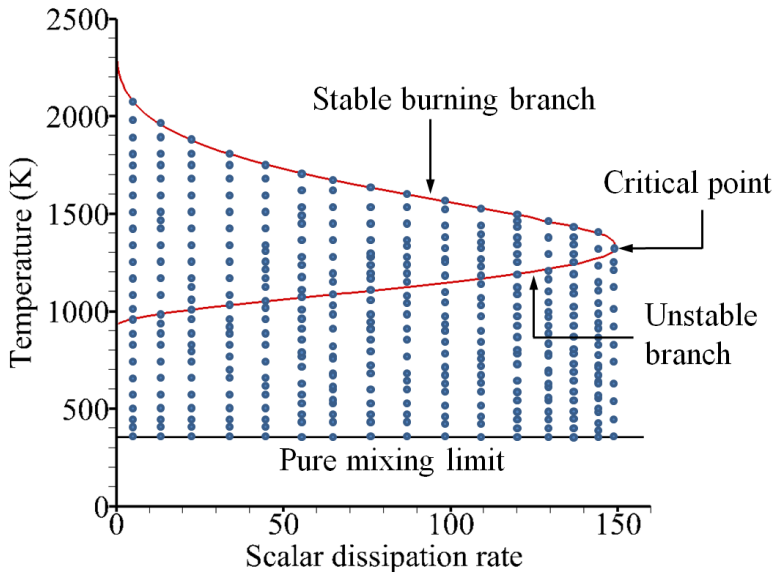

Figure 4.3 Unsteady flamelet solutions for the DLR supersonic flame. The dotted values resemble the unsteady flamelet solutions under various scalar dissipation rate conditions.

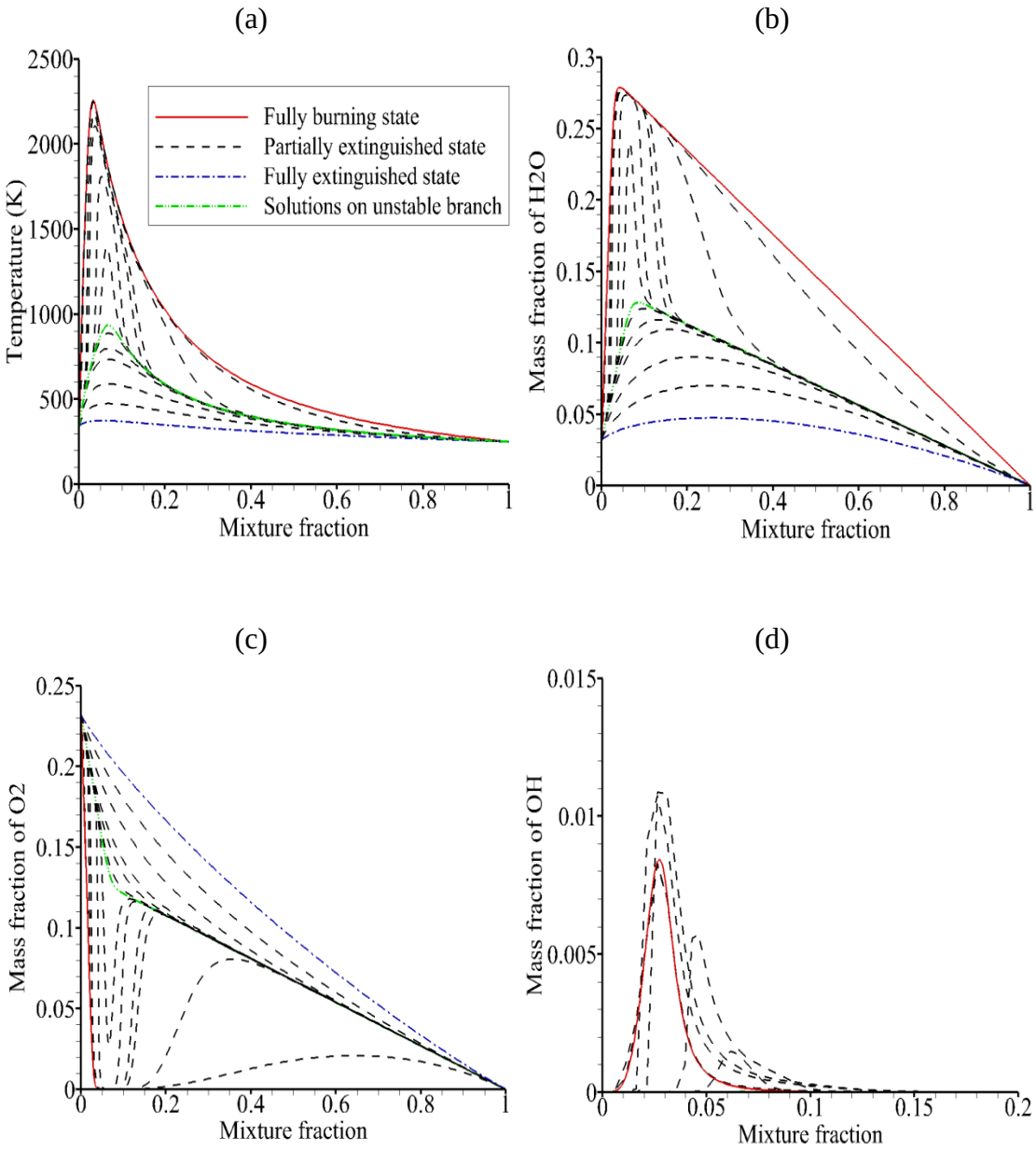

Figure 4.4 The profiles of (a) temperature, (b) *YH2O*, (c) *YO2* and (d) *YOH* obtained from the unsteady flamelet solutions for the fully burning (red solid lines), partially extinguished (black dash lines) and fully extinguished (blue dash dot lines) states at χ_{ref} = 0.5 for the DLR supersonic flame. The green dash dot dot lines show the flamelet solutions on the unstable branch of the S-shaped curve.

Figure 4.3 shows the unsteady flamelet solutions for the DLR supersonic flame. In addition to the S-shaped curve, the maximum temperature of the unsteady flamelets with respect to time under various scalar dissipation rates conditions is

shown by the dots in Figure 4.3. Figure 4.4 shows the unsteady flamelet solutions (not all the solutions) for the fully burning, partially extinguished and fully extinguished states at $\chi_{ref} = 0.5$ for the DLR supersonic flame. It is clear from Figures 4.3 and 4.4 that the unsteady flamelets facilitate unique identification of all the unsteady state solutions, including the partially extinguished solutions, and therefore bridge the discontinuity between the stable burning, middle partially extinguished and fully extinguished branches. It should be noted that the *YOH* obtained from the unsteady flamelet solutions on and below the unstable branch of the S-shaped curve at $\chi_{ref} = 0.5$ is close to 0, and therefore these profiles are not shown in Figure 4.4(d).

From Figures 4.4(a) and 4.4 (b), we observe that the maximum temperature and *YH2O* vary with time and is a monotonic function of time. Therefore, the peak temperature and *YH2O* could be used as a flamelet parameter to identify the flamelet solutions with respect to time. In order to distinguish the flamelet profiles at a given χ_{ref}, in this study the maximum *YH2O* in each flamelet profile, instead of time, is used as the flamelet parameter (denoted as λ). For instance, the flamelet parameter λ = 0.12905 at $\chi_{ref} = 0.5$ corresponds to the flamelet solutions on the unstable branch of the S-shaped curve, see the green dash dot dot line in Figure 4.4(b). Therefore, in the unsteady flamelet libraries, the scalar quantities can be regarded as a function of f, λ and χ_{st}, i.e. $\phi = \phi(f, \lambda, \chi_{st})$.

In the present study, χ_{ref} have 20 values, which range from 0.001 to 155 s^{-1} for the DLR supersonic flame and from 0.001 to 310 s^{-1} for the supersonic flame in a cavity-based combustor. A total of 100 flamelet profiles, i.e 100 values for λ, are generated at a single χ_{ref}. Later, these unsteady flamelets are converted into the unsteady PDF look-up tables which are employed in the RANS and LES UFPV modelling of the two flames.

4.3. PDF table calculation

The steady and unsteady flamelets are required to be pre-processed in order to be used during the RANS and LES modelling processes. In this section, the steady and unsteady flamelet libraries, which are generated using the method described in §4.2, are converted into the look-up tables using the in-house code.

4.3.1. PDF look-up tables for the flamelet model

As has been discussed in §4.1.2.2, the mean scalars can be computed using Equations (4.8) and (4.9). The most widely used shape for the assumed PDFs is the β-PDF function for the mixing fraction and the equations are as follows [150,154]:

$$P(f) = \frac{f^{a-1}(1-f)^{b-1}}{\int_0^1 f^{a-1}(1-f)^{b-1}df}, \tag{4.19}$$

$$a = \tilde{f}\left[\frac{\tilde{f}(1-\tilde{f})}{\widetilde{f''^2}} - 1\right], \tag{4.20}$$

$$b = (1-\tilde{f})\left[\frac{\tilde{f}(1-\tilde{f})}{\widetilde{f''^2}} - 1\right], \tag{4.21}$$

where $\tilde{f}$ and $\widetilde{f''^2}$ are the mixture fraction and its variance, respectively.

The scalar dissipation rate χ_{st} is assumed to follow the log-normal distribution [154], which is given by,

$$P(\chi_{st}) = \text{LogNormal}(\chi_{st};\, \mu, \sigma) = \frac{1}{\chi_{st}\sigma\sqrt{2\pi}}\exp\left(\frac{-[\ln(\chi_{st}) - \mu]^2}{2\sigma^2}\right), \tag{4.22}$$

where μ and σ are related to the mean value of χ_{st} by the following equations:

$$\widetilde{\chi_{st}} = \exp\left(\mu + \frac{\sigma^2}{2}\right) \tag{4.23}$$

$$\widetilde{\chi_{st}''^2} = \widetilde{\chi_{st}}^2\left(e^{\sigma^2} - 1\right) \tag{4.24}$$

Equivalently, the parameters μ and σ can be obtained if $\widetilde{\chi_{st}}$ and $\widetilde{\chi_{st}''^2}$ are known. In this study, $\widetilde{\chi_{st}}$ is obtained from the following equation,

$$\widetilde{\chi_{st}} = \mathrm{C}_{\chi}\frac{\tilde{\varepsilon}}{\tilde{k}}\widetilde{f''^2}, \tag{4.25}$$

where, both C_{χ} and σ take the value 2.0 [149].

Once $P(f)$ and $P(\chi_{st})$ are solved, $P(f,\chi_{st})$ is also obtained based on Equation (4.9). The scalars in the flamelets can be converted into the mean scalars by Equation (4.8), which is built into the in-house code, and the PDF look-up tables are generated. More information about the PDFs and the generation of the look-up tables for the steady flamelet model can be found in [162,149,154].

4.3.2. PDF look-up tables for the UFPV model

The UFPV model was develop from the flamelet model and is extended for predicting the transient unstable behaviour of the turbulent flame. The unsteady flamelets are generated using the FlameMaster code, and then they are required to be converted into PDF look-up tables for the UFPV model.

As has been discussed in §4.2.2, the scalar quantities in the unsteady flamelet libraries can be regarded a function of *f*, λ and χ_{st}, i.e. $\phi = \phi(f,\lambda,\chi_{st})$. The filtered quantities are obtained by performing the joint PDF on the three parameters, i.e.

$$\widetilde{\phi_i} = \int_0^{\chi_{st,max}} \int_{\lambda_{min}}^{\lambda_{max}} \int_0^1 \phi_i(f,\lambda,\chi_{st})\tilde{P}(f,\lambda,\chi)\, df d\lambda d\chi_{st}. \tag{4.26}$$

According to the definition of the flamelet parameter λ in §4.2.2, it is clear that *f* and λ are independent of each other, and therefore the joint PDF can be expressed as follows:

$$\tilde{P}(f,\lambda,\chi_{st}) = \tilde{P}(f)\tilde{P}(\lambda,\chi_{st}). \tag{4.27}$$

Research on employing the beta function PDFs for λ and χ_{st} is intense but the dimension of the look-up table will increase, as well as the computational cost during the simulation, in comparison with a delta PDF [149]. On the other hand, reasonable accuracy was provided during the LES of a non-premixed turbulent combustion case by the delta PDF in [170]. Therefore, both the flamelet parameter and scalar dissipation are described by a delta PDF in the present study. Further, the PDF of the mixture fraction is defined by a beta function, and this is the same as in the steady flamelet model. Thus, the joint PDF can be given as follows:

$$\tilde{P}(f,\lambda,\chi_{st}) = \beta\left(f;\tilde{f},\widetilde{f^{"2}}\right)\delta(\lambda-\lambda^{*})\delta(\chi-\chi_{st}^{*}), \tag{4.28}$$

where λ^{*} and χ_{st}^{*} can be obtained from the filtered quantities by the inversion of the integrals [170]:

$$\tilde{C} = \int_{0}^{\chi_{st,max}}\int_{\lambda_{min}}^{\lambda_{max}}\int_{0}^{1}\phi(f,\lambda,\chi_{st})\beta\left(f;\tilde{f},\widetilde{f^{"2}}\right)\delta(\chi_{st}-\chi_{st}^{*})\,df d\lambda d\chi_{st}, \tag{4.29}$$

and

$$\tilde{\chi} = \int_{0}^{1}\chi_{st}^{*}\psi(f)\beta\left(f;\tilde{f},\widetilde{f^{"2}}\right)df, \tag{4.30}$$

where $\psi(f)$ describes the mixture fraction dependence on the scalar dissipation rate, i.e.

$$\chi = \chi_{st}\psi(f). \tag{4.31}$$

Solving the inverse integrals to obtain the values as depicted in Equations (4.29) and (4.30) is eliminated by the re-interpolation technique as described in [149], and therefore the pre-processing task becomes relatively simple. The equations are built into the in-house code and then the unsteady flamelets are converted into the unsteady PDF look-up tables, in which the variables, such as the mass fraction of the species and source terms of the *C* equation, are functions of the

mixture fraction, mixture fraction variance, progress variable and scalar dissipation, see Equation (4.16). During the hybrid RANS/LES calculation, the filtered values $\tilde{f}$, $\tilde{C}$, $\widetilde{f^{"2}}$ and $\tilde{\chi}$ are obtained from the solution of the filtered transport equations and models for the variance and scalar dissipation rate. Let $\tilde{f}$, $\tilde{C}$, $\widetilde{f^{"2}}$ and $\tilde{\chi}$ obtained from the calculation fit the values of $\tilde{f}$, $\tilde{C}$, $\widetilde{f^{"2}}$ and $\widetilde{\chi_{st}}$, which is used as the indicators of the look-up tables, the mixture fraction of the species and the source term of the *C* equation are decided using the values obtained the unsteady PDF look-up tables and the interpolation technique. More information about the solution procedures is presented in the following section.

4.4. Solution procedures

When numerically solving the hybrid RANS/LES equations and the corresponding model equations, the system of linear equations obtained from the numerical discretization are solved using a time marching process. The overall solution procedure in the in-house code is given by Figure 4.5. In the present study, the second-order Runge-Kutta method is employed in the time marching procedure.

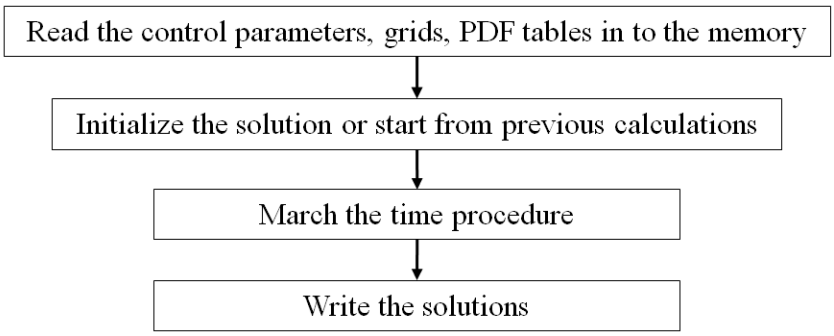

Figure 4.5 Schematic of the procedure of the solution in the in-house code.

At each time step, a number of iterations of the variables, including the density, velocity, energy, mixture fraction, progress variable, etc. are generally required in

order to ensure an adequate conservations of mass, momentum, energy and species. Solution procedures for general reacting flows have been reviewed by Sadasivuni [149]. However, the code employed by Sadasivuni [149] is mainly used for the simulation of incompressible variable density flows and a pressure/velocity correction step is included in order to ensure adequate conservation of mass. In our in-house code, which solves the transport equations and the ideal gas equation, the pressure/velocity correction step is not present any more. Further, the solution procedures at each time step, i.e. the UFPV solution procedures in the in-house code, are presented in the current study. It should be noted that the solution procedures of the flamelet and UFPV models are very similar, and therefore only the UFPV solution procedures are presented here:

Step 1. Initialization.

1.1: Choose the solution values at the current time level t_n as the initial guesses for the values of the variables at the next time level t_{n+1}.

Step 2. Calculation of the scalar transport equations.

2.1: Solve the filtered mixture fraction equation and obtain $\tilde{f}(t_n)$.

2.2: Compute the variance of the mixture fraction from its model equation and obtain $\widetilde{f''^2}(t_n)$.

2.3: Calculate the filtered scalar dissipation rate $\tilde{\chi}(t_n)$ from its model equation.

2.4: Based on $\tilde{f}(t_n)$, $\widetilde{f''^2}(t_n)$ and $\tilde{\chi}(t_n)$ obtained from steps 2.1, 2.2 and 2.3, respectively, and the filtered reaction progress variable obtained from the previous time step or iteration, namely $\tilde{C}(t_{n-1})$, calculate the filtered progress variable source term $\widetilde{\dot{\omega}}_C(t_n)$ from the look-up tables using the interpolation technique.

2.5: Solve the transport equation for the filtered progress variable using $\widetilde{\dot{\omega}}_C(t_n)$ obtained from step 2.4 and obtain $\tilde{C}(t_n)$.

Step 3. Calculate the eddy viscosity.

Step 4. Solve the mass conservation equation and obtain the density $\bar{\rho}(t_n)$.

Step 5. Solve the momentum equations and obtain the velocities.

Step 6. Calculate the energy equations.

6.1: Based on $\tilde{f}(t_n)$, $\widetilde{f''^2}(t_n)$, $\tilde{\chi}(t_n)$ and $\tilde{C}(t_n)$ obtained from steps 2.1, 2.2, 2.3 and 2.5, respectively, compute the enthalpy flux $H(t_n)$ from the look-up tables using the interpolation technique.

6.2: Solve the energy equation using $H(t_n)$ obtained from step 6.1 and obtain temperature $\tilde{T}(t_n)$.

Step 7. Calculate the species concentrations

7.1: Based on $\tilde{f}(t_n)$, $\widetilde{f''^2}(t_n)$, $\tilde{\chi}(t_n)$ and $\tilde{C}(t_n)$ obtained from steps 2.1, 2.2, 2.3 and 2.5, respectively, compute the mass fraction of species m, namely $Y_m(t_n)$ from the look-up tables using the interpolation technique.

7.2: Based on $\tilde{f}(t_n)$, $\widetilde{f''^2}(t_n)$, $\tilde{\chi}(t_n)$ and $\tilde{C}(t_n)$ obtained from steps 2.1, 2.2, 2.3 and 2.5, respectively, compute the molecular weight of species m, namely $M_m(t_n)$, from the look-up tables using the interpolation technique.

Step 8. Calculate the pressure

8.1: Calculate the pressure using $\bar{\rho}(t_n)$, $\tilde{T}(t_n)$, $Y_m(t_n)$, $M_m(t_n)$ and the ideal gas Equation (3.8).

Step 9. March the solution to $\mathbf{t_{n+1}}$ using the second-order Runge-Kutta method

9.1: Keep performing steps 2~8 until the solution at t_n is converged.

9.2: March the solution to the next time level t_{n+1} using the second-order Runge-Kutta method and keep performing steps 2~9.

Concerning the flamelet generation, the PDF table calculation and the UFPV solution, an overall flow chart for the hybrid RANS/LES modelling of the supersonic flames is given in Figure 4.6.

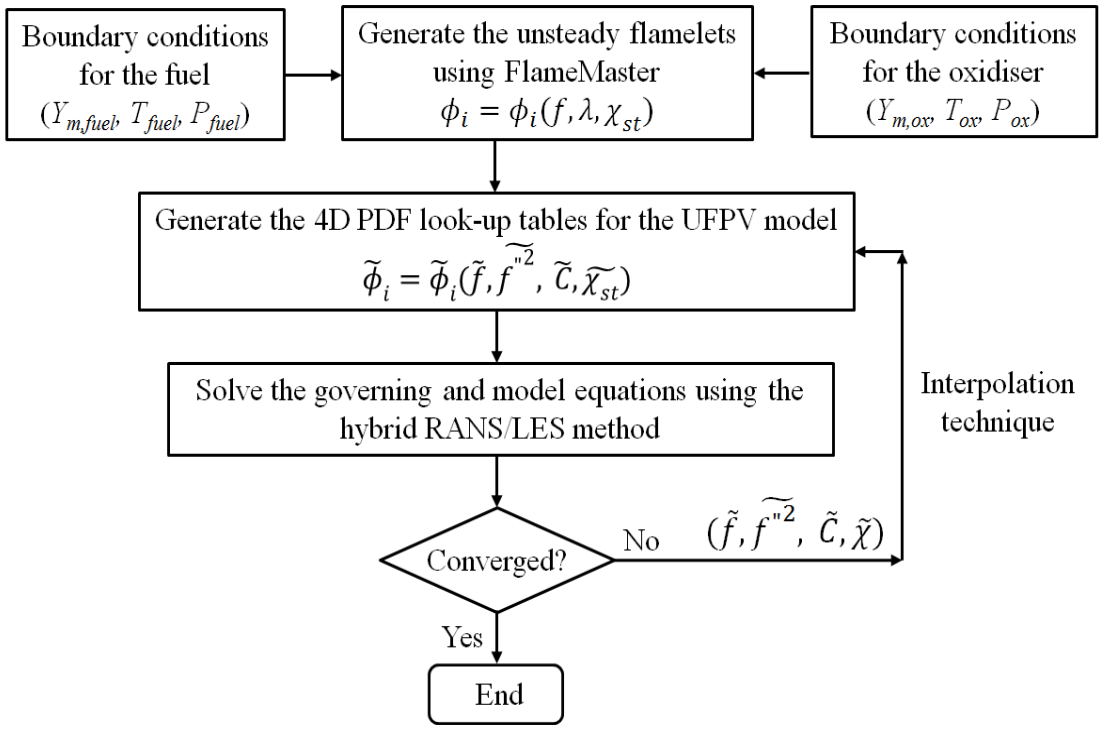

Figure 4.6 The overall flow chart for the hybrid RANS/LES modelling of the supersonic flames.

4.5. Closure

In this chapter, the scalar approach, also called the mixture fraction approach, is presented in brief following the theory behind the steady flamelet model. The advantages and disadvantages of the steady flamelet model are discussed and the advanced unsteady flamelet/progress variable combustion model is developed and built into the hybrid RANS/LES in-house code for the simulations of supersonic flames. Secondly, the generation of the steady and unsteady flamelet libraries are discussed and performed using the FlameMaster code. Further, the steady and

unsteady flamelets are converted into the PDF look-up table using the in-house code and these tables are used in the steady flamelet and the UFPV models when simulating the combustion with both strut or cavity flameholders. Finally, the solution procedures of the UFPV model and the flow chart for the hybrid RANS/LES modelling of the supersonic flames are presented.

Chapter 5
Modelling of supersonic combustion with a strut flame holder

5.1. Introduction

RANS is a computational efficient approach and dominates the turbulence modeling of the scramjet combustor system [40] but application attempts on the large eddy simulation (LES) approach are increasing. However, the modelling of the turbulence and combustion in high speed flows is still a significant challenge.

In order to validate the turbulence and combustion models employed, a reference experimental case should be carefully chosen. The laboratory scramjet combustor [174] in the Institute for Chemical Propulsion of the German Aerospace Center (DLR) is a famous and popular reference case since several experimental measurements have been performed there. In particular, the velocity and temperature distribution data and the shadow images are available and very useful for comparison and validation purposes. Both RANS [178-184] and LES [183,185-188] investigations have been made previously in computational studies on the DLR experimental configuration. Both these experimental data and the previous simulations could assist us to understand the characteristics of the supersonic flame and validate the revised combustion model, and therefore the DLR supersonic flame, i.e. the DLR case, is simulated in the present research.

Turbulent flows are significantly affected by the presence of walls. This is because walls are the main source of the mean vortices and turbulence [127]. Therefore, the near-wall modeling impacts on the fidelity of the numerical solutions. In the DLR case, the flow is bounded by the upper and lower combustor walls, while the strut wall is in the middle of the combustor and therefore it will have a large

effect on the shear flow downstream [11]. In previously published research, there is a lack of consistency in dealing with the wall boundaries in scramjet combustion models due to the presence of high-speed supersonic flows. Both the slip wall and no-slip wall assumptions have been employed by different authors to the upper, lower, and strut walls of the combustor [178-182,185-187]. The application of the near-wall treatment was artificial and the effects introduced by the different near-wall boundary conditions were not studied in-depth.

Concerning the modelling of the combustion, the flamelet model and its variants are widely employed [40,178,185,186]. In a recent review, Bilger et al. [99] found that some turbulent combustion models that have good application prospects are the flamelet model, the probability density function (PDF) approach and the conditional moment closure (CMC). The CMC method is capable of handling finite-rate chemical kinetics as well as turbulence-chemistry interactions [99]. However, this method is very computationally expensive and the low Mach number assumption restricts its applicability to supersonic combustion. The PDF approach was originally based on a low Mach number assumption and was later modified to include compressible reacting flows. However, the computational cost of this method is extremely high for 3D simulations even with a moderate number of reacting species. The flamelet concept is based on the fast chemistry assumption and the separation of scales. It views the turbulent flame as an ensemble of thin, laminar, locally one-dimensional flamelet structures embedded within the turbulent flow field. Although the flamelet model was developed based on the low-Mach number assumption, it has been extensively used in both low-speed and high-speed reacting flows [178,184-186]. Theoretical analyses and numerical simulations show that most of the supersonic combustion can be described by the flamelet model [40,174,185]. However, the flamelet model is incapable of predicting the extreme finite rate chemistry with extinction and re-ignition physics which are normal phenomena in high turbulence conditions and in particular in supersonic ramjet

flames [189], and accurate predictions of near burner region would have significant effects on the simulation of the overall combustion process. It is noted that the UFPV model [170] has been found to excel and overcome the drawbacks of the flamelet model, and it has been successfully employed to predict non-premixed [170] and partially premixed lifted flames [149]. However, it has not been widely employed and tested on supersonic combustion simulations [190].

In this chapter, the RANS modelling are firstly employed to simulate non-reacting flows in the DLR case using the commercial CFD code FLUENT in order to study the effects of the grid sensitivity, the geometry fidelity and the assumptions of the solid wall boundary conditions. Subsequently, the reacting flows are simulated using the flamelet model, which is built into the in-house code and FLUENT, and the UFPV model, which is built into the in-house code. Finally, the LES modelling is performed with the UFPV model, which is built into the in-house code.

5.2. Experimental and simulation configurations

The configuration used in the present research is the laboratory scramjet engine which was developed and experimentally investigated in the DLR [173-175]. In the scramjet engine model, the combustor consists of a one-side divergent upper wall, a flat bottom wall, two side walls and an installed wedge-shaped strut. The combustor entrance is connected to a contoured Mach 2 Laval nozzle and the cross section is 40 × 50 mm. The side and the upper walls are made from quartz glass in the experiments in order to be able to measure the flow and minimize the reflections of the scattered light on the wall opposite the observation window [173-175,186]. The strut has a half angle of 6°. The hydrogen is sonically injected parallel into the combustor along the stream direction through 15 holes which are at the base of the

strut. The diameter of the injection holes are 1 mm, and the distance between the centres of two adjacent holes is 2.4 mm. Typical mass flows in the experiments were varied between 1.0 kg/s and 1.5 kg/s for the air and between 1.5 g/s and 4.0 g/s for the hydrogen. The corresponding equivalence ratio is between 0.034 and 0.0136 [174]. The most popular case investigated was with a mass flow rate of about 1.0 kg/s for the air stream and 1.5 g/s for the hydrogen injection. The corresponding inflow conditions are given in Table 5.1. It should be noted that the turbulence parameters are not obtained from the experimental measurements but was estimated by Oevermann [178].

Table 5.1 Inflow and injection boundary conditions for the DLR case [178].

Parameters	**Air**	**Hydrogen**	**Parameters**	**Air**	**Hydrogen**
Ma	2.0	1.0	$\tilde{Y}_{N_2}$	0.736	0
$\tilde{u}$ (m/s)	730	1200	$\tilde{Y}_{H_2O}$	0.032	0
$\tilde{T}$ (K)	340	250	$\tilde{Y}_{H_2}$	0	1
$\overline{P}$ (10^5 Pa)	1	1	k (m^2/s^2)	10	2400
$\overline{\rho}$ (kg/m^3)	1.002	0.097	ε (m^2/s^3)	650	1e+8
$\tilde{Y}_{O_2}$	0.232	0			

A schematic of the scramjet experimental facility, i.e. the supersonic combustor, together with the relevant geometric dimensions for the simulations, are presented in Figure 5.1. The origin of the coordinates is at the start point of the lower wall of the combustor, the X coordinates is along the lower wall pointing downstream, and the Y coordinates is across the entrance and points towards the upper wall. The upper wall of the combustor diverges from the location X = 58 mm with a constant angle 3° in order to compensate for the growth of the boundary layer.

However, the lower wall remains flat and is 300 mm long. The strut is placed at the centerline, Y = 25 mm, in the combustor and it is 32 mm long, and its tip is located at X = 35 mm.

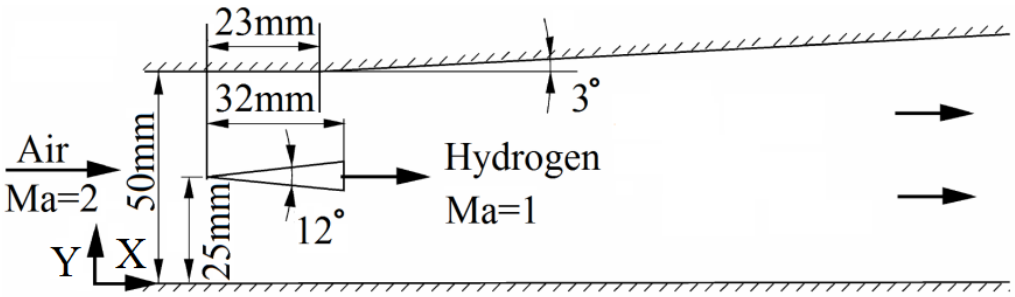

Figure 5.1 A schematic of the scramjet experimental rig [178].

In order to reduce the computational cost as much as possible, a 2D computational configuration, which has been widely adopted in previous research [178,179,181,180], is employed. In the dimensional simplification, the main geometry of the combustor and strut is maintained, but the injection holes are simplified to be a slot. On the one hand, the hydrogen injection velocity should be maintained in order to obtain a similar flow structure and mixing property in the wake zone. On the other hand, the mass flow rate of the hydrogen jet should also be maintained to be the same as in the experiments, so as to obtain the same fuel-oxidant ratio and combustion characteristics [178]. Therefore, the size of the hydrogen injection slot is approximately 0.2945 mm, much smaller than the diameter of the holes employed experimentally.

In addition to the 2D configuration, a 3D configuration is also employed during the RANS modelling of the DLR case in order to retain the main properties of the three-dimensional experimental configuration. The three-dimensional computational configuration is simplified in the sense that instead of modelling the full width of the combustor, which includes 15 holes and the side walls, a smaller domain with one half injector hole and half the size of the domain between two

adjacent holes are employed. The back surface at X = 0 mm is the symmetric surface of the two adjacent holes. The front surface at X = 1.2 mm is across the centre of the injection hole.

In the large eddy simulations, the configuration with 15 holes was not been widely used because of the huge cost in computation resources. A configuration which has 3 injection holes is used to maintain the 3D flow characteristics, consider the interaction between the holes and save on the computational resources. Under this configuration, the two surfaces in the spanwise direction were assumed to be a periodic boundary condition [185,186].

5.3. RANS modelling of the DLR case

In this section, grid sensitivity and geometry fidelity are first studied based on the simulation of the non-reacting flows. The simulation results of the non-reacting flows are also analyzed and investigated. Secondly, the reacting flows are simulated using both the flamelet model and the UFPV model built into the in-house code. Comparisons among the simulation results and the experimental data are made in order to analyse the characteristics of the supersonic non-reacting and reacting flows. Further, the ability of predicting the supersonic combustion using the flamelet and the UFPV models was examined.

5.3.1. Numerical methods and model descriptions

5.3.1.1. Numerical methods

The steady-state momentum, energy, species, and pressure-based continuity equations are solved using a pressure-based RANS solver in FLUENT. The gradients are computed according to the Green-Gauss node-based method. In order

to increase the accuracy of the solution, and reduce the numerical dissipation and the grid density requirements, the second-order scheme for the pressure equation and the second-order upwind scheme for the other equations are employed to the spatial discretization. A typical Courant-Friedrichs-Lewy (CFL) value in the pressure-based implicit solver is 4.0 [127]. In order to keep the solution certainly stable, a lower CFL value 0.5 is employed in the present study.

In the in-house code, the RANS governing equations of the continuity, momentum, energy, etc. are solved based on the finite difference method and the UFPV model is included. The fifth-order WENO scheme is used for the convective fluxes and the second-order accurate-centered scheme is used for the diffusive fluxes. The time marching proceeds with the second-order Runge-Kutta method until a steady-state solution is reached. Again, the CFL number is fixed at a value of 0.5.

5.3.1.2. Turbulence model

In contrast to the k-ε and the k-ω models, the SST k-ω model is more accurate and reliable for complex flows with, e.g. free shear flows, wall-bounded flows, adverse pressure gradient flows, and in particular shock waves [127]. Therefore, it is employed in both FLUENT and in-house code. In order to obtain good predictions of the flow near the solid surface, the y+ of the first grid node near the wall should be maintained to be about 1 [127].

5.3.1.3. Boundary conditions

The Dirichlet boundary conditions are used for all the variables at the air stream inlet and hydrogen jet inlet. As the flow fields under consideration here are supersonic, all variable values at the outlet are extrapolated from the interior

predictions. Therefore, a pressure outlet boundary condition is applied, such that the pressure at the outlet is sufficiently low so that the gas can outflow without being compressed. The fixed walls in the scramjet model consist of the combustor walls and the strut walls. To investigate the effects of the wall boundary conditions, which may be set as a slip or no-slip wall, to the main combustion process, three types of wall boundary conditions are employed for these walls, as showed in Table 5.2. The side surfaces are treated as symmetry boundaries.

Table 5.2 The three cases investigated and the corresponding wall boundary conditions.

Name of the case	**Wall boundary conditions**	
	Strut walls	Combustor walls
No-Slip-Strut	No-slip	Slip
All-Slip	Slip	Slip
All-No-Slip	No-slip	No-slip

5.3.2. Grid sensitivity and geometry fidelity study

5.3.2.1. 2D and 3D grids

The governing flow equations are numerical solved over the grid, and the grid has a profound effect on the numerical solution. Firstly, the mesh grid size is an important factor in the numerical simulations. On the one hand, numerical errors, i.e. discretization errors, arise from the combined effects of the grid and numerical scheme [191]. In order to keep the discretization errors at a low level, we have to use a fine mesh and high-order scheme. However, it is very difficult to perform the computations on a sufficiently fine mesh for a particular scheme due to the

computational limitations, especially for 3D configurations. On the other hand, the round-off errors increase as the number of grid nodes increases. Therefore, either a too coarse or too fine mesh cannot give good simulations of the experimental data and the use of an appropriate grid size is always crucial [192].

Secondly, the distribution of the mesh also affects the CFD solution. For example, in order to rigorously capture the shock waves, dense grid points near the shock wave surface are necessary [193]. If an initial grid has no clustering of the mesh in the regions where the flow parameters change rapidly, such as the region near the shear layers, the trailing edge of some transonic wings, the free jet, the turbulent boundary layer, etc., the small-levels of refinement may incorrectly indicate sufficient grid convergence, and particular features of the flow may not be captured [191]. In this DLR case, the feature of the flow is quite complicated. In the combustor, several typical flow phenomena are present, including shock waves, reflection of the shock waves, boundary layers, interactions between the shockwaves and the boundary layers, under-expanded sonic jets, supersonic shear layers, etc. In order to simulate these characteristics in the flow field, the gird in these zones should be fine.

Thirdly, the grid quality has a dramatic influence on the CFD solution [127]. High-level stretching and non-smoothness in the grid can bring inaccuracies and uncertainties into the numerical simulation, and either of them could cause a poor prediction of the flow field. It is possible for a scheme to divergence or converge locally with a low-order accuracy if the grid is poorly stretched or twisted in a particular region [191]. Overall, the grid sensitivity should be analyzed such that the numerical solutions are based on the use of good grids which have an appropriate size and distribution.

Experimental results have shown that a complex system of shock waves, expansion waves, wave reflections, compressible mixing layers present in the DLR

combustor [173-175]. A fine mesh and mesh independency research is required so as to capture the sharp discontinuities and accurately predict the flows. In this study, three different meshes are employed for the 2D case calculations and two different meshes for the 3D case. The grid sensitivity is performed for both the 2D and 3D cases. As structured grids have several considerable advantages over other grid methods [194], all the grids are blocked and structured. Along the strut, a boundary layer forms and after the strut, two shear layers are formed due to the low velocity and pressure in the recirculation region [178].

To resolve the boundary layer near the strut and the downstream shear layers, a condensed grid is required. Moreover, the hydrogen is injected sonically from the base of the strut. Therefore a denser grid is required in the region near the hydrogen injection so that the interaction between the sonic hydrogen underexpended jet and the vortices and recirculation nearby can be well simulated. Then, the mixing properties after the strut will be resolved with a high fidelity. The name and size of the meshes employed are given in Table 5.3. The configuration of the 3D case and the grid distribution of the 3DM mesh are illustrated in Figure 5.2.

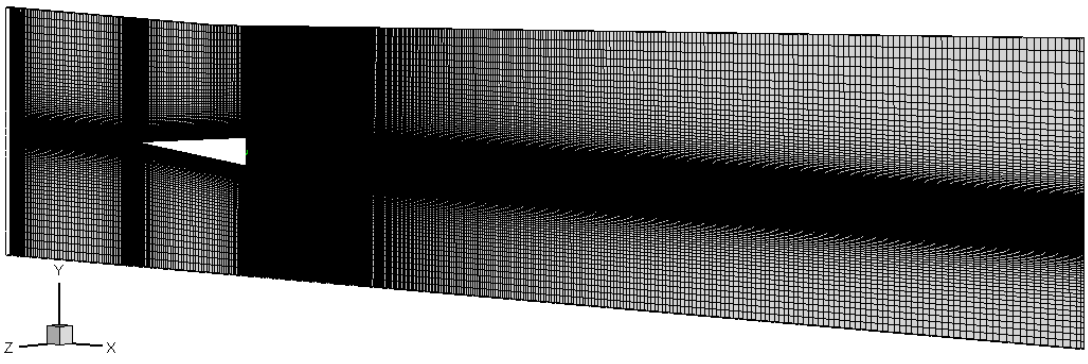

Figure 5.2 The configuration of the 3D case and the grid distribution of the 3DM mesh.

Table 5.3 Summary of the 2D and 3D grids for the RANS of the DLR case.

Dimensional	**2D**			**3D**	
Name of the case	2DC	2DM	2DF	3DC	3DM
Size (cells)	172,002	213,480	540,828	918,984	1,847,162

5.3.2.2. Grid sensitivity study

In order to check the sensitivity of the numerical results to the grid size, a grid sensitivity study is performed. As has been revealed by the experimental observations [174] and the RANS simulations by Oevermann [178], the flame is held in the region near the strut base, however the structures of the flow field in this region for the non-reacting flows are more complicated than those for the reacting flows. Also, considering that the modelling of the reacting flow takes more computational resources, therefore all the calculations for the grid sensitivity study are performed for the non-reacting cases. The no-slip-strut wall boundary condition is employed. The value of y+ of the first near-wall node in all the grids is about 1. In order to investigate the sensitivity of the results to the grid sizes, the X component of the velocity (namely *U*, or the X-velocity), at different cross sections are compared.

In the 2D calculations, the two cross sections are located at X = 64 mm and X = 207 mm. The two cross sections in the 3D calculations are located at the front surface Z = 1.2 mm and have the same X coordinates as those of the 2D case. We observe from Figure 5.3 that the *U* profiles obtained from the 2DF, 2DM and 2DC calculations are in good agreement. However, the finer is the mesh then the better are the predictions and the representation of the discontinuity. Also the same trend occurs in the 3D cases. In order to quantitatively evaluate the differences in the solutions, we define a parameter, namely *Pm*, as follows:

$$Pm = \max\left(\left|\left(U_1 - U_f\right)/U_f\right|\right) \times 100\%. \quad (5.1)$$

Here, U_1 and U_f are the X-velocities at the same coordinates obtained from the calculations that employ a coarse mesh and the finest mesh, respectively.

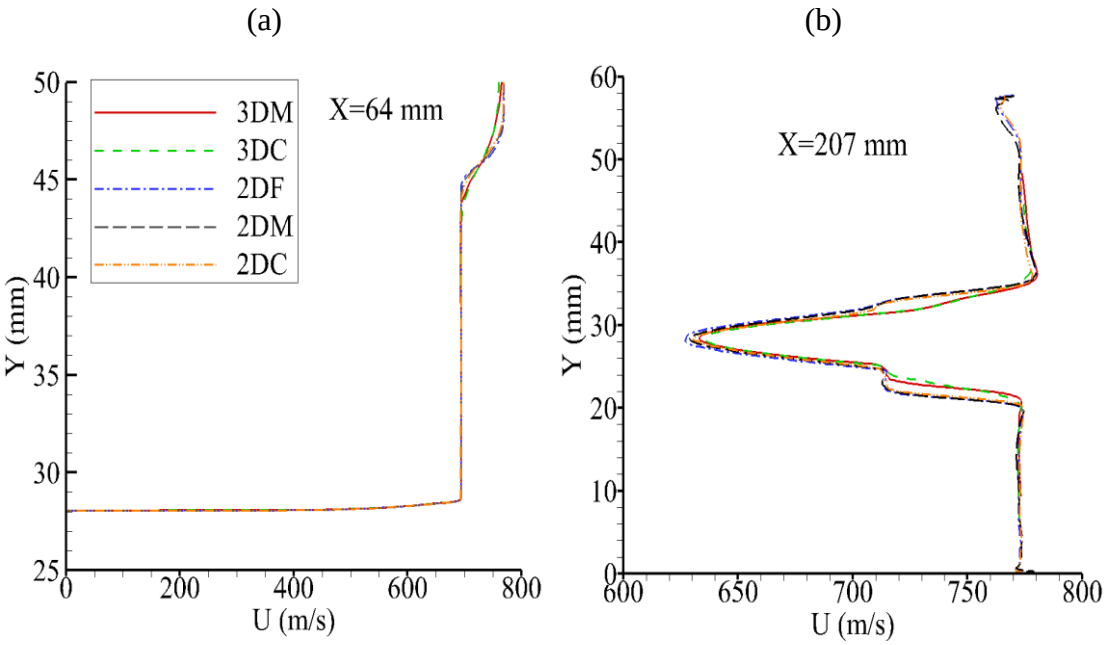

Figure 5.3 The X-velocity profiles at (a) X = 64 mm and (b) X = 207 mm; solid lines: 3DM mesh results, green dashed line: 3DC mesh results, dash dot line: 2DF results, long dash line: 2DM results, dash dot dot line: 2DC results.

In Figure 5.3(a), the profiles show that the differences between the results obtained from the 2DM and 2DF meshes are very small, *Pm* being less than 0.60%. However, the results obtained by using the 2DC mesh show a relatively large difference, namely *Pm* is about 1.45%, with the 2DF results. Further, the *Pm* in the 3D calculation is about 0.88%, and this is a small value. Therefore, we conclude that the 2DF, 2DM and 3DM meshes are successful in accurately predicting the strut boundary layer. The *U* profiles downstream at X = 207 mm are also given in Figure 5.3. We observe that the finer mesh gives a lower X-velocity in the main stream. This is because the presence of more cells in the flow field and then the better is the

discontinuity predicted. The values of *Pm* for the 2DM, 2DC and 3DC cases are all very small, namely 0.32%, 0.63% and 0.48%, respectively. Therefore, we conclude that a mesh independent solution for both the 2D and 3D meshes is obtained. In the following research, the 2DM and 3DM meshes are employed and the results obtained using these two meshes are reliable to be analyzed.

5.3.2.3. Geometry fidelity study

It is known that the holes in the experimental equipment are simplified into a slot in the 2D configuration, but the size of the slot is much smaller than the diameter of the holes in the experiments. Moreover, the wake near the strut base (near-wake zone) is divided into the upper and lower regions by the hydrogen jet. However, these two regions are not isolated from each other but connected by the gap between two injection holes. In this section, we discuss the effects of the simplification from the 3D to the 2D configuration. The shadowgraph image approach gives the second spatial derivative of the density, and it can provide a representation of expansion and shock waves [195]. In order to illustrate the features of the flows, the Mach number contours are presented in Figure 5.4.

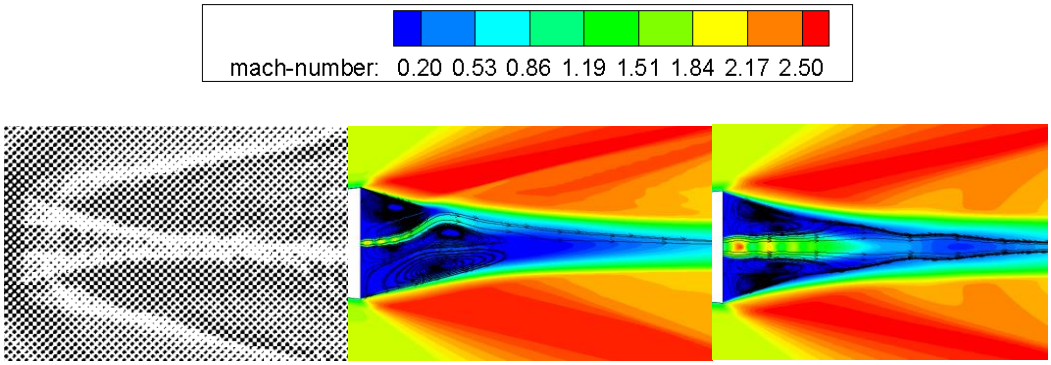

Figure 5.4 Mach number contours and stream traces near the strut base, left: experimental shadow image [178], middle: 2D results, right: 3D results.

Figure 5.4 is an enlarged view of the flows near the strut base, which are filled with expansion waves, underexpanded hydrogen jet, shear and mixing layers, recirculations and vortices. These features are represented by the shadow image and simulation results in Figure 5.4. In the simulations, the shock trains of the underexpanded hydrogen jet are well captured. The stream traces in the wake zones show clearly that the flows in the near-strut wake zone are symmetrical in the 3D model but asymmetrical in the 2D results. A more detailed analysis of Figure 5.4 shows that the hydrogen jet goes straight downstream both in the experiment and in the 3D calculation, but its tail is lifted in the 2D calculations. Moreover, the hydrogen and the near-strut wake spread much wider in the experiment and the 3D results than those in the 2D results. The expansion wave created by the divergent upper wall extends downstream of the near-strut wake zone. Further, Figure 5.4 shows that the near-strut wake zones are surrounded by supersonic flows, and clearly the expansion wave has no effect on this zone and therefore it is not responsible for the asymmetry in this zone.

In previous 2D studies by other researches [196,197,181], the asymmetry of the near-strut zone were also presented. Wepler et al. [181] showed that the wake region of the strut in the non-reacting flow, and the stream traces illustrate that the hydrogen jet is pushed down towards the lower wall. However, the hydrogen stream predicted by the 2D simulations in this study is lifted towards the upper wall. One possible explanation for the two contradictory predictions is the instability of the jet, i.e. the high-speed underexpanded hydrogen jet is unstable in nature. For supersonic mixing layers with a wake component in the mean-velocity profile, the mixing layer becomes more unstable [198]. The jet vortex structures arise from the Kelvin-Helmholtz instability of the jet-shear layer in the near field [186]. However, the steady RANS models are limited in this ability in predicting this structure due to their inability to accurately capture the unsteadiness in the flow.

Whether the jet is lifted up or pushed down is related to the grid distribution, the initial state of the calculation and the solver itself. This topic relates to the origin of the turbulence [199] and the Hopf bifurcation theory [200], and these issues are beyond the scope of this research. In the 3D case, the wake zone is not separated by the jet and this is because of the vacancy of the injection at the strut base. This means that the regions above and below the hydrogen jet are connected with each other. The differences between the pressure, density and temperature in the above and below regions are averaged and thus suppressed. Therefore, the asymmetry in the flow in the near-strut zone is not present in the 3D case. Although Figure 5.3 shows a small difference in the velocity distribution downstream between the 2D and 3D calculations, the distribution of the hydrogen at the location X = 78 mm, which significantly affects the combustion, are quite different, as can be observed in Figure 5.4. In the 2D case, the hydrogen jet is lifted up and the prediction of the combustion is not predicted correctly. Then, both the non-reacting and reacting RANS simulation results, which are based on the 2D configurations, are unreliable.

There are several ways to solve the problem in the 2D simulation, which is discussed above. Firstly, one possibility is to use a coarser mesh, and then some of the unsteady flow characteristics are filtered and thus are not predicted. However, we do not suggest this method as some important flow characteristics may not be present. Secondly, another possible solution is to use the unsteady solver to predict the unsteady characteristics of the flow, and obtain the average flow by statistical averaging. The unsteady RANS, or LES, modelling are possible methods for predicting the shear and jet flows [201,202]. However, the unsteady solver is costly in computational terms and the LES is always not recommended for 2D simulations. Finally, since a good agreement has been shown between the 3D simulation and the experiment results in the hydrogen jet region, running the case based on the 3D configuration is a good approach to investigate both the non-reacting and reacting

flows using the steady RANS solver, and this recommendation is employed in the following research on the near-wall assumptions.

5.3.3. Non-reacting flows

In this section, in order to examine the near-wall assumptions, three different cases are calculated based on the 3D configuration with different wall boundary conditions, as shown in Table 5.2. The simulation results, especially on the aspects of near-wall assumptions, are analysed in detail and also compared with the experimental data. Shadowgraph images of the experiments and the numerical shadowgraph obtained from the No-Slip-Strut case are shown in Figure 5.5. It should be noted that the All-Slip and All-No-Slip cases predict very similar overall structures of the flow field and therefore are not shown in Figure 5.5.

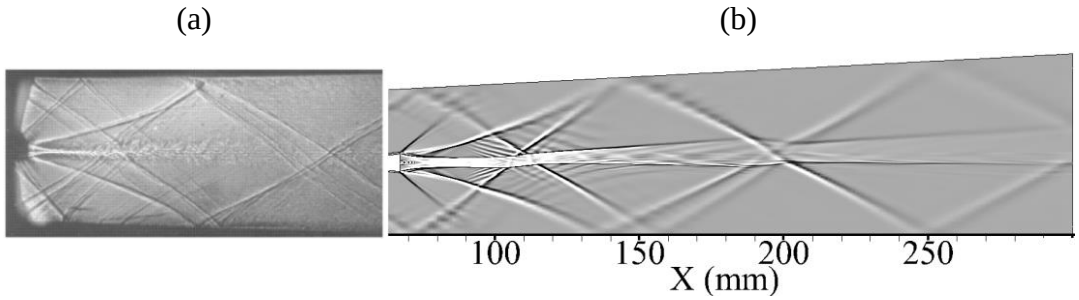

Figure 5.5 (a) A shadowgraph image [178] obtained from the experimental investigation and (b) numerical shadowgraph (essentially $\nabla^2\overline{\rho}$) image obtained from RANS simulation of the non-reacting flow.

Figure 5.5 gives a clear indication of the complex flow structure. The strut wall boundary layers separate at the base and two shear layers are formed. Near the strut, two expansion fans are formed and followed by two recompressed oblique shocks. Due to the divergence of the upper wall, the upper reflected shock wave reaches the mixing layer at X ≈ 112 mm further downstream than the lower reflected shock wave. The compressible mixing layer develops very slowly before X ≈ 105 mm, but

the mixing zone becomes wider after the shocks hit the mixing layer at X ≈ 105 and 200 mm. This indicates that the shocks enhance the mixing in the combustor. Further, Figure 5.5 illustrates that the expansion wave created by the upper combustor wall has a large effect on the downstream flow but it has virtually no effect on the flow close to the base of the strut.

On comparing the two shadow images, it is found that several shocks and their reflections are not present in the simulation results. For instance, the two shock waves which originate just in front of the strut base are missing in the simulations. These shock waves may be generated by some irregularities on the strut surface (we name them "irregular shock waves" in this study), while the simulation supplies an ideal wall surface condition [154].

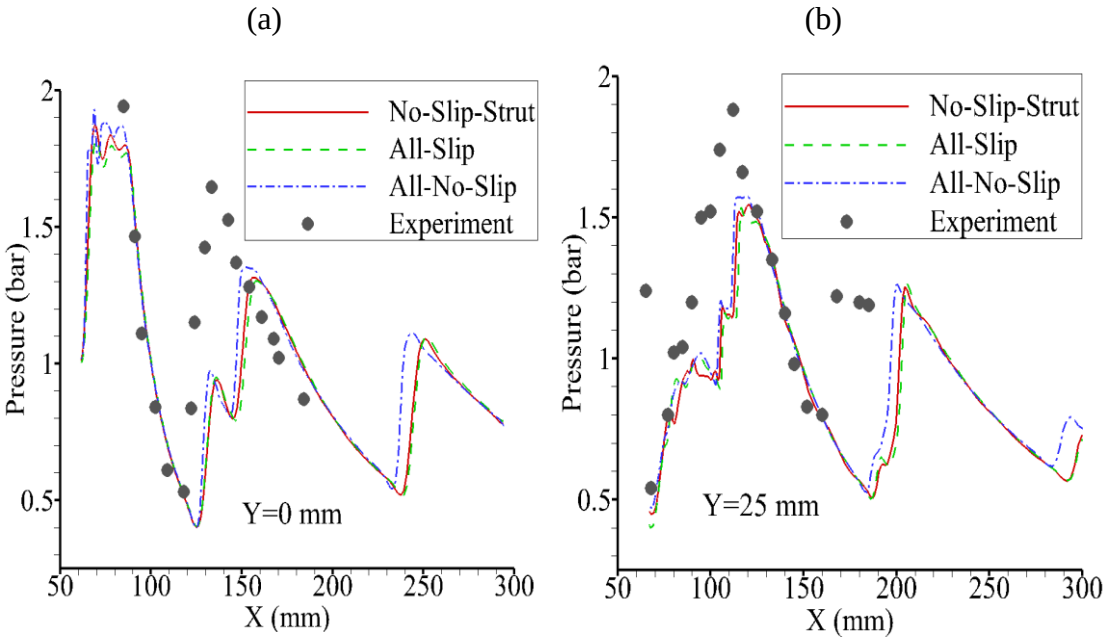

Figure 5.6 Pressure distribution along (a) the lower combustor wall (Y = 0 mm) and (b) the central line (Y = 25 mm) of the side wall, obtained from the experimental investigation [178] and RANS simulations of the non-reacting flow.

Figure 5.6 shows the pressure distribution (a) along the bottom wall and (b) on the central line of the side wall for the non-reacting case. The pressure profiles from the All-Slip case and No-Slip-Strut case match with each other very well at both positions, and show only slight differences with those obtained from the All-No-Slip case. Although the pressure and velocity profiles obtained from the All-No-Slip case shows a slightly improvement agreement with the experiment data, all the profiles obtained from the three cases are in very similar behavior and are all in reasonable agreement with the experiment data.

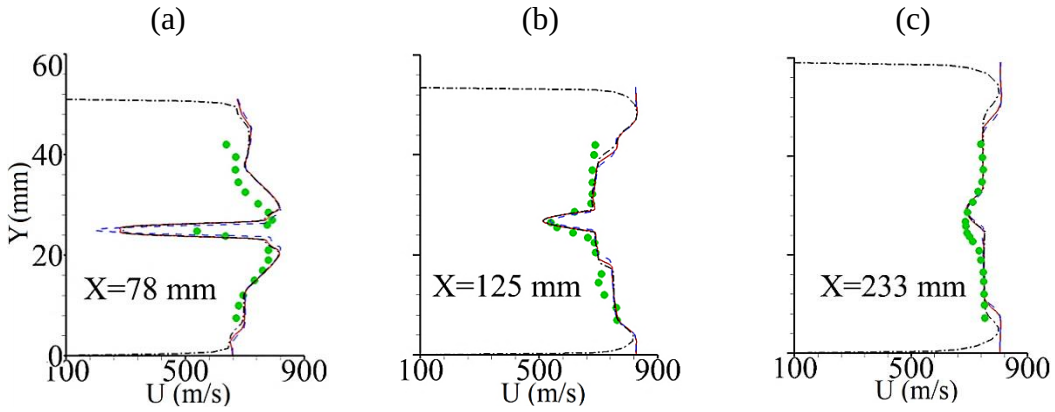

Figure 5.7 The X-velocity profiles at (a) X =78 mm, (b) X = 125 mm and (c) X = 233 mm for the non-reacting cases, red solid curves: No-Slip-Strut case, blue dashed curves: All-Slip case, black dash-dot curves: All-No-Slip case, circle symbols: experimental data [178].

In Figure 5.7, the velocity profiles for the All-No-Slip case show reasonable differences in the near-wall region with those obtained from the All-Slip and No-Slip-Strut cases. This is because the no-slip wall condition is closer to the real physical situation that exists in the experiments. However, little difference is shown in the main stream, i.e. in the region away from the wall where the hydrogen-air mixing takes place. At the cross section X = 78 mm, there is a disagreement between the experimental and the simulation results, in particular along the centerline of the

geometry, but the experimental data are rather sparse and they might not be able to follow steep velocity variations in the region immediately downstream of the strut. Both the No-Slip-Strut case and the All-No-Slip case represent double-trough X-velocity profiles in the wake region, and this means that the flow is accelerated by the high-speed hydrogen jet. The X-velocity profile in the wake region at X = 78 mm for the All-Slip case has only one trough, whose value is much smaller than those obtained from the other two cases investigated.

Figure 5.8 shows the Mach number contours obtained from the three cases. It is observed that the velocity in the expansion fan region in the All-Slip case is larger than that in the other cases. The wake region is confined and compressed by the high speed flows and the growth of the compressible mixing layer is suppressed as the convective Mach number increases [203]. Therefore, the wake region is narrower in the All-Slip case than in the other two cases. However, the momentum thickness of the boundary layer has a large effect on the development of the downstream shear layer [204]. Therefore, the mixing layer in the All-Slip case is thinner than that in the other two cases. Both the above effects contribute to the shorter hydrogen injection penetration, and the jet will not accelerate the X-velocity to a double-trough profile. Thus, the assumption of slip condition may be not appropriate to the strut walls.

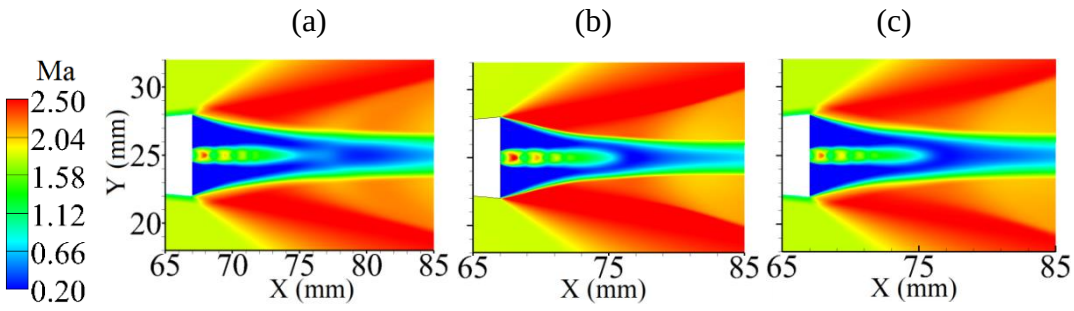

Figure 5.8 Mach number contours for the non-reacting flow, (a): No-Slip-Strut case, (b): All-Slip case, (c): All-No-Slip case, obtained from the RANS simulations.

In Figure 5.9, the X and Y components of the velocity fluctuation are denoted as *Urms* and *Vrms*, respectively. Although the simulation results match well with the experimental data, there are still certain discrepancies present. In the mixing region, near to the central line of the combustor, the velocity fluctuations are overestimated in the simulation in comparison to the experimental data. However, in the regions Y ≈ 10 and 40 mm, even the All-No-Slip case shows an underestimation of the velocity fluctuations in comparison to the experimental data. This is possibly because the irregularities on the wall surfaces in the experiments supply more origins of the turbulence and the shocks [154,173]. These shocks, which are created by the irregularities, assist the growth of the mixing layer and the transfer of the turbulent kinetic energy from the central line region to the surrounding region. Figure 5.9 also indicates that the fluctuations, i.e. the turbulence, in the All-Slip case is underestimated at the cross-section X = 182 mm because of the slip assumption on the strut walls.

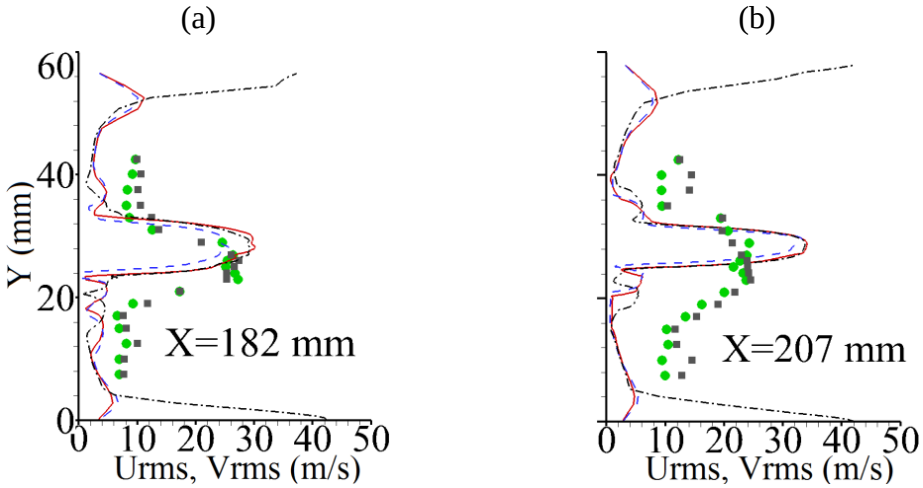

Figure 5.9 The velocity fluctuation profiles at the cross section (a) X = 182 mm and (b) X = 207 mm for the non-reacting flow, red solid curves: No-Slip-Strut case, blue dashed curves: All-Slip case, black dash-dot curves: All-No-Slip case, green circle symbols: experimental *Urms* data, grey square symbols: experimental *Vrms* data [178].

In Figures 5.7 and 5.9, in the mixing region, the profiles from the No-Slip-Strut case and the All-No-Slip case always show a better agreement with each other than with the All-Slip case. Outside the mixing region, the All-Slip and No-Slip-Strut results show better agreement with each other than with the All-No-Slip case. This is because the no-slip wall condition at the upper and lower walls changes the reflection of the shock as well as the shock-wave/mixing-layer interaction downstream. However, the values of *Urms* and *Vrms* outside the mixing region are very small in comparison to those in the mixing region, and the effects on the mixing are not significant.

In summary, the boundary layers on the strut should not be neglected in the non-reacting flows, but the treatment of the upper and lower combustor walls only slightly affect the main stream flow where the mixing and combustion takes place in the reacting cases. Therefore, the slip condition is employed on the upper and lower combustor walls and the no-slip condition is employed on the strut walls in the following calculation of the reacting flows.

5.3.4. Reacting flows

In order to validate the UFPV model and understand the characteristics of the supersonic flame in a strut-based combustor, the reacting case was simulated with both the flamelet and the UFPV models which are built into the in-house code. As recommended in §5.3.2 and §5.3.3, the 3DM grid and No-Slip-Strut wall assumption are employed during the RANS modelling of the reacting flows of the DLR case.

The global structure of the flow, including the widening of the reacting zone and a series of reflections of the shocks, is shown in Figure 5.10 by the shadow image obtained from the experiment [174,178] and the numerical shadow image obtained from the simulations. It is observed that the global structure of the reacting flow predicted by the flamelet model is similar to the one predicted by the UFPV

model. In Figure 5.10, the light intensity of the shadow image is proportional to the second spatial derivative of the density and therefore it is helpful to visualize the density difference due to heat release and compressibility. In contrast to the non-reacting flow, the reaction zone, i.e. the wake zone, becomes broader due to the heat release from the combustion. The upper and lower shocks cannot pierce into the reaction zone and therefore are reflected by the high temperature combustion surface at the positions (X ≈ 107 mm, Y ≈ 35 mm) and (X ≈ 100 mm, Y ≈ 20 mm), respectively, and these shocks significantly contribute to the development of the reacting mixing layer. Previous studies have provided evidence that these incident shock waves significantly affect the mixing efficiency and the flame stabilization processes [179].

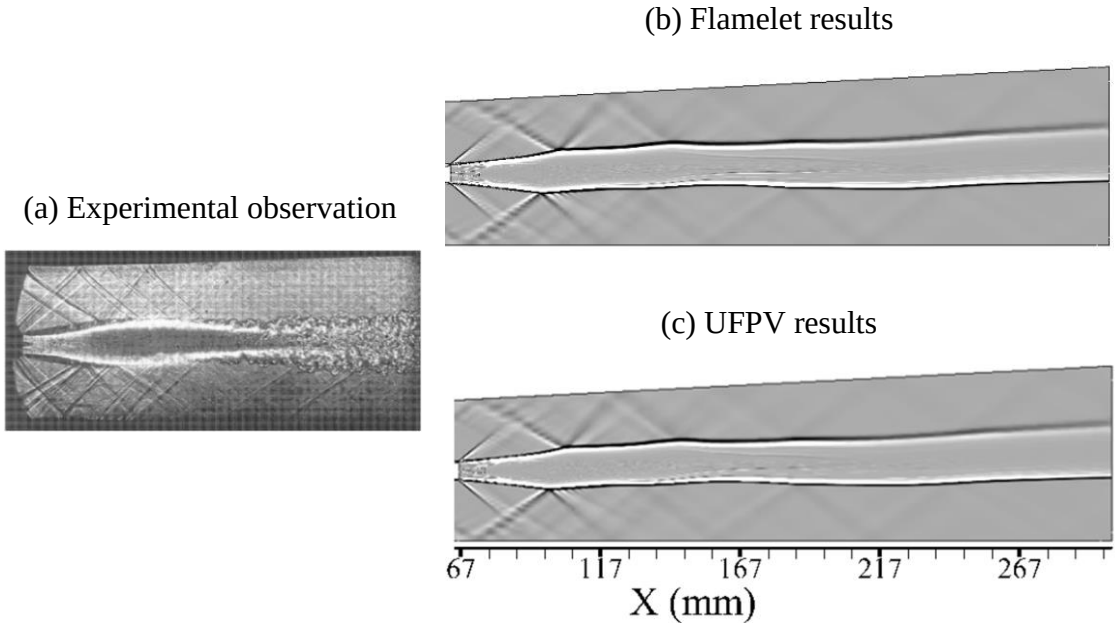

Figure 5.10 (a) A shadow images obtained from the experimental investigation [178] and the numerical shadowgraphs (essentially $\nabla^2\overline{\rho}$) for (b) the flamelet and (c) the UFPV RANS modelling of the reacting flow.

The shadow images in Figure 5.10 illustrate that the reflection of the shocks which originate just in front of the strut base suppresses the development of the

combustion zone, but these shock waves which may be generated by some irregularities on the strut surface are not present in the simulations which employ an ideal wall surface condition. Therefore, a broader combustion zone in the downstream region is predicted by the simulations. However, the overall structure of the flow field predicted by both the UFPV and the flamelet modelling appears to agree well with that illustrated by the shadow images in Figure 5.10. Also it should be noted that the predicted flow field was under steady state conditions, while the real combustion is always unsteady. Therefore the time dependent structures, e.g. the vortices shown in the shadow image will not be seen in the steady state predictions.

Figure 5.11 shows the contours of the temperature and the OH mass fraction obtained from the flamelet and UFPV modelling. The OH mass fraction contours show the intensity of the formation of the thermally and chemically excited OH radicals, and therefore they give an indication of the reacting zone and the relative extent of the reactions. From Figure 5.11, it is found that the reaction first takes place in the mixing layer after the strut and the flame propagates along with the growth of the mixing layer in all the three cases. Because of the low flow speed, and the strong mixing in the reacting zone near the strut base, the combustion can be maintained and the strut serves as a flame holder for the hydrogen diffusion flame which is anchored in the wake of the strut.

Also, the contours of the OH mass fraction shown in Figure 5.11 indicate that the main combustion predicted using the flamelet model takes place downstream of the strut in the combustor. The UFPV model predicts a shorter reaction zone, which is from the strut base up to X = 250mm, and the combustion predicted by the UFPV model is less intense than the one predicted by the flamelet model. The intense combustion predicted by the flamelet model, which is based on a fast chemistry assumption, results in a faster combustion than the experimental measures, as shown

in the OH-emission intensity images in Figure 5.12. In contrast to the flamelet model, the UFPV model considers the unstable branch of the flamelet equations and is capable of predicting the local extinctions. Therefore, a less intense flame and a slightly narrower and shorter flame zone are predicted by the UFPV model.

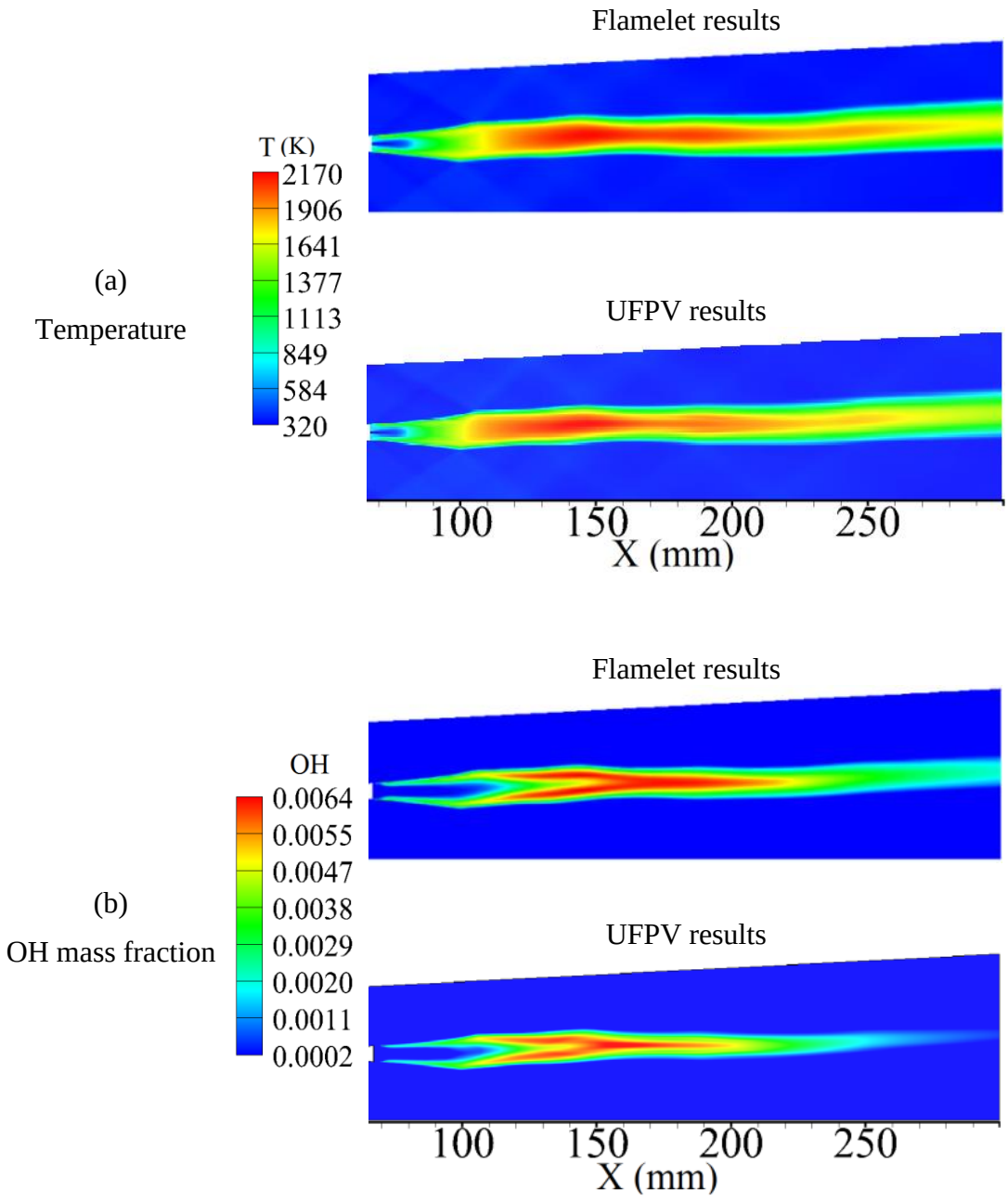

Figure 5.11 The (a) temperature and (b) OH mass fraction contours obtained from the flamelet and the UFPV RANS modelling.

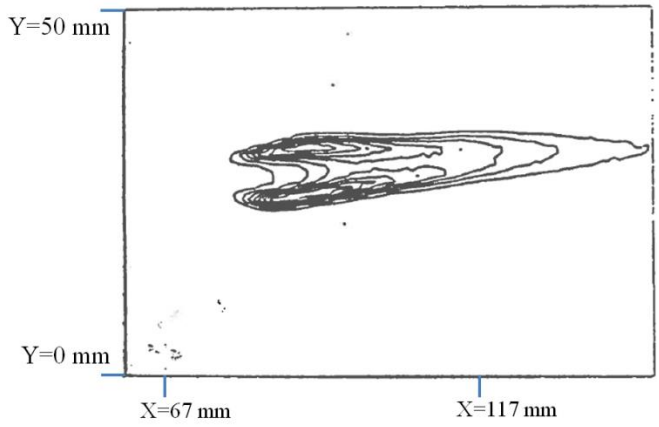

Figure 5.12 The spontaneous OH-emission intensity images (the exposure time is 150 μs) obtained from the experimental observation [174].

Figure 5.13 provides a quantitative comparison of the temperature at different cross sections of the combustor. The temperature profiles for all the three simulations performed show qualitative agreement with the experimental data, but are quantitatively overestimated at locations away from the base of the strut. Apparently, both the flamelet and the UFPV models tend to overestimate the temperature. This overprediction in the temperature downstream when using the flamelet model approach was also observed in the literatures [187,188]. It has been found that the uncertainties in the chemical kinetics have important effects on the simulation results [205], but this topic is out of the scope of the present research. Further, the neglect of the radiation effects also contributes to the over prediction of the flame temperature.

In Figure 5.13, the temperature profiles at X = 78mm are obtained from the simulations and are in a double-peak shape because of the hydrogen injection, and they are in reasonable agreement with the rather sparse experimental data. It is observed that the UFPV model predicts a slightly lower peak temperature, which is consistent with the experimental data, than the flamelet model, thus indicating a less intense combustion taking place in this region. This is also illustrated by the OH mass fraction in Figure 5.11. At the locations X = 125 mm and 233 mm, both the

modelling and the experimental data give one-peak temperature profiles, but the modelling gives a broader high temperature zone. In summary, the UFPV model predicts a less intense combustion than does the flamelet model.

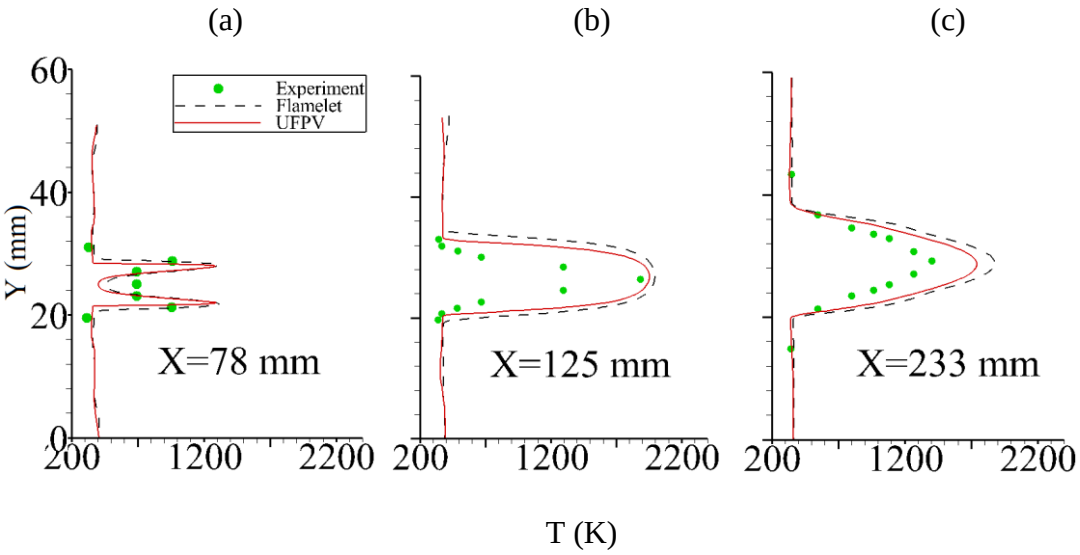

Figure 5.13 The temperature profiles at the cross section (a) X = 78 mm, (b) X = 125 mm and (c) X = 233 mm for the reacting flow, obtained from the experiments [178] and the RANS simulations.

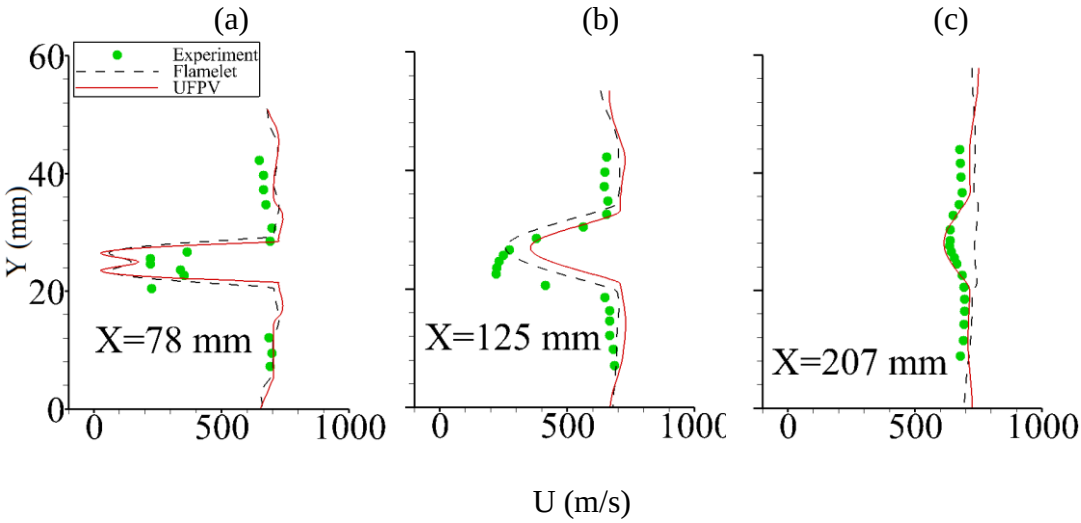

Figure 5.14 The X-velocity profiles at the cross section (a) X = 78 mm, (b) X = 125 mm and (c) X = 207 mm for the reacting flow, obtained from the experiments [178] and the RANS simulations.

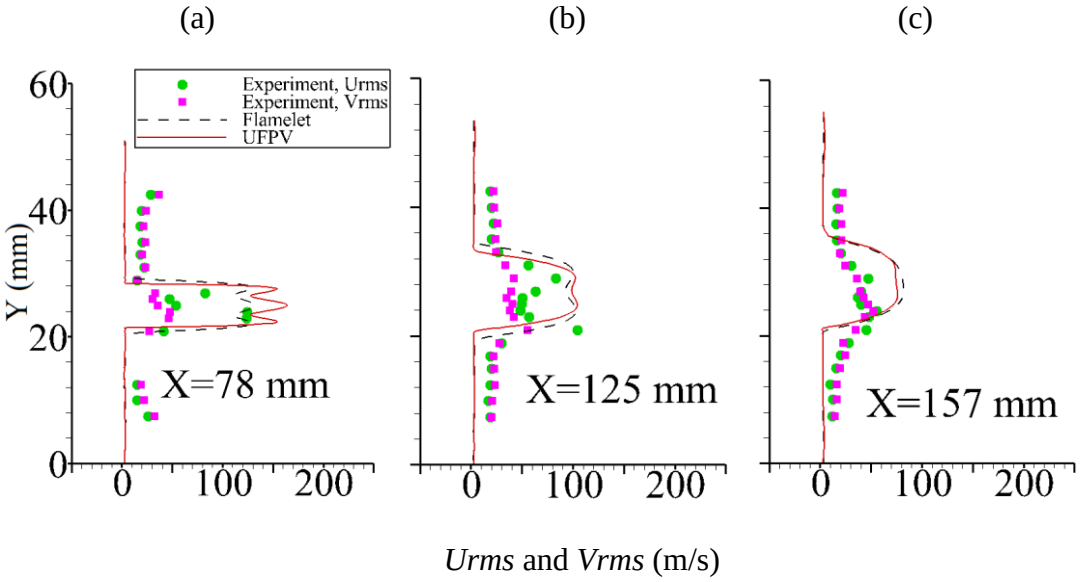

Figure 5.15 The velocity fluctuation profiles at the cross section (a) X = 78 mm, (b) X = 125 mm and (c) X = 157 mm for the reacting flow, obtained from the experiments [178] and the RANS simulations.

Figures 5.14 and 5.15 show the X-velocity and the velocity fluctuation profiles at different cross sections obtained from the modelling and the experimental data [178]. We observe that the X-velocity profiles at X = 78 mm are in double-peak shape and this is similar with the temperature profile shown in Figure 5.13. Both at the location of X = 78 mm and 125 mm, the profiles obtained from the UFPV modelling and the flamelet modelling have a similar shape and match well with the experimental data. However, at the cross section X = 233 mm, the UFPV model predicts a lower velocity than does the flamelet model and it matches better with the experimental data.

From Figure 5.15, we observe that the velocity fluctuation profiles obtained from the simulations at X = 78 mm have three peaks. Corresponding to the X-velocity profiles in Figure 5.14, it is observed that the upper and lower peaks show the effects of the compressible reacting mixing layer and the high-speed hydrogen jet contributes to the middle peak of the X-velocity profile. At the downstream

location X = 125 mm, the upper and lower mixing layers develop but the effects of the hydrogen jet vanishes, therefore there are only two peaks left in all the simulated profiles and in the experimental data. At X = 157 mm, only one peak is predicted by the flamelet model but the UFPV model predicts two and matches better with the experimental data. Further, from Figures 5.13, 5.14 and 5.15, we observe that the UFPV model predicts a narrower shape of the temperature, velocity and velocity fluctuation profiles in the central part of the combustor at the locations of X = 78 mm and 125 mm than does the flamelet model. This means that the UFPV model predicts a narrower reaction zone and less intense combustion in the region near the strut. This observation is also present in the contours of the temperature and the OH mass fraction in Figure 5.11.

In summary, the reacting flow case investigated here shows that both the flamelet model and the UFPV model are capable of predicting the supersonic combustion in the DLR scramjet engine. Also, it is indicated that the different combustion modeling approaches have an impact on the predicted flame location and shape. In contrast to the flamelet model, the UFPV model predicts a shorter reacting zone, a less intense flame, a lower temperature peak, a thinner reacting layer and a slightly narrower flame zone in the region near the strut. Comparing the modelling results with the experimental data, it is found that the UFPV model appears to give improved predictions of the peak temperatures and the flame zone near to the strut base. However, both the flamelet and the UFPV models predict a higher temperature in the region away from the strut than does the experimental data. Clearly, further investigations on the modelling of this high speed and extremely unsteady reacting flows in the scramjet combustor are necessary in terms of both the handling of the mixing and the chemical kinetics of the combustion. Unsteady and more accurate solution methods, such as large eddy simulations, may provide good prediction of the filtered and subgrid variables, as well as their time evolution to the

UFPV modelling [115], and therefore may be expected to give improved predictions of the supersonic flame.

5.4. LES modelling of the DLR case

In this section, large eddy simulations of non-reacting and reacting flows are performed to model the DLR case so as to validate the UFPV combustion model, as well as to understand the mixing, flame-holding and combustion characteristics of the gaseous fuel injected from the base of a strut.

5.4.1. Computational grid and boundary conditions

The LES calculations of the supersonic combustor have been performed in a 3D computational domain. Three injections holes are taken from the original 15 holes in the experimental rig, and the computational domain has a length of 7.2 mm in the spanwise direction. The plane at the far side in the spanwise direction is Z = 0 mm. Figure 5.16 shows the strut rigs which are used in the experiments in [174] and the large eddy simulations in the present study. It is clear that, in the LES, the geometry fidelity is achieved and the computational cost is reduced. More details of the configuration can be found in §5.2.

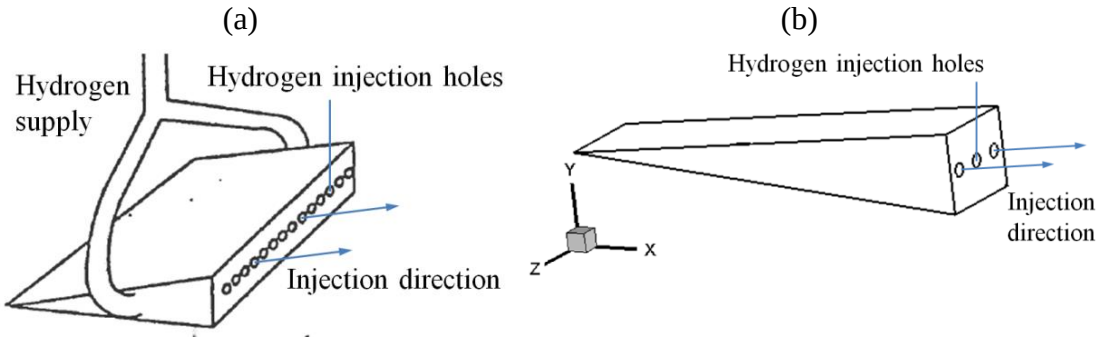

Figure 5.16 Schematic diagrams of (a) the strut rigs employed in the experiments [174] and (b) the large eddy simulations in the present study.

The computational grid is shown in Figure 5.17, in which X, Y and Z represent the streamwise, transverse and spanwise directions, respectively. The computational domain is divided into 24 blocks so as to run in parallel. The multiblock structured grid has 5,840,244 nodes and 5,708,604 cells in total, and is condensed in the vicinity of the inlet, the strut, the wake flow region and the shear layer region. The value of the y+ of the first cell near the strut wall is about 1. In general, LES requires a sufficient resolution [206]. However, without a prior knowledge of the characteristics of the flow, it is difficult to ascertain whether the grid is sufficient or not. It was pointed out by Speziale [207] that the grid independence cannot really exist in LES. This is because the LES will lose its efficiency if the grid is extremely fine and it tends to DNS as the grid resolution tends to the Kolmogorov scales. For the LES of the DLR case, Berglund et al. [186] employed the same three-hole configuration and two computational grids, which have 3.2 and 6.4 million cells, respectively. It is revealed that there are no significant differences between the results obtained for the first and second order statistical moments on the two meshes. Therefore, the grid, which has 5,708,604 cells and is employed in the present study, is sufficient to resolve the important large flow structures in the DLR case.

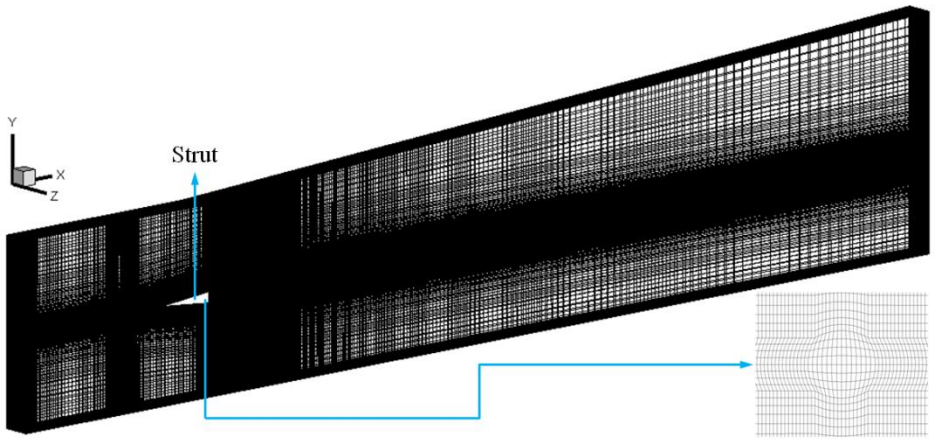

Figure 5.17 Computational domain and the distribution of the grid of the DLR case. The small figure in the corner shows the grids near one of the three hydrogen injection holes.

Strictly speaking, the air inflow and the hydrogen jet are turbulent flows. In the regime of LES, several methods have been develop to model the inflow turbulence [127,208], and there are several techniques relevant to the inflow turbulence problems that have been developed and suggested: the random fluctuation method, the matching database method, and the recycling and rescaling method [209]. However, these techniques did not show an identical performance and they all have advantages and disadvantages when used to generate turbulent inflow conditions [209,208]. Further, the inflow turbulence is not provided by the experimental data. Also, the techniques relevant to the inflow turbulence problems are out of the scope of this research. Therefore, when performing the large eddy simulations in this study, the turbulence of the inflow is neglected. Thus, the Dirichlet boundary conditions are used for all the variables at the air stream inlet and hydrogen jet inlet and the parameters are given by Table 5.1. All the variable values at the outlet are extrapolated from the interior predictions and therefore a pressure outlet boundary condition is applied. Further, adopting the recommendation in §5.3.3, the slip condition is employed on the upper and lower combustor walls and the no-slip condition is employed on the strut walls. Finally, the side surfaces in the spanwise direction are assumed to be periodic boundary conditions.

5.4.2. Non-reacting flows

In this section, the non-reacting flows are simulated in order to understand the characteristics of the supersonic flow and the mixing between the hydrogen and the air in a strut-based scramjet combustor, and to provide an initial condition for the calculations of the further reacting flows. Detailed experimental data are available for analysing the flow and mixing processes and validating the flow and mixing models.

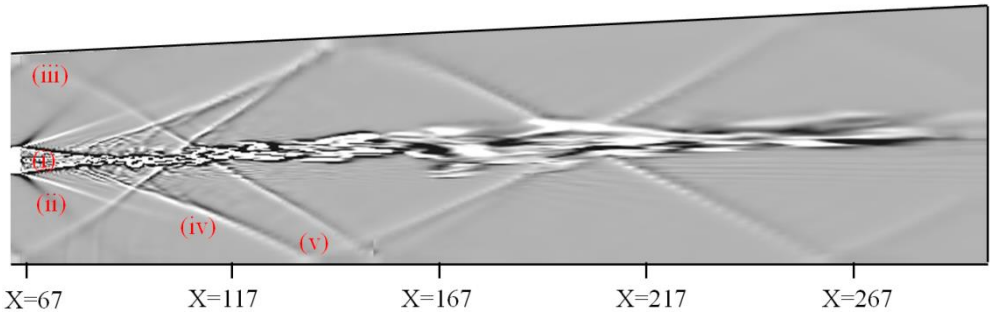

Figure 5.18 The numerical shadowgraph image for the non-reacting flow obtained from the LES.

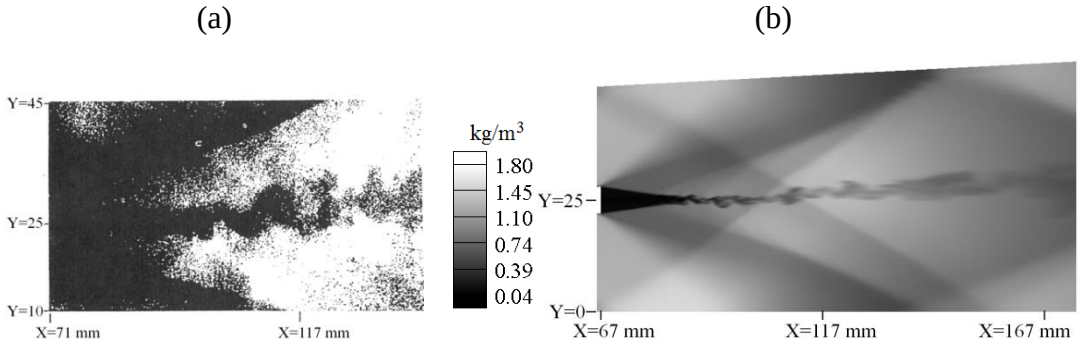

Figure 5.19 (a) The Rayleigh scattering image obtained from the experimental investigation [174] and (b) the density contours at the plane Z = 3.6 mm obtained from the LES of the non-reacting flow.

Figure 5.18 shows the numerical shadowgraph image obtained from the LES. Comparing the numerical shadow images in Figure 5.18 with the experimental shadowgraph in Figure 5.5, we observe that the simulation successfully predicts the complex flow structure: (i) the hydrogen injection behind the strut base, (ii) the expansion waves near the strut base, (iii) the reflection of the shock waves generated from the leading edge of the strut, (iv) the recompression shock waves and (v) the reflection of the recompression shock waves. Figure 5.19 shows a Rayleigh scattering image and the density contours at the central plane, i.e. Z = 3.6 mm, obtained from the experiments [174] and the LES, respectively. The recompression

shock waves are clearly visible due to the density jump along the shocks. Downstream to X ≈ 100 mm, the contour of the flowfield becomes more and more curved with periodically structures due to Kelvin-Helmholtz instabilities and this is not predicted by the RANS modelling in §5.3.3. Further, the large scale vortices result in a more effective mixing than by the diffusion controlled process and the LES predictions are in good agreement with the experimental observations.

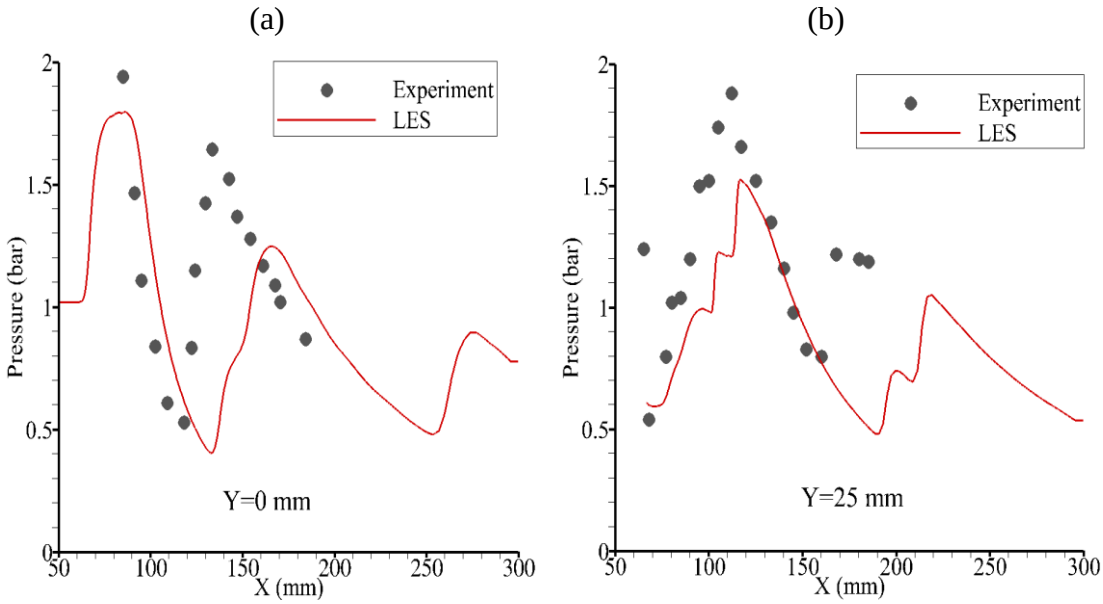

Figure 5.20 The profiles of the time-averaged pressure at (a) the lower wall (Y = 0 mm) and (b) the central line (Y = 25 mm) of the combustor for the non-reacting flow, obtained from the experiments [178] and the LES.

Figure 5.20 shows the distribution of the time-averaged pressure along the bottom wall and the central line of the combustor for the non-reacting flow. The sampled time period is 3ΔT, where ΔT is the passing through time and defined as $L_{combustor}/\tilde{u}$, where $L_{combustor}$ and $\tilde{u}$ are the length of the combustor and the mean flow velocity at the air inlet, respectively. It should be noted that, without special declaration, the sampled time period for all the simulations in this chapter is 3ΔT. Due to the presence of the shock waves, the expansion waves and the recirculation shown in Figure 5.18, the pressure in the combustor significantly changes and this is

predicted by the LES. However, in Figure 5.20, the differences between the simulation results and the experimental data are visible. It is clear that there is a mismatch of the location between the profiles obtained from the LES and the experiment and it becomes worse downstream. Also, this mismatch is shown in the RANS calculations. As has been discussed in §5.3.3, the assumption of a slip wall condition slightly contributes to this mismatch. Therefore, the discrepancy between the LES results and experimental data could be mainly due to the complex shocks that are not present in the simulations. Another possible reason is that the shock-boundary layer interaction and the reflection of the shock are not perfectly predicted.

It should be noted that the modelling of shock-boundary layer interaction is a complex research topic and has attracted the interest of many researchers [210]. Also, the modelling of shock-boundary layer interactions requires a very dense grid near the wall [211] and therefore this increases the computational cost. Further, as discussed in §5.3.3, §5.3.4 and here, there is no mixing or combustion in the region where the shock-boundary layer interaction takes place. Therefore, this interaction has no straightforward effects on the mixing and combustion. Although the shock-boundary layer interaction and the reflection of the shock may not be perfectly predicted, the effects on the mixing and combustion in the combustor are minor and the simulation results in the present study are reliable.

Figure 5.21 shows the profiles of the time-averaged X-velocity at X = 78 mm, 125 mm and 233 mm along with the experimental data. It should be noted that, without special declaration, the parameters of the flows was measured at the central plane and the corresponding parameters at the plane Z = 3.6 mm in the simulation are employed to compare with the experimental data. At the cross section X = 78 mm, a strong reverse velocity may be observed on each side of the hydrogen jet and the simulation results are in reasonable agreement with the rather sparse experimental data. Previous LES calculations by Berglund and Fureby [186] show

very similar profiles as do our predictions, at this cross section. Comparing Figures 5.21 and 5.7, we observe that the LES predicts a stronger penetration of the hydrogen jet than does the RANS and the latter fails to predict the strong reverse velocity at X = 78 mm. This difference could produce different characteristics in the mixing between the hydrogen and the air, as well as in the combustion of the mixture. Further downstream, at the cross sections X = 125 mm and X = 233 mm, the predicted X-velocity profiles is narrower than the experimental profiles. It should be noted that the previous RANS results in §5.3.3 show very similar profiles as the LES time-averaged results presented here.

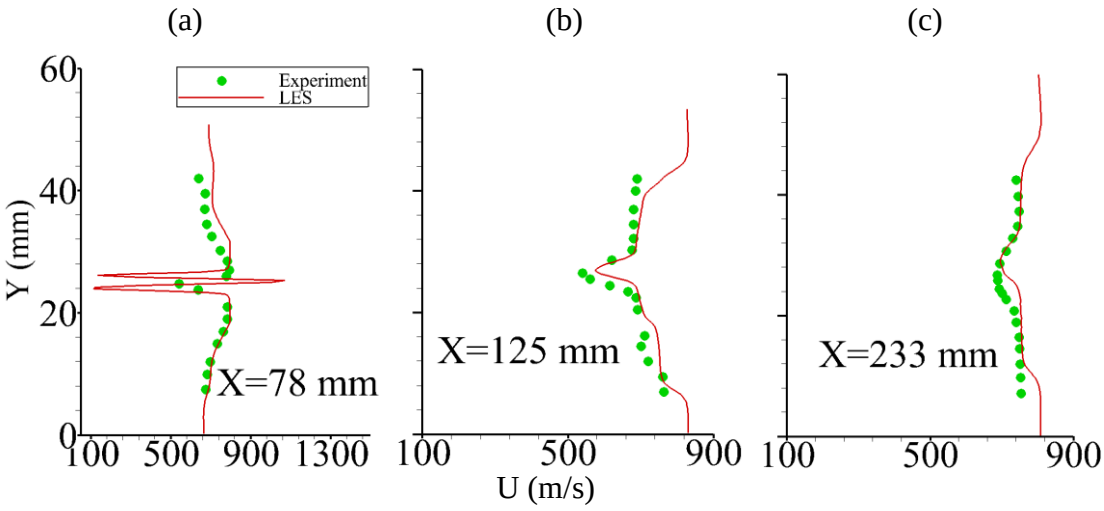

Figure 5.21 The time-averaged X-velocity profiles at the cross sections (a) X = 78 mm, (b) X = 125 mm and (c) X = 233 mm for the non-reacting flow, obtained from the experiments [178] and the LES.

In summary, the LES is capable of predicting the non-reacting flow in the strut-based combustor with reasonable accuracy. Also, the time-averaged LES results show very similar profiles to the RANS predictions. However, the LES calculations provide more instantaneous characteristics of the flow, such as the vortices and the motion of the large scale structures. Further, the large scale structure could have a significant effect on the local convection, mixing and strain of

the fluid. Therefore, the UFPV model, which takes the local extinction and re-ignition effects into account, will benefit from an investigation using the large eddy simulations.

5.4.3. Reacting flows

In this section, the reacting flows are simulated in order to validate the UFPV combustion model, which is built into the in-house code, and also assist in the understanding of the characteristics of the supersonic reacting flow in a strut-based scramjet combustor. Detailed experimental data are available for analysing the reacting flow and validate the performance of the UFPV combustion model under the regime of LES.

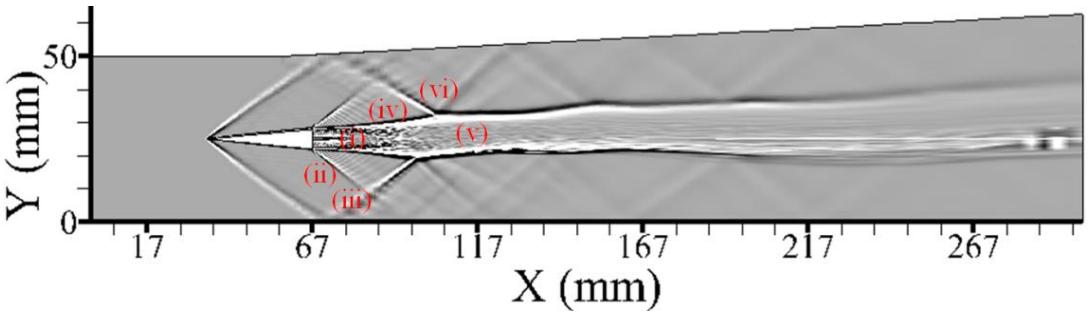

Figure 5.22 The time-averaged numerical shadowgraph image for the reacting flow obtained from the LES UFPV modelling.

Figure 5.22 shows the time-averaged numerical shadowgraph image for the reacting flow obtained from the LES UFPV modelling. From Figure 5.22, we can identify: (i) the hydrogen jet, (ii) the expansion wave, (iii) the reflection of the leading shock wave, (iv) the shear layer, (v) the combustion region behind the strut, and (vi) the reflection of the reflected shock wave at the shear layer. It is clear that the shock system in the reacting flow is less complex than that in the non-reacting flow. This is because the recompression shock and the expansion wave vanish and

only the shock waves that are produced at the leading edge, i.e. the leading shocks, are reflected between the combustor wall and the combustion region. As the reflected leading shocks are reflected as an expansion wave by the shear layer, see (vi) in Figure 5.22, the shocks cannot propagate through the combustion zone, which is an indication of a subsonic region. The reflection (vi) is also visible in Figures 5.23 and 5.24.

Figure 5.23 shows a Rayleigh-scattering image for the flow section shortly downstream of the strut and a detailed image of the shock-shear layer intersection point A [174]. Figure 5.24 illustrates the instantaneous density contours at the central plane when employing the LES. From Figures 5.23 and 5.24, the combustion is visible in the middle of the images with low density and this is due to the heat release and the high temperature in this vicinity. However, at the interface of the combustion zone and the air stream, i.e. the shear layer, the density gradient is large. Also, the shock-shear layer interaction is observed in the experiments and is predicted by the LES, see Figures 5.23 and 5.24, respectively. It is clear that the shock wave and the following expension wave cause the formation of large scale structures. These large scale structures could promote the convection activity and enhance the mixing of the reactants. On comparing Figures 5.10, 5.22, 5.23 and 5.24, on the one hand, the structure of the flow field predicted by the LES UFPV model appears to agree well with those illustrated in the experimental measurements. On the other hand, there is a mismatch in the location of (vi) and the following large scale structures, see Figures 5.23 and 5.24. This is mainly due to the irregular shock waves and the inaccuracy in the prediction of the shock-boundary layer interaction and the shock reflection, and this has been discussed in §5.3.3 and §5.4.2.

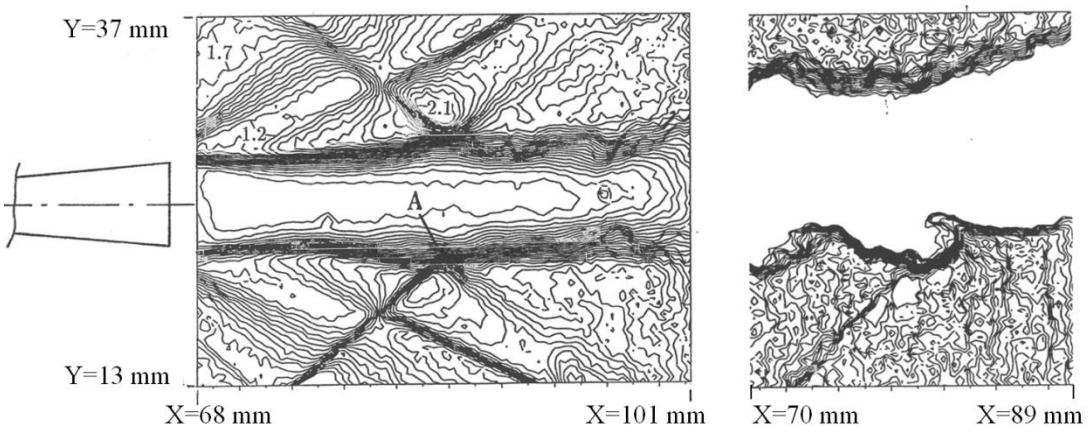

Figure 5.23 Rayleigh-scattering iso-intensity lines (left figure, contour level step ρ_{air} = 0.05 kg/m^3, integrated over 20 laser shots) and Rayleigh-scatteriing image near A (right figure, single-shot, 20 ns), obtained from [174].

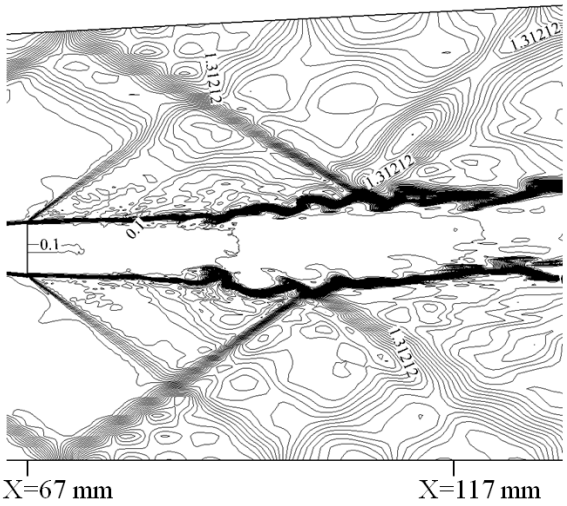

Figure 5.24 The instantaneous density contours at the plane Z = 3.6 mm (contour level step ρ_{air} = 0.02 kg/m^3) obtained from the LES UFPV modelling.

A single-shot OH-laser-induced-predissociation-fluorescence (LIPF) of the combustion region is presented in Figure 5.25 as obtained by Waidmann et al. [174]. The LIPF images are composed from different test runs and axial positions. It should be noted that the hydrogen mass flow rate is 4 g/s in the experiments when taking these LIPF images. Although these images are not exactly the same case as in our simulation case, they still qualitatively illustrate the level of the OH concentration

throughout the flame and give an impression of the larege scale strutures. Figures 5.26 and 5.27 show the contours of the instantaneous OH mass fraction and the temperature at different locations for the reacting flow obtained from the LES UFPV modelling. It is clear that the flame is in 3-dimentional shape.

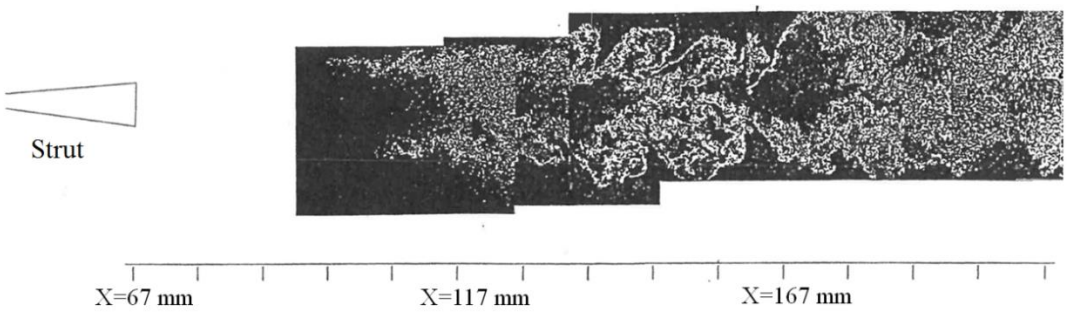

Figure 5.25 The OH-LIPF images (the exposure time is 20 ns, and the mass flow rates of the air and the hydrogen are 1.5 kg/s and 4 g/s, respectively) for the reacting flow obtained from the experiments [174].

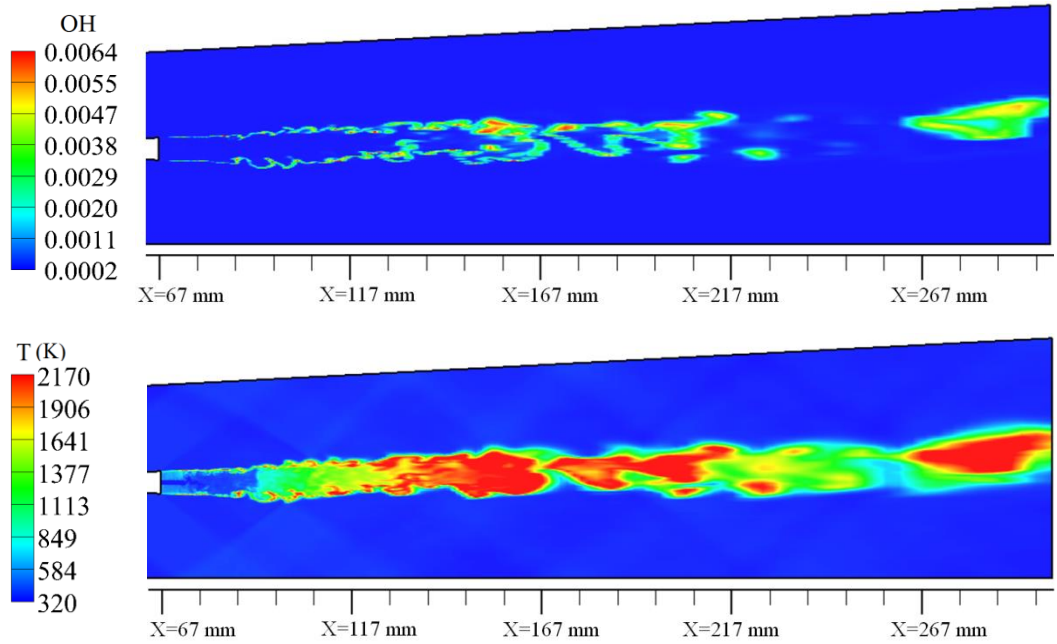

Figure 5.26 The contours of the instantaneous OH mass fraction (top figure) and temperature (bottom figure) at the plane of Z = 3.6 mm for the reacting flow obtained from the LES UFPV modelling.

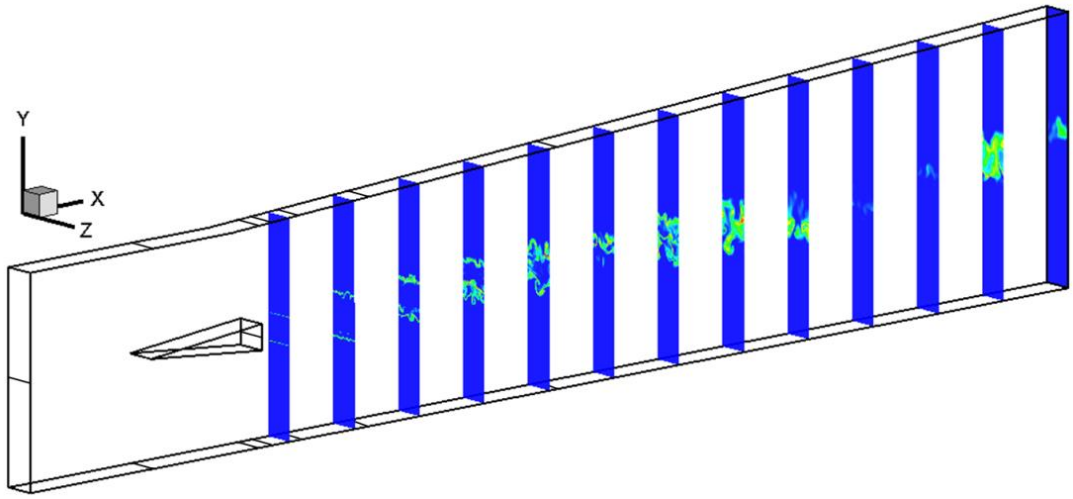

Figure 5.27 The contours of the instantaneous OH mass fraction at different locations (first plane: X = 75 mm, step size ΔX = 18.75 mm) for the reacting flow obtained from the LES UFPV modelling.

Also, from Figures 5.26 and 5.27, we observe that the shear layers, i.e. the interfaces of the air stream and the combustion zone at both sides of the flame, is ignitied shortly behind the strut and the reacting shear layer rolls up to form large scale vortices which are not stable while moving downstream and interacting with other vortices and the surrounding fluid, such as the breaking down into smaller size vortices and the coalescing of the neighbouring vortices. These restructured vortices could engulf fresh air from the supersonic outer flow region and also accelerate the molecular mixing of the reactants.

Further, as shown in Figure 5.26, a high OH and temperature intensity is observed at the troughs and crests of the wrinkled shear layer and this means that the flame has a local thickness that is dependent upon the vortex and local chemical kinetics, and therefore the UFPV model is shown to be able of predicting the local turbulence-chemistry interactions in this supersonic flame. On the other hand, the OH in the experimental observation appears to spread wider than the predictions. One possible reason is that the OH-LIPF images were obtained with the hydrgoen

mass flow rate of 4 g/s but it is 1.5 g/s in the simulation. Therefore, the combustion is more intense in the experiments during which more OH radicals were preduced and observed. Another possible reason for the underprediction of the spreading area of the OH radicals is that the inflow turbulence is not modelled in the simulations but, of course, it exists in the experiments and this enhances the mixing and the combustion of the reactants.

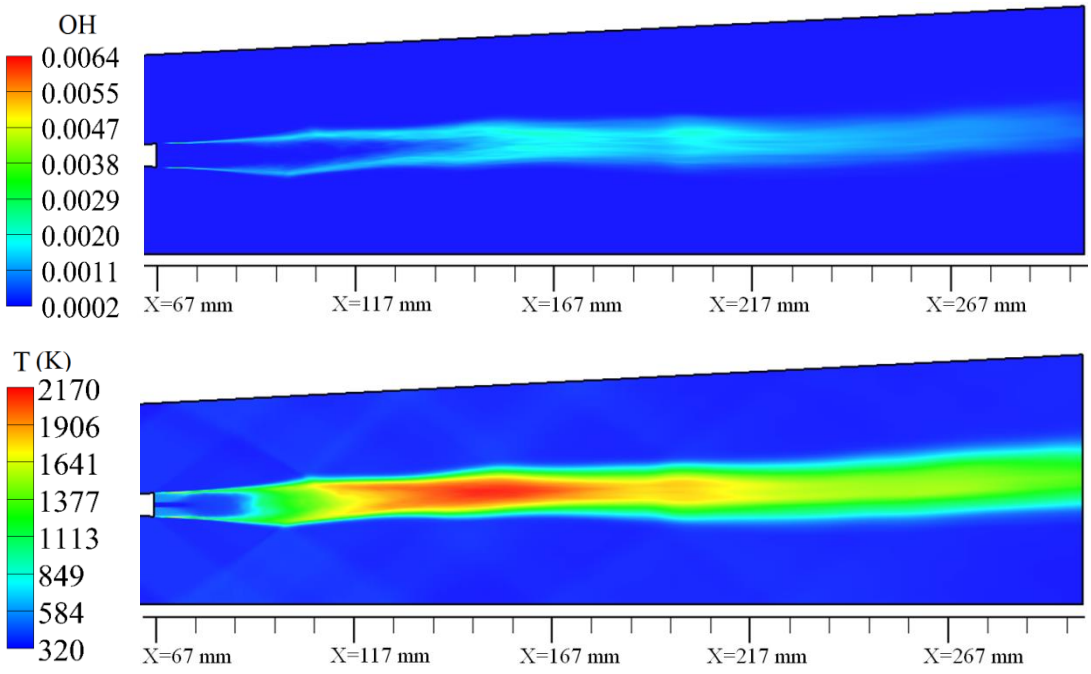

Figure 5.28 The contours of the time-averaged OH mass fraction (top figure) and temperature (bottom figure) at the plane Z = 3.6 mm for the reacting flow obtained from the LES UFPV modelling.

Figure 5.28 shows the contours of the time-averaged OH mass fraction and temperature at the central plane for the reacting flow. On comparing Figures 5.11 and 5.28, we observe that the overall structure and behaviour of the flames are very similar. However, the LES predicts a less intense distribution of the OH radicals and a shorter high temperature region than does the RANS, although the same UFPV combustion model is employed in both investigations. As in §5.3.4, the temperature is over predicted by the RANS UFPV modelling, and therefore it is expected to

predict a less intense combustion and lower temperature by the LES calculations here and this agrees better with the experimental data.

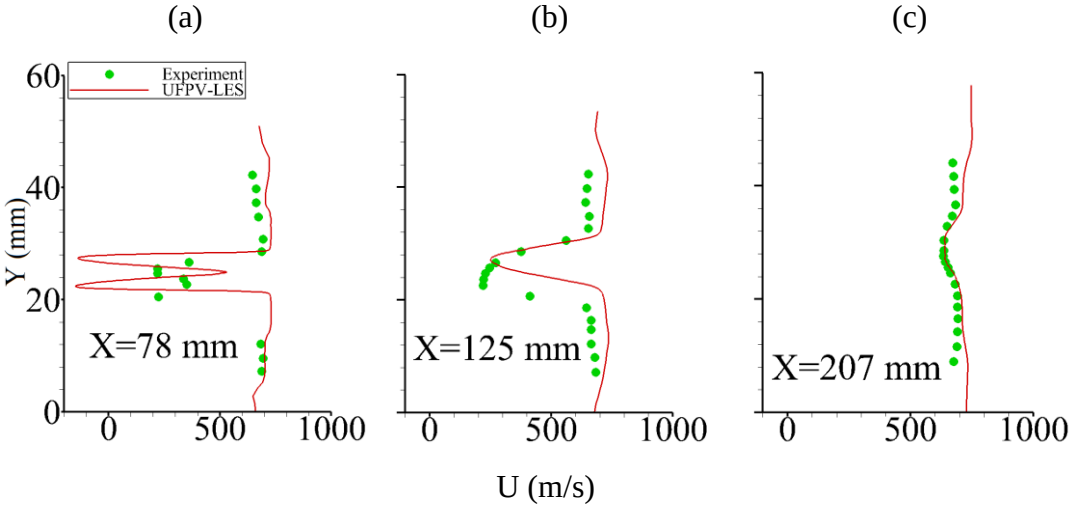

Figure 5.29 The time-averaged X-velocity profiles at the cross sections (a) X = 78 mm, (b) X = 125 mm and (c) X = 207 mm for the reacting flow, obtained from the experiments [178] and the LES UFPV modelling.

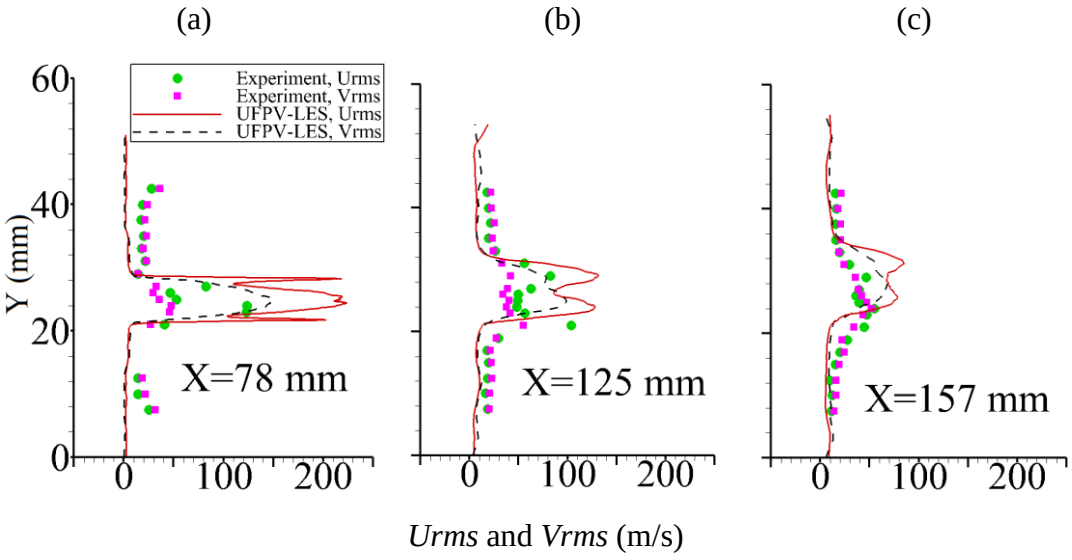

Figure 5.30 The velocity fluctuation profiles at the cross sections (a) X = 78 mm, (b) X = 125 mm and (c) X = 157 mm for the reacting case, obtained from the experiments [178] and the LES UFPV modelling.

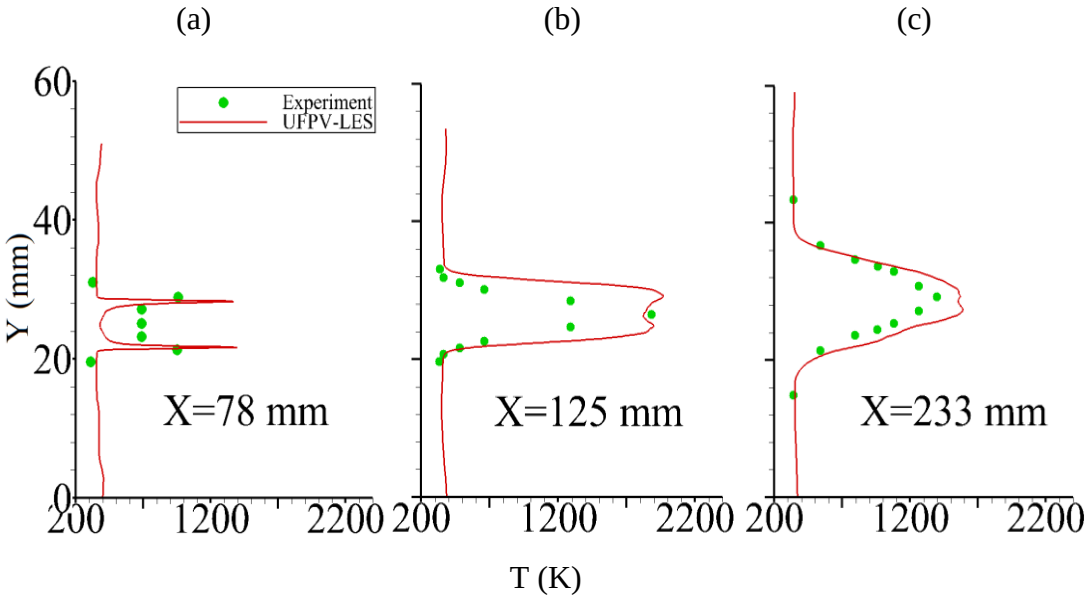

Figure 5.31 The time-averaged temperature profiles at the cross sections (a) X = 78 mm, (b) X = 125 mm and (c) X = 233 mm for the reacting flow, obtained from the experiments [178] and the LES UFPV modelling.

Figures 5.29, 5.30 and 5.31 provide a quantitative comparison of the experimental data and the LES UFPV modelling at different cross sections of the combustor. In Figure 5.29, a strong reverse velocity is observed at X = 78 mm on each side of the hydrogen jet and reasonable agreement with the rather sparse experimental data is found. However, the RANS in §5.3.4 fails to predict these reverse flows in this region.

As shown in Figure 5.29(b), the predicted X-velocity profile at X = 125 mm is narrower than the experimental X-velocity profile. Previous RANS calculations, presented in §5.3.4, and the LES predictions of Berglund and Fureby [186] show very similar profiles as presented here. Also, in §5.4.2, the LES for the non-reacting flows predicts a narrower velocity profile at X = 125 and 233 mm. At present the origin of the discrepancy between the predictions and the experimental data is unclear. However, one possible reason is the presence of the inflow turbulence and the irregular shock waves in the experiments contributes to the development of the

shear layer and therefore the wider low-speed flow region in the centre of the combustor. In the reacting flows, the combustion significantly increases the fluctuations in the velocities and the turbulence intensity, see Figures 5.9, 5.15 and 5.30; therefore the absence of the inflow turbulence and the irregular shock waves in the simulations has relatively less impact on the development of the reacting shear layer than of the non-reacting shear layer. Thus, further downstream as see in Figure 5.29(c), good agreement between the predicted and measured profiles is again obtained in the reacting flow case. Also, better agreement between the simulations and the experimental data is observed for the reacting case than for the non-reacting case.

Figure 5.30 shows the velocity fluctuation profiles at different cross sections for the reacting case and we observe that there is a satisfactory agreement between the experimental data and the LES results. Also, both the experimental data and the LES results show that the fluctuations in the X component of the velocity are stronger than the fluctuations in the Y component of the velocity. However, this difference becomes less, along with the decreasing of the velocity fluctuations, downstream and this is mainly because of the breakdown of the vortices.

Figure 5.31 shows the spatial evolution of the temperature field with downstream distance. At X = 78 mm, a good agreement between the experimental data and the LES UFPV modelling results is achieved at the shear layers. However, both the RANS (in §5.3.4) and the LES (in this section) predictions show a lower temperature in the strut wake where the hydrogen is injected. This is likely to be due to the assumption of unity Lewis number, which is the ratio of the thermal diffusivity and the molecular diffusivity, and is important in determining the relationship between mass and heat transfer coefficients [212]. At X = 125 mm, a double peak profile is obtained from the LES and this is because the combustion here is affected by the cold hydrogen jet, also shown in Figure 5.28. Further

downstream, the effects of the cold hydrogen jet vanish and good agreement is again achieved. On comparing Figures 5.31 and 5.13, it is clear that the LES predicts a lower temperature than do the RANS calculations and a better agreement, especially in the downstream region, is achieved by the LES UFPV modelling.

It should be noted that there is no radiation source term in the energy equations in (3.1) and (3.18), and this means that the radiation effects are not considered in the present study. Normally, the radiation source term can be separated from the filtered enthalpy equations in (3.1) and (3.18) and therefore can be separately modelled. However, simple radiation models bring inaccuracies into the combustion simulation, while the advanced radiation models are quite complex and time-consuming. At the beginning of the development of a combustion model, researchers normally neglect the radiation effects in order to reduce the complexity of implementing the combustion model [150]. Particularly, when developing and testing the combustion model for supersonic flames, the radiation effects are always neglected at the beginning [213]. After the combustion model has been implemented and validated, the radiation effects could be introduced into the combustion modelling [149]. In the present study, although the temperature is slightly overpredicted, which could be due to the absence of a radiation model, however, other flow characteristics, e.g. the velocity distribution and the structure of the flowfield, are well predicted by the LES flamelet and UFPV modelling. Therefore, we conclude that it is reasonable and feasible to neglect the radiation effects in this study in order to reduce the complexity and calculating time when developing and testing the combustion models and also the simulation results are reliable.

In summary, the LES UPFV modelling is capable of predicting the reacting flow in the strut-based combustor with reasonable qualitative and quantitative agreement with the experimental data. In the meantime, the time-averaged LES results show very similar behaviours to the RANS predictions. However, some

parameters, e.g. the distribution of the temperature and velocity, are better predicted by the LES UPFV modelling on comparison with the experimental data. Further, the LES calculations provide more instantaneous characteristics of the reacting flow, such as the interaction between the shock and the large scale structures, the interaction of the flame and the vortices and the evolution of the reacting shear layer. Further, on comparing with the RANS calculations, better agreement with the experimental data is achieved by the LES UFPV modelling, and therefore the UFPV model which is built into the hybrid RANS/LES model is validated to be a promising approach to predicting supersonic flames.

5.5. Closure

In this chapter, RANS and LES investigations of non-reacting and reacting flows are performed to model the DLR case so as to validate the flamelet and the UFPV combustion models, as well as to enhance our understanding of the mixing and combustion characteristics of the gaseous fuel injected from the base of a strut which is installed in the centre of the supersonic combustor.

Firstly, the RANS calculations of the non-reacting flow are performed using the commercial CFD code FLUENT in order to study the effects of the grid sensitivity, the geometry fidelity and the assumptions of the solid wall boundary conditions. Several conclusions are obtained from the simulations, namely,

(i) The RANS modelling of the non-reacting flows, which are based on the 2D configuration, are unreliable and therefore a 3D configuration is recommended for the RANS calculation.

(ii) The slip-wall assumptions of the strut walls and the combustor walls have different effects on the flow and mixing in the combustor. The assumption of no-slip-strut and slip-combustor walls is recommended.

Secondly, the RANS modelling of the reacting flows is performed with the flamelet and the UFPV models which are built into the in-house code. The results show that both the flamelet model and the UFPV model are capable of predicting the supersonic combustion in the DLR scramjet engine. However, different combustion modeling approaches have an impact on the predicted flame location and shape, and the UFPV model appears to give improved predictions and is recommended for the modelling of supersonic flames.

Thirdly, the LES is performed to simulate the non-reacting flow in the DLR case. It is shown that the time-averaged LES results have very similar profiles to those obtained from the RANS predictions. However, the LES calculations provide more instantaneous characteristics of the flow, such as the vortices and the motion of the large scale structures.

Finally, the LES modelling is performed to simulate the reacting flows in the DLR case. Overall, it is revealed that the UFPV model under the regime of LES gives better predictions of the time-averaged flow field than under the regime of RANS. In addition to the time-averaged characteristics of the flowfield, the LES UFPV modelling provides numerous instantaneous characteristics of the reacting flow, such as the interaction between the shock and the large scale structures, the interaction of the flame and vortices and the evolution of the reacting shear layer. Also, there is a reasonable qualitative and quantitative agreement with the experimental data and therefore the UFPV model, which is built into the hybrid RANS/LES code, is validated to be a promising approach to predict supersonic flames.

Chapter 6
Modelling of supersonic combustion with a cavity flame holder

6.1. Introduction

The use of a strut strategy is able to achieve different fuel-injection methods, enhance the mixing between the fuel and the high speed air flow and hold the flame in supersonic flows in a supersonic combustor. However, the installed strut is always exposed to the high speed flows and this produces relatively high stagnation pressure losses. Another promising flame strategy is installing cavities on the wall of the supersonic combustor. It is an integrated fuel injection/flame-holding approach and has been shown to be effective in stabilizing the flame without excessively decreasing the total pressure [214].

The cavities have a large impact on the surrounding flows. However, flow over cavities has been attracting the interest of many researchers in aerodynamics and aeroacoustics and now it has been extensively studied for decades, starting as early as the 1940's [215]. Lawson and Barakos [215] have presented the rich physics of cavity flows and the attempts to understand, simulate and control this unsteady turbulent flow. Supersonic flows over cavities are generally categorized into three regimes depending primarily on the length-to-depth ratio of the cavities: open, closed and transitional cavity flows. Open cavity flows occur for deep cavities which generally have length-to-depth ratios no more than 7. Closed cavity flows occur for shallow cavities which have length-to-depth ratios of more than 13. Transitional cavity flows are between the open and closed flow regimes [215]. Figure 6.1 illustrates the closed and open cavity flows for supersonic speeds.

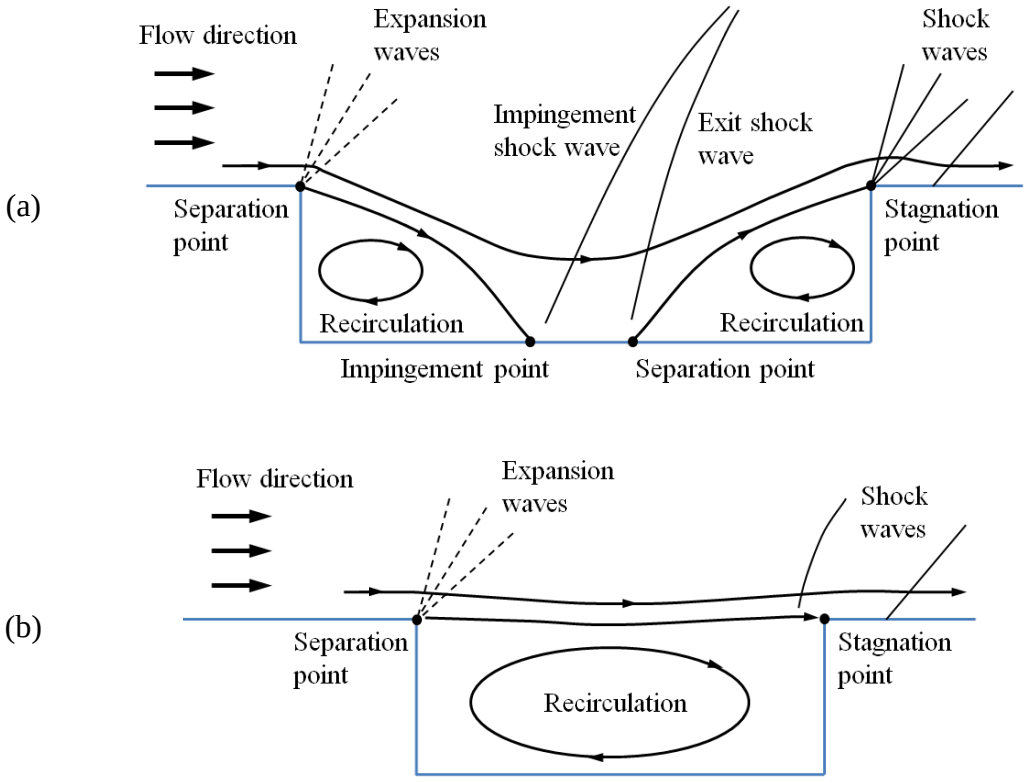

Figure 6.1 Schematic diagram of the streamlines for (a) closed and (b) open cavity supersonic flows.

A cavity was used for flame holding for the first time in a joint Russian/French dual-mode scramjet flight-test [216] in 1993. The recirculating flows in the cavity could enhance the mixing between the air and fuel, increase the residence time of the mixture, and be ignited and serve as a continuous ignition source. Ben-Yakar and Hanson [217] provided a review of cavities in supersonic flows and their use for flame holding in supersonic combustors before 2001. Further, Sun [11], Fan [154] and Wang [218] reviewed recent research efforts in the scramjet community on cavity flame holders. It is clear that cavity flame holding strategy has become even more attractive and has received more and more attention during recent years [219]. Although characteristics of the supersonic combustion in cavity-based combustors are investigated, there are still many open questions regarding the mechanisms of

ignition, flame holding and flame propagation under various injection conditions [220]. Also, as cavity flame holder plays a very important role in the scramjet research area, it is necessary to understand the characteristics of the supersonic combustion a cavity-based combustor and validate the combustion model using a cavity-based configuration.

Fan [154] performed experimental studies on a laboratory supersonic combustor with cavity flame holders and several measurements were made, such as high-speed photography, OH-spontaneous emission photography and OH-PLIF, which gave a visualized structure of the flame. In this chapter, large eddy simulations of non-reacting and reacting flows are performed to model the Fan cavity case so as to validate the UFPV combustion model, as well as to understand the mixing, flame-holding and combustion characteristics of the gaseous fuel injected upstream of the cavity.

6.2. Experimental configuration

The experimental facilities and installation as used by Fan were described in detail in [154]. The cavity was installed on the bottom wall of the supersonic combustor, see Figure 6.2. The heated air flows from the left to right hand side with a mass flow rate of 1 kg/s. In order to measure the flow, in the experiments, the side and the upper walls are made from quartz glass. The length, width and height of the combustor are 380 mm, 50 mm and 40 mm, respectively. Figure 6.3 shows a schematic of the cavity configuration. In the present study, L, D, S and θ are 64 mm, 8 mm, 10 mm and 45°, respectively, and the diameter of the hydrogen injection hole is 2 mm. Further, the inflow and injection conditions are given in Tables 6.1 and 6.2, respectively.

Table 6.1 Heated air inflow boundary conditions [154].

Mass flow rate (g/s)	Mach number	Temperature (K)	Pressure (10^5 Pa)	$\tilde{Y}_{O_2}$	$\tilde{Y}_{H_2O}$	$\tilde{Y}_{N_2}$	$\tilde{Y}_{others}$
1000.0	2.52	753.8	0.862	0.232	0.081	0.684	0.003

Table 6.2 Hydrogen injection boundary conditions [154].

Mass flow rate(g/s)	Mach number	Stagnation pressure (10^5 Pa)	Stagnation temperature (K)	Equivalence ratio
2.826	1.0	15.0	290	0.097

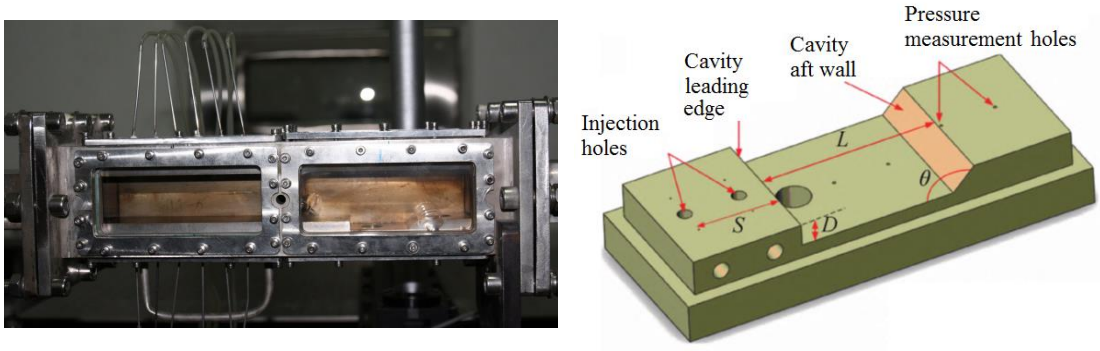

Figure 6.2 Photograph of the supersonic combustor and schematic of the cavity configuration [154]. The symbols *L*, *D* and θ denote the length, the depth and the aft wall angle of the cavity, respectively, and *S* is the distance between the injection hole and the cavity leading edge.

6.3. Computational setup for the LES

The LES calculations of the supersonic combustor have been performed in a 3D computational domain. The length of the computational domain is 160 mm, with

a 22 mm × 40 mm inlet, so that the cavity is also of width 22 mm. The computational domain is shorter and narrower than the laboratory combustor, however the geometry fidelity is achieved and the computational cost is reduced. The distance between the inlet and the cavity leading edge is 40 mm and the centre of the hydrogen injection hole is 10 mm upstream from the cavity leading edge and the diameter is 2mm. The computational domain is divided into 16 blocks so as to run in parallel and each of them has 70 × 60 × 80 nodes. Further, the multiblock structured grid has about 5.2 million cells and 5.3 million nodes in total. The grid cells are condensed near the cavity leading and trailing edges, the solid walls, the shear layer region and the hydrogen jet region and the y+ of the first cell near the strut wall is about 1.

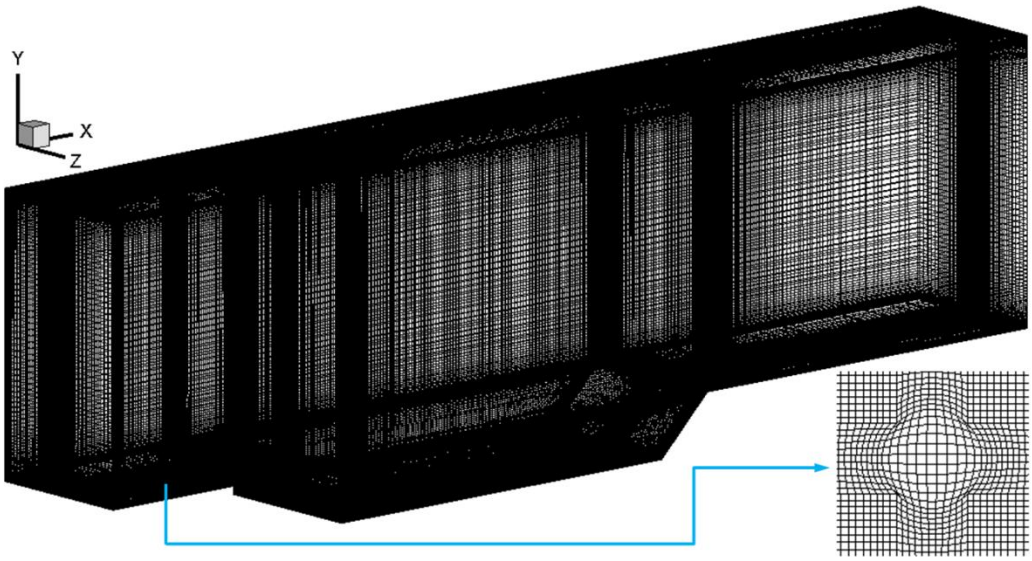

Figure 6.3 Computational domain and the distribution of the grid. The small figure in the corner shows the grids near the hydrogen injection hole.

Figure 6.3 shows the computational domain of the combustor and the distribution of the grids, in which X, Y and Z represent the streamwise, the transverse and the spanwise directions, respectively. A grid which has 3.9 million nodes was employed by Fan [154] for this configuration. It is revealed that the LES

based on this grid is capable of capturing the flow features. Therefore, it is reasonable to expect that the grid, which has 5.3 million nodes and is employed in the present study, is sufficient to resolve the important large flow structures in the cavity-based combustor.

The flow in the combustor is calculated using a hybrid RANS/LES in-house code and ANSYS FLUENT 14.5. In the in-house code, the governing equations are solved based on the finite difference method and the UFPV model is included. The fifth-order WENO scheme is used for the convective fluxes and the second-order accurate-centred scheme is used for the diffusive fluxes. A time marching procedure, which employs the second-order Runge-Kutta method, is employed [11]. In FLUENT [127], the momentum, energy, species, and pressure-based continuity equations are solved using a pressure-based coupled algorithm. The gradients are computed according to the Green-Gauss node-based method. A second-order scheme for the pressure equation and a bounded central differencing scheme for the other equations are employed to the spatial discretization. Further, the bounded second-order implicit scheme is employed to the transient formulation. In all the computations, the CFL number and time step size are 0.5 and 1e-8 s, respectively.

The Dirichlet boundary conditions are used for all the variables at the heated air inlet and hydrogen injection, and the parameters are given in Tables 6.1 and 6.2. All the values of the variables at the outlet are extrapolated from the interior predictions and therefore a pressure outlet boundary condition is applied. Further, no-slip wall assumptions have been employed at the solid surfaces, i.e. the combustor walls, and the two side surfaces at the spanwise direction are assumed to be periodic boundary conditions. Finally, the computational domain is initialized with all the quantities specified at the inlet.

6.4. Results and discussion

6.4.1. Non-reacting flows

In this section, the non-reacting flows are simulated in order to understand the characteristics of the supersonic flow over a cavity and the mixing between the hydrogen and the heated air, and to provide an initial condition for the calculations of the reacting flows.

The hydrogen jet upstream of the cavity is a classical transverse jet problem. The flow field associated with the transverse jet, or jet injected normally into crossflow has been wide investigated [221]. The structure of the gaseous jet in supersonic crossflow is generated by complicated flow interactions between the jet, the crossflow and the wall boundary layer. Some of these structures, such as the bow shock that forms upstream of the jet, the Mach disk and barrel shock structure that form within the jet, the high pressure separation region and recirculation zone that form upstream of the injection, recirculation zone that forms downstream of the injection, and so on, are shown in Figure 6.4. Our study is mainly on the flows over the cavity, and therefore we do not discuss the flow near the hydrogen jet in detail. More discussion related to the transverse jet problem can be found in [221,222].

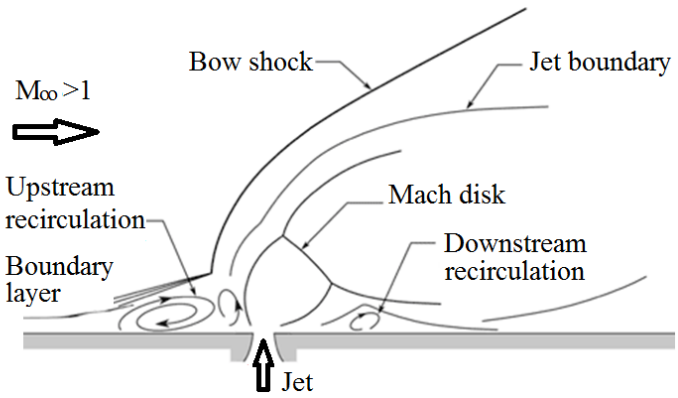

Figure 6.4 Schematic of flow structures associated with the underexpanded jet in supersonic crossflow [221].

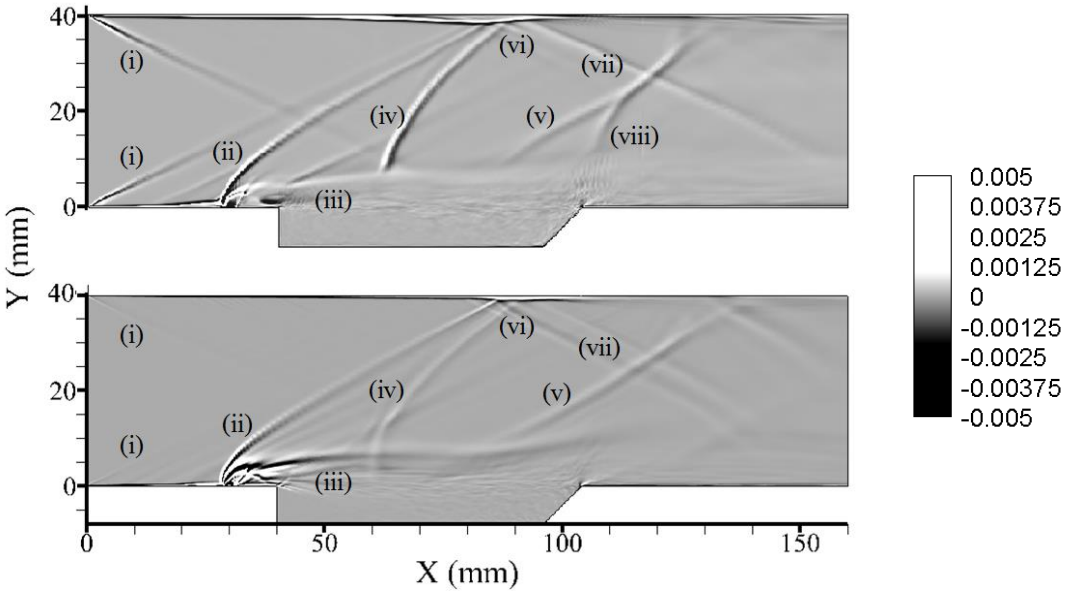

Figure 6.5 Time-averaged numerical shadowgraph images of the non-reacting flows at Z = 11 mm, obtained from the in-house code (top) and FLUENT (bottom) simulations.

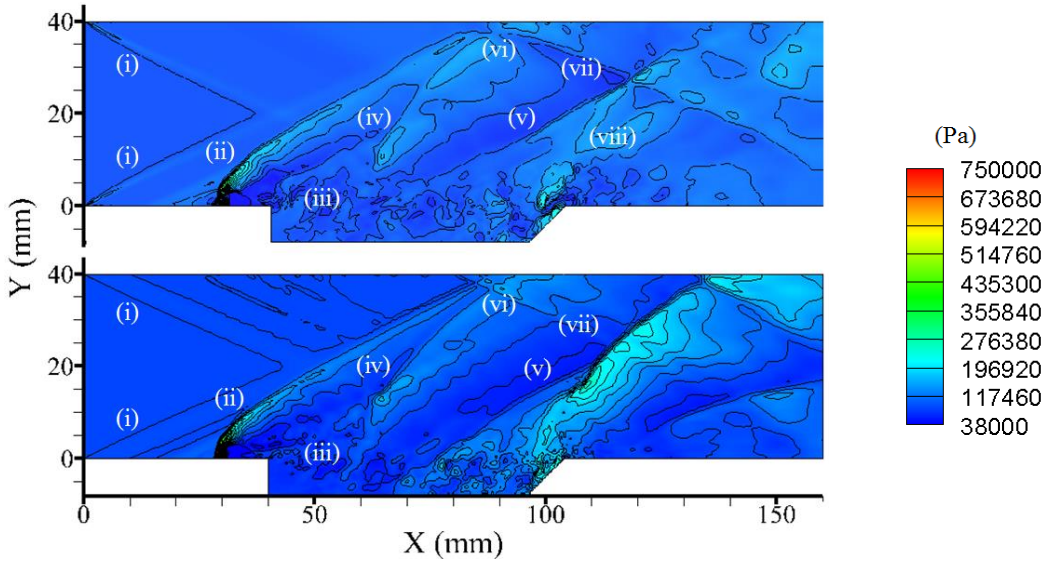

Figure 6.6 Contours of the instantaneous pressure of the non-reacting flows at Z = 11 mm, obtained from the in-house code (top) and FLUENT (bottom) simulations.

Figure 6.5 shows the time-averaged numerical shadowgraph images at the plane Z = 11 mm and it reveals the structure of the supersonic flow over the cavity. The sampled time period is 3ΔT, where ΔT is the passing through time and defined as $L_{combustor}/U_{\infty}$, where $L_{combustor}$ and U_{∞} are the length of the combustor and the flow speed at the inlet, respectively. It should be noted that, without special declaration, the sampled time period for all the simulations in this chapter is 3ΔT. Further, Figure 6.6 shows the instantaneous pressure contours at t = 2ΔT, where t = 0 is defined as the time moment that one ΔT has been run since the start of the calculation in order to obtain fully developed turbulent flows.

We observe from Figures 6.5 and 6.6: (i) the shock wave at the inlet created by the inlet boundary layer, (ii) the bowl shock wave created by the hydrogen injection, (iii) the mixing layer over the cavity, (iv) and (v) the impingement shock wave and the exit shock wave shown in Figure 6.1, (vi) the interaction between the boundary layer and the shocks, and (vii) the reflected and the induced shock waves. The interaction of the shock waves (iv) and (v) with the shear layer (iii) can be clearly identified in Figures 6.5 and 6.6. As the mixing layer develops, it passes over the cavity and its lower part impinges on the cavity aft wall. Then, the mixing layer above the cavity aft wall is raised up and the shock (viii) is formed. However, shock (viii) is only captured by the LES using the in-house code, and this is mainly because of the higher-order discretization schemes used in the in-house code being more sensitive to the flow changes than those used in FLUENT. As the near-wall treatments used in the in-house code and FLUENT are different, the structure of the boundary layers, as well as the interaction between the shock wave and boundary layer are slight differently simulated. However, on the whole, the in-house code and FLUENT predict consistent structures of the supersonic flows over the cavity.

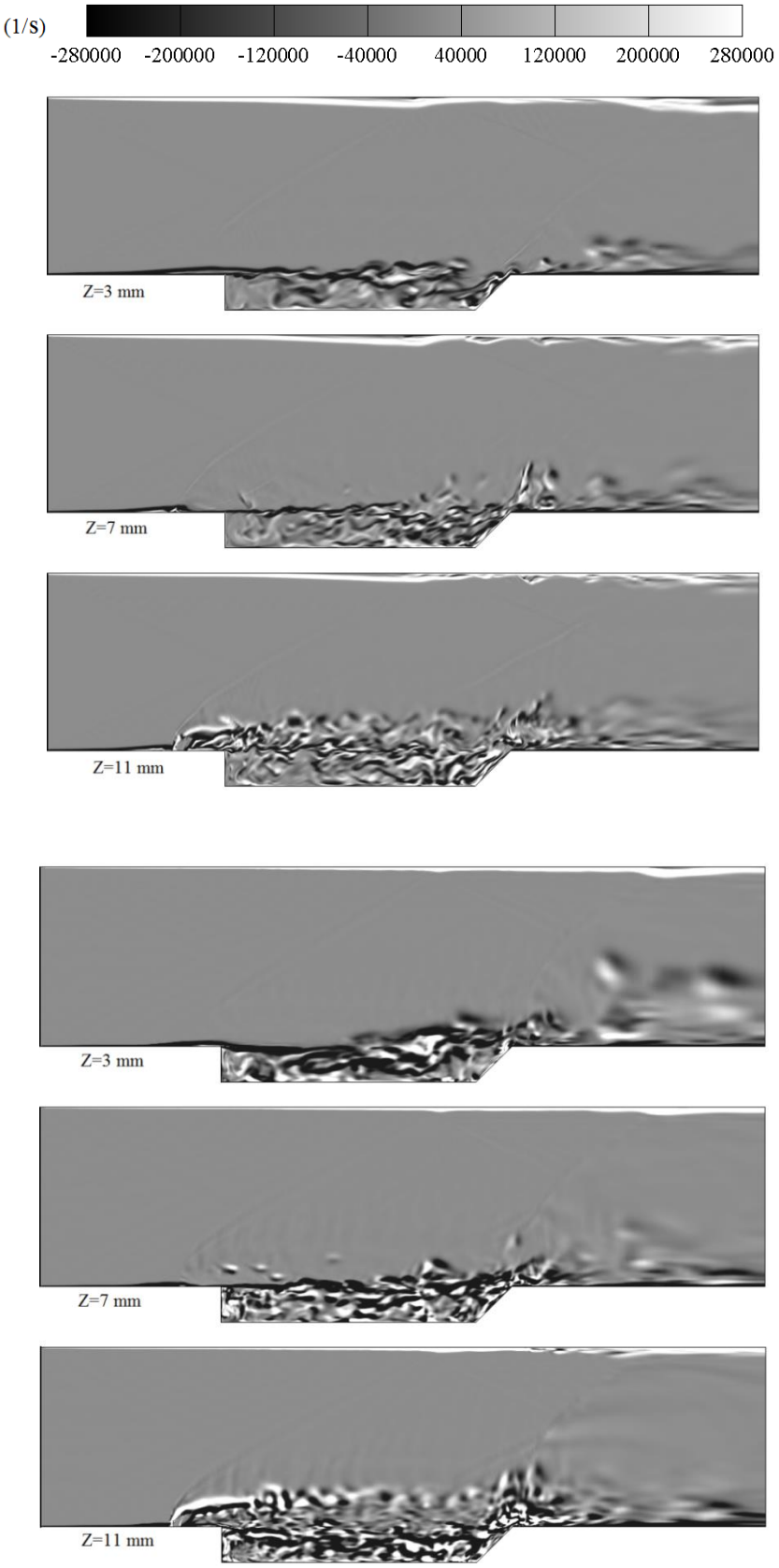

(a) In-house code results

(b) Fluent results

Figure 6.7 Contours of the instantaneous spanwise component of the vorticity of the non-reacting flows at the locations, Z = 3, 7 and 11 mm for (a) the in-house code and (b) FLUENT simulations.

Figure 6.7 reveals the instantaneous spanwise component of the vorticity, i.e. ω_z, of the non-reacting flows on the planes Z = 3, 7 and 11 mm, where ω_z is obtained using the relation $\omega_z = (\partial v/\partial x - \partial u/\partial y)$, and *u* and *v* are the velocities in the *x* and the *y* directions, respectively. On the plane Z = 3 mm, which is far from the hydrogen injection hole, the cavity shear layer develops from approximately steady state to being highly unsteady state. Downstream of the cavity leading edge, the Kelvin–Helmholtz instability dominates the growth of the shear layer. On the plane Z = 7 mm, the instability occurs early than that on the plane Z = 3 mm, and this is because the hydrogen jet has a stronger impact on the flows near the location of Z = 7 mm. On the plane Z = 11 mm, which is across the centre of the injection hole, the injection makes the shear layer motion very different from those showed on the other two planes.

Further, from Figure 6.7, the cavity shear layer is observed to be highly unsteady and a large number of vortices are created. These vortices march downstream in the streamwise direction and contribute to the transport of the hydrogen from the fuel jet to the cavity inside. When the lower part of the cavity shear layer impinges on the cavity aft wall, the large scale vortices break down and numerous smaller vortices are produced.

Figure 6.8 shows the instantaneous streamwise vorticity structures of the flowfield, i.e. the streamwise component of the vorticity $\omega_x = (\partial w/\partial y - \partial v/\partial z)$. The injection produces a high pressure region and a low pressure region which are at the front and behind of the jet, respectively, see Figure 6.6. The pressure gradient induces a counter-rotating vortex pair [223], which can be seen in both the in-house code and the FLUENT results in Figure 6.8. The pair of counter-rotating structures induce each other, interact with the flow in the cavity and are slightly lifted up as they flow downstream. The counter-rotating vortex pair become weaker downstream as the pressure gradient that originates from the jet decreases. However, the

spanwise vortices in the cavity and the shear layer develop very rapidly and become stronger downstream, see Figure 6.7. Concerning the spanwise and streamwise vortices shown in Figures 6.7 and 6.8, we can identify that the flow in the cavity is three-dimensional and with a high turbulence intensity.

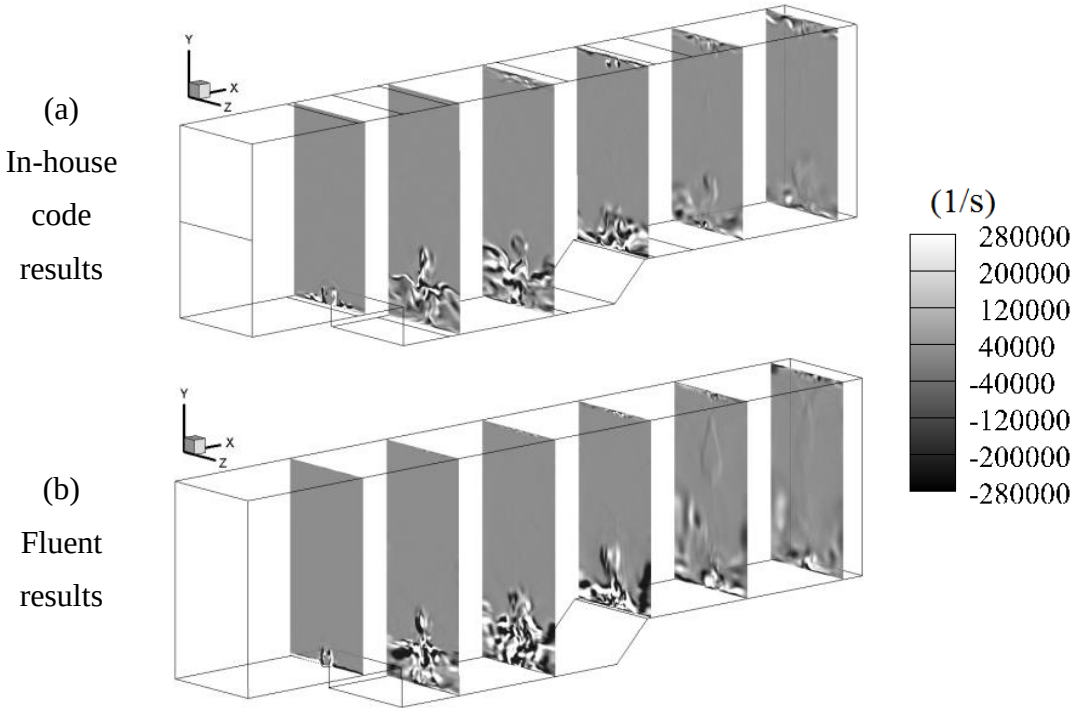

Figure 6.8 Contours of the instantaneous streamwise component of the vorticity of the non-reacting flows at X = 30, 55, 80, 105, 130 and 155 mm for (a) the in-house code and (b) Fluent simulations.

Figure 6.9 shows the hydrogen distribution in the non-reacting flows at different locations. On the one hand, the entrainment of the crossflow into the near field of the jet is visualized in Figure 6.9. On the other hand, it is interesting to observe that the contours shown in Figures 6.8 and 6.9 have a very similar shape in the region above the cavity, and therefore the streamwise vortices must play a critical role in the mixing process in this region. Further, in the cavity, both the streamwise and spanwise vortices enhance the mixing between the hydrogen and the air.

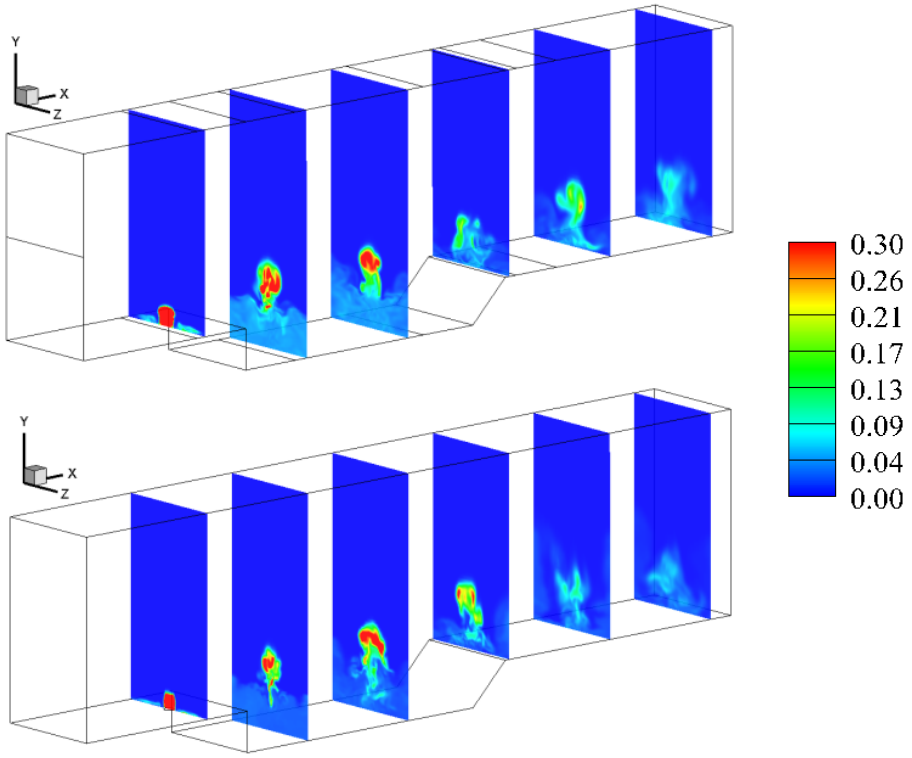

Figure 6.9 Contours of the hydrogen mass fraction in the non-reacting flows at X = 30, 55, 80, 105, 130 and 155 mm for (a) the in-house code and (b) Fluent simulations.

Figure 6.10 shows the stoichiometric mass fraction $f = f_{st}$ and $f = 0.2$ iso-surfaces of the non-reacting flows which are coloured by the magnitude of the instantaneous velocity. At first, the unsteady iso-surfaces shown in Figure 6.10 are distorted, stretched and wrinkled by the streamwise and spanwise vortices. These effects increase the contact area of the fuel and the air, and this gives the reactants more chance to mix at a molecular level. Secondly, the iso-surfaces also show the horseshoe vortices which are originated from the interaction between the boundary layer and the transvers hydrogen jet. Further, the horseshoe vortices develop into the cavity mixing layer in the downstream region and during this process, some fuel is entrained into the cavity. However, most of the fuel passes by the cavity and this phenomena is also observed in Figure 6.9.

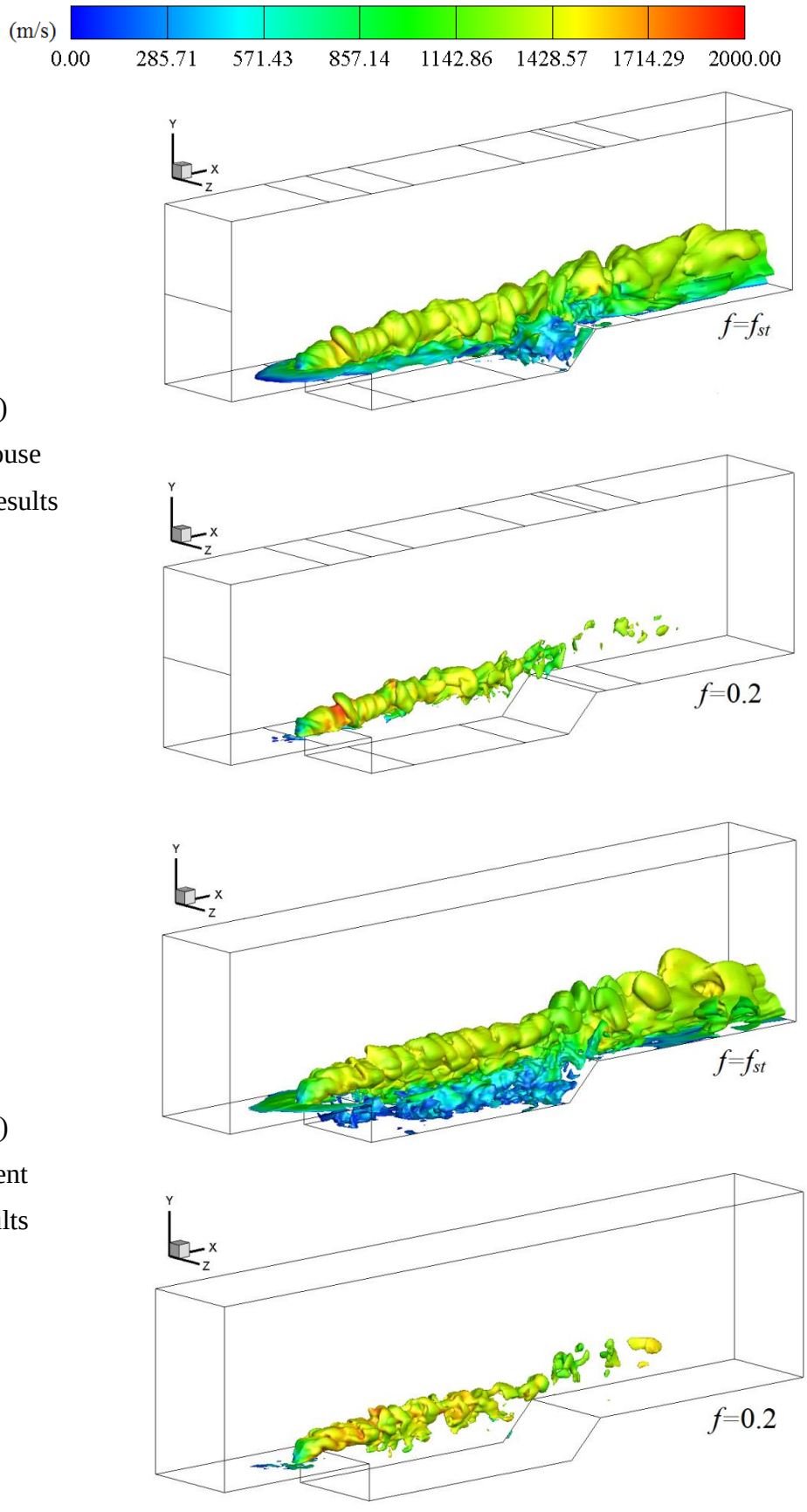

(a) In-house code results

(b) Fluent results

Figure 6.10 Instantaneous velocity magnitude contours at $f = f_{st}$ and 0.2 iso-surfaces of the non-reacting flows for (a) the in-house code and (b) FLUENT simulations.

Further, see Figure 6.10, we observe that the iso-surfaces of $f = 0.2$ break down and vanish in the downstream region, and this means that the fuel stream and the air free stream have mixed with each other to a new level and the mixing progress is rather rapid. Therefore, the iso-surfaces $f = f_{st}$ clearly have a larger area in the downstream region than those in the upstream region. Finally, the velocity magnitude contours on the iso-surfaces show that the velocity in the cavity is very low. In compressible flow, a decrease in the velocity always results in an increase in the static temperature. Therefore, the lower velocity magnitude approximately corresponds to a higher static temperature.

As ignition and combustion benefit from a low velocity magnitude and high temperature, therefore the iso-surfaces $f = f_{st}$ reveal that the region near the cavity aft wall will be a good place to ignite the mixed gas. Finally, the shape of the $f = f_{st}$ iso-surfaces in the cavity are quite differently simulated by the in-house code and FLUENT. This is possibly due to the difference between the two codes, such as the sub-grid scale models and the treatment near the wall.

6.4.2. Reacting flows

In this section, the reacting flows are simulated in order to understand the characteristics of the supersonic reacting flow over the cavity and the performance of the combustion models. Firstly, the reacting flows are simulated with the flamelet model which is built into the in-house code and FLUENT. Secondly, the reacting flows are modelled with the UFPV model which is built into the in-house code. Further, the simulation results are compared with the experimental data, and with each other.

6.4.2.1. Simulations using the flamelet model

Figure 6.11 shows the high-speed photography images obtained from the experiments which were performed by Fan in the National University of Defense Technology in China [154]. High-speed photography is a widely used technique to visualize the ignition and flame propagation processes [224].

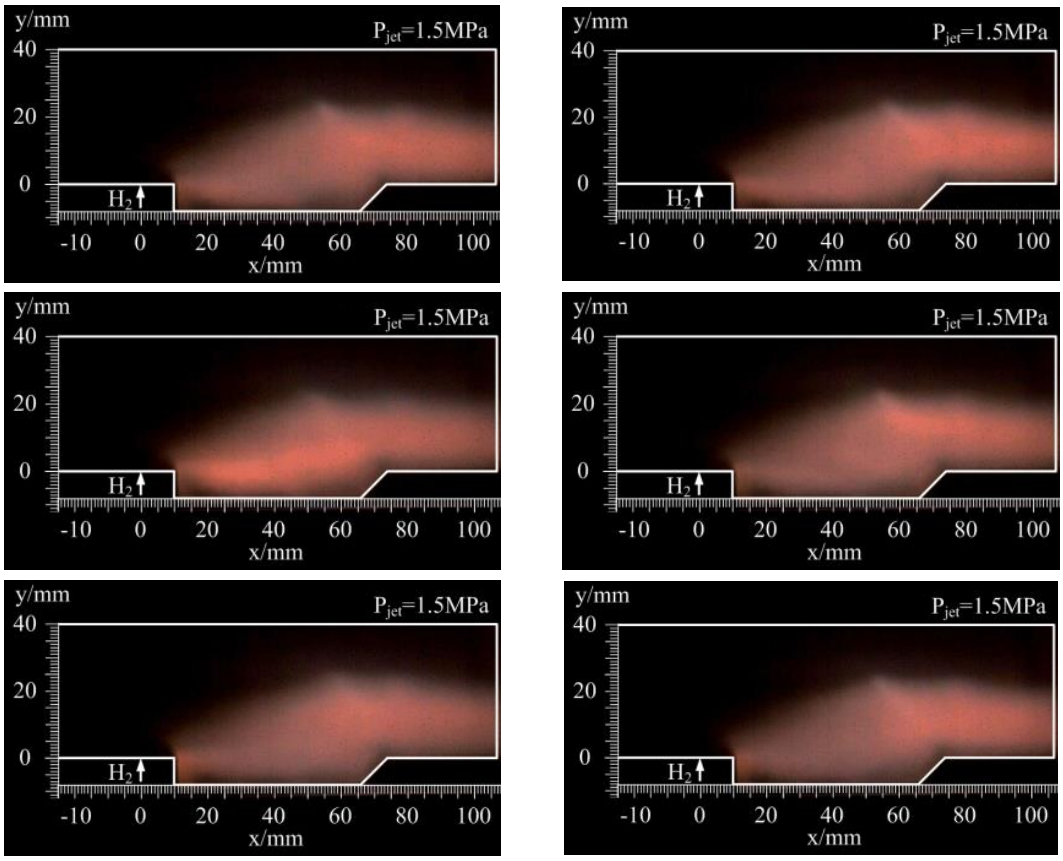

Figure 6.11 High-speed photography images at different time intervals as obtained from the experiments of Fan [154].

The images presented in Figure 6.11 show the natural luminosity of the flame and the region where light and heat is emitted. Further, in Figure 6.11, the white solid lines and the white arrow show the interval channel of the supersonic combustor and the hydrogen injection, respectively. The exposure time of every

image is 0.25 ms, and the time interval between the left and right images is 12.5 ms. More information about the setup of the high-speed photography can be found in [154]. From Figure 6.11, we observe that:

(i) There is weak combustion in the region near the hydrogen injection.

(ii) The flame is mainly in the cavity, the region above the cavity and the region above the combustor bottom wall.

(iii) The surface of the flame has two protuberances.

In order to explain the experimental data and understand the structure of the reacting flows, contours of the time-averaged temperature obtained from the in-house and FLUENT simulations are given in Figure 6.12. Because the high-speed photography images are the 2-dimentional imaging of the 3-dimentional combustion luminosity, the contours are shown at three different locations, i.e. Z = 3, 7 and 11 mm, respectively. We observe that the weak combustion in the region near the hydrogen jet is captured by the both the in-house code and FLUENT simulations, see Figure 6.12. However, the distribution of the mean temperature is very differently predicted by the two codes, although the same flamelet combustion model is employed. It is clear that FLUENT predicts a higher temperature and a more intense combustion in the cavity than in the other regions in the combustor and these predictions are not consistent with the high-speed photography images. The in-house code predicts a less intense combustion in the cavity and a lower temperature in the cavity than do the FLUENT predictions and the simulated flame shape matches better with the experimental observations.

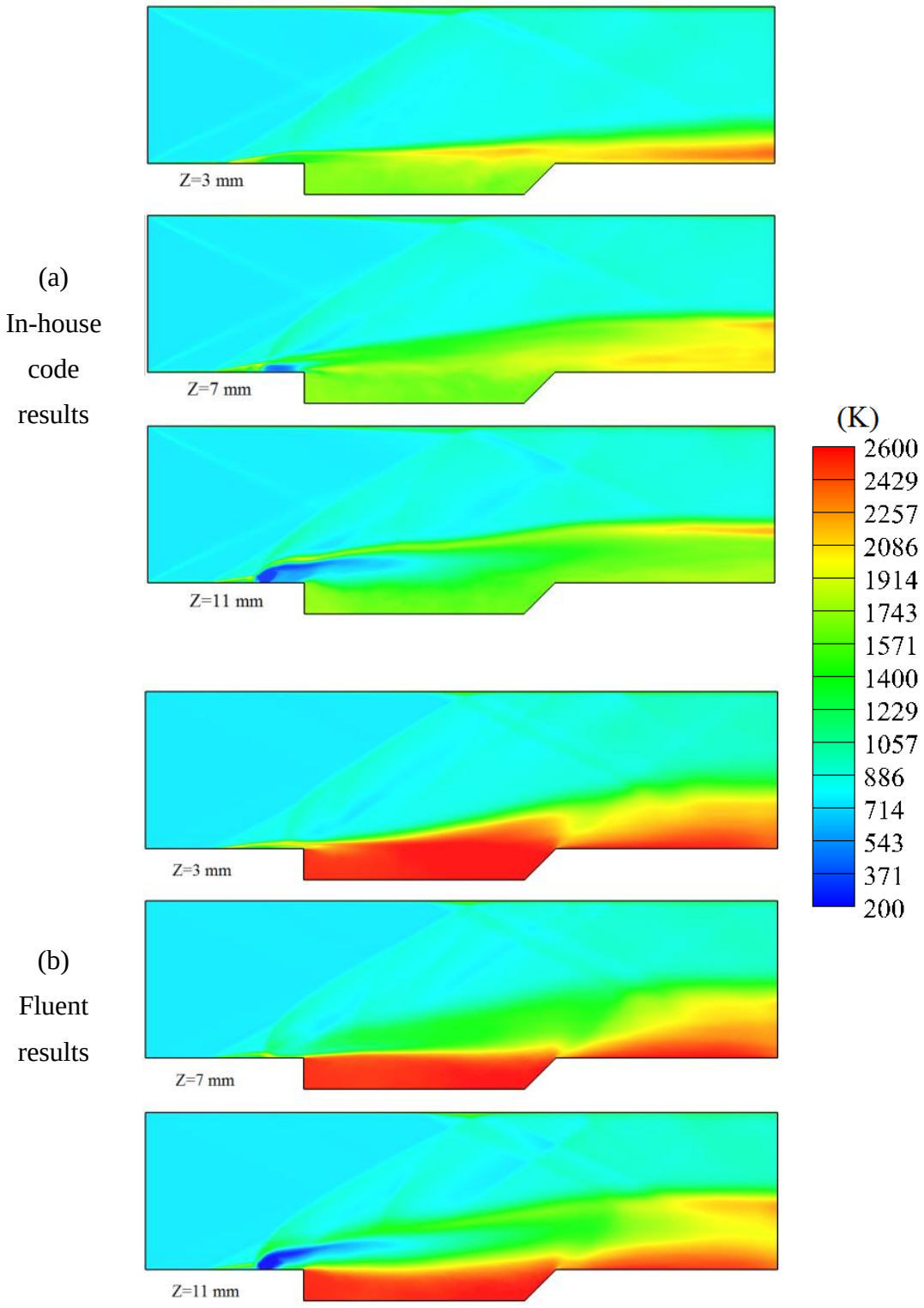

Figure 6.12 Contours of the time-averaged temperature of the reacting flows at the locations Z = 3, 7 and 11 mm obtained from (a) the in-house code and (b) FLUENT LES flamelet modelling.

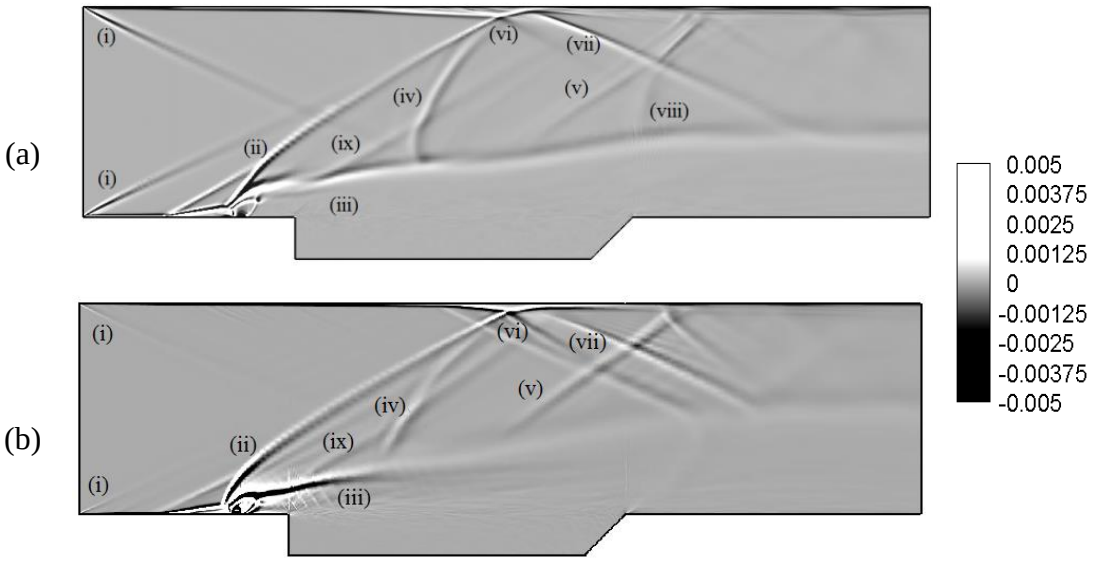

Figure 6.13 Time-averaged numerical shadowgraph images of the reacting flows at Z = 11 mm obtained from (a) the in-house code and (b) FLUENT LES flamelet modelling.

Figure 6.13 shows the time-averaged numerical shadowgraph images at the plane Z = 11 mm and it reveals the structure of the supersonic reacting flows. The sampled time period is 3ΔT, the same as those for the non-reacting case. Comparing Figures 6.13 and 6.5, we observe that the structure of the shocks in the reacting flow is very similar to that in the non-reacting flow. The main difference is that, because of the presence of combustion and heat release, the hydrogen stream is lifted more in the reacting flow than that in the non-reacting flow, and this results in the antedisplacement of the shocks in the combustor. The shock (ix) becomes clearer in the results obtained from both the two codes and this is caused by the compression effect due to the heat release in the outer interface of the hydrogen stream and air stream. After analysing the mean temperature contours and the numerical shadowgraph images at Z = 11 mm, we observe that the shock waves (iv) and (ii) are reflected by the top wall of the combustor, and the reflected shock waves (vii) intersect with the flame surface and the shape of the flame are changed. Therefore,

the two protuberances of the flame surface presented in Figure 6.11 are a result of the interaction between the flame and the reflected shocks.

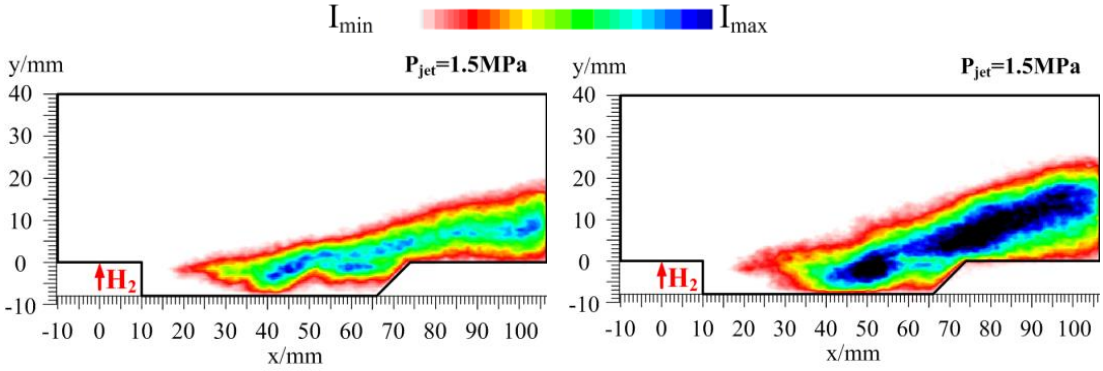

Figure 6.14 The OH radical spontaneous emission images at different time intervals as obtained from the experiments of Fan [154,225].

Figure 6.14 shows the OH radical spontaneous emission images obtained from the two different experimental operations under the same conditions [154,225] and the exposure time of each image is 0.05 ms. In hydrogen and air combustion regime, autoignition is associated with a very rapid destruction of the pre-ignition species HO_2 and a rapid generation of OH [226]. The OH radicals are very reactive and play an important role in hydrocarbon oxidation reactions, and therefore, the OH radicals may be reasonably used as an indicator of the flame front. Further, the OH radical spontaneous emission measurement has been widely used to identify the distribution and propagation of the flame [224]. More information about the OH radical spontaneous emission measurements and its setup can be found in [154,225].

Figure 6.14 indicates that the flame is mainly in the cavity, the region above the cavity and the region near the combustor bottom wall and this observation is identical with the high-speed photography observations. Further, in the regions near the hydrogen jet and near the cavity front wall, minor or no OH radicals, i.e. very weak or no combustion, are observed.

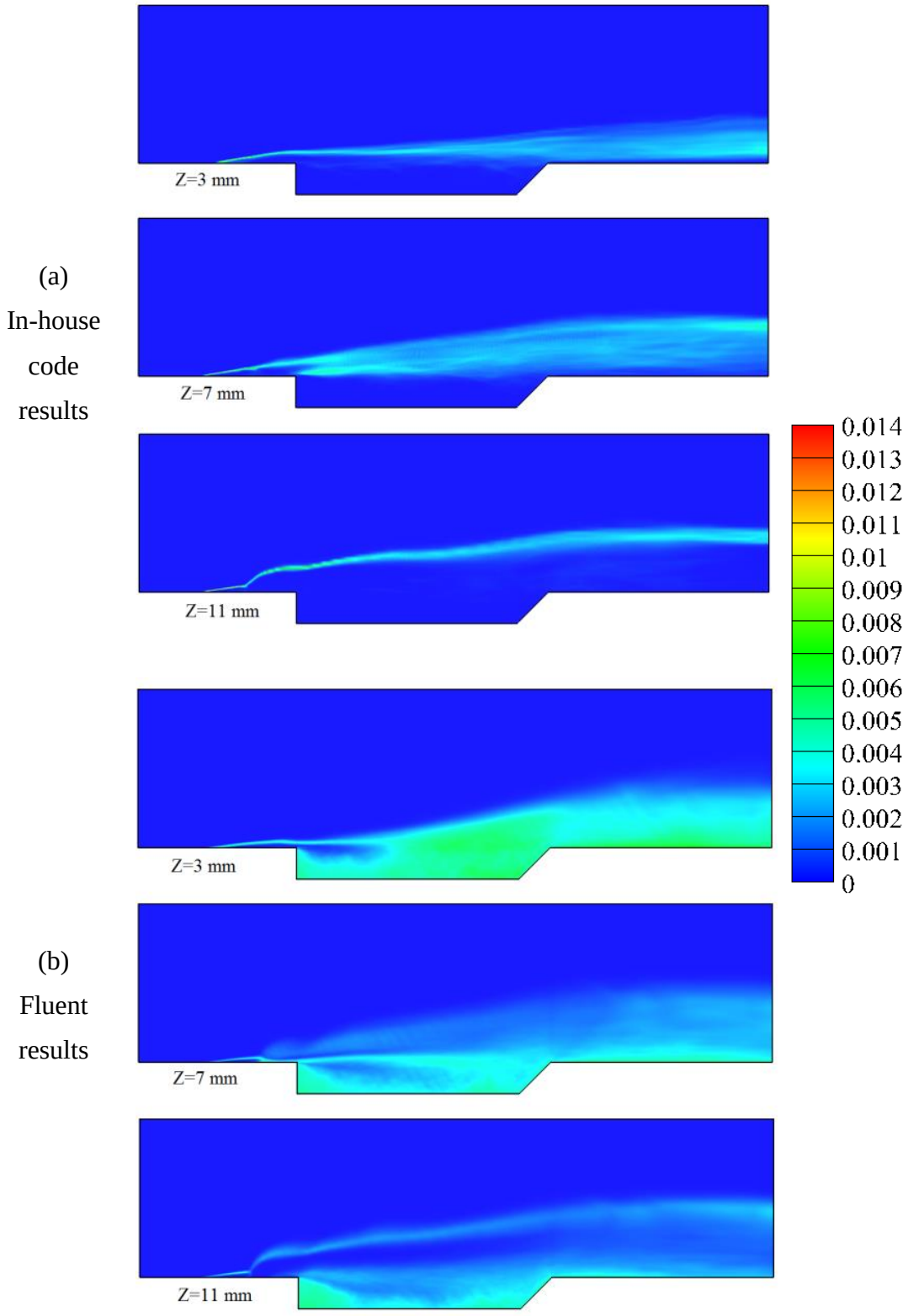

Figure 6.15 Contours of the time-averaged OH mass fraction of the reacting flows at the locations Z = 3, 7 and 11 mm obtained from (a) the in-house code and (b) FLUENT LES flamelet modelling.

Figure 6.15 shows the contours of the time-averaged OH mass fraction of the reacting flows. Similar to the high-speed photography images, the OH radical spontaneous emission images are the 2-dimentional imaging of the 3-dimentional OH radical spontaneous emission. Therefore the contours of the OH mass fraction are shown at three different locations. It is clear that the simulation results obtained from the two codes are different, as well as being different to the experimental observations. Firstly, the in-house code predicts a few of the OH radicals in the cavity, whereas the FLUENT simulations give too many. The OH radicals in the region near the cavity aft wall are not predicted by the in-house code and the OH radicals in the region near the cavity front wall, which are not presented in Figure 6.14, are predicted by FLUENT simulations. This difference is mainly due to the difference in the hydrogen distribution simulated by the two codes, see Figures 6.9 and 6.10.

Secondly, the flamelet model, which is built into the two codes predict the combustion in the region at the front of the hydrogen jet. The hydrogen stream is a typical transverse jet before it reaches the cavity and this kind of flame has been widely investigated [227,228,221]. As has been revealed in §6.4.1, a small recirculation is formed at the front of the hydrogen jet and the hydrogen and the air mix with each other. Therefore, it is possible to ignite the mixed gas. However, if the recirculation where the combustion takes place is very small, the reactive radicals, such as H, OH and O, are very near the solid combustor wall. Once these radicals hit the wall, they lose their activity, the chemical chain reaction terminates and the flame is extinguished. In the meantime, the heat transfer from the flame in the recirculation region to the cold combustor wall may also result in quenching [226]. If the recirculation is sufficiently large so as to maintain the active radicals and balance the heat release and heat loss, the flame can be held in this region [154]. However, the combustor walls in the simulations are assumed to be adiabatic and the

reaction-breaking effect is neglected. Therefore, the simulations predict that combustion occurs at the front of the hydrogen jet.

Figure 6.16 illustrates the OH-PLIF (Planar Laser-Induced Fluorescence) images obtained from three different experimental operations under the same conditions [154,225]. PLIF is an optical diagnostic technique widely used for flow visualization and it can result in quantitative measurements. The PLIF images have a very high spatial and temporal resolutions, of the order of 10^{-4} m and 10^{-9} s, respectively, and the OH-PLIF technique has been widely employed to visualize the flame front, the flame propagation, interaction between flame kernel vortex, extinction and ignition, etc. [224]. The thickness of the plane beam in the experiments of Fan is about 0.2mm and the exposure time of the PLIF is 50ns. Therefore, the OH-PLIF images can be regarded as the instantaneous OH distribution, i.e. the instantaneous flame structure, at the plane Z = 11 mm. From Figure 6.16, we observe that:

(i) The reacting flow is highly turbulent and unsteady.

(ii) The cavity mixing layer is ignited in advance of the hydrogen stream.

(iii) Combustion does not exist in the region at the front of the hydrogen jet but it occurs in the region just behind the jet, and this is consistent with the high-speed photography observations.

(iv) Minor combustion takes place in the regions near the cavity front and aft walls.

The OH-PLIF images show a consistent OH distribution with the OH radical spontaneous emission images, except in the region near the cavity aft wall. This is mainly because the OH radical spontaneous emission images are the spatial and temporal mean values. Thus, these instantaneous OH-PLIF images do not capture the combustion which may occur in the region near the cavity aft wall.

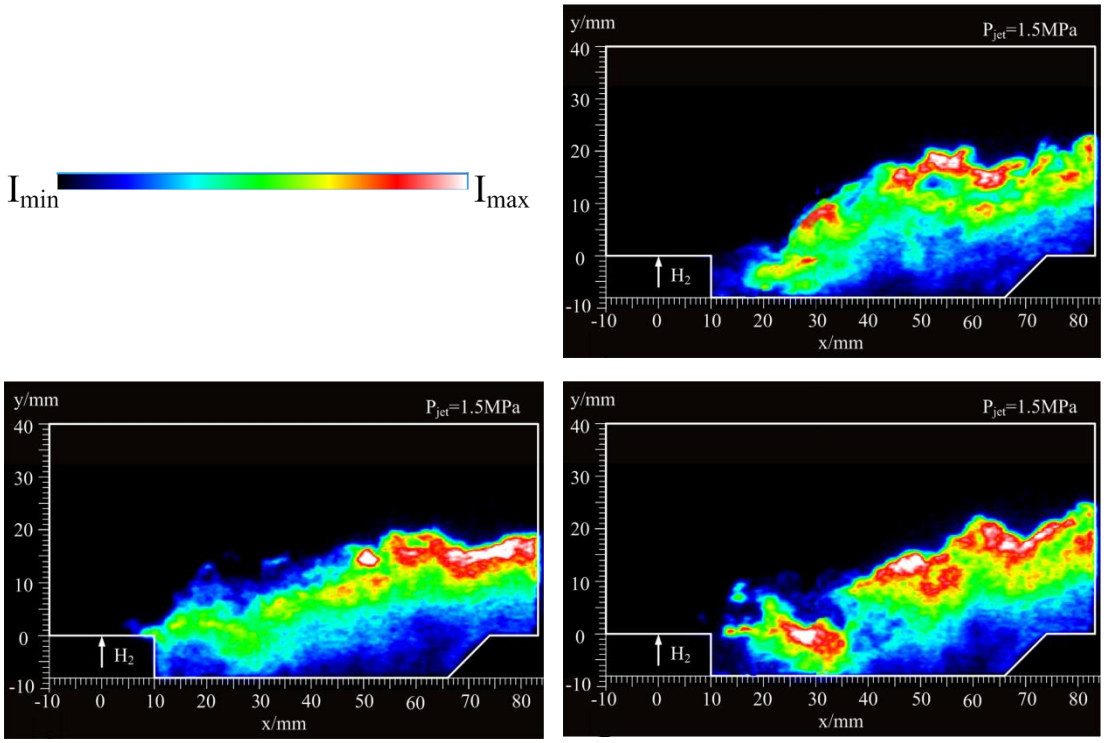

Figure 6.16 OH-PLIF images of the reacting flows at different time intervals as obtained from the experiments of Fan [154,225].

Figures 6.19, 6.17, 6.18 and 6.20 show the contours of the instantaneous OH mass fraction and static temperature of the reacting flows at different locations for the in-house and FLUENT simulations. The contours at different Z locations indicate that the fuel is ignited in the region at the front of the hydrogen jet, see in Figures 6.17 and 6.18. As the flame develops downstream, due to the Kelvin–Helmholtz instabilities, large-scale structures originate and roll up and the flame is distorted. The distorted flame can be entrained into the cavity by the vortices and may impinge the cavity aft wall and be retained in the cavity. Further, the flame becomes increasingly distorted and is shredded with increasing downstream distance due to vortex break-down and the thin flame fronts develop and propagate into reaction zones. We can see from the OH and temperature contours at the plane Z = 11 mm that both the in-house code and FLUENT predict the reaction near the hydrogen stream. However, the reaction in the cavity mixing layer is only simulated by FLUENT. As discussed before in this section, this may be attributed to the

mixing between the hydrogen and the air being differently predicted by the two codes, see Figures 6.9 and 6.10.

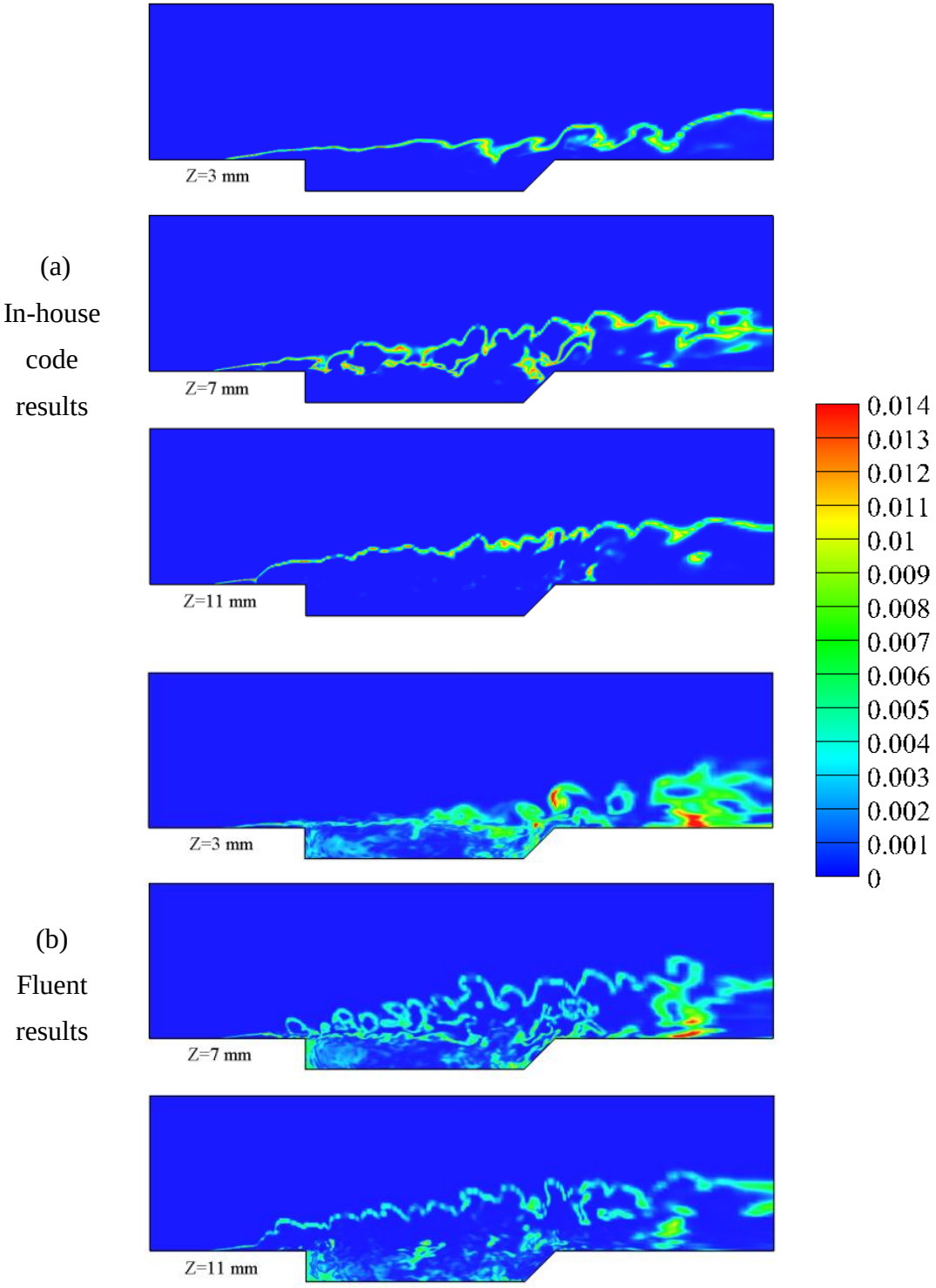

Figure 6.17 Contours of the instantaneous OH mass fraction of the reacting flows at the locations Z = 3, 7 and 11 mm, obtained from (a) the in-house code and (b) FLUENT LES flamelet modelling.

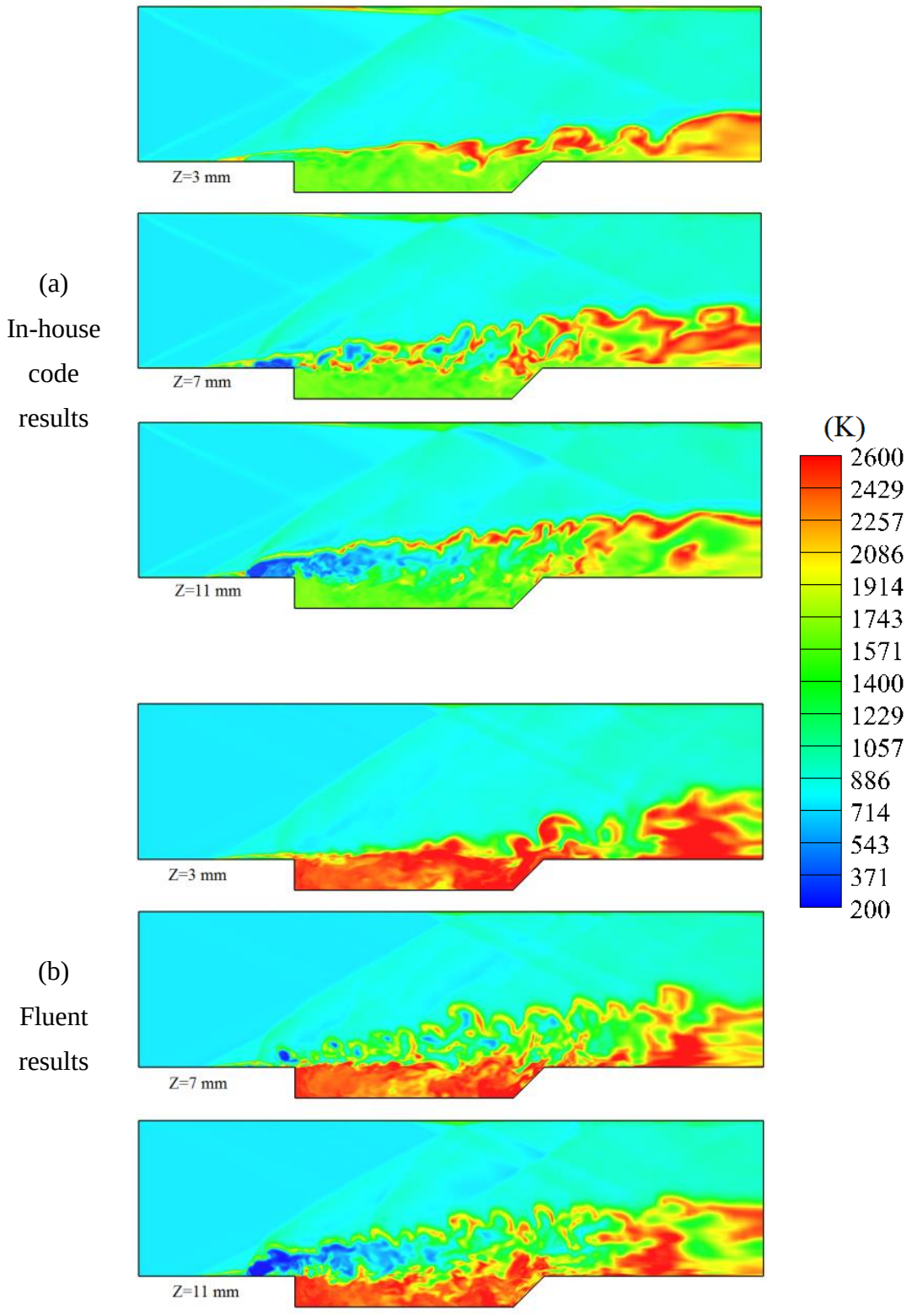

Figure 6.18 Contours of the instantaneous static temperature of the reacting flows at the locations Z = 3, 7 and 11 mm, obtained from (a) the in-house code and (b) FLUENT LES flamelet modelling.

The OH and temperature contours at different X locations, shown in Figures 6.19 and 6.20, illustrate the effects of the counter-rotating vortex pair and the streamwise vortices on the development of the supersonic flames. The pair of the counter-rotating vortices absorbs the cavity shear layer just behind the hydrogen jet and wrinkles the flame front. Also it is clear that the counter rotating vortices play a very important role in the distorting of the flame in the region behind the hydrogen jet but the effects become weaker downstream. However, the large-scale structures due to the Kelvin–Helmholtz instabilities keep playing important roles as the reacting flow progresses downstream, see Figures 6.17 and 6.18.

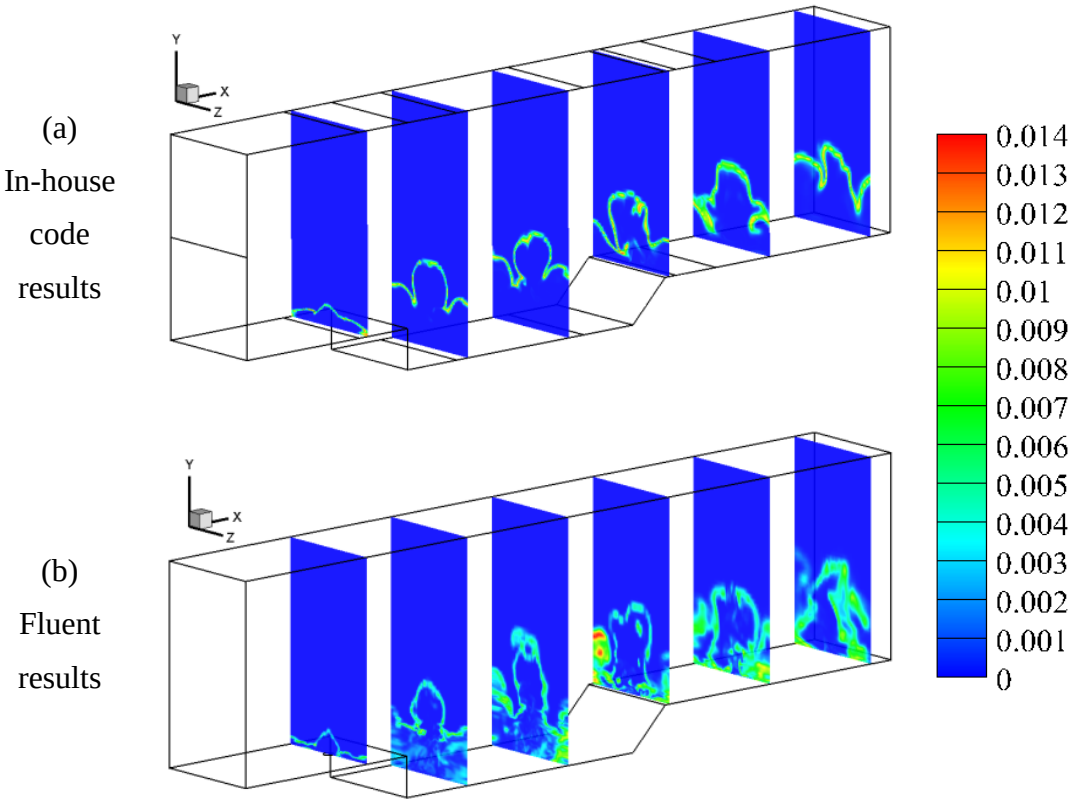

Figure 6.19 Contours of the instantaneous OH mass fraction of the reacting flows at the locations X = 30, 55, 80, 105, 130 and 155 mm, for (a) the in-house code and (b) FLUENT simulations.

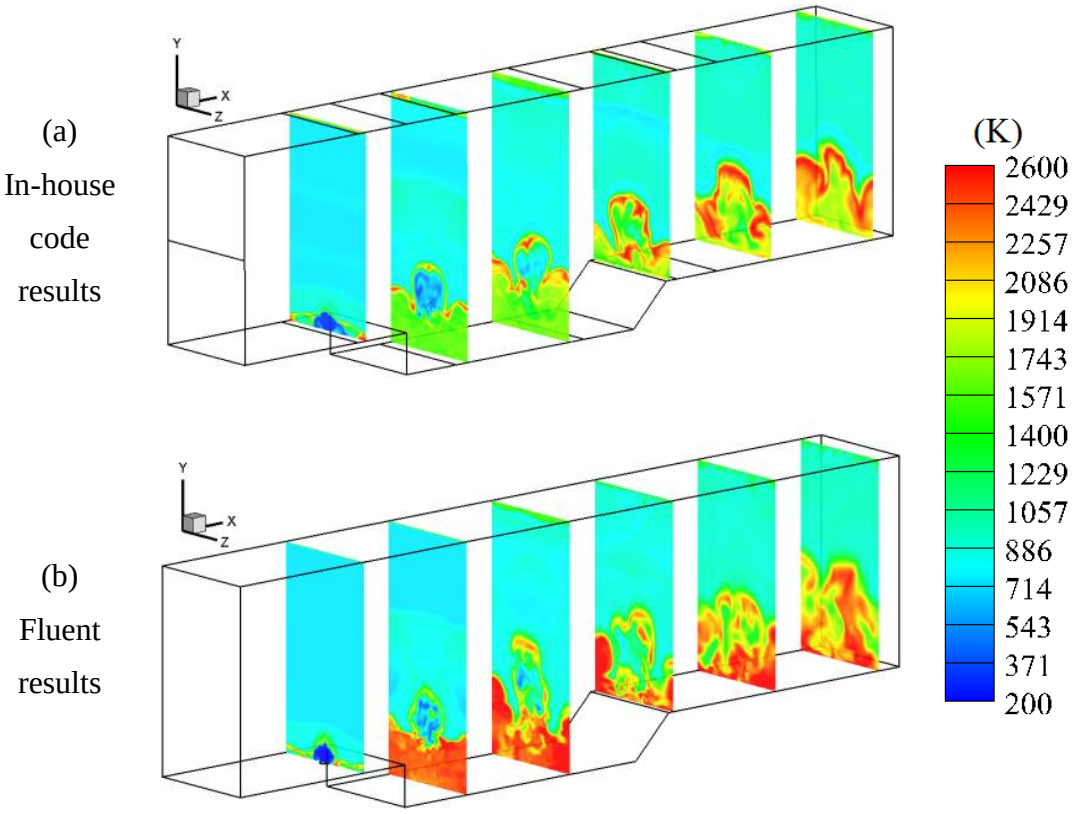

Figure 6.20 Contours of the instantaneous static temperature of the reacting flows at the locations X = 30, 55, 80, 105, 130 and 155 mm, obtained from (a) the in-house code and (b) FLUENT LES flamelet modelling.

Overall, the flamelet combustion model, which has been built into the in-house code and FLUENT, is capable of simulating the supersonic combustion process in the cavity-based scramjet combustor. However, the reacting flows in the cavity are differently predicted by the two codes. This is mainly due to the differences in the modelling of the mixing processes because the different sub-grid scale models and near-wall-treatment methods are employed in the two codes. On the other hand, in the flamelet modelling, both the in-house code and FLUENT predict the ignition of the hydrogen jet just after it is injected into the combustor, whereas the experimental observations show that the location where the hydrogen stream outer interface is ignited is over the cavity shear layer and away from the injection hole. Looking into the characteristics of the hydrogen jet in the present investigation, the jet Mach

number is 1 and the diameter-based jet Reynolds number is $Re_D \approx 30{,}000$, therefore, similar to the lifted jet flame, the high scalar dissipation rate, intense turbulence, shock waves and vortices in the region near the transverse hydrogen injection may cause local extinction and re-ignition events [229]. However, the flamelet model does not take the local extinction and re-ignition effects into account and therefore is clearly incapable of accurately modelling the supersonic flame. In order to understand the behaviour of the supersonic flame in depth, simulations with a more accurate combustion model, such as the UFPV model, is necessary.

6.4.2.2. Simulations using the UFPV model

Simulations using the UFPV model, which is built into the in-house code, are performed in this sub-section, so as to better understand the characteristics of supersonic flames in a cavity-based combustor. Also the UFPV model is test for the first time for the predicting capabilities of the supersonic combustion with a cavity flame holder.

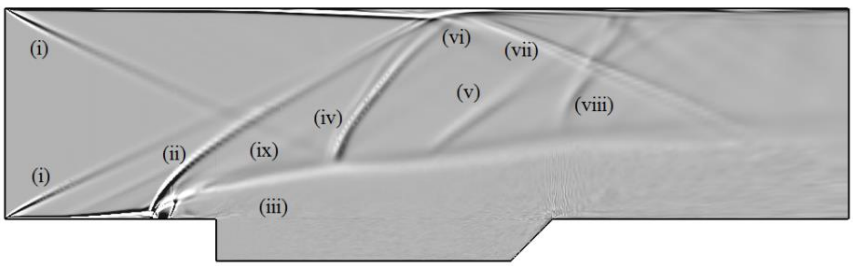

Figure 6.21 Time-averaged numerical shadowgraph image of the reacting flows at Z = 11 mm for the UFPV modelling.

Figure 6.21 shows the time-averaged numerical shadowgraph image at the plane Z = 11 mm obtained from the UFPV modelling. From Figures 6.13 and 6.21, we observe that the overall structure of the reacting flow simulated by the flamelet model and the UFPV model is quite similar but localized differences are found. The

shock (ix) shown in Figure 6.13, which is caused by the compression effects of the combustion, is not present in Figure 6.15. This indicates that there may be no, or a very weak, combustion predicted by the UFPV model in this region.

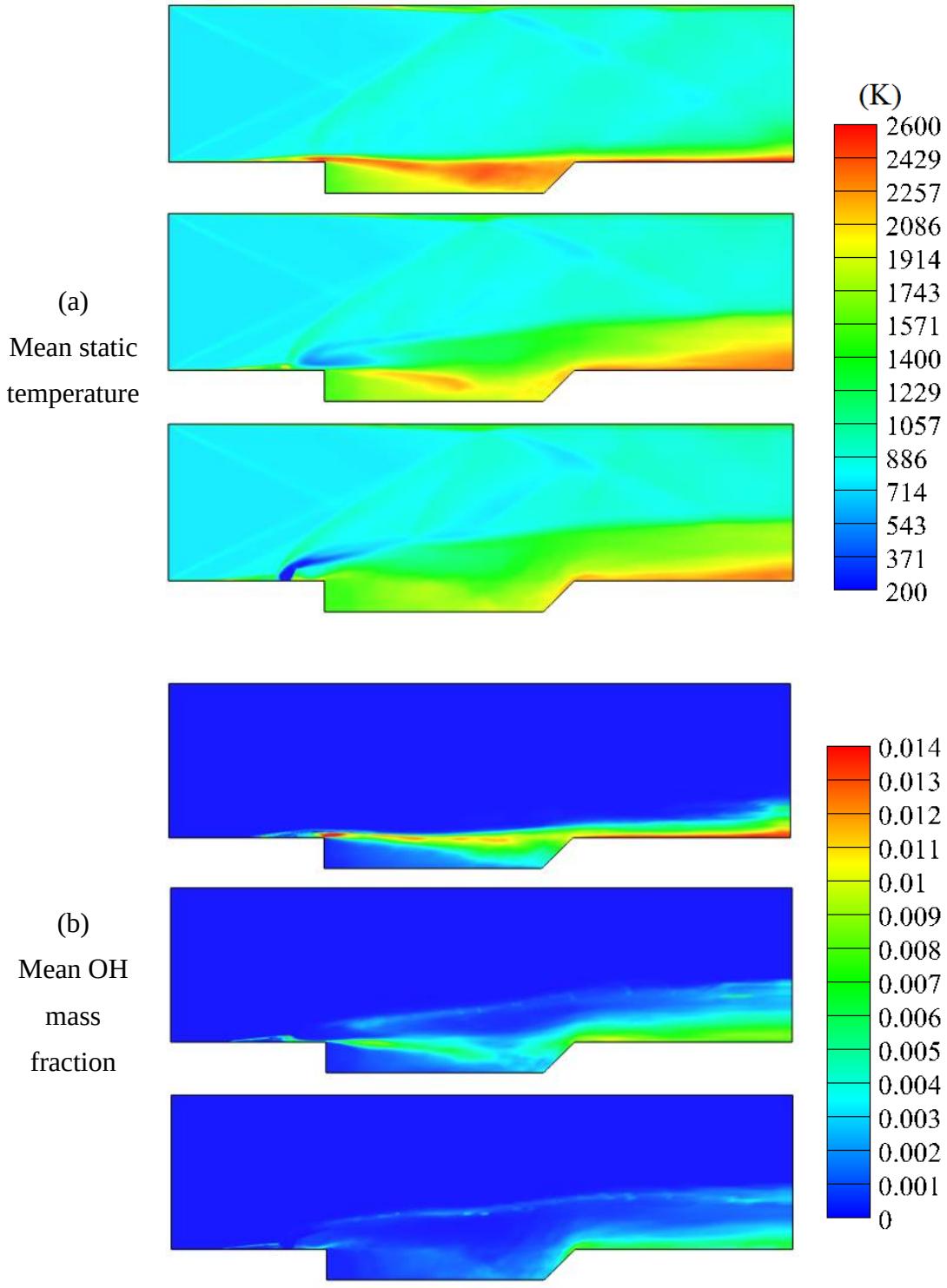

Figure 6.22 Contours of (a) the mean static temperature and (b) the mean OH mass fraction at the locations Z = 3, 7 and 11 mm for the UFPV modelling.

To look into the combustion in the chamber, the contours of the time-averaged temperature and OH mass fraction are presented in Figure 6.22. On the one hand, it is clear that the time-averaged contours predicted by the UFPV model are very different from those simulated by the flamelet model. Comparing the results obtained from the UFPV model and the flamelet model built into the in-house code, we observe that the former predicts a higher mean temperature and more OH radicals in the cavity but lower and less at the outer interface of the hydrogen and air streams. The differences indicate that there is more intense combustion in the cavity and less intense combustion in the region near the hydrogen stream as simulated by the UFPV model than by the flamelet model. On the other hand, in Figures 6.12, 6.15 and 6.22, the contours of the same physical variable obtained from the same modelling at different locations are very different from each other. This means that the reacting flow is highly 3-dimentional.

As seen in Figure 6.22, on the plane Z = 11 mm, which is across the centre of the hydrogen injection hole, the combustion is the less intense than that on the planes Z = 3 and 7 mm. At the location Z = 3 mm, the mean temperature and mean OH mass fraction in the cavity and the cavity shear layer is much higher than those at the other two locations. However, the combustion in the region near the hydrogen stream is not present in this location. This is because the hydrogen in the region where the jet interacts with the boundary layer can be brought into the cavity and the cavity mixing layer far to the location Z = 3 mm, but the hydrogen stream could not spread spanwise this far, see Figure 6.9. Comparing Figures 6.11, 6.12, 6.14, 6.15 and 6.22, we observe that the contours of the mean temperature and the mean OH mass fraction predicted by the UFPV model match better with the experimental observations, i.e. the high-speed photography images and the OH radical spontaneous emission images in Figures 6.11 and 6.14, respectively, than does the flamelet model built into both the in-house code and FLUENT. It should be noted that the images in Figures 6.11 and 6.14 are all obtained from 2-dimentional

imaging of the 3-dimentional phenomena. Therefore, the contours at the three different spanwise locations for the numerical simulations should be aggregately considered when comparing to the experimental observations.

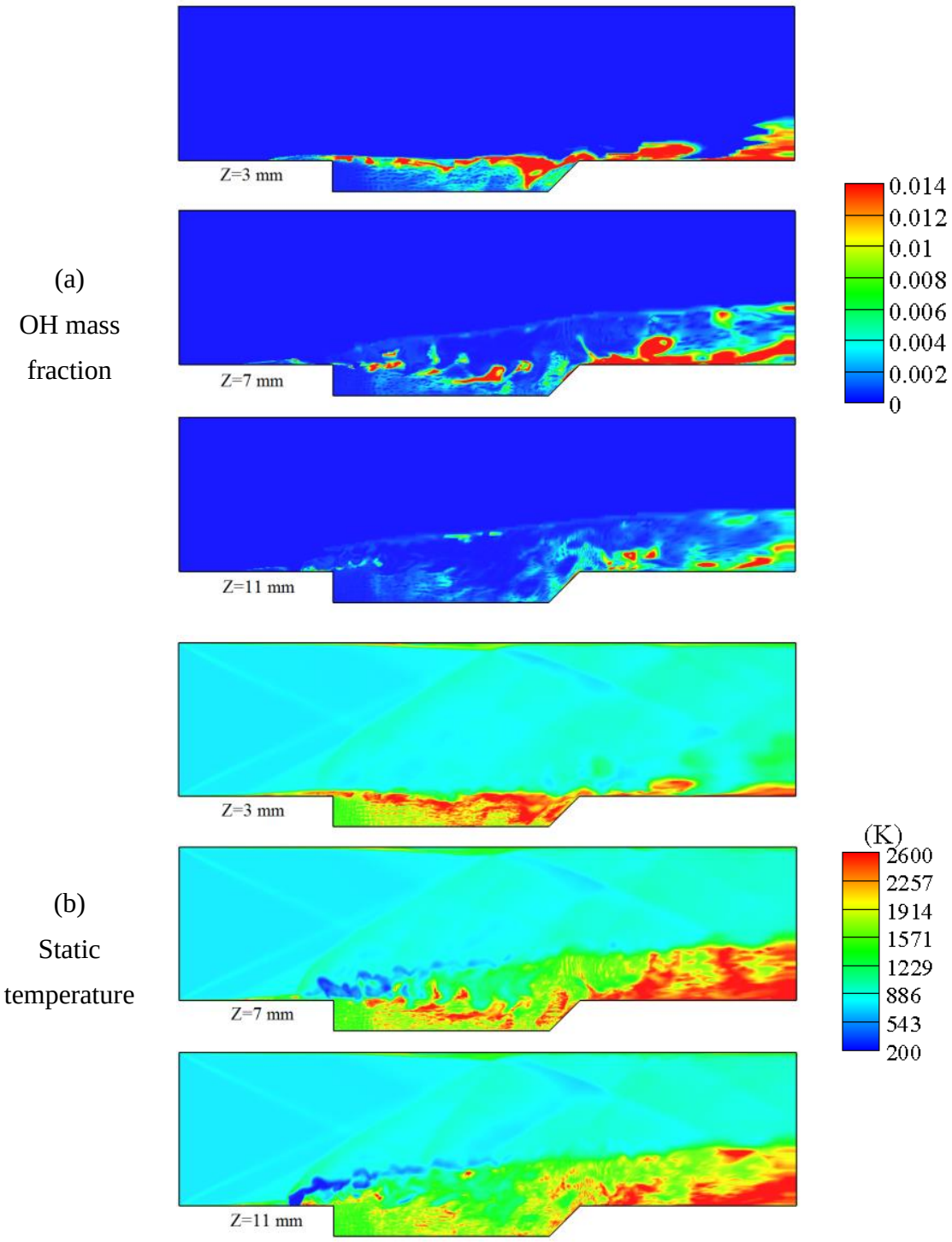

Figure 6.23 Contours of (a) the OH mass fraction and (b) the static temperature at the locations Z = 3, 7 and 11 mm for the UFPV modelling.

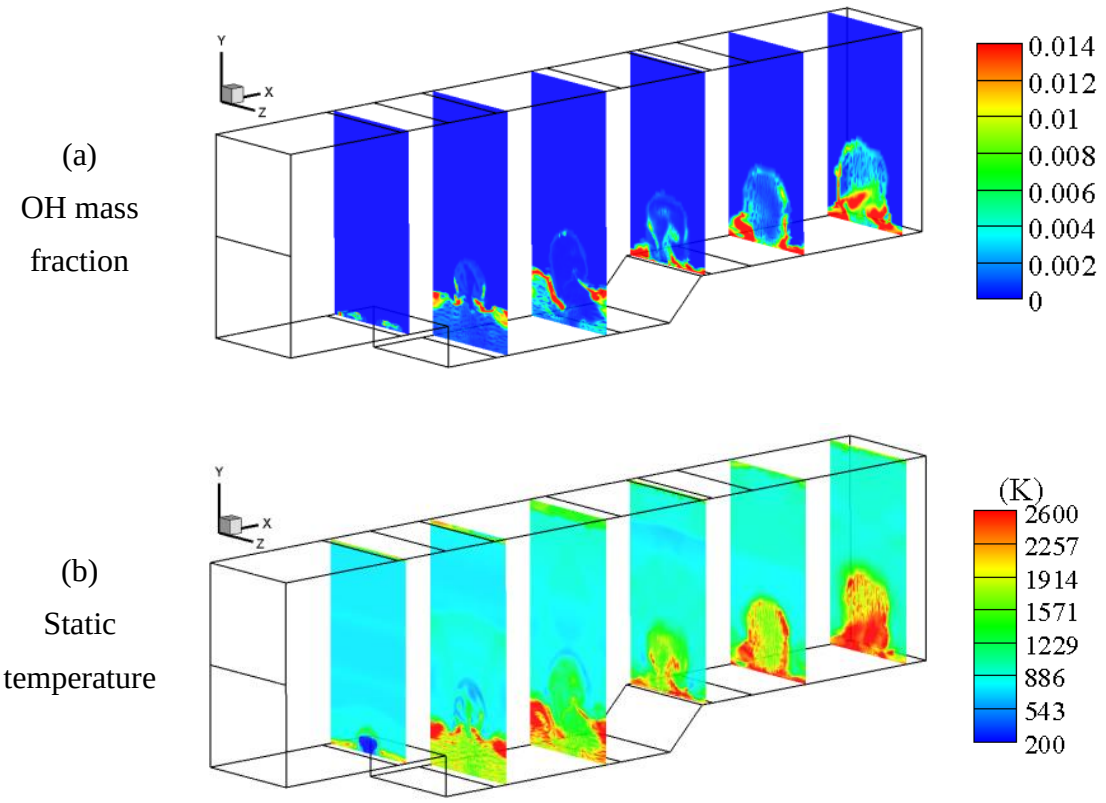

Figure 6.24 Contours of (a) the OH mass fraction and (b) the static temperature at the locations X = 30, 55, 80, 105, 130 and 155 mm for the UFPV modelling.

Figures 6.23 and 6.24 show the contours of the instantaneous OH mass fraction and the static temperature at different locations for the UFPV modelling. Without special declaration, the instantaneous quantities shown in this section are the UFPV modelling results at the time $t = t_0$, and the time $t = 0$ is not important. From Figure 6.23, we observe that both the cavity mixing layer and the outer interface of the hydrogen stream are flammable. Also, see the OH contours at Z = 11 mm in Figure 6.23, we observe that the mixture behind the jet is ignited and combustion occurs in the following cavity mixing layer, which is also revealed by the OH-PLIF images in Figure 6.16. As the flame develops downstream, the flame is distorted by the large-scale structures. Further, some flames in the reacting mixing layer are entrained into the cavity by the vortices and some are rolled up to the hydrogen stream.

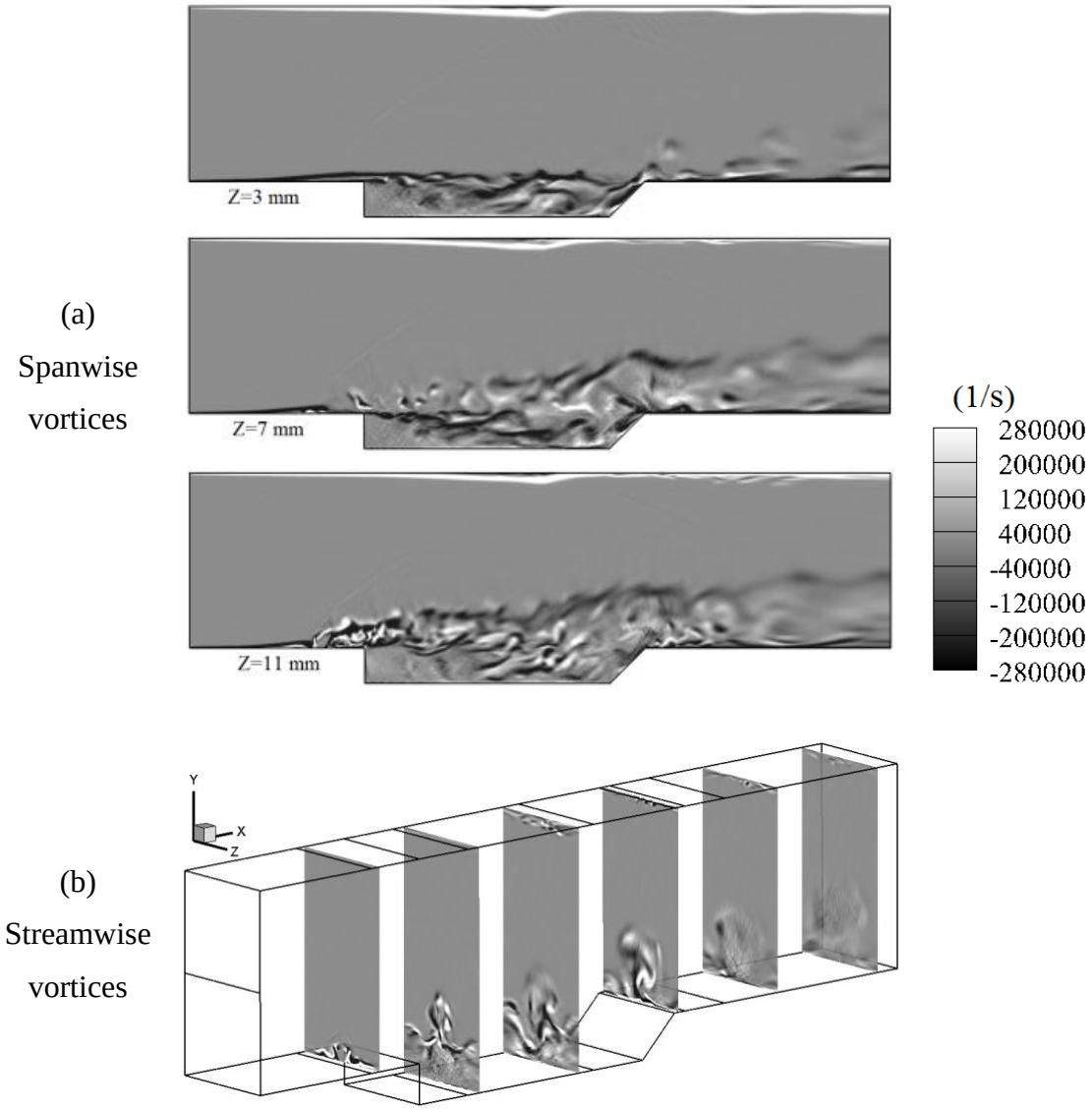

Figure 6.25 Contours of the instantaneous (a) spanwise vortices at Z = 3, 7 and 11 mm, and (b) streamwise vortices at X = 30, 55, 80, 105, 130 and 155 mm of the reacting flows for the UFPV modelling.

Figure 6.25 illustrates the instantaneous spanwise and streamwise vorticity structures of the reacting flows. As seen in Figures 6.23 and 6.25, the shape of the flame at different Z locations is quite related with the shape of the spanwise vortices, especially in the region near the cavity leading edge. Also, from the OH and temperature contours presented in Figure 6.24, and the streamwise vorticity structures in Figure 6.25 at different X locations, it is clear that the streamwise vortices also have a significant impact on the flame surfaces, especially at the

locations X = 80 and 105 mm. Further downstream, the flame develops from reaction surfaces and spots to the reaction zones, and the vortices and their effects become weak due to the heat release during the combustion.

As shown in Figures 6.23 and 6.24, in addition to the cavity mixing layer, the hydrogen stream is also flammable. Different to the flamelet modelling results shown in Figures 6.17 and 6.20, the hydrogen jet in Figure 6.23 is not ignited in the region near the injection hole. Weak combustion occurs in the outer interface of the hydrogen stream downstream and a relative intense combustion is predicted in the outer interface over the cavity. These differences are because the UFPV model has a better performance in predicting the localized extinction and re-ignition phenomena than the flamelet model. More discussion on the localized extinction and re-ignition will be given in the following section. On comparing with the OH-PLIF measurements in Figure 6.16, the distributions of the OH radicals at Z = 11 mm, shown in Figure 6.23, match well with the experimental observations and are better than the results obtained from the flamelet modelling.

Overall, the UFPV model is capable of predicting the supersonic flames in the combustor with a cavity flame holder. Combustion occurs in the cavity mixing layer, some of the reacting mixtures are entrained into the cavity by the vortices and the flames are holed by the cavity. The localized extinction, due to the high strain rate in the region near the hydrogen injection hole, is successfully predicted and the stream is ignited downstream over the reacting cavity mixing layer. Also, the reacting mixing layer and the hydrogen stream interact with each other as the flow proceeds downstream. Also, it is clear that the UFPV model predicts more accurate results than the flamelet model when comparing with the experimental observations illustrated in Figures 6.11, 6.14 and 6.16. More transient results from the UFPV modelling and discussions related to the localized extinction and auto ignition, as well as the flameholding mechanism, are presented in the following sections.

6.4.2.3. Local extinction and autoignition

Fundamentally, supersonic combustion is a complex process which exhibits important characteristics of the finite-rate chemistry, turbulence-chemistry interaction, effects of compressibility, effects of heat release, local extinction and autoignition of combustion as well as a host of other effects. It is well acknowledged that accurately predicting the local extinction and autoignition is an important reference for the performance of advanced turbulent combustion models [230]. To distinguish the capability of predicting local extinction and autoignition, one import criterion is whether the model could accurately predict the lift-off phenomena [149]. The UFPV model has been successfully used for predicting the local extinction and autoignition in non-premixed and partially premixed lifted flames in low speed flows [149]. However few efforts have focused on the local extinction and autoignition occurring in supersonic flames using the UFPV model. Although the UFPV model that is built into the in-house code captures the local extinction and autoignition near the hydrogen jet, as has been discussed in §6.4.2.2, we still need to look into how accurate the UFPV model predicts the local extinction and autoignition events, and also analyse the performance of the UFPV model and understand the characteristics of the supersonic flames in depth.

Diffusion flames may be extinguished by a number of different mechanisms, for instance aerodynamic quenching, thermal quenching and dilution quenching. These quenching effects could cause local extinction of the flame. Previous studies have shown that extinction can be explained by a single flame extinction criterion, known as the Damköhler number criterion [231,232], in which the Damköhler number Da is defined as the ratio of a characteristic fuel–air mixing time divided by a characteristic chemical time. In general, fast mixing and slow chemical reaction corresponds to a small Da number, and the extinction is assumed to occur at critically low values of the Da number [231]. Narayanan et al. [231] and Lecoustre

et al. [233] have studied a Damköhler-number-based flame extinction criterion using the large Activation Energy Asymptotic (AEA) analysis for diffusion flame conditions. In subsequent, performed by Lecoustre et al. [232], the Damköhler-number-based flame extinction criterion as provided by the AEA theory is assessed for its validity in predicting flame extinction, and the results show that the simple Damköhler-number-based criterion can accurately predict the simulated flame extinction events. Considering the relative simplicity and accuracy of the Damköhler-number-based flame extinction criterion, it is employed into the in-house code to identify the local extinction events during the UFPV modelling of the supersonic flames. In the meantime, this criterion is also helpful to analysis the re-ignition events [232].

In Lecoustre et al. [232], the AEA-based-Damköhler number, which is denoted as $\mathrm{Da_{AEA}}$, can be calculated as follows:

$$\mathrm{Da_{AEA}} = \frac{\chi_{q,ref}}{\chi_{st}} \exp\left(T_a \left(\frac{1}{T_{q,ref}} - \frac{1}{T_{st}} \right) \right), \tag{6.1}$$

where $\chi_{q,ref}$ and $T_{q,ref}$ are the stoichiometric scalar dissipation rate and the stoichiometric flame temperature and χ_{st} and T_{st} are the scalar dissipation rate and temperature at $f = f_{st}$, respectively. These quantities have been obtained from simulations of steady state counter-flow diffusion flames in CHEMKIN-CFD in the FLUENT Module [234]. Here, T_a is the activation temperature and can be obtained following the methodology presented by Sun et al. [235] from the equation:

$$T_a = -2 \frac{\partial \ln(f^0)}{\partial \left(\frac{1}{T_{ad}} \right)}, \tag{6.2}$$

where f^0 and T_{ad} are the laminar mass burning rate and the adiabatic flame temperature, which can be computed for a freely propagating adiabatic flame using PREMIX from the CHEMKIN package [236]. In this study, the values of $\chi_{q,ref}$, $T_{q,ref}$ and T_a at 1 atm pressure are about 310 s^{-1}, 1400 K and 14091 K, respectively. It

should be noted that these values vary with pressure. As the supersonic flow is compressible and shocks are present, see Figure 6.21, the pressure is not constant in the combustor. However, the pressure of the flow behind the bow shock, which is produced by the transverse hydrogen injection, is about 1 atm, and the local extinction and re-ignition events in this region are interesting in this research. Therefore the assumption of unique pressure when computing the $\chi_{q,ref}$, $T_{q,ref}$ and T_a is reasonable. Large values of Da_{AEA} correspond to near-equilibrium chemistry, while extinction events are defined as locations where $Da_{AEA} < 1$ [232].

In addition to the local extinction, autoignition or local re-ignition is also a fundamental phenomenon in combustion problems in turbulent reacting flows due to the intensive turbulence chemistry interactions. Sripakagorn et al. [237] discussed different scenarios of re-ignition and three major scenarios are identified: independent flamelet scenario, re-ignition via edge (triple) flame propagation and re-ignition through engulfment by a hot neighbourhood. In supersonic flames, autoignition could be introduced by shock waves, and this was experimentally studied by Ben-Yakar [222]. As has been reviewed in Mastorakos [226], during the autoignition induction time, little fuel and oxygen are consumed, the temperature increases but not significantly, while some intermediate species, e.g. HO_2 increase gradually, and the species HO_2 builds up to a significant level prior to the ignition. The autoignition process is associated with the rapid destruction of the HO_2 and a rapid generation of OH. In order to identify the autoignition events, Gordon et al. [238] developed two numerical indicators: the first indicator is based on an analysis of the species transport with respect to the budget of convection, diffusion and chemical reaction terms; the second indicator is the relative location of the onset of the creation of the species HO_2 ahead of the flame zone.

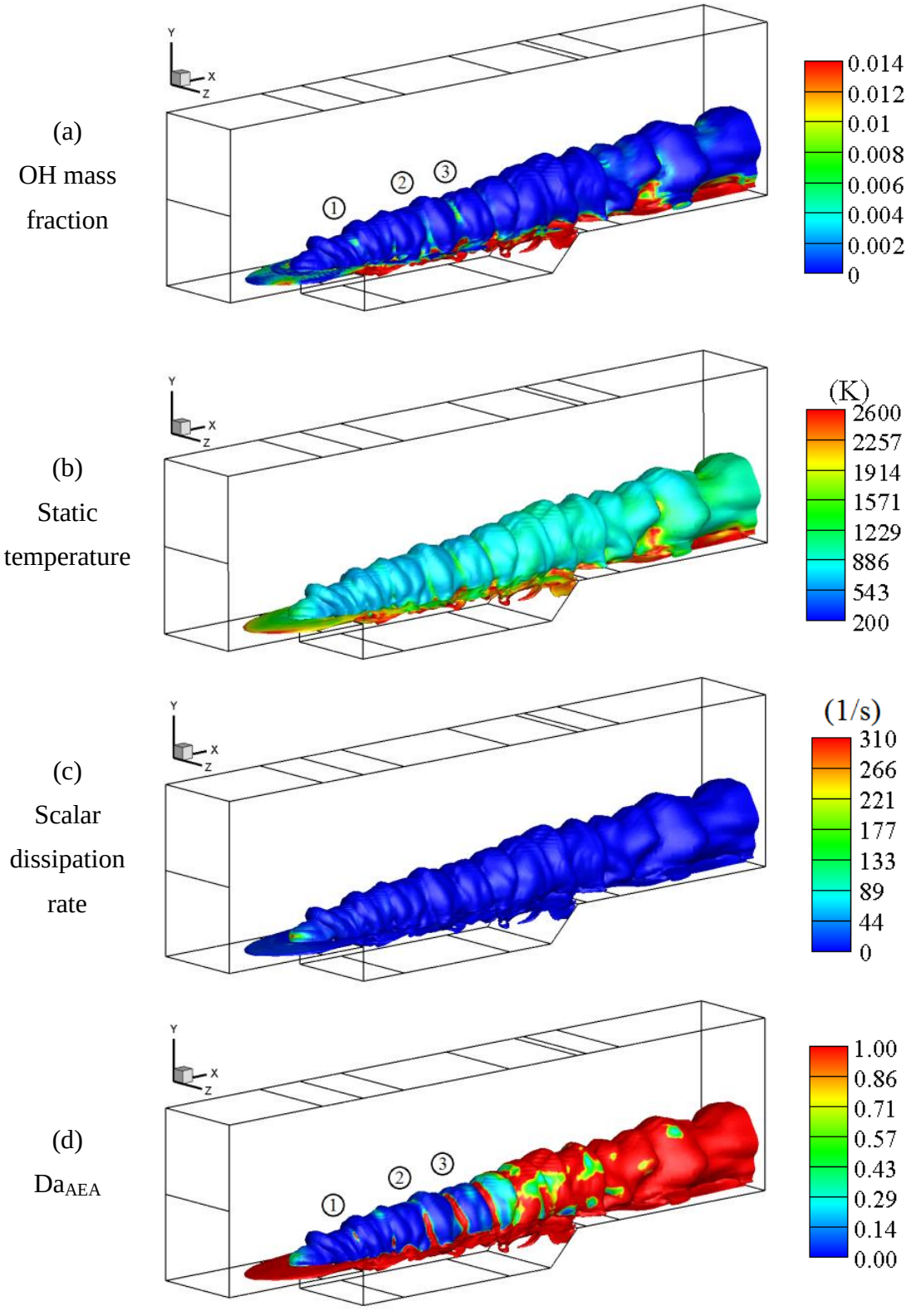

Figure 6.26 The (a) OH mass fraction, (b) static temperature, (c) scalar dissipation rate and (d) Da_{AEA} contours at $f = f_{st}$ iso-surface at time $t = t_0$ for the UFPV modelling.

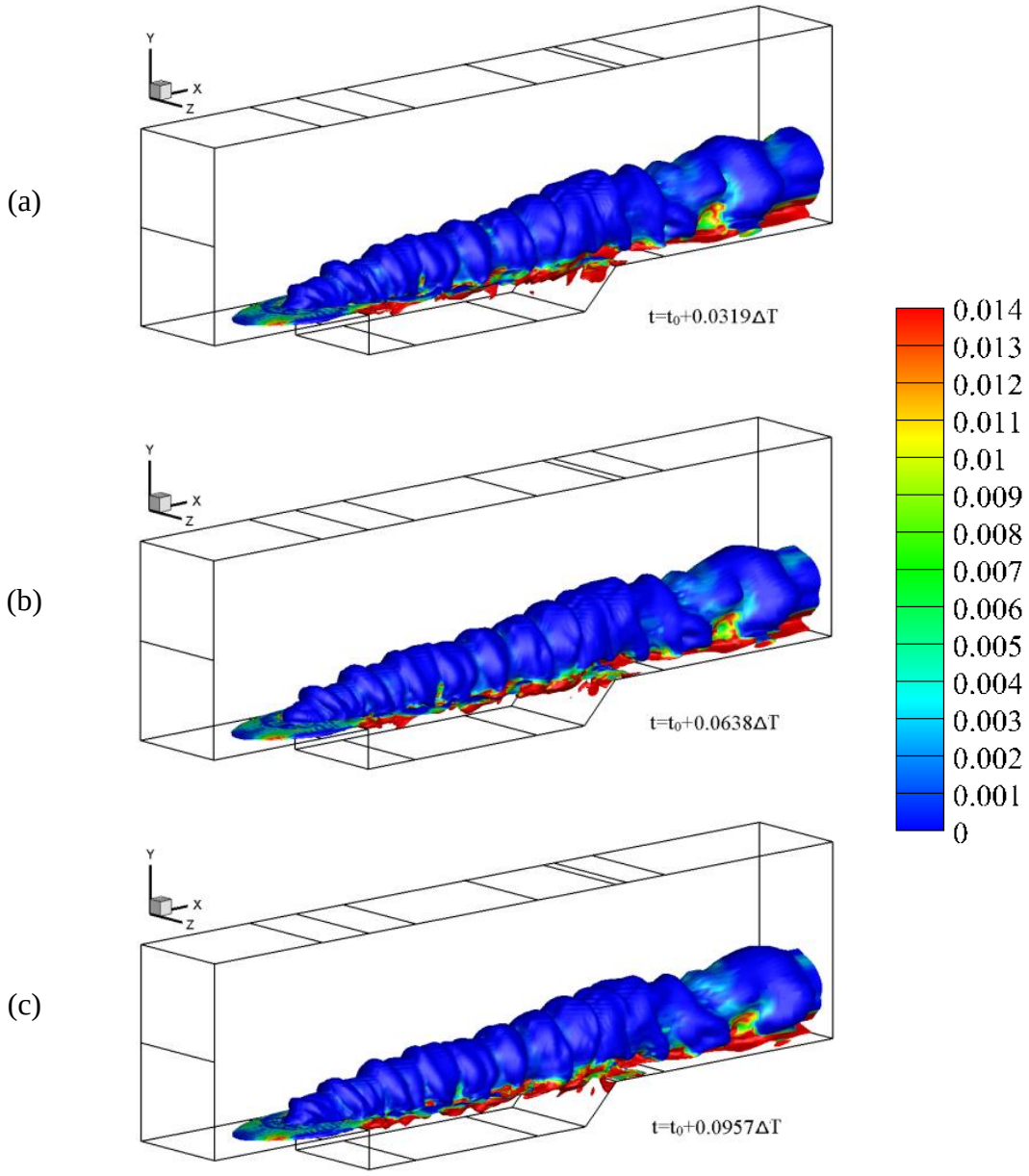

Figure 6.27 The OH mass fraction contours at $f = f_{st}$ iso-surface at different times (a) $t_0 + 0.0319\Delta T$, (b) $t_0 + 0.0638\Delta T$ and (c) $t_0 + 0.0957\Delta T$ for the UFPV modelling.

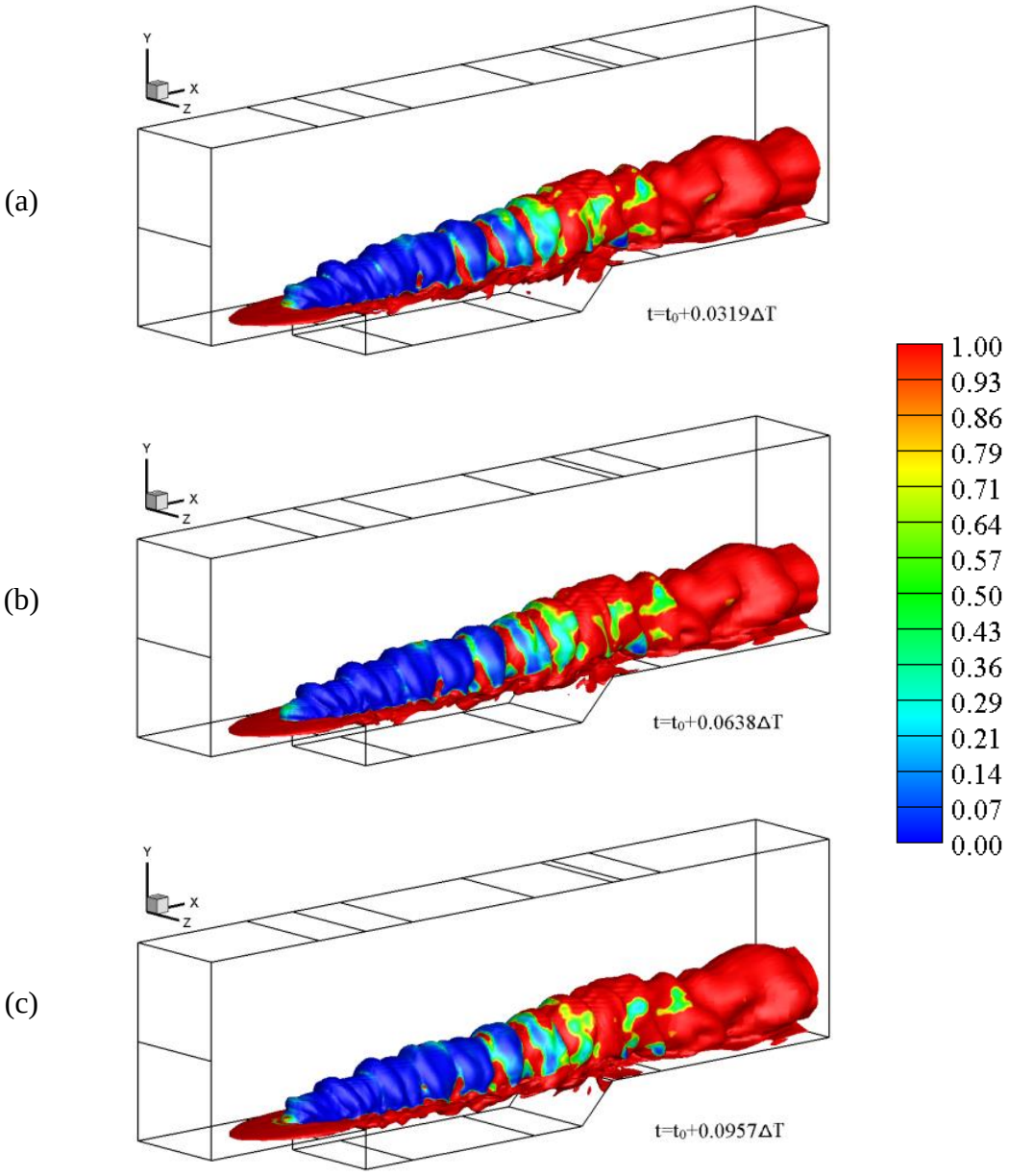

Figure 6.28 The Da_{AEA} contours at $f = f_{st}$ iso-surface at different times (a) t_0 + 0.0319ΔT, (b) t_0 + 0.0638ΔT and (c) t_0 + 0.0957ΔT for the UFPV modelling.

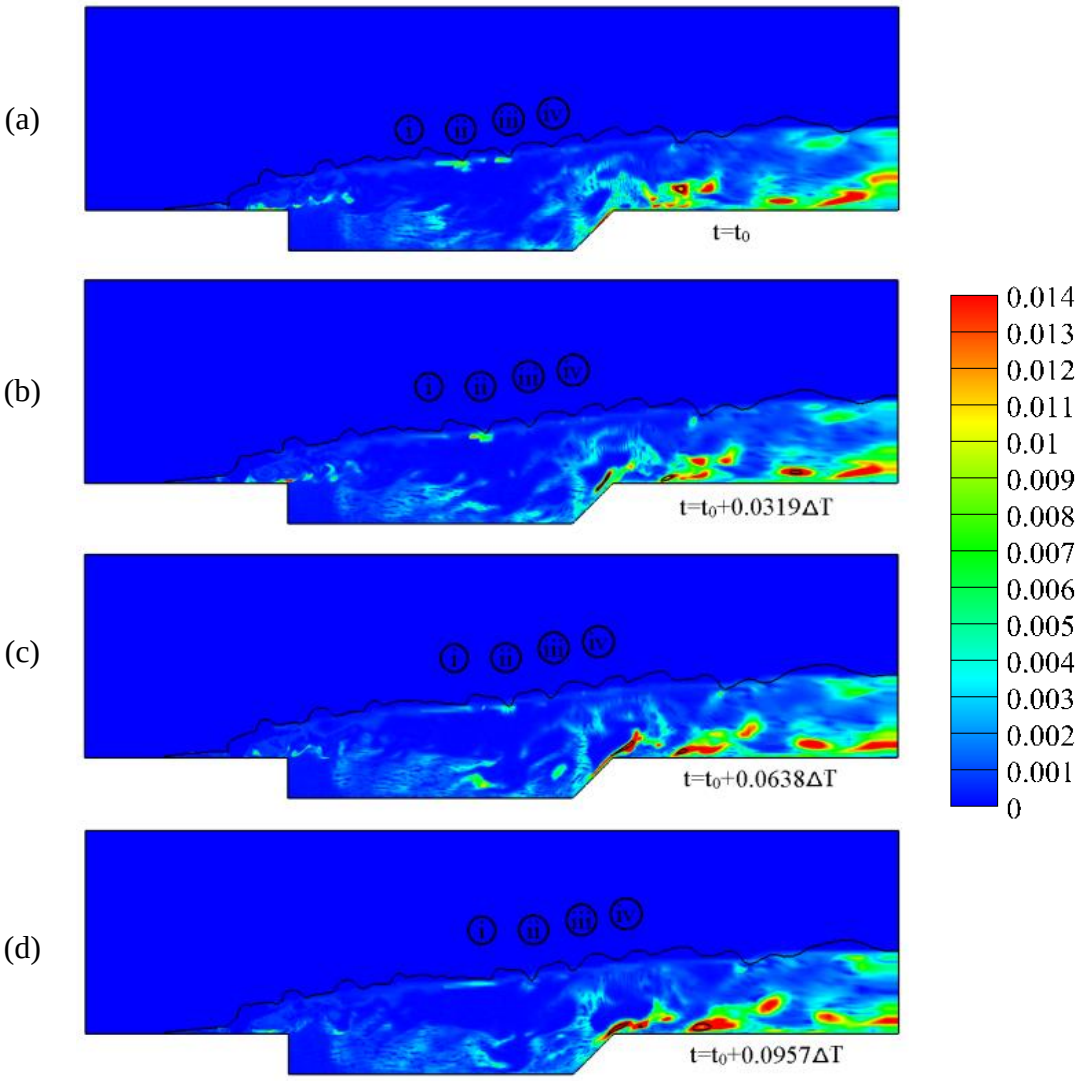

Figure 6.29 The contours of OH mass fraction at the plane Z = 11 mm at different times (a) t_0, (b) $t_0 + 0.0319\Delta T$, (c) $t_0 + 0.0638\Delta T$ and (d) $t_0 + 0.0957\Delta T$ for the UFPV modelling. The solid black lines indicate the flame stoichiometric iso-lines and the symbols (i), (ii), (iii) and (iv) denote the four troughs of the iso-lines.

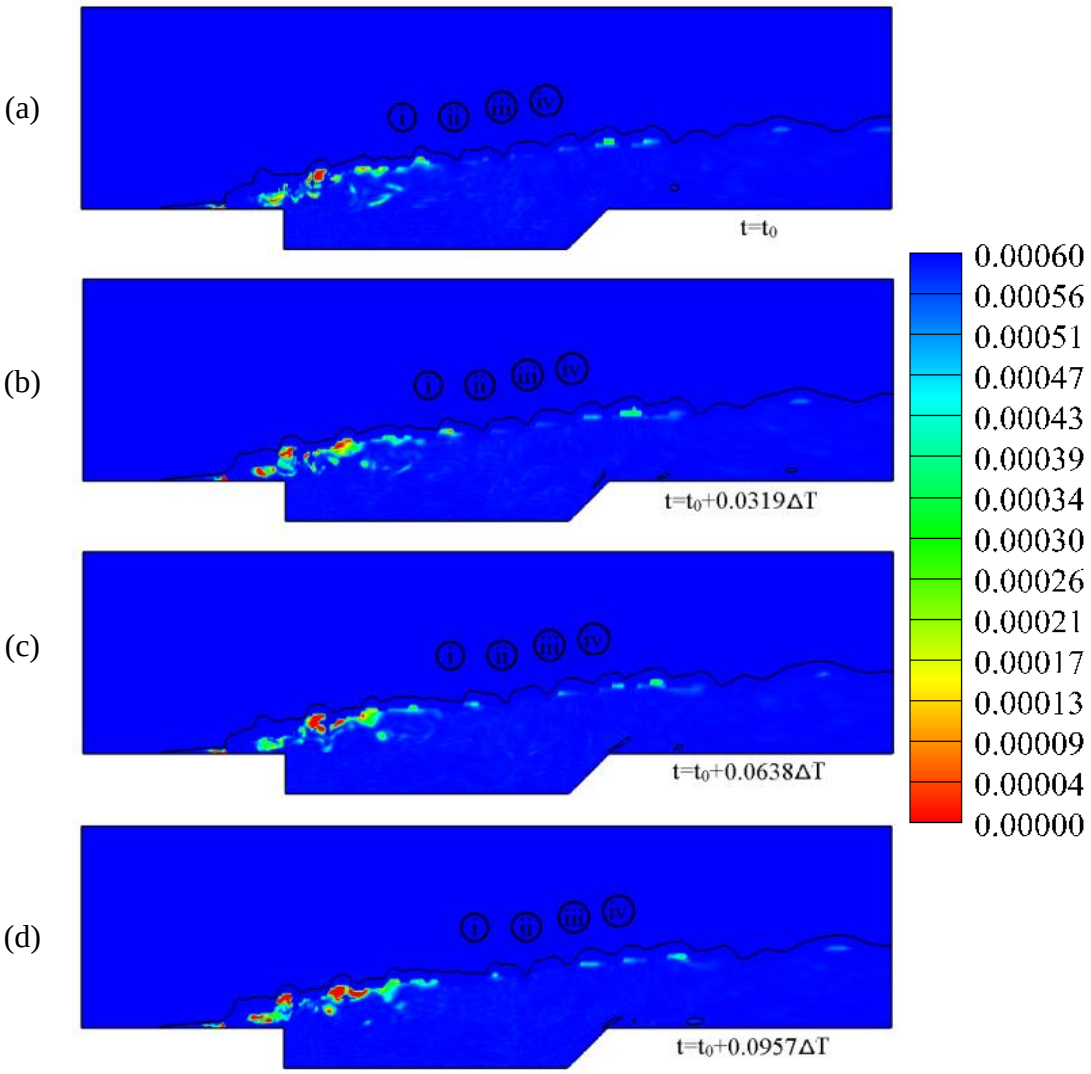

Figure 6.30 The contours of HO_2 mass fraction at the plane Z = 11 mm at different times (a) t_0, (b) $t_0 + 0.0319\Delta T$, (c) $t_0 + 0.0638\Delta T$ and (d) $t_0 + 0.0957\Delta T$ for the UFPV modelling. The solid black lines indicate the flame stoichiometric iso-lines and the symbols (i), (ii), (iii) and (iv) denote the four troughs of the iso-lines.

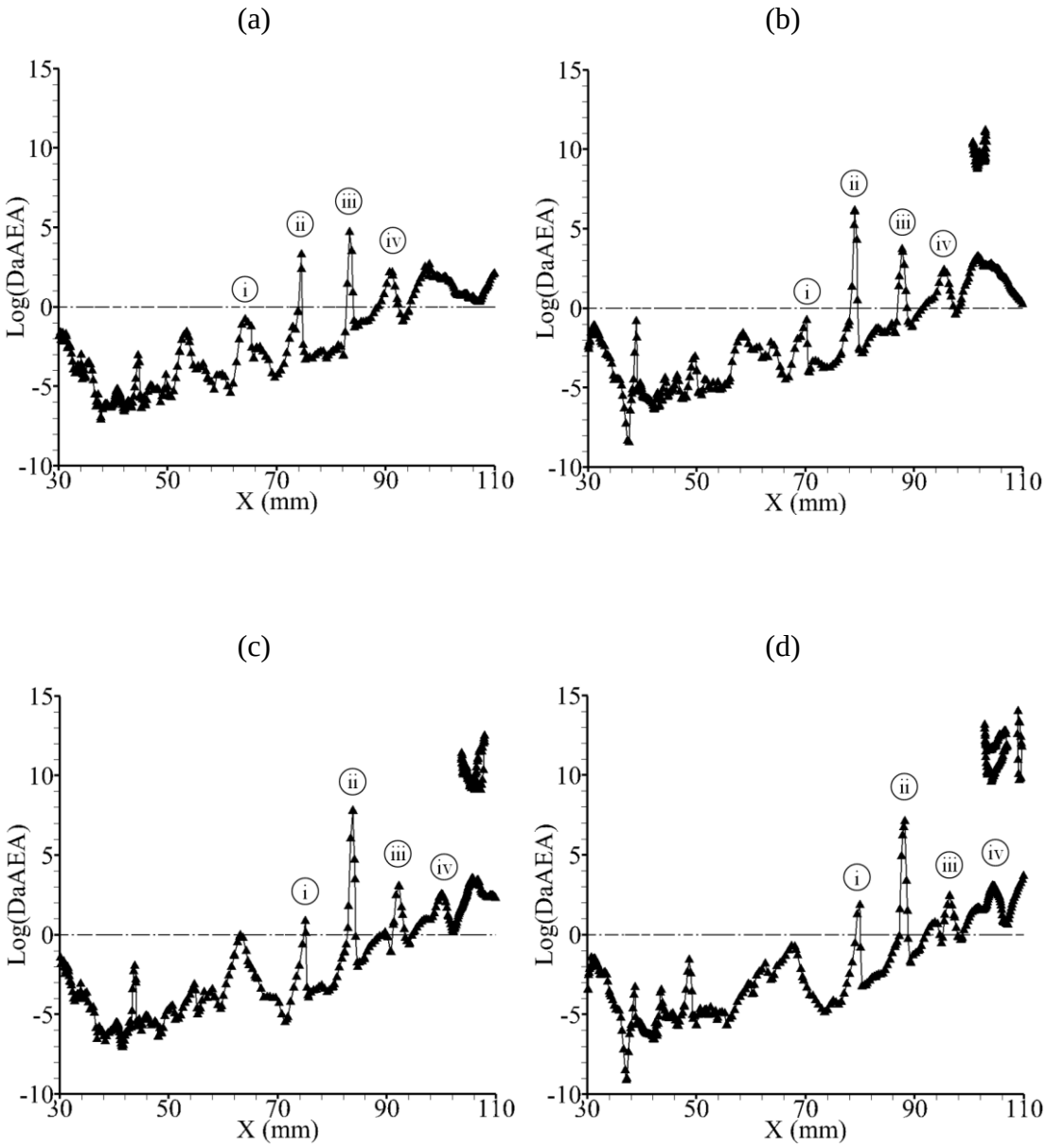

Figure 6.31 Spatial variations of the Damköhler number along the stoichiometric line at the slice Z = 11 mm at different times (a) t_0, (b) $t_0 + 0.0319\Delta T$, (c) $t_0 + 0.0638\Delta T$ and (d) $t_0 + 0.0957\Delta T$ for the UFPV modelling. The solid lines with delta symbols and the dash-dotted lines indicate the log (Da_{AEA}) and $Da_{AEA} = 1$, respectively. The symbols (i), (ii), (iii) and (iv) denote the four spikes of the log (Da_{AEA}) profiles and correspond to the four troughs of the stoichiometric iso-lines in Figures 6.29 and 6.30.

In the present study, the HO_2 indicator is employed to analyse the occurrence of autoignition, the local peak value of the radicals OH is used to characterize the combustion intensity. While, the Damköhler number Da_{AEA}, which is measured on the stoichiometric iso-surfaces, is used to identify the weakest points of the flame and the presence of extinction events.

Figure 6.26 illustrates the instantaneous contours of the OH mass fraction, static temperature, scalar dissipation rate and Da_{AEA} at the iso-surface of the stoichiometric mixture fraction $f = f_{st}$. We observe that these quantities are well correlated and provide a simple test to evaluate the validity of the AEA-based Damköhler number concept for flame extinction predictions. As seen in the contours of the OH mass fraction and the temperature, it is clear that combustion occurs at the $f = f_{st}$ iso-surfaces in the cavity mixing layer and at the downwarps of the wrinkled iso-surfaces. The hydrogen jet near the injection hole is not ignited due to the high scalar dissipation, see the scalar dissipation rate contours in Figure 6.26. However, it is clear that the flammable mixture is not always ignited, even when the scalar dissipation rate is not high. This indicates that the scalar dissipation is able to identify the region with a different strain rate which is related to the extinction, but it is not an absolute indicator to identify the extinction events

As observed in Figure 6.26, the value of Da_{AEA} at the $f = f_{st}$ iso-surfaces at the front of the hydrogen jet is greater than 1, and this means extinction events are not captured in this region. This is because of the quenching effects of the cold wall, i.e. the reaction-breaking effect and heat transport from the flame to the cold wall are not considered when defining the Da_{AEA} number. On the other hand, in the regions downstream of the cavity, a high Da_{AEA} value is shown at the $f = f_{st}$ iso-surfaces, however the OH mass fraction is not correspondingly high. This is because the temperature of the reacting flow downstream is increased, not only by the localized combustion but also it can be increased by the transport from nearby high

temperature region through convection and diffusion. This transport effect is also not considered in the definition in Equation (6.1). However, in the regions near and behind the hydrogen injection hole, and in and over the cavity mixing layer, extinction events are successfully identified. We should emphasize that the local extinction and reignition events in these regions have a great impact on the reacting flows downstream, and therefore their predictions and identifications are more important than those downstream. In these regions, the locations where the value of Da_{AEA} at the $f = f_{st}$ iso-surfaces is low, are almost identical with the locations with low OH mass fraction value. In contrast, the high Da_{AEA} number in the cavity mixing layer and the ①, ② and ③ downwarps of the wrinkled $f = f_{st}$ iso-surfaces means that the mixture may be ignited, and the OH contours show that the combustion does occur in these regions.

From the above discussion, we conclude that the local minima of Da_{AEA} are interpreted as the weakest points of the flame. Figures 6.27 and 6.28 present how the weakest points of the flame are tracked in time. Considering the reacting flows over the cavity, from Figures 6.26, 6.27 and 6.28, we can observe that combustion occurs in the ①, ② and ③ downwarps of the wrinkled $f = f_{st}$ iso-surfaces at time $t = t_0$ but gets weaker and weaker as time goes on. At time $t = t_0 + 0.0957\Delta T$, the flames in the ①, ② and ③ downwarps are totally extinguished. Therefore, the local extinction events are successfully predicted by the UFPV model and are identified by the Da_{AEA} number.

Figures 6.29 and 6.30 show the OH mass fraction and the HO_2 mass fraction contours at different times for the UFPV modelling, respectively, and the solid black lines indicate the flame stoichiometric iso-lines, i.e. $f = f_{st}$. The symbols (i), (ii), (iii) and (iv) denote the four troughs of the iso-lines. As observed in Figures 6.29 and 6.30, it is clear that the iso-lines are wrinkled and distorted by the vortices. Near the troughs of the wrinkled iso-lines, such as the troughs (ii) and (iii) at time $t = t_0$, the

OH mass fraction has a relative high value, and therefore combustion occurs nearby. This means that the vortices near the stoichiometric iso-lines can provide an ideal condition under which the mixture can be ignited, and the flames develop downstream together with these vortices. As time goes on, the OH radicals near the troughs (ii) and (iii) become fewer and fewer and this is because the intermediate species OH are consumed and also they may be transported to their surroundings. The spatial variations of the Damköhler number along the stoichiometric iso-line, shown in Figure 6.31, indicate that local extinction does not occur near (ii) and (iii) between the times t_0 and $t_0 + 0.0957\Delta T$. This means that the supersonic flames can be successfully held in the troughs of the stoichiometric iso-line, or in other words the downwarps of the stoichiometric iso-surface.

Figures 6.29 and 6.30 indicate the evolution of the reacting flows through the OH and HO_2 mass fraction contours and the Da_{AEA} number along the stoichiometric iso-lines at different times. It should be noted that the four spikes (i), (ii), (iii) and (iv) of the log (Da_{AEA}) profiles in Figure 6.31 correspond to the four troughs (i), (ii), (iii) and (iv) of the stoichiometric iso-lines in Figures 6.29 and 6.30. Therefore we use the same symbol to locate the related spike and trough in this study. At the location (i), a few of the OH radicals are predicted at time $t = t_0$. As time proceeds to $t_0 + 0.0957\Delta T$, a large number of OH radicals are built up. The value of log (Da_{AEA}) at the location of (i) develops from about -1 to 2, as shown in Figure 6.31. This indicates that the mixture near (i) evolves from no-combustion or slow-combustion state at t_0 to a relative intense combustion state at $t_0 + 0.0957\Delta T$.

From the contours of the HO_2 mass fraction in Figures 6.29 and 6.30, we find that there are a large number of HO_2 radicals prior to the flames near (i). As discussed at the beginning of this section, the HO_2 indicator has been proven to be a good indicator for identifying the autoignition events in turbulent flames [238]. Therefore we can conclude that autoignition occurs in the region near (i) and the

autoignition events contribute to the above-mentioned evolutions. Moreover, there are a number of HO_2 radicals behind (i) and before (ii). These HO_2 radicals contribute to the development of the flame near (ii).

From the mean OH mass fraction contours shown in Figure 6.22, we find that the combustion which occurs in the region of the upper interface of the air and hydrogen streams is not an accidental phenomenon. Therefore, it is reasonable to forecast that the flame near (i) at $t_0 + 0.0957\Delta T$ will develop downstream and has a similar behaviour to the flames near (ii), (iii) and (iv) as the time goes on. In the meantime, a new flame, which is upstream and similar to the flame near (i), will be formed through the autoignition of the mixture. As the hydrogen jet provides sustained fuel into the combustor, in such a way, the flames in the regions near the stoichiometric iso-line will keep going on and on.

In Figures 6.29 and 6.30, there are some small closed stoichiometric iso-lines downstream of the cavity and most of the closed curves disappear in the next time moment. This is because of the intense turbulence in this region. As observed in Figure 6.25, the bottom part of the hydrogen stream hits the cavity aft wall, intense turbulence and strong vortices are produced and the vortices distort the flames. Some of the unburnt mixture is engulfed into the distorted flames and ignited by these surrounding hot flames. The value of the Da_{AEA} number at these small closed stoichiometric iso-lines is very high, as shown by the individual profiles in each image in Figure 6.31. Therefore, these unburnt mixtures combust rapidly and do not last long. This process can be regarded as reignition or autoignition due to engulfment by the hot neighbourhood, which is the third reignition scenario in Sripakagorn et al. [237].

Overall, due to turbulent mixing fluctuations, the turbulence-chemistry interactions and compressibility effects, local extinction, reignition and autoignition events are very common phenomena in the supersonic combustion in a cavity-based

combustor. The UFPV model is able of predicting these events in this supersonic combustion case with reasonable accuracy. Thus, the AEA-based Damköhler number concept can accurately identify the occurrence of the local extinction events in the regions near and behind the hydrogen injection hole and in and over the cavity mixing layer. Further, the Da_{AEA} number is a valuable metric to identify flame weakening and extinction in supersonic flames. Together with the OH radicals, the distribution of the HO_2 radicals can assist in identifying the autoignition events in the supersonic flame and further understand the flameholding mechanism.

6.4.2.4. Flameholding mechanism in a cavity flameholder with fuel injected upstream

In order to understand the flame stabilization mechanism of the cavity flameholder, both experiments [239,11,220,240] and simulations [11,220] were performed. Rasmussen et al. [239] investigated the flame stabilization mechanism in a flameholder with a Mach 2.4 free stream through imaging laser-induced fluorescence of OH and CH_2O. During their research, the ethylene was directly injected into the cavity. When injected from the aft wall, primary combustion occurred under the shear layer and in the aft region of the cavity volume. In contrast, when fuel was injected from the floor, a jet-driven recirculation zone of hot products near the upstream wall of the cavity served as a flameholder and the combustion then occurred on the underside of the shear layer [239]. Sun [11] studied the combustion in a supersonic combustor with hydrogen injection upstream of the cavity flameholders using OH-PLIF and hybrid RANS/LES. It was shown that a recirculation-zone ignition mechanism and a triple flame stabilizing mechanism are both plausible flameholding mechanisms of cavity flameholders and these two mechanism types compete with each other on igniting the fuel.

Wang et al. [220] experimentally and numerically investigated the combustion characteristics in a supersonic combustor with hydrogen injection upstream of a cavity flameholder. They revealed that flames may intermittently appear upstream of the cavity leading edge. However, the combustion is stabilized in the cavity mode at most times and cannot be stabilized in the jet wake without the cavity flameholder. Therefore, the cavity-stabilized combustion appears to be a strongly coupled process of the flow and heat release around the cavity flameholder.

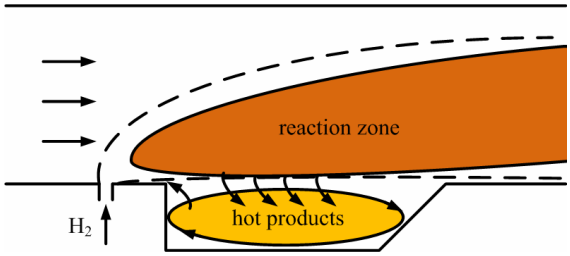

(a) Cavity assisted jet-wake stabilized combustion mode.

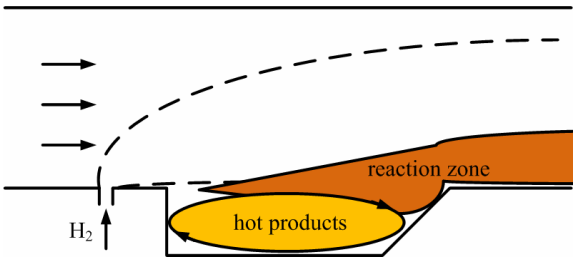

(b) Cavity shear-layer stabilized combustion mode.

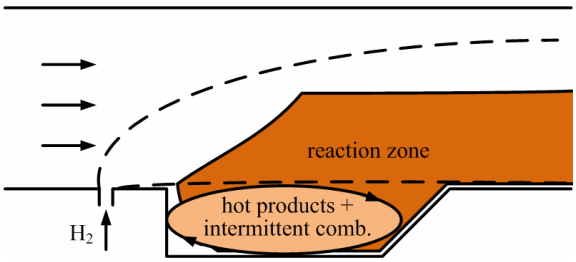

(c) Combined cavity shear-layer/recirculation stabilized combustion mode.

Figure 6.32 Schematic of the different combustion modes, obtained from [240].

In another experimental study performed by Wang et al. [240], optical diagnosis-based measurements, including OH-PLIF, OH spontaneous emission,

high-speed framing of flame luminosity and Schlieren were introduced to characterize the supersonic reacting flows in a cavity-based combustor. The hydrogen is transversely injected into the combustor upstream of the cavity. In their research, three combustion modes were observed: cavity assisted jet-wake stabilized combustion, cavity shear-layer stabilized combustion, and combined cavity shear-layer/recirculation stabilized combustion. The schematic of the combustion modes are shown in Figure 6.32. Also, it is found that the cavity assisted jet-wake stabilized combustion was the most unstable mode, while the combined cavity shear-layer/recirculation stabilized combustion mode appeared to be the most robust one [240].

Although several important characteristics of the cavity-organized supersonic combustion have been realized, there are still many open questions regarding the physical mechanisms of ignition and flameholding. From the PLIF images in Figure 6.16 and the UFPV modelling results in Figure 6.29, we can observe that combustion always takes place in the cavity, in the cavity mixing layer and at the outer interface of the air and the hydrogen streams. Then, several questions are raised:

(i) How are these flames produced?

(ii) How are these flames maintained?

(iii) How do these flames interact with each other?

The answers to these questions can assist us in understanding the flameholding mechanism in the cavity flame holder with fuel injected upstream. Based on the experimental results and the numerical results presented in §6.4.2.2 and §6.4.2.3, we can conclude that the combustion in this case is in the combined cavity shear-layer/recirculation stabilized combustion mode. Then, this section focuses on the flameholding characteristics and mechanisms in a cavity flameholder with fuel

injected upstream through analysing the experimental observation in Fan [154] and the UFPV modelling results.

In the present study, we divided the reaction zone in the cavity-based combustor into five subregions and a schematic of these reacting subregions where the combustion takes place are shown in Figure 6.33. Subregion (I) is the wake of the hydrogen jet and is regarded as the pre-ignition region, in which the species HO_2 builds up to a significant level prior to the ignition. Subregion (II) is a part of the outer interface of the air stream and hydrogen stream. Subregion (III) is the region where the cavity mixing layer locates. Subregion (IV) is the cavity region and subregion (V) is the rest of the reacting regions in the combustor. Strictly speaking, part of one subregion will overlap with the other subregions nearby.

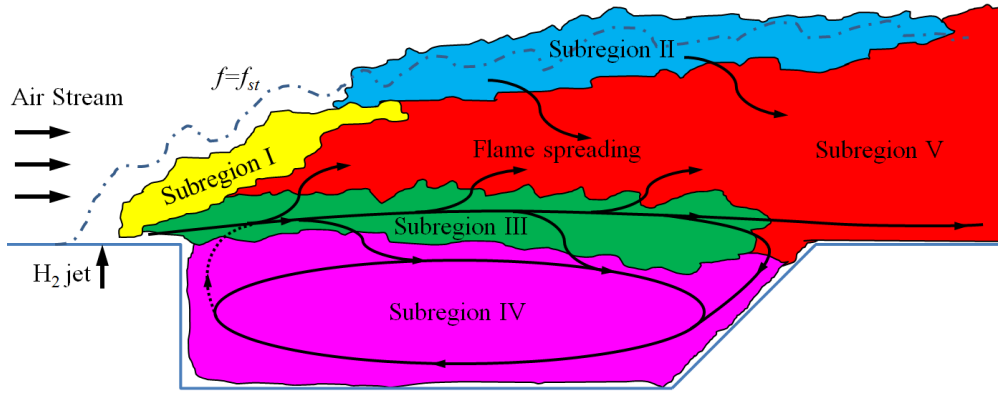

Figure 6.33 Schematic of the reacting subregions in the combustor. The dash-dot line is the stoichiometric iso-line. The arrowed solid line shows the propagation and spreading of the flames between subregions.

Figure 6.33 shows the possible flame holding and spreading in the combustor. The combustion is expected to be stabilized via a dynamic process during which the reacting flows in the different subregions interact with each other. No matter which subregion it is in, the fuel needs to be mixed on a molecular level with the air so as to become ignited. If the fuel and the air are premixed, the fluid may be ignited at a distance of l downstream, as shown in Figure 6.34. If the fuel and the air are non-

premixed, autoignition may occur at two different positions as there may be two stoichiometric iso-lines. Basically, if the premixed and the non-premixed cases are under the same condition, including fuel-air ratio, pressure, temperature and velocity, etc., l will be shorter than l_I and l_{II} because of the presence of the mixing time in the non-premixed case. Normally, l_I is shorter than l_{II}, because the fluid in the cavity is easier to ignite as the velocity there is slower than in the main stream. In addition to the velocity and the mixing process of the flow, l_I and l_{II} are also affected by the chemical kinetics of the reactants, such as the induction time τ_i.

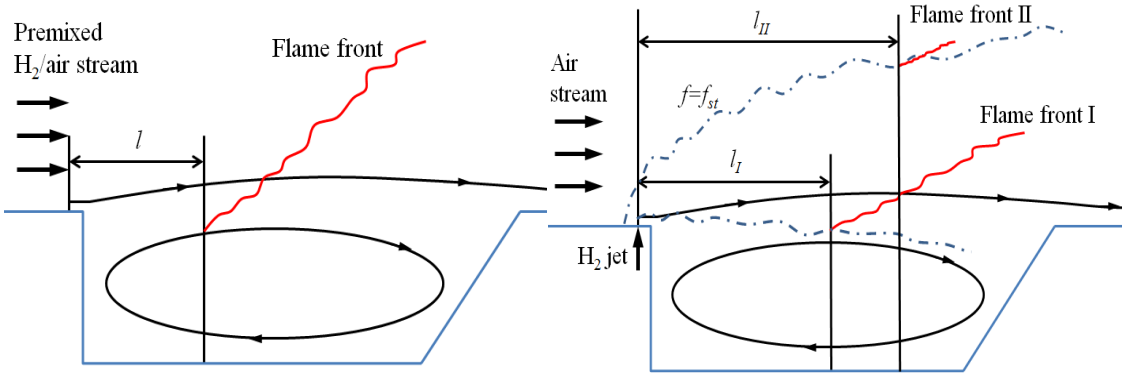

Figure 6.34 Schematic of autoignition under premixed (left) and non-premixed (right) conditions in a cavity-based combustor. l is the distance between the fuel inlet and the position where the fluid is ignited. Notes "I" and "II" are used to distinguish the two flames under non-premixed condition.

An induction period in the chemical kinetics is an initial slow stage of a chemical reaction, after which the reaction accelerates. The induction time here denotes the time from the moment that the fuel has ideally mixed with the air until the moment that autoignition occurs. In a non-premixed case, the autoignition time τ_{ai} includes the mixing time τ_m and the induction time τ_i. If τ_{ai} is too large, the reactants will not become ignited before they are blown out of the combustor. While, if τ_{ai} is small, autoignition may occur downstream. Sun [11] reviewed the experimental measurements of the ignition delay time, i.e. the induction time in the

premixed hydrogen/air combustion and calculated the ignition delay time using CHEMKIN 2.0 [236] under different conditions, as seen in Figure 6.35. It is found that, under high temperature conditions, the ignition delay time is in the range of 10~100 μs. If the hydrogen and the air are ideally mixed, the autoignition induction distance in a supersonic flow is of the order of a cm. Therefore, from the chemical kinetics aspects, autoignition is a possible event in a cavity-based supersonic combustor.

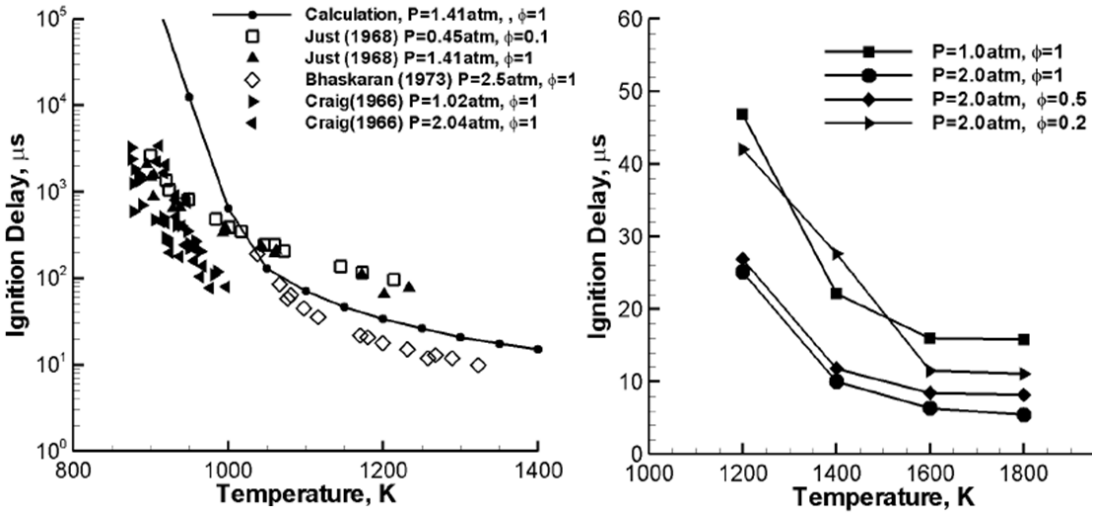

Figure 6.35 Ignition delay time of the premixed hydrogen/air combustion obtain from experimental measurements (left) and calculations (right) under different pressure, temperature and equivalent ratio conditions, from [11].

From the simulation results shown in §6.4.1 and §6.4.2, we observe that the hydrogen jet produces a small low-velocity region, i.e. a small wake behind the jet. The horseshoe vortex and the counter-rotating vortex pair formed around the jet layer tend to transport some fuel into this region, making the fluid there partially premixed. Due to the intensity of the vortices there, it is reasonable to assume that fast mixing is achieved in this region. Therefore, the mixing time τ_m is negligible and the autoignition time is dominated by the induction time τ_i. As the mixture proceeds

downstream into the subregion (I), only a small amount of the fuel and oxygen are consumed and the temperature and pressure increase. Some intermediate species, e.g. HO_2 increases gradually, and the HO_2 builds up to a significant level prior to the ignition, as shown in Figure 6.30. From the discussion in §6.4.2.3, we know that the accumulated pre-ignition species HO_2 may destruct rapidly and this is followed by a rapid generation of the species OH. This transformation means the occurrence of autoignition and takes place near the troughs of the stoichiometric iso-line or the downwarps of the stoichiometric iso-surfaces in the subregion (II). After autoignition occurs, the simulations show that reaction fronts propagate to consume the partially premixed reactants downstream. Also the flames in the subregion (II) will propagate and spread into the subregion (V).

Concerning the reacting mixing layer in the subregion (III), we know that combustion always occurs in this vicinity. It is reasonable to predict that the induction reactions in the subregion (I) and autoignition could contribute to the combustion in the cavity mixing layer. However, the distance from the hydrogen jet centre to the leading edge of the cavity is only 1 cm. In this distance, the mixing and induction reaction may not be completed, and this is because the autoignition induction distance in this case is of the order of a cm. Therefore, a combination of autoignition and diffusion from the hot fluid in the cavity is a possible flameholding mechanism for the combustion in the subregion (III).

Further, from Figures 6.23 to 6.30, we observe that the combustion in the subregions (III) and (IV) are, as expected, stabilized around the cavity mixing layer and the cavity via a dynamic process. Firstly, the vortices observed in Figure 6.25 assist in transporting some of the fuel into the shear layer, making the fluid partially premixed and combustible. Secondly, from Figures 6.29 and 6.33, it is observed that the flames in the cavity mixing layer impinge with the cavity aft wall. Some of the flames curl into the cavity and the other passes over the cavity. The flames in the

reacting mixing layer can also be directly entrained into the cavity by the vortices. All these flames can enhance the combustion in the cavity and remain in the cavity to ensure a continuous environment with a high temperature. Thirdly, the recirculation in the cavity is available to provide a low-speed location where the flow and the flame propagation could achieve a balance. Fourthly, the combustion and the hot products within the cavity recirculation are beneficial to enhance the ignition and combustion in the subregion (III). Finally, the hot recirculation in the cavity lifts the reacting mixing layer. The hot products in the cavity could be transported to the leading edge of the cavity, thus increase the pressure and temperature, bring more intermediate radicals and reduce the induction time. These effects could even reach the subregion (I) because of the presence of the vortices and recirculation upstream of the cavity leading edge. Therefore, the flameholding characteristics of the mixing layer and the cavity are highly coupled and the combustion in these two regions interacts with the induction reactions in the wake of the hydrogen jet.

Overall, combustion is observed at the outer interface of the air stream and hydrogen stream, in the cavity mixing layer and in the cavity. Combustion at the outer interface of the air and the hydrogen streams is mainly dominated by autoignition. However, the cavity plays a more important role on the flameholding than does the autoignition. Without the cavity, stable combustion may not be maintained and the combustion in the cavity and in the cavity mixing layer is highly coupled. However, the combustion in the cavity is dominated by flame propagation. Both the autoignition and flame propagation contribute to the combustion in the mixing layer. Once the combustion is stabilized in the subregions (II), (III) and (IV), the flames spread to the main flow and ignite the mixture in subregion (V). In the traditional sense, the flameholding is considered to be accomplished through mass and heat diffusion. However, it is impossible to be achieved under supersonic combustion conditions due to the low flame speeds (about 10 m/s) but very high

flow velocity (about 1000 m/s) [220]. Therefore, the reactants could be ignited through autoignition and flame propagation processes; however, the spreading of the flame is achieved not only by the diffusion process but also by the convection process.

6.5. Closure

In this chapter, large eddy simulations of non-reacting and reacting flows are performed to model the Fan's cavity case in order to validate the flamelet and the UFPV combustion models, as well as to understand the mixing, local extinction and autoignition, flameholding and combustion characteristics of the gaseous fuel injected upstream of the cavity.

Firstly, simulations of the non-reacting flow are performed using the in-house code and FLUENT. The results obtained reveal that the difference between the two codes, such as the sub-grid scale models and the treatment of the wall, can produce differences in the predictions. However, several common conclusions are obtained from the simulations, namely,

(i) The velocity is lower and the temperature is higher in the cavity than in the other regions.

(ii) Both the streamwise and spanwise vortices enhance the mixing between the hydrogen and the air in the cavity, the cavity mixing layer and the outer interface of the hydrogen and air streams.

(iii) The region near the cavity aft and bottom walls has an ideal mixing level of the reactants and a low flow velocity and therefore will be a good place to ignite the mixed gas.

Secondly, the reacting flows are simulated with the flamelet and the UFPV models. The flamelet model is capable of simulating the supersonic combustion process in the cavity-based scramjet combustor, with the capturing of most of the characteristics of the flame, such as the combustion in the cavity and the cavity mixing layer, the interaction between the flame and the turbulence, etc. However, on the one hand, the reacting flows in the cavity are differently predicted by the two codes. This mainly results from the differences in the modelling of the mixing process because different sub-grid scale models and near-wall-treatment methods are employed in the two codes. On the other hand, the outer interface of the hydrogen jet is ignited just after the injection in the flamelet modelling. This is because the flamelet model does not take the local extinction and re-ignition effects into account and therefore is clearly incapable of accurately modelling the supersonic flame. Subsequently, the reacting flows are modelled with the UFPV model which is built into the in-house code. In addition to the characteristics of the flame revealed by the flamelet modelling, the localized extinction due to the high strain rate in the region near the hydrogen injection hole is successfully predicted. Also it is clear that the UFPV model predicts more accurate results than does the flamelet model when comparing the predictions with the experimental observations.

Thirdly, local extinction, reignition and autoignition phenomena are investigated based on the experimental observations in Fan [154] and the UFPV simulations in the present study. It is found that due to the turbulent mixing fluctuations, turbulence-chemistry interactions and compressibility effects, local extinction, reignition and autoignition events are very common phenomena in the supersonic combustion in a cavity-based combustor. The UFPV model is able to predict these events in this supersonic combustion case with reasonable accuracy. The Da_{AEA} is a valuable metric to identify the flame weakening and extinction in supersonic flames. Together with the OH radicals, the distribution of the HO_2

radicals can assist in identifying the autoignition events in the supersonic flame and further understand the flameholding mechanism.

Finally, the flameholding characteristics and mechanisms in a cavity flameholder with fuel injected upstream are analysed. The cavity plays a very important role on the flameholding because it can provide a stable ignition source to the fluid. Further, the combustion in the cavity is dominated by flame propagation and the combustion at the outer interface of the air and hydrogen streams is mainly dominated by autoignition. Both autoignition and flame propagation contribute to the combustion in the mixing layer and the combustion in the cavity and in the cavity mixing layer are highly coupled. Further, the combustion in the cavity mixing layer also has an effect on the induction reactions in the wake of the hydrogen jet and reduces the induction time of the autoignition.

Chapter 7
Conclusions and future work

The scramjet, which can be the promising air-breathing engine for hypersonic vehicles due to its relatively simple structure and good performance, has been under theoretical, numerical and experimental development since the 1950s. In a scramjet combustor, the flow is supersonic and the fuel remains in the combustor for only an extremely short time (of the order of 1 ms), during which the fuel and air have to be mixed on a molecular level and the combustion has to be completed before the fuel leaves the combustor. It has been revealed that a flameholder, e.g. strut and cavity, is always required in order to enhance the mixing and maintain the flame in the scramjet combustor [1]. However, the complex geometries of the flameholder bring complexity to the flow field. Further, the mixing of the reactants and the stability of the flame is a significant problem in the scramjet and these are not been well understood. A number of experimental investigations have been performed across the world which proved to be extremely expensive and time consuming [1].

With the development of the computing techniques, the CFD approach has become an efficient tool for the investigation of the scramjet aerodynamics and combustion. The RANS approach is the most computational efficient and dominates the turbulence modelling of the scramjet combustor system, however application efforts of the LES approach are increasing and the modelling of the turbulence and combustion in high speed flows is still a significant challenge.

The present research investigates the supersonic combustion in scramjet combustors with strut and cavity flame holders through the RANS and LES strategies. Firstly, the steady flamelet and the UFPV models for turbulent

combustion in a low-speed flow are introduced and extended to supersonic flows and the revised UFPV model takes into account the effects of compressibility. A new strategy are developed and employed to generate the PDF look-up tables for the UFPV model. Secondly, the RANS and LES modelling are employed to a strut-based scramjet engine model in order to understand the mixing and combustion characteristics, and the combustion models are validated on comparing with the experimental data. Thirdly, the LES are performed to simulate the non-reacting and reacting flows in a cavity-based supersonic combustor so as to further validate the flamelet and the UFPV combustion models, as well as to better understand the mixing, local extinction and autoignition of gaseous fuel injected upstream of the cavity. Finally, the flameholding characteristics and mechanisms in a cavity flameholder with fuel injected upstream are analysed.

7.1. Conclusions

The major conclusions from the current research work are as follows:

(i) The steady flamelet and UFPV models for turbulent combustion in a low-speed flow are introduced and extended to supersonic flows and they take into account the effects of compressibility. A new strategy are developed and employed to generate the PDF look-up tables for the UFPV model. These combustion models and the generation strategy of the PDF look-up tables are built into the hybrid RANS/LES in-house code which is used for the simulations of supersonic flames.

(ii) The RANS calculations of the non-reacting flows in a strut-based scramjet engine model are performed using the commercial CFD code FLUENT in order to study the effects of the grid sensitivity, the geometry fidelity and the assumptions of the solid wall boundary conditions. It is revealed that the simulations, which are based on the 2D configuration, are unreliable and therefore a 3D configuration is

recommended for the RANS calculation. Further, the slip-wall assumptions of the strut walls and the combustor walls have different effects on the flow and mixing in the combustor. Thus, the strut wall should be treated as a no-slip surface, however the upper and lower combustor walls only slightly affects the main stream flow and therefore can be treated as slip walls.

(iii) The RANS modelling of the reacting flows in the strut-based combustor is performed with the flamelet and the UFPV models which are built into the in-house code. The results show that both the flamelet model and the UFPV model are capable of predicting the supersonic combustion in the DLR scramjet engine. However, different combustion modelling approaches have an impact on the predicted flame location and shape and the UFPV model appears to give improved predictions.

(iv) The LES is performed to simulate the non-reacting and reacting flows in the strut-based combustor. It is shown that the time-averaged LES results have very similar profiles to those obtained from the RANS predictions. However, the LES calculations provide instantaneous characteristics of the flows, such as the vortices, the motion of the large scale structures, the interaction between the shock and the large scale structures, the interaction of the flame and vortices, and the evolution of the reacting shear layer. Also, there is a reasonable qualitative and quantitative agreement with the experimental data and therefore the UFPV model which is built into the hybrid RANS/LES code is validated to be a promising approach to predict supersonic flames.

(v) The LES is performed to model the non-reacting and reacting flows in a cavity-based combustor. The results indicate that due to the turbulent mixing fluctuations, turbulence-chemistry interactions and compressibility effects, the local extinction, reignition and autoignition events are very common phenomena in the supersonic combustion in a cavity-based combustor, and the UFPV model is able to

predict these events in this supersonic flame with reasonable accuracy. Further, an activation-energy-asymptotic-based Damköhler number concept is a valuable metric to identify flame weakening and extinction in supersonic flames. Together with the OH radicals, the distribution of the HO_2 radicals can assist in identifying the autoignition events in the supersonic flame and further understand the flameholding mechanism.

(vi) The flameholding characteristics and mechanisms in a cavity flameholder with fuel injected upstream are analysed. The cavity plays very important roles on the flameholding because it can provide a stable ignition source to the fluid. Further, the combustion in the cavity is dominated by flame propagation. However, on the outer interface of the air stream and hydrogen stream, the combustion is mainly dominated by autoignition. Both autoignition and flame propagation contribute to the combustion in the mixing layer and the combustion in the cavity and in the cavity mixing layer is highly coupled. Further, the combustion in the cavity mixing layer also has an effect on the induction reactions in the wake of the hydrogen jet and reduces the induction time of the autoignition.

7.2. Present contribution

The major contributions from the current work are:

(i) The UFPV model for turbulent combustion in a low-speed flow is introduced and extended to supersonic compressible flows.

(ii) A new strategy are developed and employed to generate the PDF look-up tables for the UFPV model.

(iii) The UFPV combustion models and the generation strategy of the PDF look-up tables are built into the hybrid RANS/LES in-house code which can be used for the simulations of supersonic flames.

(iv) The performance of the UFPV model is first ever evaluated in predicting the supersonic flames in strut-based and cavity-based supersonic combustors.

(v) The activation-energy-asymptotic-based Damköhler number concept is employed to identify flame weakening and extinction in supersonic flames. Together with the OH radicals, the distribution of the HO_2 radicals is employed to identify the autoignition events in the supersonic flame.

(vi) The flameholding characteristics and mechanisms in a cavity flameholder with fuel injected upstream are analysed. It is found that the cavity provides a stable ignition source to the fluid and the combustion in the cavity is dominated by flame propagation. However, on the outer interface of the air and hydrogen streams, the combustion is mainly dominated by autoignition. Both autoignition and flame propagation contribute to the combustion in the mixing layer. Also, the combustion in the cavity mixing layer can have effects on the induction reactions in the wake of the hydrogen jet and reduce the induction time of the autoignition.

7.3. Recommendations for future work

In view of the complexity of the turbulent supersonic combustion issues, as well as the constraints of the computing and time issues, a number of potential research topics related to the present dissertation can be further investigated:

(i) When calculating the flamelet libraries, it is worth to try some other chemical kinetic solvers, e.g. CHEMKIN [236], and some other hydrogen chemical reaction mechanisms, e.g. the GRI-MECH 3.0 [241]. The effect of the chemical

kinetic solves and the mechanisms on the flamelet libraries and the combustion modelling can be evaluated.

(ii) The techniques relevant to the generation of the inflow turbulence could be built into the hybrid RANS/LES in-house code and generate appropriate inlet boundary conditions for the air and fuel streams.

(iii) Even though the UFPV model can predict the supersonic flames in the strut-based and the cavity-based combustors, it is worth testing the UFPV model with other configurations, e.g. a supersonic lifted co-flowing hydrogen-air diffusion flame by Cheng et al. [134].

(iv) The radiation, pressure and non-unity-Lewis-number effects could be accounted for when calculating the unsteady flamelet libraries and the UFPV approach can be developed and extended into the non-adiabatic UFPV model. These improvements would increase the dimension of the look-up tables, as well as the computational cost, but might result in more accurate predictions.

(v) The UFPV approach can be extended to account for heat transfer to boundaries by solving an additional transport equation for the total enthalpy along with the mixture fraction and progress variable.

(vi) The assumed delta PDFs for progress variable and scalar dissipation rate used in the present research does not account for the effects of subgrid fluctuations. Future improvements could be performed by employing the beta PDF for the progress variable. This improvement would increase the dimension of the look-up tables, but might result in more accurate flow field predictions and flame lift mechanisms.

References

[1] Segal, C., *The scramjet engine: processes and characteristics*, Cambridge University Press, New York, 2009.

[2] Gross, R.A., Chinitz, W., A study of supersonic combustion, *Journal of the Aerospace Sciences*, 27(7): 517-524, 1960.

[3] Yuan, S.X., On supersonic combustion, *Science in China Series a-Mathematics Physics Astronomy*, 42(2): 171-179, 1999.

[4] Heiser, W.H., Pratt, David T., Daley, Daniel H., Mehta, Unmeel B. , *Hypersonic airbreathing propulsion*, AIAA education series, American Institute of Aeronautics and Astronautics, Inc., Washington, 1994.

[5] Roy, G.D., *Combustion processes in propulsion: control, noise and pulse detonation*, Elsevier Butterworth-Heinemann, United States of America, 2006.

[6] Tishkoff J M, D.J.P., Edwards T, Nejad.: Future directions of supersonic combustion research: Air Force/NASA workshop on supersonic combustion. In., pp. AIAA Paper 97-1017. 1997.

[7] Curran, E.T., Murthy, S. N. B., Scramjet propulsion, *Progress in astronautics and aeronautics*, 189: 211-245, 2002.

[8] Jin, L., *Configuration design and performance research for an Airframe/Scramjet integrated hypersonic vehicle*, National University of Defense Technology, Changsha, 2008.

[9] Ferri, A., Mixing-controlled supersonic combustion, *Annual Review of Fluid Mechanics*, 5: 301-338, 1973.

[10] Bakos, R.J., Morgan, R.G., Axisymmetric scramjet thrust production, *Eleventh Australasian Fluid Mechanics Conference, Vols 1 and 2*: 295-298, 1307, 1992.

[11] Sun, M.B., *Flow and flameholding mechanisms of cavity flameholders in supersonic flows*, Doctor of Philosophy, National University of Defense Technology, Changsha, China, 2008.

[12] Hallion, R.P., The history of hypersonics: or, "Back to the future-again and again", Paper presented at the *43rd AIAA Aerospace Sciences Meeting and Exhibit*, 2005.

[13] Curran, E.T., Scramjet engines: The first forty years, *Journal of Propulsion and Power*, 17(6): 1138-1148, 2001.

[14] Ferri, A., Review of Scramjet Technology, *Journal of Aircraft*, 5(1): 3-10, 1968.

[15] Waltrup, P.J., Anderson, G.Y., Stull, F.D., Supersonic combustion ramjet (scramjet) engine development in the united states, (Compendex): 835-861, 1976.

[16] Waltrup, P.J., JOHNS HOPKINS UNIV LAUREL MD APPLIED PHYSICS LAB: Hypersonic airbreathing propulsion: evolution and opportunities. In. 1987.

[17] Waltrup, P.J., White, M.E., Zarlingo, F., Gravlin, E.S., History of ramjet and scramjet propulsion development for US Navy missiles, *Johns Hopkins Apl Technical Digest*, 18(2): 234-243, 1997.

[18] Waltrup, P.J., White, M.E., Zarlingo, F., Gravlin, E.S., History of US Navy ramjet, scramjet, and mixed-cycle propulsion development, *Journal of Propulsion and Power*, 18(1): 14-27, 2002.

[19] Andrews, E.H., Mackley, E. A., Review of NASA's hypersonic research engine preoject, *AIAA Paper 93-2323; also NASA TM1077591*993.

[20] Andrews, E.H., Scramjet development and testing in the United States, Paper presented at the *AIAA/NAL 10th International Space Planes and Hypersonic Systems and Technologies Conf*, 2001.

[21] Fry, R.S., A century of ramjet propulsion technology evolution, *Journal of Propulsion and Power*, 20(1): 27-58, 2004.

[22] McClinton, C.R., Andrew, E. H., and Hut, J. L., Engine development for space access: past, present and future, Paper presented at the *International Symposium on Air Breathing Engines*, 2001.

[23] Curran, E.T., Scramjet engines: The first forty years, *Journal of Propulsion and Power*, 17(Compendex): 1138-1148, 2001.

[24] Henry, J.R., and Anderson, G. Y.: Design considerations for the airframe-integrated scramjet. In: NASA TM X-2895. 1973.

[25] National aero-space plane: A technology development and demonstration program to build the X-30. In: Report GAO/NSIAD-88-122. United States General Accounting Office, Washington, April 1988.

[26] McClinton, C.R., Rausch, V. L., Sitz, J., and Reukauf, P., Hyper-X program status, Paper presented at the *10th International Space Planes and Hypersonic Systems and Technologies Conference*, 2001.

[27] National aero-space plane: restructuring future research and development efforts. In: Report GAO/NSIAD-93-71. United States General Accounting Office, Washington, 1992.

[28] Marguet, R., Cazin, P., Falempin, F. H., and Petit, B., Review and comment on ramjet research in France, *AIAA 97-7000*: 3-13, 1997.

[29] Bissinger, N.C., Koschel, W., Sacher, P. W., and Walther, R., *Scram-jet investigations within the german hypersonic technology program (1993-1996)*, Vol. 189 of Progress in Astronautics and Aeronautics, AIAA, 2000.

[30] Romashkin, A., Russian hypersonic technologies, *Cosmonautics*: 60-62, 2002.

[31] McClinton, C.R., Ricketts, R. H., and Peddie, C. L., Airbreathing hypersonic technology vision vehicles and development dreams, Paper presented at the *AIAA 9th International Space Planes and Hypersonic Systems and Technologies Conference, AIAA 99-4978*, Norfolk, 1999.

[32] Matt Bille, T.W., and Victor Villhard, Reusable space vehicles: lessons from four decades of futility Paper presented at the *4Ist Aerospace Sciences Meeting, AIAA 03-0659*, Reno, 2003.

[33] McClinton, C.R., Rausch, V.L., Nguyen, L.T., Sitz, J.R., Preliminary X-43 flight test results, *International Astronautical Federation - 55th International Astronautical Congress*, Vancouver, Canada, International Astronautical Federation - 55th International Astronautical Congress 2004, pp. 8493-8501, 2004.

[34] McClinton, C.R., Rausch, V.L., Shaw, R.J., Metha, U., Naftel, C., Hyper-X: Foundation for future hypersonic launch vehicles, *International Astronautical Federation - 55th International Astronautical Congress*, Vancouver, Canada, International Astronautical Federation - 55th International Astronautical Congress 2004, pp. 8682-8689, 2004.

[35] The NASA Hyper-X project, http://www.abovetopsecret.com/forum/thread60782/pg1, 2014.

[36] X-51 hypersonic fails in test flight, http://www.airnewstimes.co.uk/x-51-hypersonic-fails-in-test-flight-11467-news.html, 2011.

[37] Chinzei, N., Scramjet engine tests at NAL-KPL, Japan, Paper presented at the *International Symposium on Air Breathing Engines*, 2003.

[38] Chinzei, N., Progress in scramjet research at JAXA-Kakuda, Japan, *Proceedings of Asian Joint Conference on Propulsion and Power*, China, Proceedings of Asian Joint Conference on Propulsion and Power, 2007.

[39] Kumar, A., Bushnell, D.M., Hussaini, M.Y., Mixing augmentation technique for hypervelocity scramjets, *Journal of Propulsion and Power*, 5(Compendex): 514-522, 1989.

[40] Ladeinde, F., A critical review of scramjet combustion simulation, *47th AIAA Aerospace Sciences Meeting including the New Horizons Forum and Aerospace Exposition*, Orlando, United States, 2009.

[41] NASA, http://www.nasa.gov/, 2014.

[42] Ladeinde, F., Advanced computational-fluid-dynamics techniques for scramjet combustion simulation, *AIAA Journal*, 48(Compendex): 513-514, 2010.

[43] Baurle, R.A., Modeling of high speed reacting flows: Established practices and future challenges, *42nd AIAA Aerospace Sciences Meeting and Exhibit*, Reno, NV, United States, AIAA Paper, pp. 2717-2731, 2004.

[44] Welcome to the VULCAN home page, http://vulcan-cfd.larc.nasa.gov/, 2014.

[45] Givi, P., Subgrid scale modeling in turbulent combustion-a review, Paper presented at the *39th AIAA/ASME/SAE/ASEE Joint Propulsion Conference and Exhibit*, 2003.

[46] Givi, P., Filtered density function for subgrid scale modeling of turbulent combustion, *AIAA Journal*, 44(1): 16-23, 2006.

[47] Givi, P., Sheikhi, M.R.H., Drozda, T.G., Madnia, C.K., Invited review: Reliable and affordable simulation of turbulent combustion, Reno, NV, United States, Collection of Technical Papers - 45th AIAA Aerospace Sciences Meeting, pp. 2229-2238, 2007.

[48] Heinz, P., Large-Eddy Simulation of Turbulent Combustion, *Annual Review of Fluid Mechanics*: 453-482, 2006.

[49] Grinstein, F.F., CFD for non-premixed jet combustion, a perspective Paper presented at the *39th Aerospace Sciences Meeting and Exhibit*, Reno, NV, 2001.

[50] Berglund, M., Wikstrom, N., Fureby, C.: Numerical simulation of scramjet combustion. In., vol. FOI-R-1650-SE. Swedish Defence Research Agency, Tumba, 2005.

[51] Mathieu, J., Scott, J., *An introduction to turbulent flow*, Cambridge University Press, New York, 2000.

[52] Jones, W.P., Whitelaw, J.H., Calculation methods for reacting turbulent flows-a review, *Combustion and Flame*, 48(1): 1-26, 1982.

[53] Bardina, J.E., Huang, P. G., Coakley, T.J. , Turbulence modeling validation Paper presented at the *AIAA 97-2121*, 1997.

[54] Jeung, I.S., Choi, J.Y., Numerical simulation of supersonic combustion for hypersonic propulsion, Paper presented at the *5th Asia-Pacific Conference on Combustion*, Adelaide, Australia, 2005.

[55] Menter, F.R., Two-equation eddy-viscosity turbulence models for engineering applications, *AIAA Journal*, 32(8): 1598-1605, 1994.

[56] Xiao, X., Hassan, H.A., Baurle, R.A., Modeling scramjet flows with variable turbulent Prandtl and Schmidt numbers, *AIAA Journal*, 45(6): 1415-1423, 2007.

[57] Edwards, J.R., Advanced implicit algorithm for hydrogen-air combustion calculation, Paper presented at the *AIAA Paper 1996-3129*, 1996.

[58] Edwards, J.R., A low-diffusion flux-splitting scheme for Navier-Stokes calculations, *Computers & Fluids*, 26(6): 635-659, 1997.

[59] Brown, J.L., Turbulence model validation for hypersonic flows, Paper presented at the *8th AIAA/ASME Joint Thermophysics and Heat Transfer Conference*, St Louis, MO, 2002.

[60] Baurle, R.A., Eklund, D.R., Analysis of dual-mode hydrocarbon scramjet operation at Mach 4-6.5, *Journal of Propulsion and Power*, 18(Compendex): 990-1002, 2002.

[61] Smagorinsky, J., General circulation experiments with the primitive equations, *MONTHLY WEATHER REVIEW*, 91(3): 99–164, 1963.

[62] Deardorff, J.W., A numerical study of three-dimensional turbulent channel flow at large Reynolds numbers, *Journal of Fluid Mechanics*, 41: 435-452, 1970.

[63] Pitsch, H., Large-Eddy Simulation of turbulent combustion, *Annual Review of Fluid Mechanics*, 38: 453-482, 2006.

[64] Wagner, C., Sagaut, P., *Large-Eddy Simulation for acoustics*, Cambridge University Press, 2007.

[65] Pope, S.B., *Turbulent flow*, Cambridge University Press, New York, 2000.

[66] Garnier, E., Adams, N., Sagaut, P.: Large Eddy Simulation for compressible flows. Springer. 2009.

[67] Lesieur, M., Metais, O., Comte, P., *Large-eddy simulation of turbulence*, Cambridge University Press, New York, 2005.

[68] Mathew, J., Large Eddy Simulation, *Defence Science Journal*, 60(6): 598-605, 2010.

[69] Grinstein, F., Margolin, L., Rider, W., *Implicit large eddy simulation*, Cambridge University Press, New York, 2007.

[70] Stephen, B.P., Ten questions concerning the Large-Eddy simulation of turbulent flows, *New Journal of Physics*, 6(1): 35, 2004.

[71] Wind-US, http://www.grc.nasa.gov/WWW/winddocs/, 2014.

[72] Nelson, C.C., An overview of the NPARC Alliance's Wind-US flow solver, Orlando, FL, United States, 48th AIAA Aerospace Sciences Meeting Including the New Horizons Forum and Aerospace Exposition, 2010.

[73] Ott, J.D., Kannepalli, C., Brinckman, K., Dash, S.M., Scramjet propulsive flowpath prediction improvements using recent modeling upgrades, Reno, NV, United States, 43rd AIAA Aerospace Sciences Meeting and Exhibit - Meeting Papers, pp. 12651-12664, 2005.

[74] Craft Tech, https://www.craft-tech.com/, 2014.

[75] Bathe, K.J., *Computational fluid and solid mechanics 2003*, . Oxford, 2003.

[76] Air force research laboratory, http://www.wpafb.af.mil/AFRL/, 2014.

[77] Xiao, Y.L., Song, W. Y., S. H., Yang, Application of Large Eddy Simulation in supersonic combustion, *WORLD SCI-TEH R&D*, 30(3): 256-259, 2008.

[78] Spalart, P.R., Jou, W. H., Strelets, M., Allmaras, S. R., Comments on the feasibility of LES for wings, and on a hybrid RANS/LES approach, Paper presented at the *1st AFOSR International Conference on DNS/LES*, 1997.

[79] Chapman, D.R., Computational aerodynamics development and outlook, *AIAA Journal*, 17(12): 1293-1313, 1978.

[80] Sun, M.-B., Liang, J.-H., Wang, Z.-G., Hybrid RANS/LES simulation of the supersonic flow over two-dimensional cavities, *Tuijin Jishu/Journal of Propulsion Technology*, 27(Compendex): 119-123, 2006.

[81] Menter, F.R., Kuntz, M., Langtry, R., Ten years of industrial experience with the SST turbulence model, Paper presented at the *Proceedings of the Fourth International Symposium on Turbulence, Heat and Mass Transfer*, Antalya, Turkey, 2003.

[82] Germano, M., Piomelli, U., Moin, P., Cabot, W.H., A dynamic subgrid-scale eddy viscosity model, *Physics of Fluids A (Fluid Dynamics)*, 3(7): 1760-1765, 1991.

[83] Orszag, S.A., Analytical theories of turbulence, *Journal of Fluid Mechanics*, 41: 363-&, 1970.

[84] Modi, A.: Direct numerical simulation of turbulent flows. Available on Internet. http://www.anirudh.net/courses/ae525/paper.pdf. http://www.anirudh.net/courses/ae525/paper.pdf, 1999.

[85] Martín, M.P., *Direct numerical simulation and Large Eddy Simulation closure of reacting turbulence in hypersonic flows*, University of Minnesota, Minnesota, 1999.

[86] Martín, M.P.: Numerical challenges for DNS and LES of highly compressible turbulence. http://robson.birs.ca/~08w5024/Talks/martin.pdf, 2008.

[87] Li, X.-L., Fu, D.-X., Ma, Y.-W., Liang, X., Direct numerical simulation of compressible turbulent flows, *Acta Mechanica Sinica/Lixue Xuebao*, 26(6): 795-806, 2010.

[88] Mahle, I., *Direct and large-eddy simulation of inert and reacting compressible turbulent shear layers*, Technical University of Munich, Munich, 2007.

[89] Mahle, I., Foysi, H., Sarkar, S., Friedrich, R., On the turbulence structure in inert and reacting compressible mixing layers, *Journal of Fluid Mechanics*, 593: 171-180, 2007.

[90] Guan, F., Wang, Q., Zhu, N., Li, Z., Shen, Q., A DNS approach to stability sturdy about a supersonic mixing layer flow, *Computational Methods in Multiphase Flow IV*, 56: 359-368, 2007.

[91] Shen, Q., Guan, F.M., Zhuang, F.G., Wang, Q., Direct numerical simulation of stability of a supersonic mixing layer flow, *New Trends in Fluid Mechanics Research*: 273-276, 2007.

[92] Sandham, N.D., Sandberg, R.D., Direct numerical simulation of the early development of a turbulent mixing layer downstream of a splitter plate, *Journal of Turbulence*, 10(1): 1-17, 2009.

[93] Edwards, J.R., Upwind relaxation multigrid method for computing three-dimensional, viscous internal flows, *Journal of Propulsion and Power*, 12(Compendex): 146-154, 1996.

[94] Delarue, B.J., Pope, S.B., Application of PDF methods to compressible turbulent flows, *Physics of Fluids*, 9(9): 2704-2715, 1997.

[95] Colucci, P.J., Jaberi, F.A., Givi, P., Pope, S.B., Filtered density function for large eddy simulation of turbulent reacting flows, *Physics of Fluids*, 10(2): 499-515, 1998.

[96] Hanifi, A., Alfredsson, P. H., Johansson, A. V., Henningson, D. S., *Transition, turbulence and combustion modelling*. Kluwer Academic Publishers, Netherlands, 1998.

[97] Peters, N., *Turbulent combustion*, Cambridge University Press, Cambridge, 2004.

[98] Pope, S.B., *Turbulent premixed flames*, vol. 19. Annual Review of Fluid Mechanics, Annual Reviews Inc, Palo Alto, CA, USA, 1987.

[99] Bilger, R.W., Pope, S.B., Bray, K.N.C., Driscoll, J.F., Paradigms in turbulent combustion research, *Proceedings of the Combustion Institute*, 30: 21-42, 2005.

[100] Burke, S.P., Schumann, T.E.W., Diffusion flames, Paper presented at the *Proc. Combust. Inst. 1*, pp. 2-11, 1928.

[101] Hawthorne, W.R., Weddell, D.S., Hottel, H.C., Mixing and combustion in turbulent gas jets, Paper presented at the *Proc Combust Inst 3*, pp. 266–288, 1948.

[102] Homsy, C.A., *Similitude in turbulent free-jet diffusion flames*, Massachusetts Institute of Technology, November, 1959.

[103] Ferri, A., Fox, H., Analysis of fluid dynamics of supersonic combustion process controlled by mixing: 1105-1113, 1968.

[104] Libby, P.A., Bray, K.N.C., Implications of the laminar flamelet model in premixed turbulent combustion *Combustion and Flame*, 39(1): 33-41, 1980.

[105] Peters, N., Laminar diffusion flamelet models in non-premixed turbulent combustion, *Progress in Energy and Combustion Science*, 10(3): 319-339, 1984.

[106] Liew, S.K., Bray, K.N.C., Moss, J.B., A stretched laminar flamelet model of turbulent nonpremixed combustion, *Combustion and Flame*, 56(2): 199-213, 1984.

[107] Favier, V., Vervisch, L., Edge flames and partially premixed combustion in diffusion flame quenching, *Combustion and Flame*, 125(1-2): 788-803, 2001.

[108] Bilger, R.W., Future progress in turbulent combustion research, *Progress in Energy and Combustion Science*, 26(4-6): 367-380, 2000.

[109] Vervisch, L., Hauguel, R., Domingo, P., Rullaud, M., Three facets of turbulent combustion modelling: DNS of premixed V-flame, LES of lifted nonpremixed flame and RANS of jet-flame, *Journal of Turbulence*2004.

[110] Dopazo, C., O'Brien, E.E., Functional formulation of nonisothermal turbulent reactive flows, *Physics of Fluids*, 17(11): 1968-1975, 1974.

[111] Pope, S.B., The relationship between the probability approach and particle models for reaction in homogeneous turbulence, *Combustion and Flame*, 35(1): 41-45, 1979.

[112] Haworth, D.C., Progress in probability density function methods for turbulent reacting flows, *Progress in Energy and Combustion Science*, 36(2): 168-259, 2010.

[113] Xu, J., Pope, S.B., PDF calculations of turbulent nonpremixed flames with local extinction, *Combustion and Flame*, 123(3): 281-307, 2000.

[114] Hsu, A.T., Tsai, Y.L.P., Raju, M.S., Probability density function approach for compressible turbulent reacting flows, *AIAA Journal*, 32(7): 1407-1415, 1994.

[115] Echekki, T., Mastorakos, E., *Turbulent combustion modeling: advances, new trends and perspectives*. Springer Press, New York, 2011.

[116] Kilmenko, A.Y., Multicomponent diffusion of various scalars in turbulent flows, *Fluid Dynamics*, 25(3): 327-334, 1990.

[117] Bilger, R.W., Conditional moment closure for turbulent reacting flow, *Physics of Fluids B Plasma Physics*, 5(4): 436-436, 1993.

[118] Klimenko, A.Y., Bilger, R.W., Conditional moment closure for turbulent combustion, *Progress in Energy and Combustion Science*, 25(6): 595-687, 1999.

[119] Sabel'nikov, V., Deshaies, B., Da Silva, L.F.F., Revisited flamelet model for nonpremixed combustion in supersonic turbulent flows, *Combustion and Flame*, 114(3-4): 577-584, 1998.

[120] Roomina, M.R., Bilger, R.W., Conditional moment closure (CMC) predictions of a turbulent methane-air jet flame, *Combustion and Flame*, 125(3): 1176-1195, 2001.

[121] Borghi, R., *On the structure and morphology of turbulent premixed flames*. Plenum Press, New York, NY, 1985.

[122] Peters, N., The turbulent burning velocity for large-scale and small-scale turbulence, *Journal of Fluid Mechanics*, 384: 107-132, 1999.

[123] Zimont, V.L., Pagnini, G., Lagrangian properties of turbulent diffusion with passive chemical reaction in the framework of the premixed combustion theory, *Physics of Fluids*, 23(3)2011.

[124] Zimont, V.L., Gas premixed combustion at high turbulence. Turbulent flame closure combustion model, *Experimental Thermal and Fluid Science*, 21(1-3): 179-186, 2000.

[125] Zimont, V.L., Battaglia, V., Joint RANS/LES approach to premixed flame modelling in the context of the TFC combustion model, *Flow Turbulence and Combustion*, 77(1-4): 305-331, 2006.

[126] Zimont, V.L., Muhin, E.S., Theoretical maximum efficiency and specific impulse of the external burning scramjet, *16th AIAA/DLR/DGLR International Space Planes and Hypersonic Systems and Technologies Conference*, Bremen, Germany, 16th AIAA/DLR/DGLR International Space Planes and Hypersonic Systems and Technologies Conference, 2009.

[127] ANSYS Inc. FLUENT, , Ansys fluent, theory guide, 2013.

[128] Knudsen, E., Kim, S.H., Pitsch, H., An analysis of premixed flamelet models for large eddy simulation of turbulent combustion, *Physics of Fluids*, 22(11)2010.

[129] Grout, R.W., Bushed, W.K., Blair, C., Predicting the ignition delay of turbulent methane jets using conditional source-term estimation, *Combustion, Theory and Modelling*, 11(6): 1009-1028, 2007.

[130] Lindstedt, R.P., Vaos, E.M., Transported PDF modeling of high-Reynolds-number premixed turbulent flames, *Combustion and Flame*, 145(3): 495-511, 2006.

[131] Domingo, P., Vervisch, L., Bray, K., Partially premixed flamelets in LES of nonpremixed turbulent combustion, *Combustion, Theory and Modelling*, 6(4): 529-551, 2002.

[132] Vervisch, L., Using numerics to help the understanding of non-premixed turbulent flames, *Proceedings of the Combustion Institute*, 28: 11-24, 2000.

[133] Zimmermann, I., Pfitzner, M., Combustion modeling of partially premixed flames, *Proceedings of the Asme Turbo Expo 2010, Vol 2, Pts A and B*: 335-351, 2010.

[134] Cheng, T.S., Wehrmeyer, J.A., Pitz, R.W., Jarrett Jr, O., Northam, G.B., Raman measurement of mixing and finite-rate chemistry in a supersonic hydrogen-air diffusion flame, *Combustion and Flame*, 99(1): 157-173, 1994.

[135] Balakrishnan, G., Williams, F.A., Turbulent combustion regimes for hypersonic propulsion empolying hydrogen-air diffusion flames, *Journal of Propulsion and Power*, 10(3): 434-437, 1994.

[136] Ingenito, A., Bruno, C., Physics and regimes of supersonic combustion, *AIAA Journal*, 48(3): 515-525, 2010.

[137] Baurle, R.A., Hsu, A.T., Hassan, H.A., Assumed and evolution probability density-functions in supersonic turbulent combustion calculations, *Journal of Propulsion and Power*, 11(6): 1132-1138, 1995.

[138] Baev, V.K., Golovichev, V.I., Tretyakov, P.K., Combustion in supersonic-flow, *Combustion Explosion and Shock Waves*, 23(5): 511-521, 1987.

[139] Billig, F.S., Combustion processes in supersonic-flow, *Journal of Propulsion and Power*, 4(3): 209-216, 1988.

[140] Chandra, K.P.B., Gupta, N.K., Ananthkrishnan, N., Park, I.S., Yoon, H.G., Modeling, simulation, and controller design for an air-breathing combustion system, *Journal of Propulsion and Power*, 26(3): 562-574, 2010.

[141] Gao, Z.X., Lee, C.H., A numerical study of turbulent combustion characteristics in a combustion chamber of a scramjet engine, *Science China-Technological Sciences*, 53(8): 2111-2121, 2010.

[142] Ingenito, A., De Flora, M.G., Bruno, C., Giacomazzi, E., Steelant, J., A novel model of turbulent supersonic combustion: Development and validation, Sacramento, CA, United States, Collection of Technical Papers - AIAA/ASME/SAE/ASEE 42nd Joint Propulsion Conference, pp. 423-436, 2006.

[143] Bradshaw, P., Compressible turbulent shear layer, *Annual Review of Fluid Mechanics*, 9: 33-54, 1977.

[144] Shyy, W., Krishnamurty, V.S., Compressibility effects in modeling complex turbulent flows, *Progress in Aerospace Sciences*, 33(9-10): 587-645, 1997.

[145] Lele, S.K., Compressibility effects on turbulence, *Annual Review of Fluid Mechanics*, 26: 211-254, 1994.

[146] Bradshaw, P., Turbulence modeling with application to turbomachinery, *Progress in Aerospace Sciences*, 32(6): 575-624, 1996.

[147] Ingenito, A., De Flora, M. G., Bruno, C., LES modeling of scramjet combustion, Paper presented at the *44th AIAA Aerospace Sciences Meeting and Exhibit*, 2006.

[148] Ingenito, A., Bruno, C., Giacomazzi, E., Steelant, J., Advance in supersonic combustion modelling and simulations, *45th AIAA Aerospace Sciences Meeting*, Reno, NV, United States, Collection of Technical Papers - 45th AIAA Aerospace Sciences Meeting, pp. 10182-10193, 2007.

[149] Sadasivuni, S.K., *LES modelling of non-premixed and partially premixed turbulent flames*, Loughborough University, Loughborough, UK, 2009.

[150] Pierce, C.D., *Progress-variable approach for Large-Eddy simulation of turbulent combustion*, Stanford University, 2001.

[151] Gardiner, W.C., *Combustion chemistry*. Springer-Verlag, New York, 1984.

[152] Leonard, A., Energy cascade in large eddy simulation of turbulent fluid flow, *Adv. Geophys*, 18A: 237-248, 1974.

[153] Thomas, F., Ming, T., Jack, E., Hassan, H., Robert, B., *Validation of a hybrid Reynolds-averaged/large-eddy simulation method for simulating cavity flameholder configurations*, 15th AIAA Computational Fluid Dynamics Conference. Fluid Dynamics and Co-located Conferences, American Institute of Aeronautics and Astronautics, 2001.

[154] Fan, Z.Q., *Investigation of validation, modelling and application of flamelet model in supersonic turbulent combustion*, Doctor of Philosophy, National University of Defense Technology, Changsha, China, 2011.

[155] Yoshizawa, A., Horiuti, K., A statistically-derived subgrid-scale kinetic energy model for the Large-Eddy simulation of turbulent flows, *Journal of the Physical Society of Japan*, 54(8): 2834-2839, 1985.

[156] Shu, C., High order weighted essentially nonoscillatory schemes for convection dominated problems, *Siam Review*, 51(1): 82-126, 2009.

[157] Shu, C.-W., *High order ENO and WENO schemes for computational fluid dynamics*, High-Order Methods for Computational Physics, vol. 9. Lecture Notes in Computational Science and Engineering, Springer Berlin Heidelberg, 1999.

[158] John D. Anderson, J., *Computational fluid dynamics.the basics with applications,*, McGraw-Hill, Inc., 1995.

[159] Garnier, E., Sagaut, P., Deville, M., Large eddy simulation of shock/boundary-layer interaction, *Aiaa Journal*, 40(10): 1935-1944, 2002.

[160] Cannizzaro, F.E., Ash, R.L.: Investigation of upwind, multigrid, multiblock numerical schemes for three dimensional flows. Volume 1: Runge-Kutta methods for a thin layer Navier-Stokes solver. In., vol. NASA-CR-191648. 1992.

[161] Gottlieb, S., Shu, C.-W., Total variation diminishing Runge-Kutta schemes, *Math. Comp.*, 67: 73--85, 1998.

[162] Ravikanti, M., *Advanced flamelet modelling of turbulent non-premixed and partially premixed combustion*, Loughborough University, Loughborough, UK, 2008.

[163] Terrapon, V.E., Ham, F., Pecnik, R., Pitsch, H.: A flamelet-based model for supersonic combustion. center for turbulence research. In: Annual Brief. Stanford University, 2009.

[164] Bilger, R.W., The structure of turbulent non-premixed flames, Paper presented at the *Twentysecond Symposium (International) on Combustion*, pp. 475-488, 1988.

[165] Pitsch group flamemaster, http://www.itv.rwth-aachen.de/en/downloads/flamemaster/, 2014.

[166] Pitsch, H., Peters, N., A consistent flamelet formulation for non-premixed combustion considering differential diffusion effects, *Combustion and Flame*, 114(1-2): 26-40, 1998.

[167] Ferreira, J.C., *Flamelet modelling of stabilization in turbulent non-premixed combustion*, The Swiss Federal Institute of Technology Zurich, Zurich, Switzerland, 1996.

[168] Pierce, C.D., Moin, P., Progress-variable approach for large-eddy simulation of non-premixed turbulent combustion, *Journal of Fluid Mechanics*, 504: 73-97, 2004.

[169] Ihme, M., Pitsch, H., LES of a non-premixed flame using an extended flamelet/progress variable model, Reno, NV, United States, 43rd AIAA Aerospace Sciences Meeting and Exhibit - Meeting Papers, pp. 7489-7502, 2005.

[170] Pitsch, H., Ihme, M., An unsteady/flamelet progress variable method for les of nonpremixed turbulent combustion, Reno, NV, United States, 43rd AIAA Aerospace Sciences Meeting and Exhibit - Meeting Papers, pp. 2593-2606, 2005.

[171] Ihme, M., See, Y.C., Prediction of autoignition in a lifted methane/air flame using an unsteady flamelet/progress variable model, *Combustion and Flame*, 157(10): 1850-1862, 2010.

[172] Ahmed, I., Swaminathan, N., Simulation of turbulent explosion of hydrogen–air mixtures, *International Journal of Hydrogen Energy*, 39(17): 9562-9572, 2014.

[173] Waidmann, W., Alff, F., Bohm, M., Brummund, U., Clauss, W., Oschwald, M., Supersonic combustion of hydrogen/air in a scramjet combustion chamber, *Space Technology*, 15(6): 421-421, 1995.

[174] Waidmann, W., Brummund, U., Nuding, J., *Experimental investigation of supersonic ramjet combustion (Scramjet)*. Taylor and Francis, Washington, D.C., 1995.

[175] Guerra, R., Waidmann, W., Laible, C., An experimental investigation of the combustion of a hydrogen jet injected parallel in a supersonic air stream, Paper presented at the *AIAA Third International Aerospace Planes Conference*, Orlando, FL, USA, 1991.

[176] Chemical-kinetic mechanisms for combustion applications, mechanical and aerospace engineering (combustion research), University of California at San Diego, http://web.eng.ucsd.edu/mae/groups/combustion/mechanism.html, 2012.

[177] Weydahl, T., Poyyapakkam, M., Seljeskog, M., Haugen, N.E.L., Assessment of existing H2/O2 chemical reaction mechanisms at reheat gas turbine conditions, *International Journal of Hydrogen Energy*, 36(18): 12025-12034, 2011.

[178] Oevermann, M., Numerical investigation of turbulent hydrogen combustion in a SCRAMJET using flamelet modeling, *Aerospace Science and Technology*, 4: 463-480, 2000.

[179] Mura, A., Izard, J.F., Numerical simulation of supersonic nonpremixed turbulent combustion in a scramjet combustor model, *Journal of Propulsion and Power*, 26(4): 858-868, 2012.

[180] Chandraprakash, T., Computational simulation of scramjet combustors - a comparison between quasi-one dimensional and 2-D numerical simulations, Paper presented at the *17th AIAA International Space Planes and Hypersonic Systems and Technologies Conference*, 2011.

[181] Ulrich, W., Wolfgang, K., Numerical investigation of turbulent reacting flows in a scramjet combustor model, Paper presented at the *38th AIAA/ASME/SAE/ASEE Joint Propulsion Conference & Exhibit*, 2002.

[182] Pandey, K.M., Roga, S., Singh, A.P., Numerical analysis of supersonic combustion using strut injector with turbulent non-premixed combustion model, *Transaction on Control and Mechanical Systems*, 1(2): 73-81, 2012.

[183] Potturi, A.S., Edwards, J.R., LES/RANS simulation of a supersonic combustion experiment, Paper presented at the *50th AIAA Aerospace Sciences Meeting including the New Horizons Forum and Aerospace Exposition*, 2012.

[184] Luo, W., Ma, L., Ingham, D.B., Pourkashanian, M., Fan, Z., Huang, W., Numerical investigation of reacting flow in a scramjet engine using flamelet and flamelet/progress variable models, Paper presented at the *Eighth Mediterranean Combustion Symposium*, Cesme, Turkey, 2013.

[185] Fan, Z., Liu, W., Sun, M., Wang, Z., Zhuang, F., Luo, W., Theoretical analysis of flamelet model for supersonic turbulent combustion, *Science China Technological Sciences*, 55(1): 193-205, 2012.

[186] Berglund, M., Fureby, C., LES of supersonic combustion in a scramjet engine model, *Proceedings of the Combustion Institute*, 31(2): 2497-2504, 2007.

[187] Genin, F., Menon, S., Simulation of turbulent mixing behind a strut injector in supersonic flow, *AIAA Journal*, 48(3): 526-539, 2010.

[188] Fan, Z.Q., Sun, M.B., Liu, W.D., Three dimensional large eddy simulation of supersonic combustion flowfield with strut, *Guofang Keji Daxue Xuebao/Journal of National University of Defense Technology*, 33(1): 1-6, 2011.

[189] Pitsch, H., Trouillet, P., Pierce, C.D., A joint experimental/large eddy simulation study of a model gas turbine combustor, *Meeting of the Western States Section of the Combustion Institute*, San Diego, 2002.

[190] Fan, Z.Q., Sun, M.B., Liu, W.D., Flamelet/progress variable model for supersonic reacting flows, *Hangkong Dongli Xuebao/Journal of Aerospace Power*, 26(8): 1750-1755,

[191] Christopher L. Rumsey, D.O.A., Robert T. Biedron, Pieter G. Buning, Thomas G. Gainer, Joseph H. Morrison, S. Melissa Rivers, Stephen J. Mysko, David P. Witkowski: CFD sensitivity analysis of a modern civil transport near Buffet-Onset conditions. In., vol. NASA / TM-2001-211263. Langley Research Center, Hampton, Virginia, USA, 2001.

[192] Gebreslassie, M.G., Tabor, G.R., Belmont, M.R., CFD simulations for sensitivity analysis of different parameters to the wake characteristics of tidal turbine, *Open Journal of Fluid Dynamics*, 2(3): 56-64, 2012.

[193] Oliver, A.B., Lillard, R.P., Schwing, A.M., Blaisdell, G.A., Lyrintzis, A.S., Assessment of turbulent shock-boundary layer interaction computations using the OVERFLOW code, Reno, NV, United states, Collection of Technical Papers - 45th AIAA Aerospace Sciences Meeting, pp. 1182-1212, 2007.

[194] Hirsch, C., *Chapter 6 - structured and unstructured grid properties*, Numerical Computation of Internal and External Flows (Second Edition). Butterworth-Heinemann, Oxford, 2007.

[195] Settles, G.S., *Schlieren and shadowgraph techniques: visualizing phenomena in transparent media*, 2nd ed, Experimental Fluid Mechanics, Springer, 2006.

[196] Xing, J.W., Le, J.L., Application of flamelet model for the numerical simulation of turbulent combustion in scramjet, Paper presented at the *International Conference on Methods of Aerophysical Research, ICMAR 2008*, Akademgorodok, Novosibirsk Russia, 2008.

[197] Yang, Y., Xing, J.-W., Le, J.-L., Wang, J.-N., Effect of turbulent combustion model on simulation of hydrogen supersonic combustion, *Hangkong Dongli Xuebao/Journal of Aerospace Power*, 23(4): 605-610, 2008.

[198] Zhuang, M., Dimotakis, P.E., Instability of wake-dominated compressible mixing layers, *Physics of Fluids*, 7(10): 2489-2495, 1995.

[199] Davidson, P.A., *Turbulence: an Introduction for scientists and engineers*, Oxford University Press, Oxford, UK, 2004.

[200] Hassard, B.D., Kazarinoff, N.D., Wan, Y.-H., *Theory and applications of hopf bifurcation*, vol. 41, London Mathematical Society Lecture Note Series, The Press Syndicate of the University of Cambridge, Cambridge, 1981.

[201] Tkatchenko, I., Kornev, N., Jahnke, S., Steffen, G., Hassel, E., Performances of LES and RANS models for simulation of complex flows in a coaxial jet mixer, *Flow, Turbulence and Combustion*, 78(2): 111-127, 2007.

[202] Hassan, E., Boles, J., Aono, H., Davis, D., Shyy, W., Supersonic jet and crossflow interaction: Computational modeling, *Progress in Aerospace Sciences*, 57(0): 1-24, 2013.

[203] Vreman, A.W., Sandham, N.D., Luo, K.H., Compressible mixing layer growth rate and turbulence characteristics, *Journal of Fluid Mechanics*, 320: 235-258, 1996.

[204] Gai, S.L., Tarnopolsky, A., Riley, A.J., Study of a mxing layer formed by a supersonic main stream of air and a co-flowing supersonic helium jet, *Flow, Turbulence and Combustion*, 68(3): 195-226, 2002.

[205] Mueller, M.E., Iaccarino, G., Pitsch, H., Chemical kinetic uncertainty quantification for Large Eddy Simulation of turbulent nonpremixed combustion, *Proceedings of the Combustion Institute*, 34(1): 1299-1306, 2013.

[206] Gaitonde, U.: Quality criteria for Large Eddy simulation. In: First year transfer report. School of MACE, University of Manchester, 2008.

[207] Charles, S., *Turbulence modeling for time-dependent RANS and VLES - A review*, 13th Computational Fluid Dynamics Conference. Fluid Dynamics and Co-located Conferences, American Institute of Aeronautics and Astronautics, 1997.

[208] Liu, K., Pletcher, R.H., Inflow conditions for the large eddy simulation of turbulent boundary layers: A dynamic recycling procedure, *Journal of Computational Physics*, 219(1): 1-6, 2006.

[209] Huang, S.H., Li, Q.S., Wu, J.R., A general inflow turbulence generator for large eddy simulation, *Journal of Wind Engineering and Industrial Aerodynamics*, 98(10–11): 600-617, 2010.

[210] Edwards, J.R., Numerical simulations of shock/boundary layer interactions using time-dependent modeling techniques: A survey of recent results, *Progress in Aerospace Sciences*, 44(6): 447-465, 2008.

[211] John, B., Kulkarni, V.N., Natarajan, G., Shock wave boundary layer interactions in hypersonic flows, *International Journal of Heat and Mass Transfer*, 70(0): 81-90, 2014.

[212] Aspden, A.J., Day, M.S., Bell, J.B., Lewis number effects in distributed flames, *Proceedings of the Combustion Institute*, 33(1): 1473-1480, 2011.

[213] Moule, Y., Sabelnikov, V., Mura, A., Highly resolved numerical simulation of combustion in supersonic hydrogen–air coflowing jets, *Combustion and Flame*, 161(10): 2647-2668, 2014.

[214] Mathur, T., Gruber, M., Jackson, K., Donbar, J., Donaldson, W., Jackson, T., Billig, F., Supersonic combustion experiments with a cavity-based fuel injector, *Journal of Propulsion and Power*, 17(6): 1305-1312, 2001.

[215] Lawson, S.J., Barakos, G.N., Review of numerical simulations for high-speed, turbulent cavity flows, *Progress in Aerospace Sciences*, 47(3): 186-216, 2011.

[216] Roudakov, A.S., Y; Semenov, V; Novelli, Ph; Fourt, O., Flight testing an axisymmetric scramjet-Russion recent advances, Paper presented at the *44th IFA Congress*, 1993.

[217] Ben-Yakar, A., Hanson, R.K., Cavity flame-holders for ignition and flame stabilization in scramjets: An overview, *Journal of Propulsion and Power*, 17(4): 869-877, 2001.

[218] Wang, H.B., *Combustion modes and oscillation mechanisms of cavity-stabilized jet combustion in supersonic flows*, Doctor of Philosophy, National University of Defense Technology, Changsha, China, 2012.

[219] Wang, H., Wang, Z., Sun, M., Qin, N., Large-Eddy/Reynolds-averaged Navier–Stokes simulation of combustion oscillations in a cavity-based supersonic combustor, *International Journal of Hydrogen Energy*, 38(14): 5918-5927, 2013.

[220] Wang, H., Wang, Z., Sun, M., Qin, N., Combustion characteristics in a supersonic combustor with hydrogen injection upstream of cavity flameholder, *Proceedings of the Combustion Institute*, 34(2): 2073-2082, 2013.

[221] Karagozian, A.R., Transverse jets and their control, *Progress in Energy and Combustion Science*, 36(5): 531-553, 2010.

[222] Ben-Yakar, A., *Experimental investigation of mixing and ignition of transverse jets in supersonic crossflows*, Stanford university, 2000.

[223] Cortelezzi, L., Karagozian, A.R., On the formation of the counter-rotating vortex pair in transverse jets, *Journal of Fluid Mechanics*, 446: 347-373, 2001.

[224] Sick, V., High speed imaging in fundamental and applied combustion research, *Proceedings of the Combustion Institute*, 34(2): 3509-3530, 2013.

[225] Fan, Z.-Q., Liu, W.-D., Lin, Z.-Y., Sun, M.-B., Experimental investigation on supersonic combustion flame structure with cavity injectors, *Tuijin Jishu/Journal of Propulsion Technology*, 34(1): 62-68, 2013.

[226] Mastorakos, E., Ignition of turbulent non-premixed flames, *Progress in Energy and Combustion Science*, 35(1): 57-97, 2009.

[227] Hasselbrink, E.F., Mungal, M.G., Transverse jets and jet flames. Part 1. Scaling laws for strong transverse jets, *Journal of Fluid Mechanics*, 443: 1-25, 2001.

[228] Hasselbrink, E.F., Mungal, M.G., Transverse jets and jet flames. Part 2. Velocity and OH field imaging, *Journal of Fluid Mechanics*, 443: 27-68, 2001.

[229] Kolla, H., Grout, R.W., Gruber, A., Chen, J.H., Mechanisms of flame stabilization and blowout in a reacting turbulent hydrogen jet in cross-flow, *Combustion and Flame*, 159(8): 2755-2766, 2012.

[230] Zhang, H., Garmory, A., Cavaliere, D.E., Mastorakos, E., Large Eddy Simulation/Conditional Moment Closure modeling of swirl-stabilized non-premixed flames with local extinction, *Proceedings of the Combustion Institute*(0)

[231] Narayanan, P., Baum, H.R., Trouvé, A., Effect of soot addition on extinction limits of luminous laminar counterflow diffusion flames, *Proceedings of the Combustion Institute*, 33(2): 2539-2546, 2011.

[232] Lecoustre, V.R., Arias, P.G., Roy, S.P., Luo, Z., Haworth, D.C., Im, H.G., Lu, T.F., Trouvé, A., Direct numerical simulations of non-premixed ethylene–air flames: Local flame extinction criterion, *Combustion and Flame*(0)

[233] Lecoustre, V.R., Narayanan, P., Baum, H.R., Trouvé, A., Local extinction of diffusion flames in fires, *Fire Safety Science*, pp. 583-595, 2011.

[234] Chemkin-CFD for fluent 20112, reaction design: San Diego. In. 2013.

[235] Sun, C.J., Sung, C.J., He, L., Law, C.K., Dynamics of weakly stretched flames: quantitative description and extraction of global flame parameters, *Combustion and Flame*, 118(1–2): 108-128, 1999.

[236] Chemkin 10131, Reaction Design: San Diego. In. 2013.

[237] Sripakagorn, P., Mitarai, S., Kosály, G., Pitsch, H., Extinction and reignition in a diffusion flame: A direct numerical simulation study, *Journal of Fluid Mechanics*, 518: 231-259, 2004.

[238] Gordon, R.L., Masri, A.R., Pope, S.B., Goldin, G.M., A numerical study of auto-ignition in turbulent lifted flames issuing into a vitiated co-flow, *Combustion Theory and Modelling*, 11(3): 351-376, 2007.

[239] Rasmussen, C.C., Dhanuka, S.K., Driscoll, J.F., Visualization of flameholding mechanisms in a supersonic combustor using PLIF, *Proceedings of the Combustion Institute*, 31(2): 2505-2512, 2007.

[240] Wang, H., Wang, Z., Sun, M., Wu, H., Combustion modes of hydrogen jet combustion in a cavity-based supersonic combustor, *International Journal of Hydrogen Energy*, 38(27): 12078-12089, 2013.

[241] GRI-MECH 3.0 mechanism, http://www.me.berkeley.edu/gri_mech/, 2014.